TECHNISCHE UNIVERSITÄT MÜNCHEN
Lehrstuhl für Leichtbau

Multicriteria Optimization of Fiber Composite Structures with Respect to Structural Performance and Manufacturing

Markus Edwin Schatz

Vollständiger Abdruck der von der Fakultät für Maschinenwesen der Technischen Universität München zur Erlangung des akademischen Grades eines

Doktor-Ingenieurs (Dr.-Ing.)

genehmigten Dissertation.

Vorsitzender: Univ.-Prof. Dr.-Ing. Manfred Hajek

Prüfer der Dissertation:

1. Univ.-Prof. Dr.-Ing. Horst Baier

2. Univ.-Prof. Dr.-Ing. Klaus Drechsler

Die Dissertation wurde am 27.01.2016 bei der Technischen Universität München eingereicht

und durch die Fakultät für Maschinenwesen am 22.06.2016 angenommen.

♦ **Dedication** ♦

To my parents and brother, who have always been there for me.
Due to their great encouragement and never-ending support,
I was able to study in Munich and proceed to my Ph.D..
Their inspirational lifes have been an example,
keeping me focused throughout my studies.

Acknowledgments

First and foremost, I express my special appreciation and gratitude to my advisor Professor Dr.-Ing. Horst Baier, who has been a tremendous support. This is not only because of his great experience and deep understanding in the vast field of numerical design optimization, but also because he thoroughly guided and encouraged my research work, while still allowing space to grow as a scientist. I would also like to thank Professor Dr.-Ing. Manfred Hajek the chairman and Professor Dr.-Ing. Klaus Drechsler the second examiner for supporting this thesis by being active members of the adjudication committee.

I also owe special thanks to all of my colleagues at the Institute of Lightweight Structures of the Technische Universität München. The collegial and friendly atmosphere has been a great stimulus. Further, the emergence of huge collective projects such as EOS did enormously contribute. In this regard, I especially have to thank Erich Wehrle, Luiz da Rocha-Schmidt and Andreas Hermanutz, who each especially enriched my research work by mutual exchange of simulation models, software et cetera and moreover for advising me. For proofreading my thesis, I would also like to thank Martin Mahl and, again, Erich Wehrle.

My parents and brother, supported my achievements the best a family could ever do, which I greatly appreciate. Finally I would like to give acknowledgment to the massive contribution through the research conducted by all of my thirty-eight students I had the honor to advise during my time at the institute.

Olching, January 2016

Markus Schatz

Abstract

Herein, methods for the holistic multiobjective design optimization of composite structures are developed and discussed. Consideration of manufacturing effort is the the first pillar of realizing holistic optimization. The modeling of manufacturing effort is based on expert knowledge, where soft computing facilitates the emulation of expert's judgment competence. An enrichment to prior effort models have been realized by extending capabilities providing reason and giving refinement advice. Beside this technical pillar of the optimization process, the structural-mechanics has been strengthened by a decoupled multi-scale homogenization approach. Lastly, numerics–as another important column of optimization–are equipped by methods for equidistant approximations of Pareto frontiers, which commonly form in vector optimization. These aspects are studied on comprehend-able academic examples, as well as industry relevant ones.

Kurzfassung

In dieser Arbeit werden Methoden zur multikriteriellen ganzheitlichen Optimierung von Faserverbundstrukturen entwickelt und anschließend diskutiert. Die Berücksichtigung von Fertigungsaufwänden repräsentiert hierbei die erste Säule der ganzheitlichen Optimierung. Um diese Aufwände quantifizierbar zu machen, wird auf Methoden der weichen Modellbildung zurückgegriffen. Hierbei wird eine Bereicherung zu vorherigen Aufwandsmodellen realisiert, indem diese um eine Begründung des Ausgabe und mögliche Ausgestaltungshinweise erweitert werden. Neben dieser technischen Säule des ganzheitlichen Optimierungsprozesses, wird auch die der Strukturmechanik durch einen entkoppelten Mehrskalenhomogenisierungsansatz gestärkt. Zu guter Letzt, wird der letzte Pfeiler des ganzheitlichen Optimierungsprozesses gesetzt; die Numerik. Hierfür wird eine Methode zur Findung von äquidistanten Approximationen von Pareto-Fronten implementiert und untersucht. Diese Fronten stellen häufig die gesuchte Lösungsmenge in der Vektoroptimierung dar. Die erarbeiteten ganzheitlichen Methoden werden zuerst an akademischen Beispielen aufgezeigt und im Weiteren auf große Strukturproblem angewandt.

Contents

List of Figures

List of Tables

Part I.

Prelude

1 Introduction

This first section depicts the goals the conducted research was proceeding to. This is done by first providing the key idea and, thus, the core of the motivation for the research work done. The subsequent section underlines this motivation by giving a brief review on contemporary literature, thereby highlighting the momentum of this topic. Finally, the goals of this work will be stated and the structure of the thesis will be outlined.

Contents

1.1. Motivation and scope of thesis

It is well-known, that carbon fiber reinforced polymers CFRP bear a huge lightweight potential. An example can be found in their promising mass specific properties, such as their favorable ratio of Young's modulus in reinforcement direction to density. In addition to that, they present more design parameters and unseen possibilities in manufacturing, such as to build integrally or functionalize structures. On the contrary to that, they also bring forth higher designing complexity, due to the multitude of parameters, which do demand optimal determination. Specifically, an engineer needs to assign fiber material, matrix material, volume fraction and many more for an unidirectional ply. Ascending in the length scales, the stacking and orientation of these unidirectional plies need to be determined as well. As already observable, this marks the challenge: Explicitly, to overlook and handle all parameters involved in composite design in an optimal fashion, so as to unlock the full lightweight potential, thereby making the material as competitive to established lightweight materials as possible. This challenge encompasses not only such sophisticated physical disciplines as structural mechanics. But moreover, technical ones, where the most appropriate manufacturing technique is to be chosen and considered, such that the final composite structure can be realized at low or tolerable effort levels and hence costs.

To address this challenge, a general optimization framework, spanning several relevant disciplines, is set-up in this thesis. First and foremost, the requirements of structural mechanics are met by forming the optimization process upon a mechanical basis. This basis is defined by structural continuum mechanics, being complemented by material models. These material models are defined based on a decoupled multi-scale homogenization approach. The decoupling is thereby realized by a novel approach being development by this research work. In addition to the consideration of these briefly outlined physical aspects, the established optimization process also regards technical aspects as well. For that matter, an approach deduced from the discipline soft computing, is adopted so as to capture and thereafter expressing expert knowledge concerning the manufacturing of composites.

Finally, the scope of this thesis lies on the early design phase, where most designing freedoms are at disposal for the optimization process and, in that consequence, most of the lightweight potential can be released.

1.2. State of the art

Composite design is predestinated for the application of optimization for multiple reasons. This is particularly due to the manifold of parameters inherently being involved in designing composite structures. Moreover, these parameters such as the orientation of reinforcements do substantially interact with the composite structure's realizable stiffness and strength quantities. A challenge being seldomly addressed, but of paramount importance, is the simultaneous consideration of structural mechanics and manufacturing aspects. This is of relevance, since manufacturing processes not only have a strong imprint onto the mechanical properties of the composite material, but also onto the realizable designs, i.e. design parameter and variable values, and even further onto the associated manufacturing costs. This clearly request the optimization process to be general enough to account responses originating from structural mechanics and manufacturing, such that parameters can be adjusted to strike optimal compromise in-between both goals; i.e. maximal structural efficiency and minimal manufacturing effort. Beside the necessity of a general profound optimization framework, there is obviously also the demand for efficient, reliable and robust modeling procedures for capturing manufacturing aspects at early design phases. The latter is because of the fact, that optimization itself can deploy its beneficial effects most effectively at the beginning of the designing process, where most parameters exhibit great designing freedom.

In the past decades, great effort has been made to meet the aforementioned demands by incorporating technical constraints into structural design optimization, thereby leveraging it towards higher technical significance. Wang and Costin (1991) optimized a composite wing box structure for which they considered three different manufacturing constraints via analytic expressions, with which they essentially bounded the design space of the optimization problem. The three constraints discussed in their work were: ply orientation percentage (controlling the relative thickness of each ply via upper and lower design variable limits), maximum drop-off slopes (Lower the delamination tendency at the considered ply drop-offs by defining maximal allowable slopes) and, finally, the interleaving of plies (aims to mitigate stiffness jumps and to assure a certain structural integrity by probing for continuing plies). Sure enough, the significance of the optimization approach has been increased by ensuring that the optimized designs are closer to a technical reality in terms of manufacturing. This work marks one starting point for more sophisticated approaches, which for instance enable the consideration of more complex technical manufacturing considerations, where interactions are regarded as well.

Henderson et al. (1999) optimized a composite stiffened panel while simultaneously considering composite failure and associated manufacturing effort. In this work, the manufacturing effort has been derived for a resin film infusion (RFI) with which resin is brought into the dry textile carbon fiber preform. RFI is regarded as a cost effective process for resin transforming. By considering both, mass and manufacturing time of the stiffened panel as an objective, Henderson et al. show that both can have an competitive relationship. These contra-acting objectives did ultimately lead to pareto frontiers, where pareto-optimal solutions, each representing an optimal compromise, are gathered. Irisarri et al. (2014) present a state of the art realization of this approach.

Another source of inspiration is the work of Ghiasi et al. (2008), in which a globalized Nelder-Mead algorithm is applied on a composite bracket in Z-form. Therein, the spring-in of the bracket after curing, is set to be the manufacturing objective along with structural objectives and constraints, such as mass, deflection and load factor. Due to the presence of multiple objectives, they had solve a vector optimization problem. In Ghiasi et al. (2010) the mentioned globalized Nelder-Mead algorithm is applied on a braided bicycle stem connecting the handlebar with the bicycle's fork. In this work,

resin transfer molding (RTM) has been used as the vehicle to discuss simultaneous optimization of structural and manufacturing objectives. The objectives namely were: weight, failure index and manufacturing time. A hollow braid structure could be realized by an inflatable bladder and the involved process parameters were considered as well (bladder-assisted RTM process). By varying the design variables braid diameter and process pressures pareto optimal solutions are found. The variation of braid fiber orientation, thickness and fiber volume fraction is covered via curve fitting based on the braid diameter. A major outcome of the work is given by the set of solutions of the vector optimization, where each is derived by simultaneously considering the structure's mass, failure indices and manufacturing time as objectives. In addition, they made it comprehensible, how different conflicting goals could arise in an optimization problem originating from physical and technical areas.

Further examples of research on vector optimization simultaneously considering mechanical and manufacturing aspects can be found with ease. For instance, Nadir et al. (2004) performed shape optimizations, while considering an abrasive water jet cutting as the manufacturing process and Park et al. (2004) optimized a composite panel produced via a RTM process incorporating design variables which directly influence both models. More examples are given by Dimopoulos and Zalzala (2000), where several problems and their solution are being discussed. Nonetheless, most of the so far discussed research activities use rather simple analytic expressions for quantifying manufacturing effort caused by the related manufacturing technique. An attractive approach mitigating this, is the modeling of qualitative information or, speaking more generally, soft aspects. By doing so, expert knowledge regarding that manufacturing technique can be made accessible and exploitable for studying processes that involve many parameters, whose interactions are highly complex or partially unknown. This is for instance the case for many preforming techniques, such is for braiding. Moreover, manufacturing models should be able to mimic human capabilities in evaluating complex situations and making decisions based on provided knowledge and gained experience. This would broaden the range of application of structural design optimization at least in a practical setting. Therefore, one of the major goals of this work is to meet this demand for more holistic manufacturing models being capable to consider known sharp relationships as well as soft aspects based on verbal expertise.

One of the first steps into this direction, has been made by Huber (2010) how studied and propagated the framework for doing so; the framework of fuzzy logic as a representative of the discipline soft computing. A similar framework has for instance been used by Iqbal et al. (2007) in his work, where a knowledge-based system has been determined to study and evaluate performance measures for milling. Another contribution into the direction of capturing soft aspect is made by Zhou and Saitou (2015). In this work, a intelligent machine is developed to capture process associated aspects. The intelligent machine was trained by multiple process simulations. Recently, many publication in structural design optimization pointing into this direction of enriching the optimization process by quantifying soft aspects. Two examples underpinning this are given by Yildiz (2013) and Huang et al. (2015). Both use the soft computing methodology so as to capture qualitative and therefore aspects being hard to model with classical approaches. Both researcher demonstrate how the optimization process is being lifted to a higher significance. Singh et al. (2012) present a survey of research papers pointing into the same direction. Studying this recent progresses reveals, that the significance of the optimization process is lifted since the soft computing of qualitative aspects made the optimization models more holistic. But, however, most researcher utilize zero order optimization algorithms and, hence, may compromise in terms of numerical efficiency.

An introduction into the wide composite field and the manufacturing techniques to produce them is given by Mazumdar (2002) with his book on composite manufacturing. Schürmann (2005) and Jones (1999) shall be recommended as basic literature addressing composite designing and the associated manufacturing aspects.

1.3. Aims and structure of the thesis

As outlined above, so far, there is no research work–at least known to the author–explicitly addressing the issue of optimizing composite parts, while simultaneously considering physical and technical criteria, while, moreover, exploiting gradient-based algorithms in an efficient way. Figure 1.1 provides an overview on the three columns on which the thesis shall rest on. As can be seen, the key topic, addressed herein, is the holistic optimization of composite structures. Since optimization tasks are obtained spanning several disciplines (multidisciplinary) and involving conflicting criteria (multi-criteria), a profound mathematical framework needs to be set up.

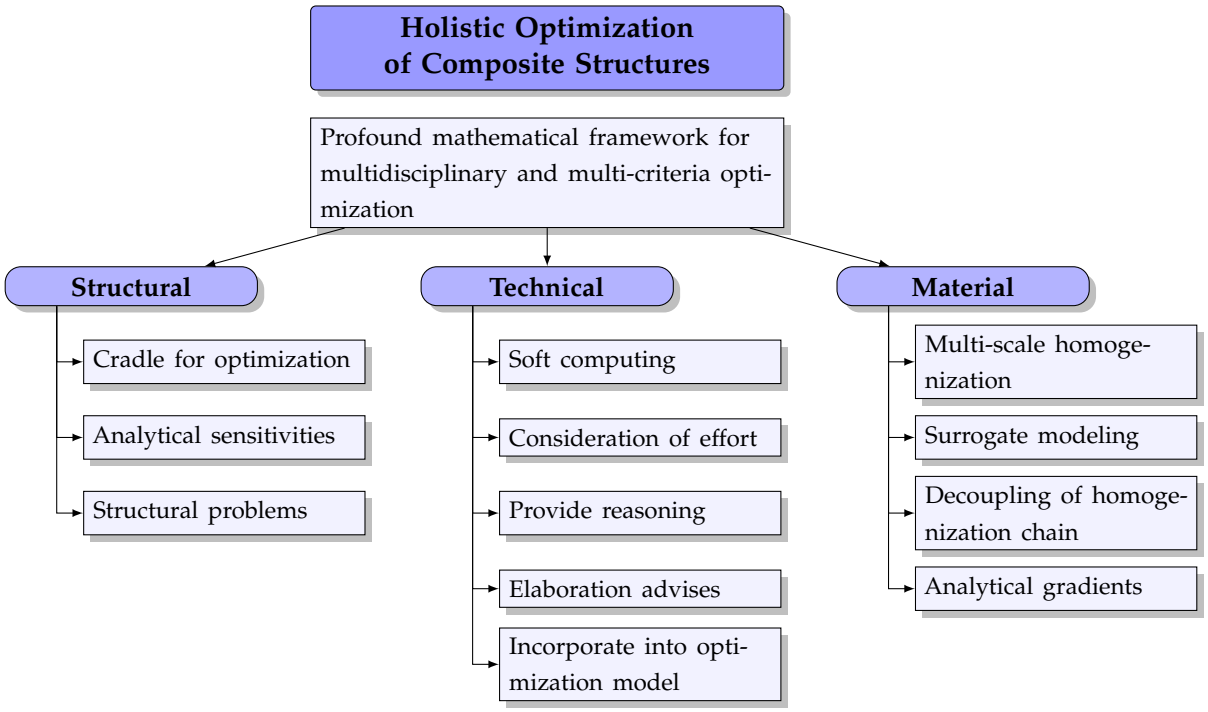

Figure 1.1.: The three columns of the thesis, where a list of key topics being considered for each is given as well

The columns are defined by structural, technical and material aspects, which jointly form a holistic optimization framework, herein used for designing composite structures. Furthermore, a list of key topics as being explicitly discussed within this thesis are given in figure 1.1 underneath each column. Therefore, it will be discussed how continuum mechanics form the basis of the optimization and, further, how their can be differentiated analytically with respect to the design variables. Last but not least, the mechanics of actual structural design problems will be presented and upon which the holistic optimization process will be set up. Technical aspects definitely represents one of the strongest column of this thesis, since their consideration via soft computing methodologies will be discussed elaborately. This will lead to the definition of manufacturing effort models capable of evaluating the process inherent manufacturing effort for a given design proposal. Moreover, these models and especially their development will be generalized and expended, such that they are able to provide reasoning and even return elaboration advises pointing into the direction of optimal improvement. Of course the incorporation of these models and how they actually enrich the optimization process will be studied, evaluated and discussed for two different manufacturing techniques: braiding and prepreg laying. The last column is presented by the development of efficient but yet accurate and reliable material models. This is herein realized via an approach based on the idea of decoupling the homogenization chain. This approach will be presented at length and illustrated for the braiding process, which evidently yields a complex fiber architecture. The key to this decoupling will thereby given by meta modeling, which equips this approach with unseen advantages such as mapping-free

implementation, ease of verification, possible hybridization (e.g. numerical and experimental data points) and many more.

The subsequent chapters 2 and 3 will provide most of the necessary fundamentals. Those two will be followed by chapter 4, addressing the modeling of soft aspects. Therein, the development of general soft models and key features of the implemented manufacturing effort models; one for braiding and the other for prepreg manufacutring, will be discussed. Chapter 5 is devoted to the definition of a decoupled multi-scale homogenization material model. Therein, the braid specific fiber architecture and associated meso and micro scales will serve as a vehicle for demonstrating this approach; yet, it will also become clear, that it is of general validity and applicability. The developed approaches and models will be utilized to actually solve industry relevant structural design problems in chapter 7, 8 and 9. By doing so, they are probed for application in a actual technical environment. Once the significance of the derived approaches and outlined ideas has been underlined, all findings and their scope of their application are exposed in the last chapter, chapter 10.

2 Structural design optimization

Within this chapter, fundamentals regarding optimization will be given. In Baier et al. (1994), Gürdal and Haftka (1992), Rao (2009) and Vanderplaats (2007) more details about the broad topic of structural design optimization can be found.

Contents

2.1. General problem statement

In general a optimization problem can be stated as follows;

$$
\begin{array}{rll}
\underset{\vec{x}\in\chi}{\text{minimize}} & f_i(x_j), & i = 1,\ldots,n_{\mathrm{O}},\ j = 1,\ldots,n_{\mathrm{DV}} \\
\text{subject to} & h_k(x_j) = 0, & k = 1,\ldots,n_{\mathrm{EC}} \\
\text{and} & g_l(x_j) \le 0, & l = 1,\ldots,n_{\mathrm{IC}} \\
\text{with} & \chi = \{x_j \in \mathbb{R}^{n_{\mathrm{DV}}} : x_j^l \le x_j \le x_j^u\}, & \\
\text{where} & &
\end{array}
\tag{2.1}
$$

χ design space,
x_j n_{DV} design variables,
$f_i(x_j)$ n_{O} objective functions,
$h_k(x_j)$ n_{EC} equality constraint functions,
$g_l(x_j)$ n_{IC} inequality constraint functions.

This is the general mathematical form of an optimization problem. In case there is more than one objective to be considered $n_{\mathrm{O}} > 1$, it is also denoted as a vector or multi-obejctive or multi-criteria optimization problem. On the contrary, problems with one objective function, thus $n_{\mathrm{O}} = 1$, are called

single objective optimization problems. For the sake of simplicity, the introduction of the optimization basics first concentrates on those single objective optimization problems. Optimization problems involving multiple objectives and their solutions are discussed at length in chapter 6.

2.2. Optimality in optimization

2.2.1. Optimality for single objective optimizations

A solution of an optimization problem as posed with equation set (2.1) is called an optimum $\vec{x}^{\mathrm{opt}}$. It is hence defined as a vector of design variables, where the objectives are minimal, while still fulfilling all imposed constraints. In case there are no constraints imposed, i.e. $n_{\mathrm{EC}} + n_{\mathrm{IC}} = 0$, the optimization problem is referred to as an unconstraint optimization problem and moreover any optimal solution–thus, either local or global–is characterized by $\frac{\partial f}{\partial x_j} = 0$. This optimality criteria however only holds for unconstraint problems and needs to be augmented for constraint optimization problems–thus for problems where constraints such as $\vec{g}$ are imposed–by the sensitivities of those constraints. This augmented optimality criteria is given by the Karush-Kuhn-Tucker (KKT) conditions. These conditions are based on the Lagrangian or also called dual formulation of the original, or in this context, primal optimization problem (2.1), where $\mathcal{L}$ represent the well-known Lagrangian function.

$$\begin{aligned} \underset{\vec{\lambda}\geq 0,\vec{\mu}}{\text{maximize}} \quad & g(\vec{\lambda},\vec{\mu}) \\ \text{with} \quad & g(\vec{\lambda},\vec{\mu}) := \inf_{\vec{x}\in\chi} \mathcal{L}(\vec{x},\vec{\lambda},\vec{\mu}) \\ \text{and} \quad & \mathcal{L}(\vec{x},\vec{\lambda},\vec{\mu}) = f(\vec{x}) + \vec{\mu}\vec{h}(\vec{x}) + \vec{\lambda}\vec{g}(\vec{x}) \end{aligned} \tag{2.2}$$

The KKT conditions can basically be interpret, as the stationary solution $\left.\frac{\partial \mathcal{L}}{\partial x_j}\right|_{x'_j} = 0$ and can be stated as follows:

$$\begin{aligned} &\text{Stationary:} && \left.\frac{\partial f}{\partial x_j}\right|_{x'_j} = -\sum_k \mu_k \left.\frac{\partial h_k}{\partial x_j}\right|_{x'_j} - \sum_l \lambda_l \left.\frac{\partial g_l}{\partial x_j}\right|_{x'_j} \\ &\text{Primal feasibility:} && h_k(x') = 0, \forall k \\ & && g_l(x') \leq 0, \forall l \\ &\text{Dual feasibility:} && \lambda_l \geq 0, \forall l \\ &\text{Complementary slackness:} && \lambda_l g_l(x') = 0, \forall l \end{aligned} \tag{2.3}$$

Any solution $\vec{x}'$ needs to fulfill those mentioned KKT conditions, otherwise it can not be called an optimal solution $\vec{x}^{\mathrm{opt}}$. At this point, the mathematical nature of the objective and constraint functions becomes relevant. Since, if these functions are non-convex–causing the optimization problem to be multi-modal in terms of possible solutions–the KKT is only a necessary condition. Thus it does not allow for the reverse argumentation, that any solution $\vec{x}'$ fulfilling the KKT conditions is per se an optimal solution $\vec{x}^{\mathrm{opt}}$ of the general optimization problem (2.1). Figure 2.1 illustrates via isolines how the KKT can be interpreted geometrically.

The design vector at point one can be regarded optimal, thus $\vec{x}' = \vec{x}^{\mathrm{opt}}$, since all KKT conditions are fulfilled and there is no better solution nearby. However, looking at point three, which is clearly a better optima due to the lower objective function value, it becomes clear that the optima at point one is a local optimum, whereas the one at point three is a global optimum. The reason for that can be found in the non-convexity in both constraint functions g_1 and g_2. The evaluation of the KKT at the point two should clearly reveal that $\vec{x}' \neq \vec{x}^{\mathrm{opt}}$ because the objective is decreasing for both design variables x_1 and x_2. However, as also can be seen, there is linear combination of ∇f and ∇g_2 for $\lambda_2 > 0$, which in turn

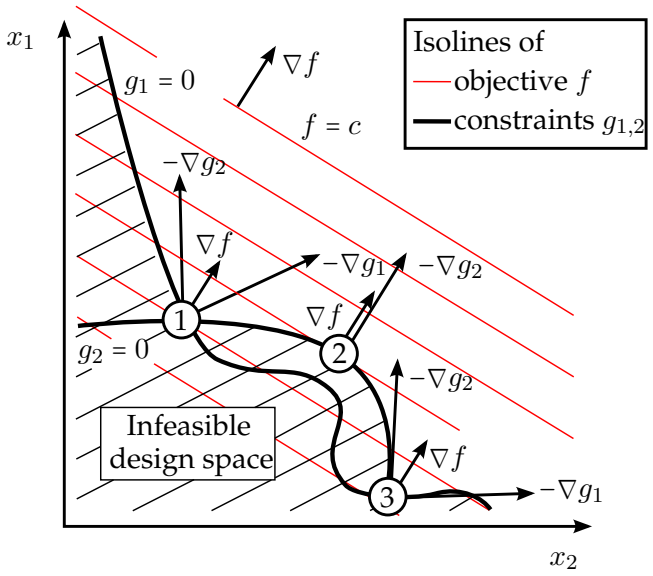

Figure 2.1.: Illustration of the optimality criteria KKT

means the KKT conditions would be fulfilled, even though the design vector is not optimal. The false identification by the KKT can also be lead back to the non-convexity, wherefore the KKT is regarded as a necessary but not sufficient condition for optimality for non-convex optimization problems.

2.2.2. Shadow prices

Once the KKT has been evaluated one can abstract more useful information by taking advantage of the obtained Lagrangian parameters λ_l and μ_k. Because linearizing the Lagrangian (2.2) at the optima reveals that those parameters provide insight into the sensitivity of the objective with respect to the active constraints (see equation (2.4)). They hence allow, based on the linearizion, an extrapolation of the reduction in the objective for a certain relaxation of the constraints. Because of this outlined imprint or shadow of the constraints onto the objective function value, they are are called shadow prices within the context of optimization. Another visual interpretation would be, that the shadow prices reveal the hidden unseen potential by loosening restriction limits. More information is given by Baier et al. (1994) and Vanderplaats (2007).

$$\lambda_l = -\left.\frac{\partial f}{\partial g_l}\right|_{x_j^{\mathrm{opt}}} \tag{2.4}$$

For instance, if an active constraint g_1 is given by $g_1 = \frac{r}{c} - 1$, with r being the constraint response and c its corresponding bound, one can linearize the objective at the optima with respect to the restricting bound c by

$$\begin{aligned} \mathrm{Lin}(f(c+\Delta c)) &= f|_{\vec{x}^{\mathrm{opt}}} + \frac{\partial f}{\partial c}\Delta c \\ &= f|_{\vec{x}^{\mathrm{opt}}} + \frac{\partial f}{\partial g_1}\frac{\partial g_1}{\partial r}\frac{\partial r}{\partial c}\Delta c \\ &= f|_{\vec{x}^{\mathrm{opt}}} - \lambda_1 \frac{1}{c}\Delta c. \end{aligned} \tag{2.5}$$

2.2.3. Pareto optimality

For the case of a vector optimization problem ($n_o > 1$)–which would be the case for a simultaneous minimization of mass and manufacturing effort–multiple optima can be obtained if the objectives

are conflicting, which is normally the case. Special interest is lying on the so called Pareto optimal or efficient solutions. These solutions are characterized by the fact that there is no improvement for one objective without worsening at least one other objective. So, mathematically speaking, any optimal solution $\vec{x}^{opt}$ is referred to as being Pareto optimal in case it dominates all other solutions in a sense, that it is smaller or equal in all objectives and for at least one objective strictly smaller:

$$\begin{aligned} f_i(\vec{x}^{opt}) \leq f_i(\vec{x}) \quad & \forall i = 1, \ldots, n_{\mathrm{O}} \text{ and } \vec{x} \in \chi \\ \exists i: \quad & f_i(\vec{x}^{opt}) < f_i(\vec{x}). \end{aligned} \tag{2.6}$$

Figure 2.2a graphically illustrates this mathematical statement by gathering all Pareto optimal solutions in a pareto frontier and highlighting them in red. When considering equation (2.6) it becomes clear, that point one is dominated by point two in the second objective, which is why it is not considered Pareto optimal. In case the optimization algorithm asks for a single objective optimization, such as all gradient-based ones do, figure 2.2b illustrates a possibility by condensing the vector to the norm of eachs objective distance to its single optimal value. The equation set (2.7) gives an example for such an reduction from the general vector optimization problem (2.1). This class of optimization problems and the determination of optimality will be discussed at lenght in section 6.1.

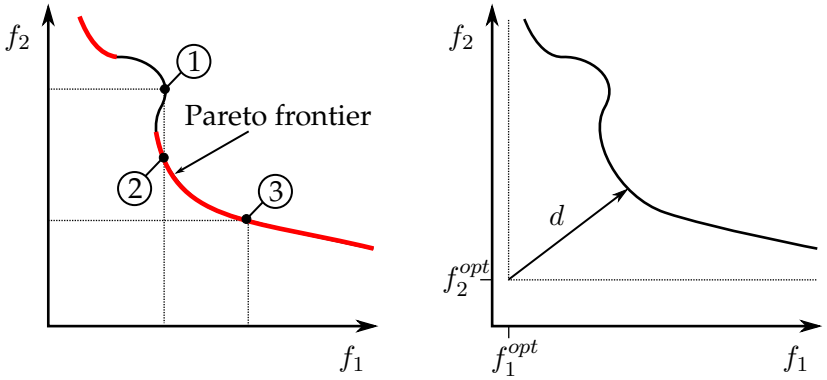

(a) Pareto optimality (b) Norm approach

Figure 2.2.: Pareto optimality and gradient-based vector optimization

$$\begin{aligned} \underset{\vec{x} \in \chi}{\text{minimize}} \quad & f = d = \| f_i - f_i^{opt} \|_2, && i = 1, \ldots, n_{\mathrm{O}}, \\ \text{subject to} \quad & h_k(x_j) = 0, && k = 1, \ldots, n_{\mathrm{EC}} \\ \text{and} \quad & g_l(x_j) \leq 0, && l = 1, \ldots, n_{\mathrm{IC}} \\ \text{with} \quad & \chi = \{ x_j \in \mathbb{R}^{n_{\mathrm{DV}}} : x_j^b \leq x_j \leq x_j^u \}, && j = 1, \ldots, n_{\mathrm{DV}}. \end{aligned} \tag{2.7}$$

2.3. System equations

So far, the perspective towards the optimization problem was purely mathematically based. Thus the physical or technical nature of objective and constraint has not been discussed yet. However, when performing optimizations, the nature of these optimization responses becomes as important as the mathematical basis of the optimization itself. This especially holds for structural design optimization, since optimization algorithms stringently evaluate the underlying models without any physical or technical plausibility check as opposed to an engineer, who intuitively checks his designs for consistency. It is rather up to the optimizer, thus again the engineer, to conduct a plausibility check afterwards and also verify the models via parametric investigations, thereby ensuring also a strong physical and technical basis. For that sake, the underlying system equations in the context of structural

mechanics will be discussed next. One basic balance law in linear continuum mechanics is given by the balance of linear momentum, which is also known as Chauchy's first law of motion:

$$\rho\ddot{\vec{u}} = \nabla \cdot \underline{\sigma} + \rho\vec{b}, \tag{2.8}$$

where $\vec{u}$ is the vector of displacements and $\ddot{\vec{u}}$ respectively the vector of accelerations, ρ the density, $\underline{\sigma}$ the stresses and $\vec{b}$ the body forces. In statics, $\rho\ddot{\vec{u}}$ is equal to zero. Within this work the FEM will be used to solve for displacements and stresses over the whole solution domain Ω. The FEM is based on the weak formulation of (2.8)

$$\int_\Omega \delta\vec{\epsilon}^T\vec{\sigma}\ \mathrm{d}V = \int_\Omega \delta\vec{u}^T\vec{b}\ \mathrm{d}V + \int_\Gamma \delta\vec{u}^T\vec{t}\ \mathrm{d}A, \tag{2.9}$$

with $\vec{t}$ being the traction force acting on the boundary Γ of the domain Ω. Please also note that the stresses and strains are given in Voigt notation, hence $\vec{\sigma} = \{\sigma_{xx}, \sigma_{yy}, \sigma_{zz}, \sigma_{yz}, \sigma_{xz}, \sigma_{xy}\}$. The weak form is commonly first approached by a discretization of the design domain Ω. Further the displacement field $\vec{u}^{(e)}$ within one finite element, i.e. $\Omega^{(e)}$ is represented by linear functions, the so called shape functions $\underline{N}$ with

$$\vec{u}^{(e)} = \underline{N}\tilde{\vec{u}}^{(e)}, \tag{2.10}$$

where $\tilde{\vec{u}}^{(e)}$ are the nodal displacements acting on the nodes of one finite element e. With the constitutive law $\vec{\sigma} = \underline{C}\vec{\epsilon}$ and the strain displacement relationship $\vec{\epsilon} = \vec{L}\vec{u}$ the discretized stress displacement relationship becomes

$$\underline{\sigma} = \underline{C}\underline{L}\underline{N}\tilde{\vec{u}}^{(e)}. \tag{2.11}$$

The linear shape functions can then in tandem with the discretization be used to derive the following equations

$$\sum_e \left[\delta\vec{u}^{(e)^T}\{\underline{k}^{(e)}\tilde{u}^{(e)} - \vec{f}^{(e)}\}\right] = 0 \tag{2.12}$$

$$\begin{aligned} \text{with}\quad \underline{k}^{(e)} &= \textstyle\int_{\Omega^{(e)}} \underline{B}^T\underline{C}\underline{B}\ \mathrm{d}V \\ \underline{f}^{(e)} &= \textstyle\int_{\Omega^{(e)}} \underline{N}^T\vec{b}\ \mathrm{d}V + \int_{\Gamma^{(e)}} \underline{N}^T\vec{t}\ \mathrm{d}A, \end{aligned}$$

which include the local element stiffness matrix $\underline{k}^{(e)}$ and local element force vector $\underline{f}^{(e)}$. The assembly $\mathcal{A}$ over all elements finally yields the well known equation

$$\underline{K}\vec{U} = \vec{f} \tag{2.13}$$

$$\begin{aligned} \text{with}\quad \underline{K} &= \mathcal{A}\underline{k}^{(e)} \\ \vec{U} &= \mathcal{A}\vec{u}^{(e)} \\ \vec{F} &= \mathcal{A}\vec{f}^{(e)} \end{aligned}$$

Prior to solving equation (2.13) for $\vec{U}$, the Dirichlet boundary conditions are to be imposed. Once, the displacement field has been computed all secondary quantities such as strains, stresses and so on will be computed in the post-processing. These quantities can be in nonlinear dependency to the design variables $\vec{x}$ and do consequently lead to nonlinear optimization responses, which is frequently the case within structural optimization and ultimately leads to a nonlinear optimization problem.

2.4. Sensitivities in optimization

In structural optimization, the availability of response sensitivities with respect to the design variables $\vec{x}$ drastically enhance the performance of gradient-based optimization algorithms. This especially holds since the computation of response sensitivities can be carried out efficiently in FEA. To examplify this, let us consider the response displacement $\vec{U}$, which should be differentiated with respect to any given design variable x_1. Equation (2.14) illustrates three possible cases for the differentiation. The design sensitivity for the nodal displacement vector with respect to the design variable x_i can be computed via the following three distinct approaches:

$$\frac{\partial \vec{U}}{\partial x_i} \begin{cases} = \underline{K}^{-1} \left\{ \frac{\partial \vec{f}}{\partial x_i} - \frac{\partial \underline{K}}{\partial x_i} \vec{U} \right\} & \text{analytical gradient} \\ \approx \underline{K}^{-1} \left\{ \frac{\partial \vec{f}}{\partial x_i} - \frac{\Delta \underline{K}}{\Delta x_i} \vec{U} \right\} & \text{semi-analytical gradient} \\ \approx \frac{\Delta \vec{U}}{\Delta x_i} & \text{finite differences} \end{cases} \tag{2.14}$$

The first case is the so called analytical gradient, which is owing its name to the analytical differentiation of equation (2.13). As can be seen, the inverse of the stiffness matrix $\underline{K}^{-1}$ is not modified, wherefore the determination of the sensitivity can be comprehended as simply another load case with the fictitious force $\tilde{f} = \frac{\partial \vec{f}}{\partial x_1} - \frac{\partial \underline{K}}{\partial x_1} \vec{U}$. However, there is a drawback in determining $\frac{\partial \underline{K}}{\partial x_1}$, since this gradient needs to implemented in the FE code a priori for all possible design sensitivities. Just to provide two examples of commercial FE tools, which provide those analytical sensitivities for almost any design variable and response type, NASTRAN and RADIOSS shall be mentioned. Beside, this concept of analytical design sensitivities can also be applied in other analysis types as well. So, for instance, Schroll (2013) did show, that structural responses obtained by a transient nonlinear analysis (e.g. crash simulations) are derivable analytically. Alternatively, the second case uses finite differences so as to approximate the stiffness sensitivity, i.e. $\frac{\partial \underline{K}}{\partial x_1} \approx \frac{\Delta \underline{K}}{\Delta x_1}$. This semi-analytical case is attractive since its computationally efficiency is almost comparable to the one of the analytical approach but circumvents considerably high implementation efforts. The Abaqus FEM tool strives a reasonable compromise by utilizing semi-analytical gradients for shape and some sizing variables and analytical gradients for rather simple sizing variables such as element thickness. The latter case is given by simply using finite differences. Despite its straightforward implementation, it is quite unattractive because of the high associated computational efforts, since equation (2.13) basically needs to solved for each and every design variable.

2.5. General concepts in structural design optimization

Optimization is a powerful tool, since it can facilitate the optimal design even for complex situations, where a wide range of constraints and design variables are present. Those complex situations often arise for structural design problems, where multiple load cases need to be considered and at least as many design parameters need to be determined. However, so as to enable the optimization with such power that it actually solves for the optimal solution, the choice of the adequate optimization algorithm is vital. This is why, some basics regarding optimization concepts, thus algorithms and approaches, will be discussed below.

2.5.1. Evolutionary algorithms

Evolutionary algorithms are based on the idea of computationally mimicking biological evolution. For that reason, they are also reference to as biology inspired algorithms. These kind of algorithms are characterized by an metaheuristic or stochastic character, the mere demand for system responses

(no sensitivities needed) and their possibility to come to the global optima (global search algorithm). The latter only holds for certain parameter choices and may results in extensive computations. An exemplary flow chart of an evolutionary algorithm or more specifically an evolutionary strategy is given with figure 2.3 and discussed at length in the following.

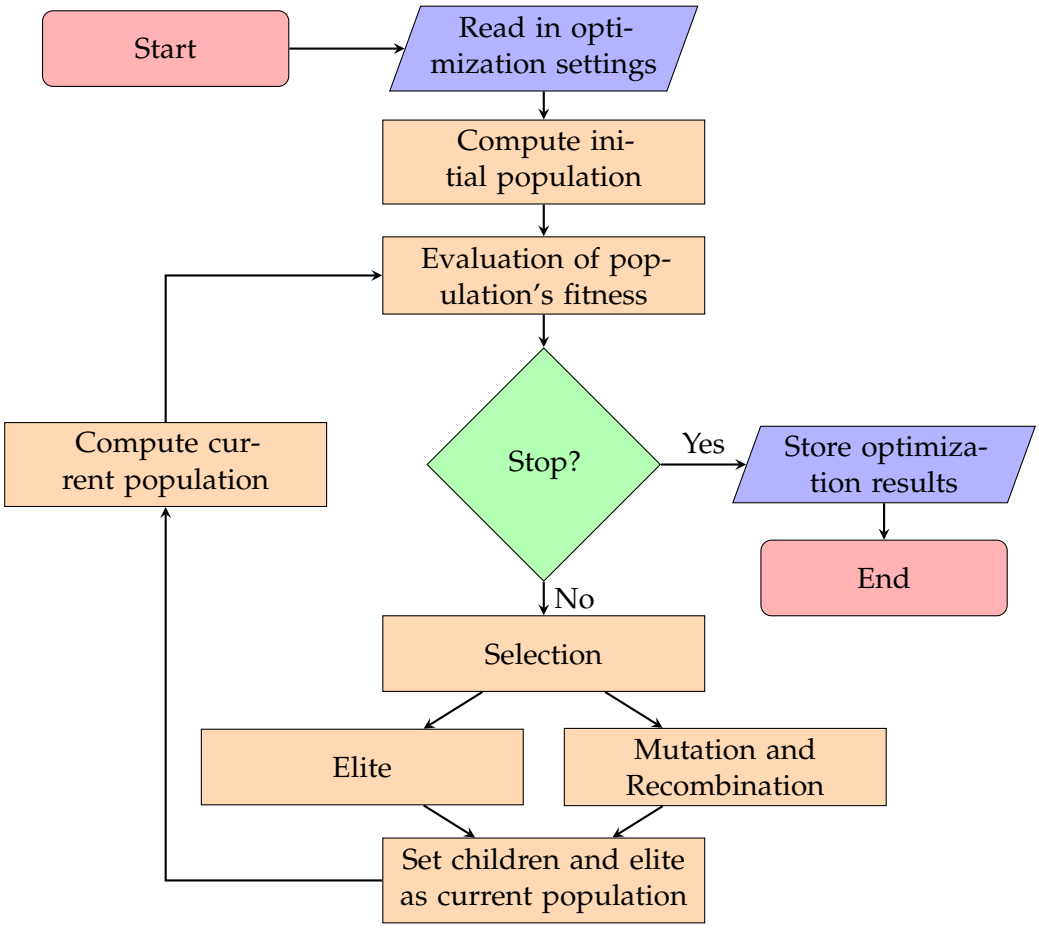

Figure 2.3.: Flowchart of an exemplary evolutionary strategy

The mechanisms which are adopted from the biological evolution are: reproduction, mutation, recombination, natural selection and the survival of the fittest. Mutation and recombination steer the diversity of the population, i.e. the exploration of the design space and natural selection together with the concept of survival of the fittest can increase the populations quality, i.e. the exploitation in the vicinity of optima. In most evolutionary algorithms exploration and exploitation are opposed goals and therefore difficult to satisfy simultaneously. A parameter triggering this, is the so called selection pressure, which basically is the ratio of elite and population size. In general, algorithms of this class start with reading in the optimization settings including for instance population size and number of generations. Thereafter, the design responses of the initial population are computed (Initial generation). A population is thereby a gathering of several individuals, namely a set of design vectors, which will be altered over generations, i.e. iterations. Then the fitness of each individual of the population is evaluated based on its objective value and–if active constraints are present–the degree of violation of bounds and restrictions. Once the fitness has been evaluated, it is being decided whether the optimization algorithms stops or not. At this point, it should be mentioned, that mathematically speaking, evolutionary algorithms do in general not converge in a strong sense. They rather show small changes in the average fitness value or reach a pre-defined maximum number of generations (provided by the user). If the stopping criteria are not fulfilled, the algorithms proceeds to the selection of the fittest individuals, which then are gathered in an elite and/or used for mutation and recombination. Most frequently, the process of mutation is implemented by a modification of random

entries of the design variable vectors, where the modification is determined based on stochastics (e.g. Gaussian normal distribution) and influenced by the current generation number. Recombination on the other hand, can be realized by combining two design vectors by averaging, interchanging entries or similar approaches. Next, a new generation is formed by combining the individuals from the elite and the ones obtained by mutation and recombination to a new population and the process basically starts all over again. This sort of algorithms are regularly straight forward to implement and do commonly display high robustness with regard to weak discontinuities, noisy design responses and similar mathematical shortcomings in the underlying system equations. Further advantages are the possibility to directly consider discrete variables and the direct optimization of vector problems. The latter beneficial feature can be unlocked by formulating the fitness function based on pareto optimality. Last but not least, evolutionary algorithms charm because of their intuitive notion, making them comprehensible.

Despite these advantages, algorithms of this class should be used cautiously, since they can pose irresolvable problems. For instance, if a satisfactory compromise between exploration and exploitation is desired, one may ends up with a huge population size over many generations. This can ultimately result in high computational expenses, which especially holds in case sophisticated FEAs are involved. Parallelization, to which evolutionary algorithms are generally compliant, can mitigate this dilemma. However, there are limitations from hardware and licensing side as well. The situation worsens for problems involving a huge number of design variables, because the number of individuals needs to grow somewhat exponentially so as to ensure some degree of exploration of the design space. This major drawback can in last consequence be drawn back to the fact that no gradient information is being used in most of these algorithms. This is why, subsequently, another class of optimization algorithms–gradient-based algorithms–are being introduced and discussed. Lastly, it should also be noted, that there is no mathematically founded convergence or optimality criteria for the discussed class of biologically inspired algorithms, which can make it difficult to tell whether or not the optimization has converged and even more so to state optimality.

2.5.2. Gradient-based algorithms

The main idea for gradient-based algorithms is to not only use optimization responses but also to acquire and utilize their sensitivities. This new dimension enables this class with high computational efficiency and additionally unlocks new potentials in the interpretation of optima (see KKT condition (2.3)). However, this also restricts this class of algorithms to be a local search algorithm. Hence, algorithms from this class have a certain likelihood of converging to local optima for optimization problems with non-convex optimization responses. Figure 2.4 principally illustrates, how gradient-based algorithms iteratively solves general optimization problems (see equation (2.1)) for the optimal solution $\vec{x}^{\mathrm{opt}}$. In this figure, the black dot marks the starting point, which is also referred to as initial design vector $\vec{x}^{(0)}$. The white point highlights the optimal solution $\vec{x}^{\mathrm{opt}}$ and the dashed ones the design vector $\vec{x}^{(i)}$ at the current iteration i. From iteration to iteration, the design vector is updated based on a priorly determined search direction $\vec{s}^{i}$ and the step length α^{k}. The process of determining the optimal step length α^{k} is called line search and k the inner iterations. Therefore, the dashed lines highlight associated convergence paths. In this exemplary figure, two convergence paths are given (convergence path A and B). These two convergence paths are given–even though their difference is exaggerated here–to highlight, that there are variations in how the search direction $\vec{s}^{i}$ is determined from algorithm to algorithm. For instance, SLP algorithms sequentially linearize the optimization problem by using gradient information for the determination of $\vec{s}^{i}$. The class of SQPs enhance this approximation by incorporating second order gradient information, leading to sequential quadratic approximations. With figure 2.5 a flow chart of a typical gradient-based optimization algorithm is given. The details are discussed next.

$$\vec{x}^{(i+1)} = \vec{x}^{(i)} + \alpha^k \vec{s}^i \tag{2.15}$$

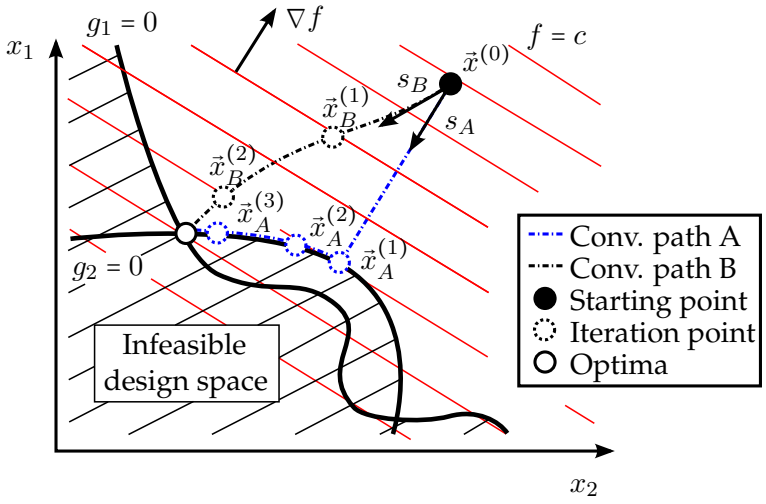

Figure 2.4.: Illustration of possible convergence paths

In general the optimization starts by reading in the initial design variables $\vec{x}^{(0)}$ and initializing the optimization by loading settings (i.e. convergence tolerances etc.), setting iterators and initializing variables. Next, the system responses are computed, which are most frequently solved with FE in structural design optimization. As the name already indicates, the gradients are used, which is why a sensitivity analysis needs to be conducted. In many FE programs such as NASTRAN and Abaqus, sensitivities can be computed efficiently (see section 2.4). Even though the analysis of system responses and their sensitivities only form two process boxes in this flow chart, they together raise almost all computational effort throughout the optimization process. Once both, the responses and their sensitivities have been computed the optimization quantities: objective f and the constraints h_k and g_l can be formed. Except for the first iteration, this step is followed by a check whether the line searched has converged. If not, the inner iteration proceeds by updating the step length α^k such that a maximal improvement in terms of minimizing the objective, while all constraints remain fulfilled. Subsequently the inner iterator k is incremented, as well as the design variable vector as given with (2.15). Then the process of evaluating system responses, sensitivities and assigning them to the optimization quantities f, h_k and g_l is repeated until the line search has converged. Thereafter and in case the overall optimization did not yet converge, a new search direction $\vec{s}^{i+1}$ is computed based on for instance linear approximations for a SLP or quadratic ones for a SQP. The outer iteration is closed by an update of the iterator i and the initialization of the line search. After the outer iterations - which basically are a cascade of inner iterations - end in convergence, the optimization quantities are prepared for interpretation and stored. This marks the end of this algorithm.

Summing up, advantages of gradient-based algorithms are, that a profound convergence criteria is available. In addition to that, the gradient information can be used to evaluate optimality based on the KKT criteria (2.3). Another beneficial aspect is the possibility to further exploit gradient information for extrapolating the influence of each bound, either on constraints or design variable onto the objective. This extrapolation is facilitated by the shadow prices (see (2.5) and (2.4)) and supports engineers in interpreting, making the optimization result plausible and re-designing a given structure. Finally, it can be concluded, that gradient-based algorithms are in general superior in terms of computationally efficiency due to fewer function calls. This especially holds for large-scale problems involving a high number of design variables and if sensitivities are available, which is often the case in structural design optimization. Minor drawbacks are the need of reformulating vector optimization problems and that gradient-based algorithms, as a member of the class of local search algorithms, can bring forth local optima.

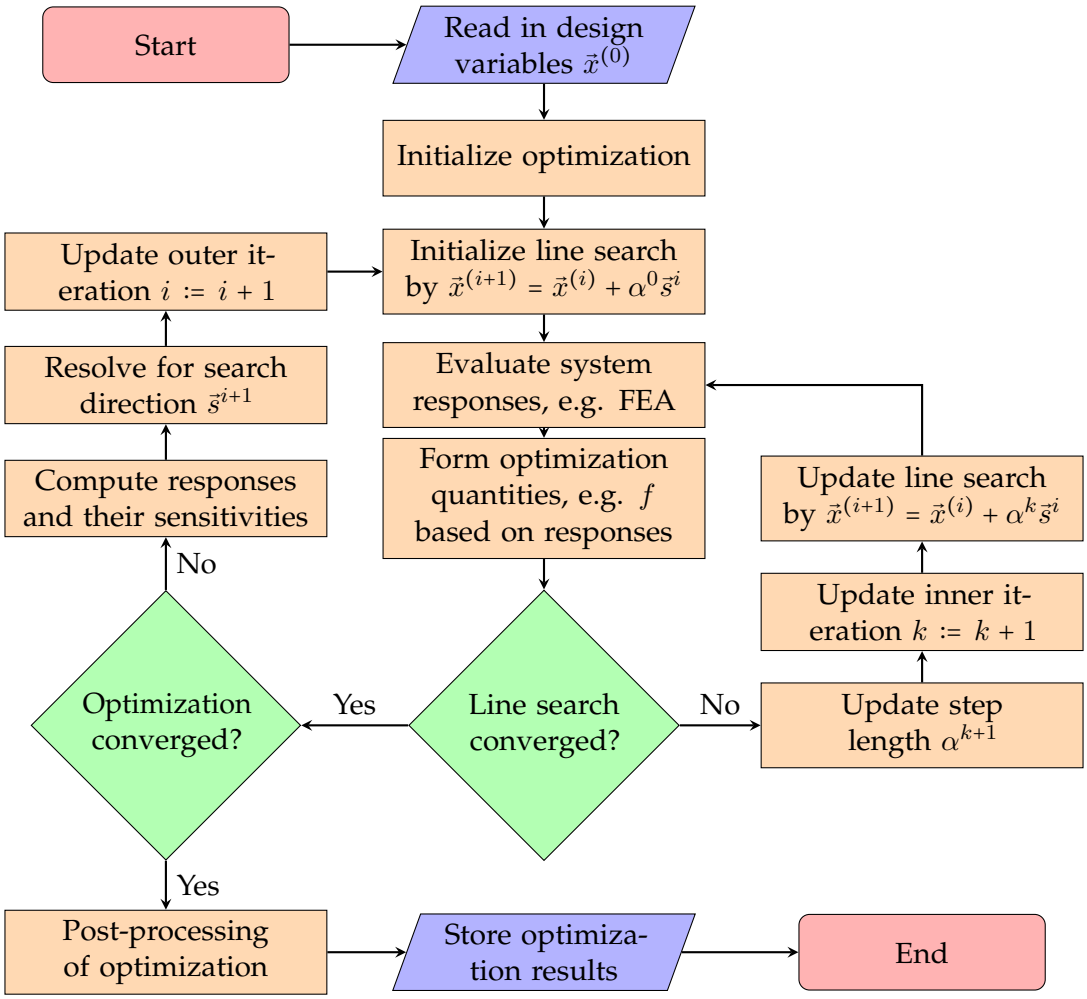

Figure 2.5.: Flowchart of an exemplary gradient-based algorithm

2.5.3. Hybrid algorithms

Another class of algorithms is given by hybrid algorithms. These algorithms combine aspects of both afore mentioned algorithm classes. This is intuitively plausible, because evolutionary algorithms are attractive due to their global search capability but do often lack in computational efficiency and fast convergence in the vicinity of optima. On the opposite side, gradient-based algorithms are computationally efficient and do show high convergence rates (notably SQP algorithms), but may convergence to local optima. Hybrid algorithms aim to combine both classes so as to mitigate each of the mentioned drawbacks. Commonly, evolutionary algorithms are used as a platform into which gradient-based algorithms are implanted leading to a hybridization. There are basically two approaches for this hybridization. First of all, one could perform both algorithm classes sequentially. This can be achieved for instance by starting gradient-based optimizations for the elite of the last generation. Secondly, one could start gradient-based optimizations at each generation. An example for this would be the GAME algorithm. GAME has been developed at the institute of lightweight (see Langer (2005) and Langer et al. (2004)).

2.5.4. Meta modeling within design optimization

In meta modeling, engineers seek for surrogate models approximating the responses of the original problem within certain limits on the design space as well as on the precision of the approximation.

Owing to that nature, these models are also referred to as response surface approximations (RSA). The formation of such RSA models can be divided into two phases. In the first phase, the support points of the RSA need to be determined. So as to maximize the information gain and thereby most likely reduce approximation errors the support points need to be distributed throughout the whole design domain. The process of determining the distribution of the support points is called design of experiments (DoE). This phase is followed by a phase where the values of the responses of the original model are computed at the support points and thereafter the computation of the coefficients of the chosen RSA type. In some more sophisticated approaches, the described phases are carried out iteratively based on error estimations which enable the enhancement of the DoE and in that consequence the quality of the approximation overall in terms of number support points needed or approximation errors. An example of this would be the work of Xu, who extended surrogate modeling by adding sample points such that expected improvement is being maximized (see Xu (2014)). Next, both phases are being discussed in brevity.

Design of experiments as the first phase pre-determines the computational effort associated with the RSA generation, since it defines the support or also called sample points, where the system equations need to be evaluated. Moreover, it also influences the overall quality of the RSA by its sample points distribution. For these two reasons, one seeks to strike a compromise in-between exploration of design space and number of prospective system evaluations, hence, as few as necessary. An straight forward approach for planing the sampling, thus performing a DoE, is to simply consider all possible combinations, which is then referred to as full factorial design (FFD). This approach, however, brings forth a high number of sample points resulting in high computational efforts especially for high dimensional problems. Contrary to the FFD, the latin hypercube sampling (LHS) method is independent of the dimension of the design space since it projects points of the design space to an two dimensional domain. The basic principle of LHS is the generation of sample points based on a grid, whereby each column or row has only one sample point. This is illustrated in figure 2.6. Summing up, LHS is superior to FFD because of the fact, that minimal sampling number is independent of the design space's dimension (although oversampling is highly advised) and that it generates well-scattered samples even for high dimensional design spaces.

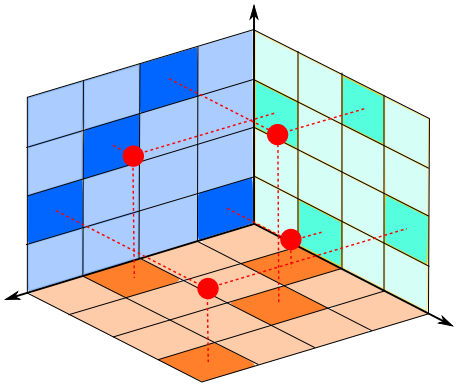

Figure 2.6.: Latin Hypercube Sampling in a design space of dimension three (inspired by Xu (2014))

Once the DoE is finished, the actual computation commences by the evaluation of the system equations for the design responses at the sample points and right thereafter, the computation of the RSA's coefficients. RSAs can be distinguished in either regression or interpolation. In case of the latter, an interpolation, the approximation passes through each sample point's response value exactly, whereas a regression yields approximations which fit the data points at a minimal error norm. The use of a regression can be advantageous, when the underlying model yields noisy responses for which the regression can then predict a global smoothed trend. An example of a regression is given with formula (2.16), which represents a polynomial regression of degree two, with β being the RSA's coefficients

and $\widetilde{r}_k$ the approximation of the response r_k.

$$\widetilde{r}_k = \beta_{k,0} + \sum_i \beta_{k,i} x_i + \sum_{ij} \beta_{k,ij} x_i x_j \quad \text{with } i, j = 1, 2, \ldots, n_{\mathrm{DV}} \tag{2.16}$$

For such a polynomial regression, the minimum sampling size can be given with the number of coefficients $n_\beta = \frac{1}{2}(1 + n_{\mathrm{DV}})(2 + n_{\mathrm{DV}})$. However, in most cases an oversampling of at least fifty percent is advised and reasonable to foresee a possible poor DoE or weak scattered sampling points in a spacious design domain. Opposed to the polynomial regression, Kriging (or Gaussian process) interpolates the data points at each sampling point. More regarding surrogate modeling and the different approaches, can be found in Forrester et al. (2008) and in the work of Xu (2014).

Table 2.1.: Illustration of the curse of dimensionality, i.e. exponential increase in minimal sampling size ~ n_β over the dimensions n_{DV} for a quadratic regression

Dimensions n_{DV}	Minimal sample size n_β
1	3
2	6
3	10
6	28
12	91

Finally, it should be noted, that meta modeling is limited to the well-known curse of dimensionality, which is illustratively exemplified with numbers in table 2.1 for the case of a polynomial regression of degree two. An example of a polynomial regression of degree two is given with equation (2.17).

$$\widetilde{r} = \beta_0 + \beta_1 x_1 + \beta_2 x_2 + \beta_{11} x_1^2 + \beta_{12} x_1 x_2 + \beta_{22} x_2^2 \tag{2.17}$$

As can be seen in table 2.1, the number of the minimal number of samples increases exponentially. This can be observed more or less for any meta modeling approach and can in that consequence limit the number of design variables to be approximated at a desirable precision. Nevertheless, RSAs can facilitate numerical efficient optimizations and should be considered in every planing of an optimization strategy. Moreover, it can be advantageous to use any sort of approximation if the use of gradient-based algorithms is aspired and integer variables are present, since they are then continuilized.

3 Structural mechanics of composites

As discussed earlier, understanding the underlying system equation is of vital importance for the successful and significant optimization of structures. Beyond that, the understanding also helps the optimizer to interpret the derived optimum. For that sake, this chapter is addressing mechanics and further aspects of composites, such that the system equations of the subsequently introduced composite design optimization tasks become transparent to the reader. Basic knowledge regarding composites is given with Jones (1999) and Schürmann (2005), whereas Mazumdar (2002) focuses on the composite manufacturing aspects.

Contents

3.1. Unidirectional composite layers

Fiber-reinforced polymers (FRP) are composed of three materials: fibers, polymer and the coating. The fibers equip the composite with high specific stiffness and strength quantities and this is why their volume content is usually the greatest of all three materials; commonly around sixty percent. Because of their predominant influence, FRPs can be categorized according to the fiber length; endless–or also called continuous–fiber (e.g. $l_f > 50$ mm), long fibers (e.g. $l_f \approx 10$ mm) and short fibers (e.g. $l_f \approx 0.5$ mm) respectively. However, the afore mentioned high stiffness and strength properties are solely available in fiber direction (L-direction see fig. 3.1a) and do drop in orthogonal direction (T-direction see fig. 3.1a). Typical fiber materials are carbon, glass and aramid. In industry, most composite structures are build with endless fibers due to their superior stiffness and strength contribution to the composite (Schürmann (2005)).

The second material–or matrix phase–consists of polymer, which is considerably softer and displays lower strength. It basically has the purpose of supporting the fibers, such that they can actually withstand shear and compression loading. Moreover, they also protect the fibers from the environment. The most commonly used polymer type is thermosetting, whereas thermoplastic polymers are recently uprising to their promising melting characteristics enabling them for instance with short cycle times in manufacturing. Coating, the last of all three materials, has the purpose to

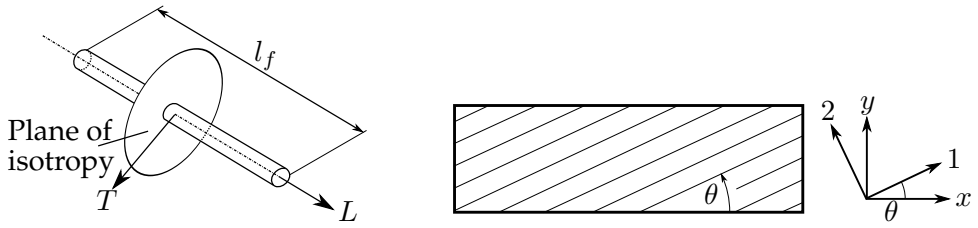

(a) Plane of isotropy (b) Coordinate systemes

Figure 3.1.: Plane of isotropy and coordinate system definition (Schatz (2012))

improve the adhesion in-between the fiber and matrix phase. It also protects the fibers during the manufacturing process from mechanical damage. Coating is most often neglected in micro mechanical models due to its very low volume percentage. Figure 3.1b depicts the local $(1,2)$ and respectively the global coordinate system (x,y) for an UD ply. The constitutive law for an unidirectional FRP layer can be given in $(1,2)$ coordinate system with

$$\vec{\sigma} = \underline{Q}\vec{\epsilon}, \tag{3.1}$$

$$\text{with } \vec{\sigma} = \begin{Bmatrix} \sigma_{11} \\ \sigma_{22} \\ \tau_{12} \end{Bmatrix}$$

$$\underline{Q} = \frac{1}{1-\nu_{12}\nu_{21}} \begin{bmatrix} E_{11} & \nu_{21}E_{11} & 0 \\ \nu_{12}E_{22} & E_{22} & 0 \\ 0 & 0 & G_{12}\left(1-\nu_{12}\nu_{21}\right) \end{bmatrix},$$

$$\vec{\epsilon} = \begin{Bmatrix} \epsilon_{11} \\ \epsilon_{22} \\ \gamma_{12} \end{Bmatrix},$$

where four independent material parameters describe the transversely isotropic behavior. The transformation of the stiffness tensor $\underline{Q}$ based in local coordinates $(1,2)$ to the stiffness $\bar{\underline{Q}}$ into global coordinate system (x,y) can be carried out by,

$$\bar{\underline{Q}} = \underline{T}\underline{Q}\underline{T}^T, \tag{3.2}$$

$$\text{with} \quad \underline{T} = \begin{bmatrix} c^2\theta & s^2\theta & -2s\theta c\theta \\ s^2\theta & c^2\theta & 2s\theta c\theta \\ s\theta c\theta & -s\theta c\theta & c^2\theta - s^2\theta \end{bmatrix},$$

$$\text{and} \quad s\theta := \sin(\theta),$$

$$c\theta := \cos(\theta),$$

$$s^2\theta := \sin^2(\theta),$$

$$c^2\theta := \cos^2(\theta).$$

The transformation matrix $T(\theta)$ is not symmetric since the Voigt notation is being used. Studying this transformation reveals two relevant characteristics about the mechanics of FRP UD plies. First

of all, the stiffness drastically decreases–even for small deviations–from the ideal orientation $\theta = 0°$. This is being illustrated in figure 3.2, which is based on an UD ply derived for a T300 carbon fiber and a typical epoxy matrix. As can be seen, the stiffness E_{xx} drops to half of the initial value of E_{11} at about twelve degrees. Further it should be noted, that at this point even for $\theta = 0°$ the mere presence of matrix material scales down the promising fiber stiffness. Secondly, the stiffness varies nonlinearly with respect to θ, e.g. $\sim \sin^4(\theta)$. This will later affect the optimization in a sense that stresses–which will be evaluated for the determination of failure or similar responses–will be nonlinear as well. They may moreover form non-convex constraint or objective functions. This has already been shown in the PhD thesis of Baier (1978), where multi-modality and its cause, local optima, are discussed amongst other aspects.

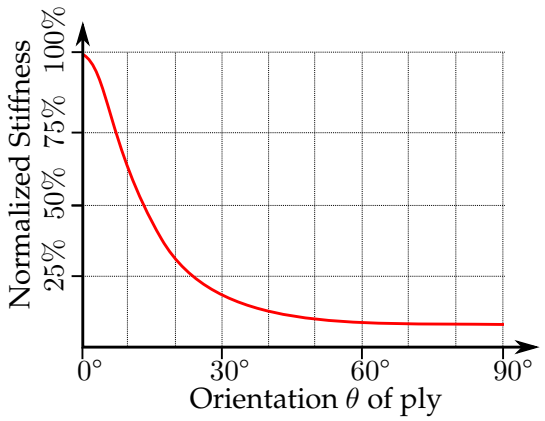

Figure 3.2.: Stiffness drop for different orientations θ of a typical UD ply

3.2. Mechanics of composites

Next, the actual composite is formed by defining the stacking sequence, thus the staple order, orientation, material and thickness of each unidirectional ply (UD ply). This is illustrated in figure 3.3, where six plies form a composite, which is at this point not a material any more but rather a structure already.

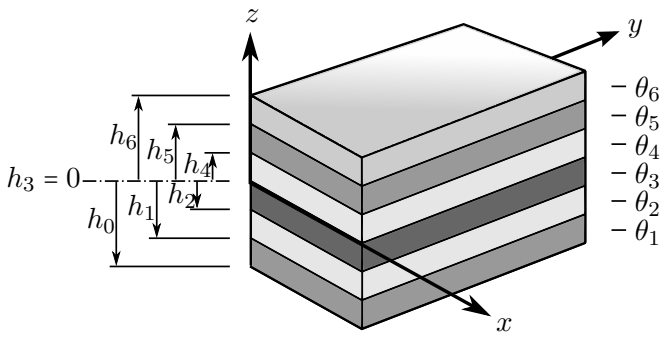

Figure 3.3.: Definition of the coodinate system and quantities for the CLT

To provide some insight into the mechanics of composites, the classical lamiante theory (CLT) is derived. This theory is based on the Kirchhoff-Love plate theory and are derived based on the following assumptions:

- Linear elasticity
- Small deflections (first-order theory)

- Plane stress state
- Shear rigidity (Bernoulli's assumption)
- Thin laminate
- Constant laminate thickness
- Perfect bondings (No slip within plies)

With these assumptions, the kinematics of the plate can be described with

$$\vec{\epsilon}(z) = \begin{Bmatrix} \epsilon_x(z) \\ \epsilon_y(z) \\ \gamma_{xy}(z) \end{Bmatrix} = \begin{Bmatrix} \epsilon_x^0 \\ \epsilon_y^0 \\ \gamma_{xy}^0 \end{Bmatrix} + z \begin{Bmatrix} \kappa_x \\ \kappa_y \\ \kappa_{xy} \end{Bmatrix}, \tag{3.3}$$

with ϵ_x^0 being the membrane strain in the reference or mid-plane of the composite plate and κ_x^0 its curvature. By integrating over the composite's thickness and using the constitutive law given by equation (3.2), the line forces n_x, n_y and n_{xy} can be obtained.

$$\vec{n} = \begin{Bmatrix} n_x \\ n_y \\ n_{xy} \end{Bmatrix} = \sum_k \int_{h_{k-1}}^{h_k} \vec{\sigma}(z)\mathrm{d}z = \sum_k \int_{h_{k-1}}^{h_k} \underline{\bar{Q}}(z)\{\vec{\epsilon}^0 + \vec{\kappa}z\}\mathrm{d}z. \tag{3.4}$$

Similarly, the line moments n_x, n_y and n_{xy} are defined as

$$\vec{m} = \begin{Bmatrix} m_x \\ m_y \\ m_{xy} \end{Bmatrix} = \sum_k \int_{h_{k-1}}^{h_k} \vec{\sigma}(z)z\mathrm{d}z = \sum_k \int_{h_{k-1}}^{h_k} \underline{\bar{Q}}(z)\{\vec{\epsilon}^0 z + \vec{\kappa}z^2\}\mathrm{d}z. \tag{3.5}$$

Those two equations (3.4) and (3.5) can be condensed to the so called ABD matrix as,

$$\begin{Bmatrix} n_x \\ n_y \\ n_{xy} \\ m_x \\ m_y \\ m_{xy} \end{Bmatrix} = \begin{bmatrix} \underline{A} & \underline{B} \\ \underline{B} & \underline{D} \end{bmatrix} \begin{Bmatrix} \epsilon_x^0 \\ \epsilon_y^0 \\ \gamma_{xy}^0 \\ \kappa_x \\ \kappa_y \\ \kappa_{xy} \end{Bmatrix} \tag{3.6}$$

$$\text{with } A_{ij} := \textstyle\sum_k \bar{Q}_{ij}^k \{h_k - h_{k-1}\}$$

$$B_{ij} := \tfrac{1}{2} \textstyle\sum_k \bar{Q}_{ij}^k \{h_k^2 - h_{k-1}^2\}$$

$$D_{ij} := \tfrac{1}{3} \textstyle\sum_k \bar{Q}_{ij}^k \{h_k^3 - h_{k-1}^3\}$$

This ABD matrix and especially the coupling matrix $\underline{B}$ not only forms due to the orthotropy of the material in each ply, but because of the property change throughout the thickness, i.e. $\underline{\bar{Q}}(z) \neq \text{const}$. This is why the coupling matrix $\underline{B}$ basically couples in-plane forces with out-off-plane deflections and vice versa. Therefore, these couplings needs to be monitored in most engineering applications to circumvent undesired modes of deflection. Just to visualize representative coupling modes, such as the tension-bending coupling, figure 3.4 is given.

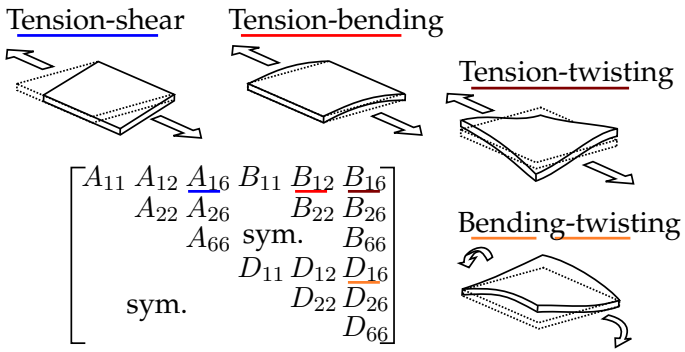

Figure 3.4.: Illustrative coupling effects for a general composite plate

Beside the comprehension of possible coupling modes, the ABD matrix chiefly constitutes the material law for composite plates by linking line forces and moments with strains and curvatures. Wherefore it also provides insight into the stiffness of a composite plate. Figure 3.5 shows an exemplary polar plot of an $(0/30/-30/90)_{\text{sym}}$ laminate based on the UD matrerial properties as used in figrure 3.2, i.e. a T300 carbon fiber and an epoxy matrix. The plot has been created via eLamX 2.2, which is a license free program developed by the TU Dresden. As can be seen there, the membrane stiffness A_{11} varies enormously from over seventy GPa to about forty, thereby marking another drop in FRPs' material properties along with the loss due to the presence of matrix material and the orthotropy of fibrous stiffened UD ply.

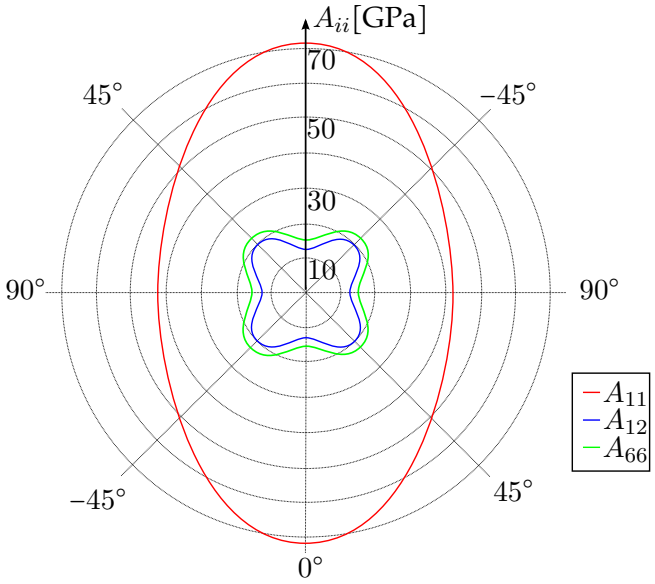

Figure 3.5.: Polar plot of A_{11}, A_{12} and A_{66} for the $(0/30/-30/90)_{\text{sym}}$ laminate

Concerning the design optimization of composite structures, the ABD matrix and its mathematical derivation is involving variables, which are of discrete nature. Hence, they can not be varied continuously in practice. An example would be the thickness of each ply, which can only take discrete values in an actual Prepreg lamination process. This is of relevance for the optimization process, since the presence of discrete variables result in a new and quite challenging problem class: Mixed Integer Nonlinear Programming (MINLP) problems. Another interesting fact is, that the orientation has a great lever on the overall stiffness behavior of composite plates, but does not influence the structural mass at all. For that reason, engineers have to be aware of these zero sensitivities of the design response mass, when posing the general optimization statement as given with equation set (2.1). This especially holds, when gradient-based algorithms are chosen. It has also been highlighted earlier, that the transformation of UD plies brings forth nonlinear and non-convex responses for stresses and

others, which needs to be considered as well.

3.3. Failure of composite materials

At the beginning of this section, it was stated that most FRPs consists of three phases. Beside the influence on stiffness, e.g. the orientation sensitivity, these different phases do also utter complex failure mechanisms. First and foremost, failure is differentiated between inter and intra lamina failure; hence, in failure in-between and within FRP plies. The inter lamina failure is characterized by a debonding of plies and is referred to as delamination. This mode of failure involves stresses which are directed out-off plane. For that reason, FEA with shell elements or CLT analyses do not provide any measure, whether or not delamination occurs, because of the mechanical abstraction, i.e. the assumption of plane stress. In intra lamina failure, the failure originates within a ply. Physically, the fibrous structure and the presence of fiber and matrix material cause several different modes of failure such as fiber breakage, fiber buckling or matrix cracks (inter-fiber failure). To evaluate, whether failure exists or not, there are many different failure criteria such as Tsai-Hill, Hashin and Cuntze, just to mention a view. They all share the notation of a failure index as a measure based on stress $\underline{\sigma}$ and strength $\vec{R}$ information, as given with the following equation set (3.7).

$$\mathcal{FI}(\underline{\sigma}, \vec{R}) \begin{cases} < 1 & \text{No failure} \\ = 1 & \text{Exactly critical loading} \\ > 1 & \text{Failure within failure theory} \end{cases} \tag{3.7}$$

In this thesis, the failure criteria according to Puck (1996) is detailed and used, because it can differentiate in distinct failure modes and did also show to perform superior in many cases within the World-Wide-Failure-Expersie II (see Kaddour and Hinton (2013)). The formulas for computing the failure index (3.7) are given with (3.8) for fiber failure and with (3.9). As can be seen, the puck failure criterium distinguishes in-between fiber failure and different modes of inter-fiber failure. These three modes (Mode A, B, C) occur for different ratios and signs of the fiber transversal stress σ_{22} and the shear stress τ_{12}. The information of which inter-fiber mode prevails, discloses how the failure propagates and how critical it is. For instance, in mode C, a wedge forms, which is pressed out of the lamina, subsequently probably causing delaminations.

Fiber failure

$$\mathcal{FI}_F = \frac{1}{e_{22,(t/c)}} \left\| \epsilon_{11} + m_{\sigma F} \sigma_{22} \frac{\nu_{21,F}}{E_{11,F}} \right\| \tag{3.8}$$

Inter-fiber failure

$$\begin{aligned} \text{Mode A:} \quad & \mathcal{FI}_{IF-A} = \sqrt{\left(\frac{\tau_{12}}{R_{12}}\right)^2 + \left(1 - p_{12,t}\frac{R_{22,t}}{R_{12}}\right)^2 \left(\frac{\sigma_{22}}{R_{22,t}}\right)^2} + p_{12,t}\frac{\sigma_{22}}{R_{12}} \\ \text{Mode B:} \quad & \mathcal{FI}_{IF-B} = \frac{1}{R_{12}}\sqrt{\tau_{12}^2 + \left(p_{12,c}\sigma_{22}\right)^2} + p_{12,t}\sigma_{22} \\ \text{Mode C:} \quad & \mathcal{FI}_{IF-C} = \left[\left(\frac{\tau_{21}}{2(1+p_{22,c}R_{12})}\right)^2 + \left(\frac{\sigma_{22}}{R_{22,c}}\right)^2\right]\frac{R_{22,c}}{-\sigma_{22}} \end{aligned} \tag{3.9}$$

Next, the Puck failure criteria for the earlier mentioned UD ply is depicted in figure 3.6a. One can see the characteristic discontinuity in the derivative in 1 direction, which originates from the transition inter-fiber failure to fiber failure and basically looks like cuts. The cut on the lower left of figure 3.6a,

also reveals the failure surface for the inter-fiber failure, which frankly speaking looks like a potato with an asymmetry towards compression. This asymmetry is reasonable because the failure modes transits from mode A over B to C. Further the crack surface and angle for mode C is higher, resulting in higher stress levels than for mode A. So far, the failure of one ply has been discussed. However, for a laminate, the failure index needs to be evaluated for each ply individually depending on each stress state $\underline{\sigma}$ and strength properties $\vec{R}$. In figure 3.6b the color coding represents the different plies which fail according to Puck. The yellow surfaces in this figure represent the inter fiber failure of the $-30°$ ply, the red ones of the $0°$ and green ones of the $90°$ ply respectively. Therefore, one can not only observe a discontinuity in each ply's failure body due to failure mode transitions but also on a laminate scale, where different plies become critical. These discontiuities in the derivatives may also lead to convergence problems for gradient-based optimization strategies, wherefore they should be noted and approached. It should also be noted that this only marks the initial failure of the composite laminate and that the laminate may be loaded even further until fatal failure is reached.

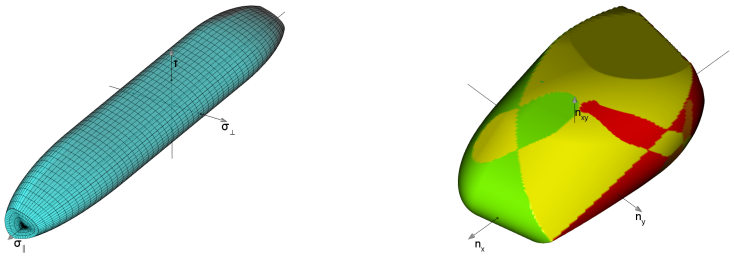

(a) (0) (b) $(0/30/-30/90)_{\text{sym}}$

Figure 3.6.: Failure bodies of a UD ply (left) and a laminate (right)

Last but not least, it should also be mentioned, that the failure of composites evolves nonlinearly over the loading level. This is owned to the fact, that once a ply shows first signs of failure (initial failure) the stiffness and residual strength is decreased. By further load increase, the failure propagates through the whole ply and then, thereafter through the entire laminate. During this progressive failure process, load shifting and crack growth portray the nonlinearity. Progressive failure is herein not further detailed. Wegmann (2015) performed preliminary investigations. The discussion on failure of composites with the focus on the numerical determination should be closed by putting the performance of current failure criteria into context. Hinton and Kaddour conducted the World Wide Failure Exercise WWFE-II over several years and published their results in Kaddour and Hinton (2013). The key idea of the WWFE-II was to investigate the performance of the most promising modern failure criteria. In Kaddour and Hinton (2013) the description of the investigated test cases, detailed discussions on the theoretical foundation of each failure criteria and grading of each failure criteria based on quantitative and qualitative performance is given. One key outcome is a ranking based on the grading (quantitative and qualitative) of each failure criteria. This ranking is given with figure 3.7. Before this figure is studied, one should consider, that all failure criteria for which modifications in terms of parameter adjustment are marked by an additional B. The ranking is provided for two reasons. First of all, to underline the performance capabilities of the Puck failure criteria, for which no modifications and no parametric adjustment has been made. Secondly, to stimulate a certain sensitivity regarding numerical failure prognosis in the field of composites. It is the case, that the quality of failure predictions varies drastically from case to case, which is reflected by those rather moderate grades.

3.4. Manufacturing of composites

Owing to the two composed phases of FRPs, the manufacturing techniques vary considerably from those of isotropic materials such as aluminum. This is why, there exists a multitude of manufacturing

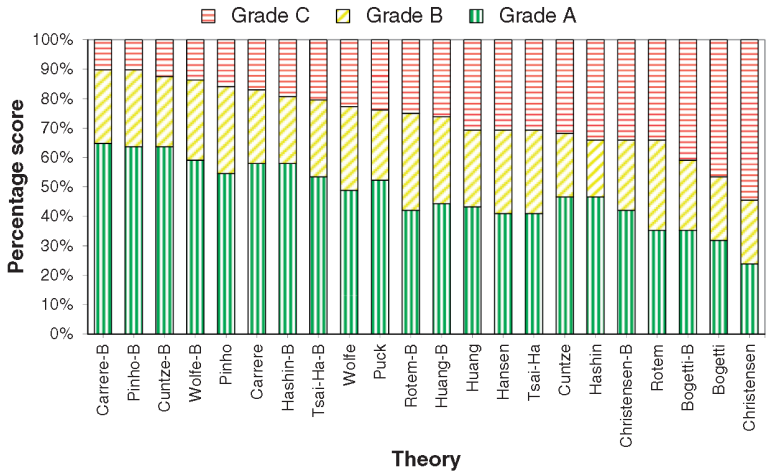

Figure 3.7.: Ranking of failures theories taking part in the WWFE-II (Kaddour and Hinton (2013))

approaches, yielding different fiber architectures (i.e. woven, braided etc.), fiber length (e.g. short fiber polymers) and mechanical overall properties. Moreover, in composite design, available manufacturing techniques evince a significant contrast in associated manufacturing effort and comprised costs, which is mainly due to individual characteristics in realizable production scales, degree of automation, prices of semi-finished goods, machine costs and many more (Mazumdar (2002)). There are several possibilities to group manufacturing processes; wet (e.g. prepreg) versus dry (e.g. preform) or by processed matrix system (thermosetting, thermoplastic or both), just to mention two possibilities. Figure 3.8 provides a brief overview over the variety of composite manufacturing processes by providing details for the prepreg technology, resin transfer molding, injection molding, pultrusion and sheet molding compound. All five manufacturing processes demonstrate strong distinctions in the core ingredients of composite manufacturing, which namely are: impregnation of fibers, stacking of plies (lay-up), consolidation and solidification.

In the first step, the impregnation, fibers are basically wetted with resin. This can for instance be accomplished by wetting fiber mats with brushes and rollers or by pulling fibers through a resin bath. Contrarily, in prepreg manufacturing, the semi-finished goods are already impregnated–as the name prepreg already indicates–before they are processed. In resin transfer molding (RTM) processes, the dry fiber preforms are impregnated via infusion or injection of resin into a mold (one or two-sided molds). There are several variation possible regarding pressure/vacuum application on either inlet and/or outlet and variation of the applied temperature on the mold. These variations are necessary to address sharp distinctions of available resin materials in viscosity and reaction kinetics and to account different demands on the final structures performance. In this regard, thermoplastics display a manifold higher viscosity than thermosettings, thereby demanding higher pressure gradients during the filling process. An example of a thermoplastic manufacturing of a complex structure is given by Lee (2014), where the focus was also lying on the scalability to mass production. This step is followed by the lay-up. In prepreg technology, the lay-up is carried out by stacking several plies. For the RTM process, the lay-up is defined by the preform technology. Therefore, when multi-axial or unidirectional non-crimp fiber mats are used, the stacking process is similar to the one of the prepreg technology. Nevertheless, for braided preforms, the lay-up is determined by the complex braiding process including a pronounced fiber architecture and is, in that consequence, quite opposed. Consolidation, the subsequent process step, mainly aims towards the solidification of the matrix phase, which is being discussed in the following. Aside from this, it can further promote drainage of abundant matrix material (called bleeding), squeeze out of voids and to circumvent dry spots. The latter two sorts of air traps reduce the stiffness of the composite and especially lower its strength because of the earlier onset of failure at those regions. This is why consolidation is of vital importance for the

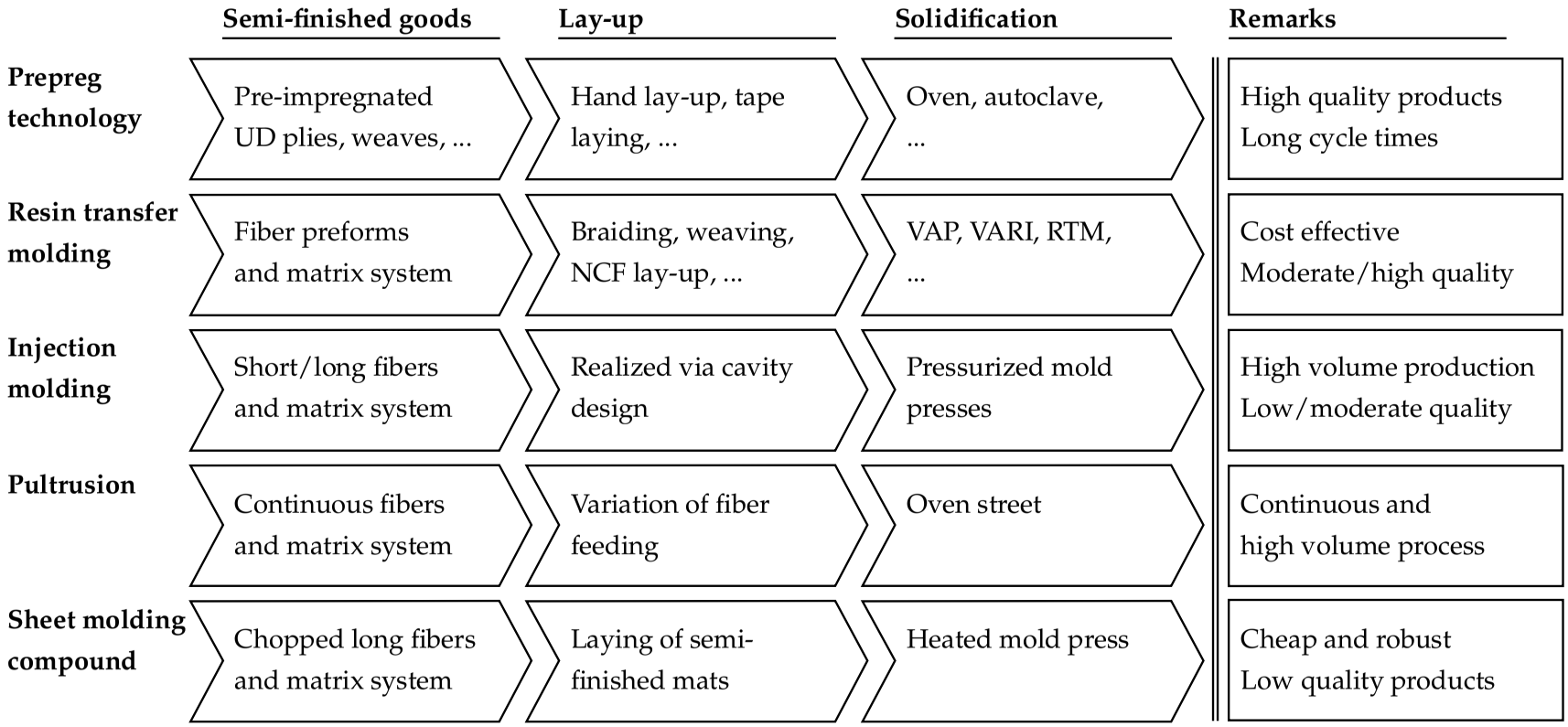

Figure 3.8.: Overview of some representative manufacturing techniques based on the used semi-finished goods, lay-up and solidification characteristics

manufacturing of high quality parts. The autoclave process marks the ideal process environment with respect to consolidation, because the composite part is exposed to a high pressure while being bagged into a vacuum bag. The combination of pressure and vacuum is promoting the escaping of trapped air and the bleeding out of redundant resin. In the solidification phase, the resin is cured at certain temperatures and pressure levels. These levels are in most cases determined by the used resin system. The solidification itself can take seconds for thermoplastics, which are normally solely melted, whereby they do not undergo any chemical reaction, and can even go up to more than two hours for certain thermosets. It should be noted that the production rate is related to the solidification time. For instance, the sheet molding compound (SMC) process is characterized by short solidification times enabling high achievable production rates and levering low cost parts via high volume production. This is why, SMC is the leading technology in 2013 annual over-all GFRP production (25% in 2013; see Witten et al. (2014)).

3.4.1. Injection molding for shooting short fiber composites

The injection molding process is qualitatively illustrated with figure 3.9. As can be seen there, the molding compound is transported via a screw conveyor into the mold cavity. Alternatively, a hydraulic plunger can provide the pressure for injecting the molding compound into the cavity. The molding compound consists of short or long fibers, which typically make up to 20 weight-%.

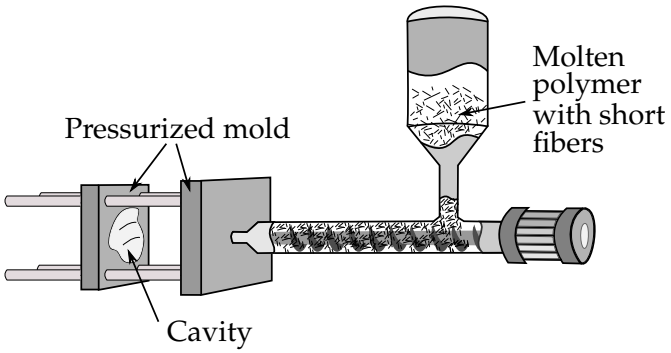

Figure 3.9.: The injection molding process

In a typical injection molding process the mold has a temperature of 150 degree Celsius, the injection takes three seconds and the shot size is about 250 Gram. The shot then remains for twenty-five seconds in the mold, which is meanwhile clamped with a force of five tons (see Mazumdar (2002)). The injection molding process is attractive for industrial application because of its short cycling times and low costs for high volume production. The latter is mainly due to the high degree of automation. However, the upfront investment costs are high, e.g. tooling costs are hundred times higher than for a filament winding process. In addition to that the obtainable material properties are poor in light of stiffness and strength. This is due to the fiber type and their low content in the final composite. Nevertheless, the manufacturing technique has its benefits and is responsible for almost one tenth of the CFRP production in 2013 (see Witten et al. (2014)).

3.4.2. Braiding as a preform technology

Braiding is a textile preforming technique; putting forth preforms consisting of two helical fiber yarns–called braider yarns–for the bi-axial and another longitudinal fiber for the tri-axial braiding case. On the left side of figure 3.10 the basic braiding process is being illustrated, whereas, on the right side a detailed view of the braid structure with the characteristic braiding angle φ is given.

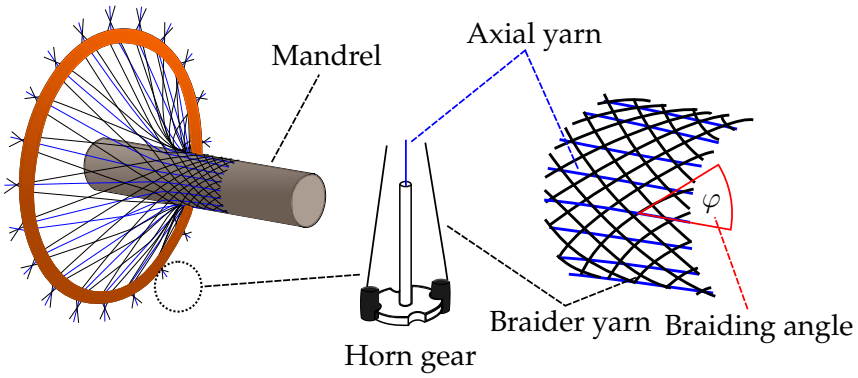

Figure 3.10.: Braiding and the obtained tri-axial braid

Once the preform is braided it can thereafter be impregnated with resin, consolidated and solidified in one step. A possibility to do so, is given by the RTM technology, for which, as mentioned earlier, several variations do exists. The use of RTM technologies in tandem with the highly automatable braiding process facilitates low production cycle times of composites. These low cycle times with minimal hand operation solely translates into low manufacturing costs, in case high volume production of composite parts amortize high upfront investment costs. This was also highlighted by the work of Knaier (2015). Further associated drawbacks are the limitation on a certain range of realizable braiding angles and possibly suboptimal stiffness properties of the obtained composites, which especially holds in the braiding fiber yarns' direction. The reduced stiffness quantities can be lead back to the presence of strong undulations. However, it should be noted, that the interlaminar properties of the derived composite are superior to those of layered composites because of the interwoven structure. These drawbacks can–to a certain extend–be alleviated by using different yarn sizes or fiber types for braider and axial yarn. In addition to this, the obtained preform can be augmented in stiffness and strength properties by adding UD or multiaxial NCF preform plies. On this mentioned grounds and due to low preform costs per composite part (in case of a high volume production), braiding is recently gaining pace.

3.4.3. Prepreg tape laying

The prepreg technology is owing its wide spread success in many industry fields to the fact, that high mechanical properties can be realized. This fact makes it clear that prepreg materials are most notably deployed in applications asking for high performance lightweight materials; as is for instance the case in aerospace. Further, high mechanical properties deduce from high fiber volume contents in the semi-finished goods, along with the ideal consolidation and solidification, for the case, curing is put into effect in an autoclave. Semi-finished goods are in this manufacturing technique, pre-impregnated fibers in the form of weaves, UD or multiaxial plies, tapes or patches. UD plies can be draped into forms by either hand or machine to realize defined laminate lay-ups. Prepreg tapes are commonly draped by machines via gantry robot heads or portal machines as illustrated in figure 3.11. When portal robots or similar machineries are involved, the mold does not necessarily be rotational symmetric. Prior to the placement of the continuous tapes, they are made sticky by warming them up (*Heating* in figure 3.11), so as to ensure a certain adhesion.

Different fiber orientation can be actualized by either automatically cutting the current tape and recommencing after re-orientating the draper head or by rotating the draper head during the draping process. The latter is only viable for certain rotation rates and is in inverse dependence on the mold's curvature. These restrictions arise, because wrinkles need to be circumvented. On the negative side, prepreg technologies are critical in terms of storage of the semi-finished goods, the prepregs itself, because of the often high labor intensive draping, if for instance realized by hand and the long

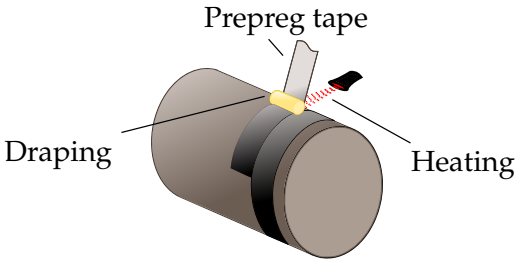

Figure 3.11.: The prepreg tape laying

cycling times for the autoclave cure. The first drawback is determined by the most frequently used thermosetting polymer matrix material, which would start to polymerize, i.e. the chemical reaction realizing the solidification, if uncooled or stored too long. The latter disadvantage results in high part costs and marks the bottleneck in terms of number of parts per annum. On the contrary, advantages of the technology are the high performance products and high designing freedoms for engineers. The high quality of the obtained composite parts can be traced back to the small fiber misalignments in production, neglect-able undulations, high volume content of fibers and the almost absence of air traps. For engineers, prepregs offer a multitude of design parameters which are only slightly restricted. An example for this would be the orientation of plies or tapes, which can in most cases be varied almost freely.

3.4.4. Further manufacturing techniques

Beside those mentioned manufacturing techniques, there do exist a great variety. Further examples would for instance be the filament winding, being frequently used for producing pipelines or the pultrusion as depicted with figure 3.12. To preserve some compactness of the thesis, the discussion of those shall be redirected to the work of Mazumdar (2002), Jones (1999) and Schürmann (2005).

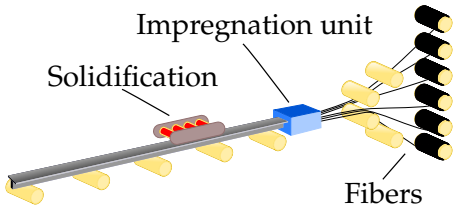

Figure 3.12.: Illustration of the pultrusion technology

3.5. Summary of thesis relevant fundamentals

The following items shall provide a summary of thesis relevant composite fundamentals in light of numerical design optimization.

Great stiffness drop from fiber material properties to final composite
Therefore it is essential to design composite structures in such a way that fibers predominately carry loads. This can ideally be realized with the use of structural design optimization.

Variety of manufacturing processes and variations
Demand for efficient and intuitive modeling strategies which enable the qualitative consideration of associated manufacturing effort and their impact on structural mechanics even at early design phases.

Strong coupling of manufacturing and mechanics

In composite manufacturing, the manufacturing process itself pre-defines fiber architecture and many more aspects of the final composite and does thereby have a great impact on achievable mechanical properties (e.g. undulations in braid fiber direction for the braiding process).

Zero design sensitivities for mass with respect to some variables

Mass is by far the most frequently used objective in design optimization. Yet, when optimizing composites, the optimizer needs to mind variables such as fiber orientation, since they lead to zero sensitivities in gradient-based optimization and in consequence may cause convergence issues.

Non-convex and nonlinear system equations

Non-convexity and nonlinear design responses stemming from UD transformations, thickness integration, switching of failure modes can lead to multi-modal optimization problems. These problems can pose issues regarding convergence to the global optima for local optimization strategies.

Presence of integer variables

When composite structures need to be parametrized, variables which are inherently of discrete nature can arise. Examples would be the number of plies or fiber type. These variables lead to a more complex problem class; mixed integer nonlinear programming problems.

Part II.

Interlude

4 | Quantifying manufacturing aspects

Within this chapter, a method for the capturing of topic-specific verbal knowledge regarding manufacturing effort will be presented. First, an overview on general concepts for the integration of manufacturing aspects is given. This is followed by an introduction into the soft computing methodology. At last, two manufacturing effort models will be developed, discussed and compared in detail.

> "In general, complexity and precision bear an inverse relation to one another in the sense that, as the complexity of a problem increases, the possibility of analyzing it in precise terms diminishes. [...] From this point of view, the capacity of a human brain to manipulate fuzzy concepts and non-quantitative sensory inputs may well be one of its most important assets. Thus, 'fuzzy thinking' may not be deplorable, after all, if it makes possible the solution of problems which are much too complex for precise analysis."
>
> Lotfi Zadeh (1921 – present)

Contents

4.1. Concepts for considering manufacturing aspects

In general, one can distinguish between two categories of possibilities for integrating manufacturing aspects into the optimization process, namely: explicit and implicit modeling. For each category, there are classes of approaches, such as the direct simulation and the simplified analytics for the explicit category and soft computing for the implicit respectively. This is depicted in figure 4.1.

The direct simulation or coupling approach is the by far most intuitive approach, since one simply couples process and structural simulations. In practice, there exists a wide variety of coupling

approaches. One approach would be the sequential evaluation of process responses and structural responses, where a subset of the process simulation's responses are passed as inputs to the structural simulation. The direct passing of available and detailed information–albeit dependent on the made abstractions and modeling degree of the process simulation–leverages the design optimization to a great degree of generality. This is mainly because most relevant manufacturing aspects are being considered directly. However, this high degree of generality comes in tandem with high numerical expenses, which are composed of computational as well as model building expenses. The latter is especially limiting, when considering the fact, that the process simulation needs to be fully parametrized and, moreover, an interface in-between process and structural simulations needs to be developed, so as to facilitate a coupled evaluation, where parameters and results are mutually exchanged. This coupling approach for considering manufacturing aspects can advantageously be utilized for the optimization of short fiber reinforced parts produced via injection molding. The process simulation in this context is a fluid simulation, which will not only provides information on the resin flow including void and weld line formations, but also give essential insight into the distribution and alignment of the short fibers. This fiber distribution is influenced by the part's geometry–or also called cavity in the context of injection molding–and process parameters such as gate location, injection pressure et cetera and will therefore have a crucial effect upon structural performance of the short fiber composite part by determining its stiffness and strength. Swoboda (2014) has first set up the frame for coupling and controlling both simulations. It did actually need another two works, Stadler (2015) and Müller (2015), so as to actually perform a structural design optimization on fully coupled structural and process simulations. Despite these development expenses, the optimizations themselves could be performed quite satisfactory in terms of computational effort and the significance of the optima they yielded. The latter especially holds, since the whole imprint of the manufacturing via the fiber orientation, weld and melt line information was processes onto stiffness and strength behavior on the structural level.

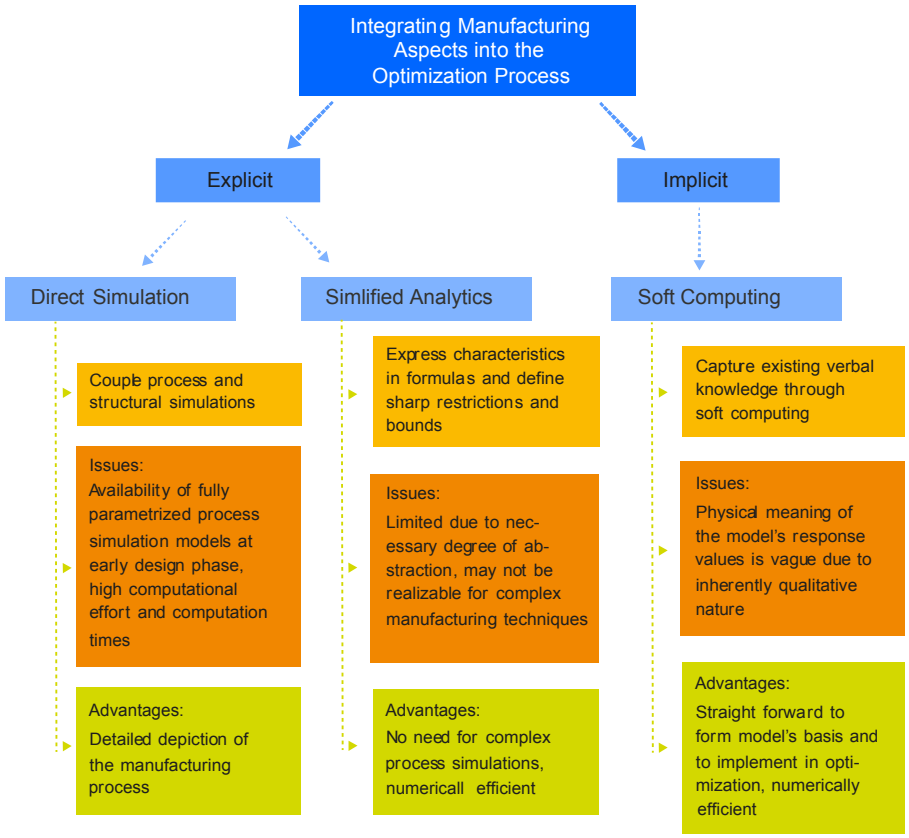

Figure 4.1.: Cathegories for modeling manufacturing aspects such that they can be introduced into the optimization process

Alternatively, one could use the second approach, which is the simplified analytics approach aiming to directly model the essential characteristics of the underlying manufacturing process via highly abstracted analytics. In this context, direct modeling is hence to be understood as a mathematically modeling with the use of analytical expressions. As not every physical and technical aspect of a given manufacturing process can analytically be formalized with ease, one needs to compromise on the level of detail and the complexity of captured interactions. Further, the analytical expressions need to be phrased such that they can be incorporated as constraints and bounds into the optimization process. Nevertheless, the advantage of having analytical system equations for the process responses empowers this approach with numerically efficiency and thereby places this approach in a more favorable light. Two examples of design optimizations conducted involving this approach are given by the chopper optimization performed by Schwarz (2013), Weinzierl (2014) and Nagarajan (2015) and the optimal design of a TU-Fast racer's monocoque by Kastner (2014) and Dolansky (2014). In all these research works, the rather straight forward consideration of manufacturing aspects enabled a numerically efficient optimization process. Lastly, soft computing representing an implicit approach is, as all priorly mentioned approaches, able to pass crucial information adhering to the manufacturing process. But, however, as the implicit already indicates, this approach models the manufacturing process in an indirect way, by actually capturing verbal and thus inherently qualitative expert knowledge. Soft computing, as it is compliant to uncertainty and fuzziness in values and their dependencies, can be used to form a model established on a expert knowledge. It is the qualitative nature of this verbal knowledge base used as a root for the later derived models, why soft computing methods are used instead of conventional methods. This is opposed to the finite element modeling in structural mechanics, where hard numbers and formulas form the basis. It is characteristic to this sort of approaches, that they are rather straight forward to implement. This is because of their intuitive and human-like evaluation, by processing qualitative information defined by the afore assessed verbal knowledge. Moreover, models build by taking advantage of soft computing methodologies are numerically efficient even in case the underlying physics are complex and challenging to capture with conventional approaches. Last but not least, the foundation on expert knowledge in combination with an ease of implementation enable a model development at early product development phases along with low expenses, i.e. no extra experiments for material characterization nor extra licensing costs for new software tools.

Summing up, the approach of implicit modeling bridges the advantages of both, the coupling and the direct modeling approach. This is because of its ability to capture optimization relevant process aspects by allowing a certain degree of complexity, while still being numerically efficient and displaying ease of implementation. Figure 4.1 summarizes the discussion lead in a single graph. In this work the latter approach of modeling the associated manufacturing effort of a given process implicitly through soft computing of verbal expert knowledge will be developed, displayed for two manufacturing techniques and critically discussed. The theoretical basis will be given next, which is followed by two tangible manufacturing effort models: one for the braiding technique and the other for Prepreg lamination process.

4.2. Soft computing as a tool for creating effort models

This chapter is addressing the challenge of creating a parametrized model capable of evaluating the level of effort linked to a manufacturing technique. Hence, the theoretical background for generating manufacturing effort models will be given first. Thereafter, a general outline on how a manufacturing effort model is actually developed will be given. This chapter will then be framed by the discussion and presentation of two manufacturing effort models: one for braiding and one for prepreg technology.

4.2.1. Theory and practice of knowledge-based systems

A knowledge-based system is characterized by its specific architecture and its foundation on a knowledge base, also called knowledge domain. The system processes information, interpolates and reasons about quantitative inputs by evaluating information based on the provided knowledge base. It can hence also be defined as a system, which attempts to emulate human capabilities in analyzing and solving complex problems, by decision making and reasoning based on afore assessed knowledge (Rosenman et al. (1986)). Since a given knowledge-based system is not able to extrapolate knowledge by its own, the boundaries of this knowledge domain describe the limits of the solving competence of a given knowledge-based system, as mentioned by Shortliffe and Buchanan (1975). The science studying how to derive such a knowledge domain is referred to as knowledge engineering. Figure 4.2 depicts the general architecture of a knowledge-based system.

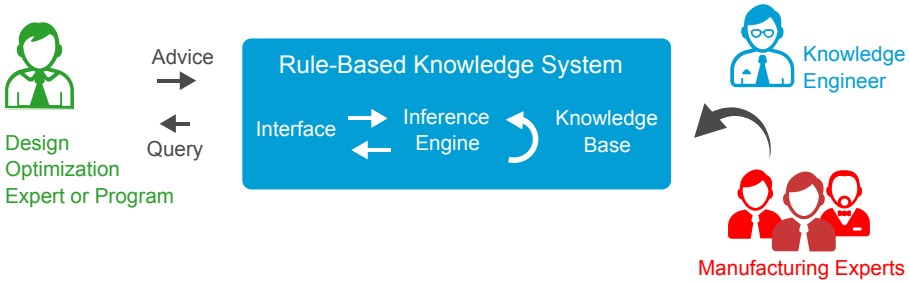

Figure 4.2.: Architecture of a knowledge-based system including interface to optimization program and manufacturing experts

As illustrated, a general knowledge-based system consists of an interface, inference engine and as aforementioned the knowledge base (Russell and Norvig (2009)). The knowledge base is derived via knowledge engineers from expert knowledge of one or more specialist in the desired field or fields (Miles and Moore (2012)). With the help of the inference engine, the knowledge-based system is able to make evaluations and decisions based on its knowledge base. Nguyen and Sugeno (2012) show how this inference engine can be realized via fuzzy logic. The interface module then basically links the knowledge-based system to the design optimization expert or program demanding expertise by passing inputs and outputs from one to the other. For more insight into knowledge-based systems and their architecture consult Hayes-Roth et al. (1984) and into weak and strong artificial intelligence see Russell and Norvig (2009) and Luger (2004).

Summing up, the most relevant features of knowledge-based systems are:

- Specialized in purposed science disciplines (knowledge domain),
- Interpolate knowledge based on implemented knowledge domain,
- Provides rationale about decisions made.

Looking at the history of the field of artificial intelligence, knowledge-based systems can be regarded to be the first representatives. This is mainly because they were first to be successful implemented and applied in many disciplines, albeit they solely exhibit so-called weak artificial intelligence (Luger (2004)). They are categorized as weak artificial intelligence, because they lack many human capabilities like sentience, self-consciousness, self-awareness et cetera, which are for instance needed for creative and innovative solution finding. The applications of knowledge-based systems range from studying hypothesis about the structure of molecules (DENDRAL by Lindsay et al. (1993)) over medical diagnosis of severe infections (MYCIN by Shortliffe and Buchanan (1975)) to geological appraisal of sites for commercial development and planty more. One of the most renowned knowledge-based system is MYCIN, developed by Eduard Shortliffe during his Ph.D. at

the Stanford University. This knowledge-based system–or in this specific case the expert system–mimics doctors of medicine in detecting bacterial infections, e.g. bacteremia, meningitis et cetera, and assigning the most appropriate drug treatment. MYCIN is further able to rank appropriate treatments, provide a confidence factor and reason about decisions made. Medical treatment proposals included a recommendation of antibiotics with their dose rates in dependency on the patient's infection type and body weight. The knowledge base has been formed by roughly six hundred rules, for which, implementing took about five years. Remarkably, the final program was able to reach up to 65 percent of correct answers and was superior to five medical specialist from the Stanford medical faculty, whose ratings range from 42.5 to 62.5 percent as discussed by Yu et al. (1979). However, as it is a common drawback of knowledge-based systems, the MYCIN is highly specialized on bacterial infections, but has no "common-sense", which is why it could make mistakes being obvious for doctors. Additional problems linked to the MYCIN project are ethical and legal issues in case of a wrong diagnosis, the need for a person interacting with MYCIN and the computational effort at that time. More practical applications of knowledge-based systems originated between 1995 and 2004 can be found in Liao (2004).

4.2.2. Soft computing

Up to this point, the general definition and capability of a knowledge-based system has been outlined; yet, the question on how the knowledge base, as depicted in figure 4.2, can actually be formed and be implemented has not been answered. In contrast to conventional programming, soft computing methods are not founded on an analytical or numerical representation of the underlying physics, but instead on qualitative information. Owing to this fact, one needs to seek for methods being compliant to imprecision, uncertainty and partial truth. Hence, methods coping with fuzzy numbers and/or relationships. One class fulfilling these requirements and in that sense, similarly working to a human brain, is formed by soft computing methods (see Zadeh (1994) and Hajela (2002)), where the soft already indicates, that instead of being based on conventional sharp or "hard" analytics and numerics it processes information in a "soft" manner as we humans do as well. Hajela (2002) gives an overview on soft computing methods, while also including viability in his discussions.

Most common representatives of soft computing methods are:

- Neural networks
- Fuzzy logic
- Evolutionary computation or search
- Probabilistic approaches, e.g. Bayesian networks
- Support vector machines

It will be the fuzzy logic founded by Zadeh (1965), which will be used as the soft computing method to form the manufacturing effort model in this work. Neural networks, as comprehensively discussed in Eberhart (2014), would have been an attractive alternative. For that reason they have been investigated and tested for modeling manufacturing effort as well. However, as it did turn out, these neural computing methods require extensive acquisition of information, so as to ensure a sufficiently large training set and ultimately for asuring a certain approximation quality. Due to the aim of being applicable at early design phases, the number of interviews or expert talks for the acquisition of the manufacturing effort's knowledge domain, shall be restricted to a minimum. This is obviously in conflict with the demand for huge training sets. Bayesian networks as used in MYCIN could be excluded for similar reasons. Evolutionary search approaches have been excluded, because the choice of optimization algorithm shall not be dictated or limited by the manufacturing effort

model. Moreover, the manufacturing effort model is also foreseen to not only be applied within an optimization framework, but also in the analysis or even design of structures.

As a sidemark, another dazzling application of the fuzzy logic arithmetic is to grasp uncertainty and thereby leveraging optimization schemes to a higher level of significance is shown and discussed by Wehrle (2015). In this work, the consideration of fuzziness increased the robustness of design optima concerning load, geometry and material variances, while still designing light weight. In a wider sense, the approach shown in the subsequent sections also addresses uncertainty brought forward by the qualitative nature of verbal expert knowledge.

4.2.3. Building a manufacturing effort model

So far, general information regarding knowledge engineering and soft computing have been given. Now, both disciplines will combined such they can be utilized to form a manufacturing effort model (MEM). The term MEM shall henceforth refer to a model capable of capturing verbal expert knowledge concerning the associated level of effort for a manufacturing technique in light. Subsequently, two MEM will be formed, one for braiding and the other addressing effort originating from the prepreg laying process. The process of developing such a MEM is a balancing act on two demanding levels: the knowledge engineering and soft computing level. This generalization has been elaborated after having developed two distinct knowledge-based systems and applying them in computing manufacturing effort within an optimization frame. The latter mentioned discipline, the soft computing, is addressing the difficulty of emulating and handling qualitative information, which is described by a knowledge base. Whereas the first involves the challenge of acquiring knowledge by enquiring knowledge and experience of domain-specific experts and thereafter translating it into a well-structured knowledge base of general nature. As can be observed, one link between both levels is the knowledge base, over which they mutually express and exchange information. With figure 4.3 a sketch of these two levels is given. This figure will support and guide the following description of the general process of how to build a manufacturing effort model.

Level: Knowledge engineering

First, the knowledge base needs to be formed by querying verbal expert knowledge. This demand of enquiring and assessing verbal information is the core of the discipline knowledge engineering, which also marks the first level. This discipline is designated to the coping and formulation of knowledge, such that it can be used in rule-based systems in a manner, that complex problems demanding a high level of human expertise can be solved with ease. Hence, it is an intermediate step towards the final knowledge-based system by defining its basis; the knowledge base. In that sense, knowledge engineering can–in analogy to the FEA, where the integration of isoparametric elements and the assembly of those lead to the final system equations as given with the equation set (2.13)–be understood as a pre-processing step. As shown in figure 4.3 with *Sources of information*, the first step is marked by the gathering of basic knowledge from different sources of information. Possible sources thereby are: literature, data bases, norms or even some preliminary simulations. This gathering shall be understood as a first inspection of the knowledge domain and purely aims to get in touch with the domain-specific terminology and peculiarities. This step is actually of paramount importance for two reasons. First and foremost, the knowledge engineers needs to get familiar with the involved vocabulary, since otherwise the quality of the knowledge base will suffer from incompleteness or inconsistency caused by communication problems. Further the knowledge engineer is per se not familiar with the knowledge he is intending to enquire, but yet has to appear competent enough for being taken seriously. Evidently, this especially holds if the knowledge engineer has to consult experts from outside of his radius of renownedness or even outside of this own institution. For that reason, prior to the first expert dialog, the vocabulary associated with the braiding manufacturing technique,

e.g. braiding angle, axial yarn width, bobbins et cetera, have been learned and comprehended via a brief literature review and sight of lecture notes, to provide an example.

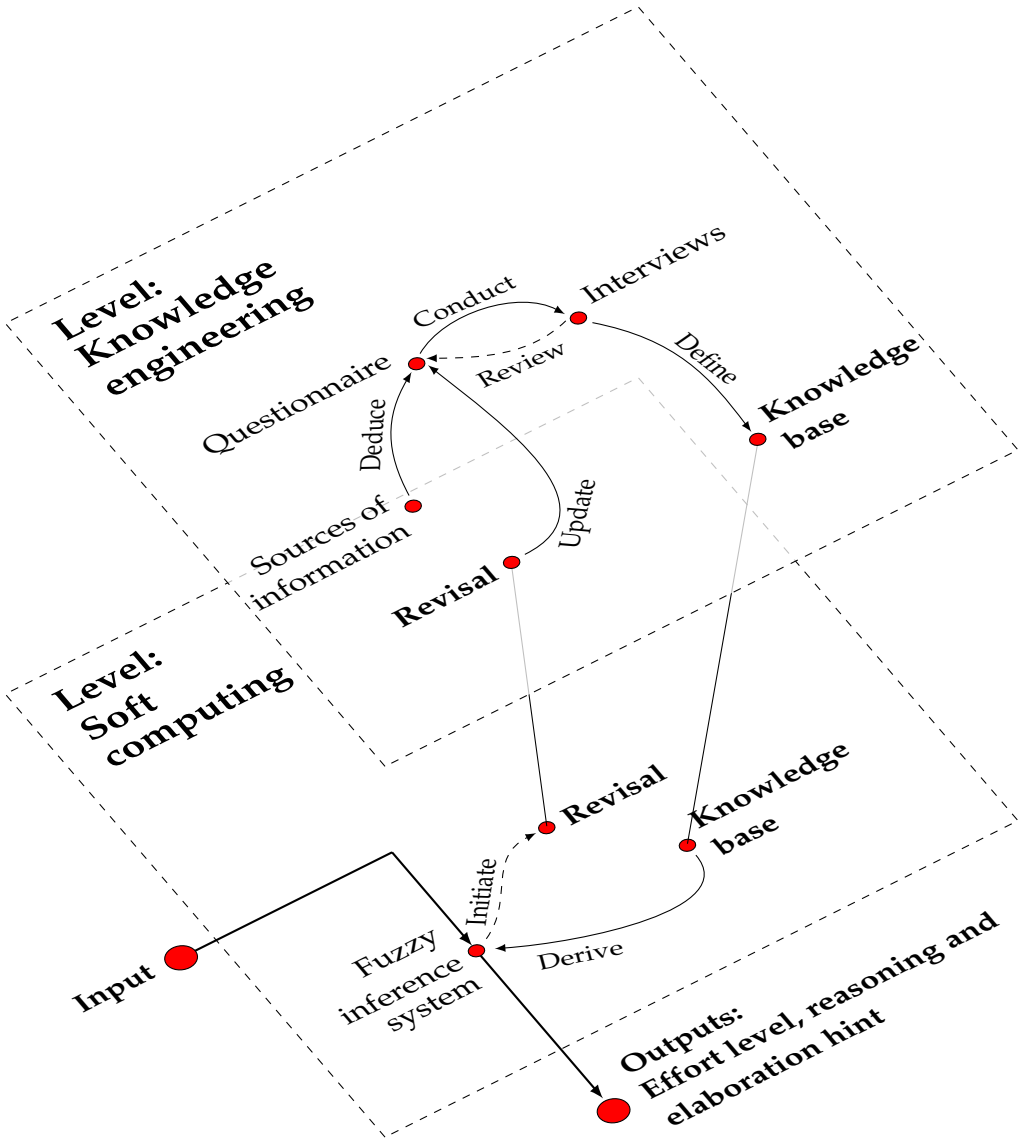

Figure 4.3.: Illustration of engineering knowledge and soft computing level involved in building a manufacturing effort model

Once, the knowledge engineer is familiar enough to phrase the meaningful and relevant questions, a questionnaire as a basis for the subsequent expert interviews shall be set up next (item *Questionnaire* in figure 4.3). This questionnaire is intended to support the knowledge engineer in conducting the interview unbrokenly and fluently. It further needs to be organized in such a way, that it facilitates a simple, but comprehensive recording, such that the expert interview can be conducted efficiently. This is important since most contemplable experts have little time. Most importantly, the questionnaire shall not feature or forward any bias. Figure 4.4 gives an example, of how questions have been posed. Note, that the lines in *Example 1* and the cross in *Example 2* were interactively editable by the manufacturing expert in the electronic version of the questionnaire, e.g. the cross was movable by clicking on it. Therefore, it could be answered even without meeting in person. Nonetheless, it is highly advisable to use the questionnaire as a conversation guidance for the knowledge engineer, allowing for dynamics in terms of rephrasing questions or going into interesting aspects, as they can evolve during the conversation. Speaking of which, the interview itself most probably leads to complete new aspects, change perspectives or even bring forth unnoticed facets of the knowledge domain

for the knowledge engineer. This can be made clear, by considering, that the knowledge engineer is most commonly outside the experts subject area. Wherefore, the development of questionnaires and the the subsequently conducted interviews shall be understood as an iterative process. This is insinuated by the dashed *Review* arrow in figure 4.3. Over these iterations, the knowledge engineer gains more and more insight into the topic and is therefore able to particularize his questions from iteration to iteration. Ultimately, this leads to an evolvement from open to closed questions, where open questions do not ask for one specific answer, but closed do. Moreover, in case of closed questions the knowledge engineer has some idea of how the expert could answer, e.g. within certain bounds, whereas he explores new areas of the knowledge domain with open ones. In figure 4.4, *Example 1* represents an open example, since it could be one or multiple parameters given as an answer and, moreover, the knowledge engineer may probes for the unexpected. Opposed to that, *Example 2* can be regarded as a closed one, due to the specific query about the minimal ratio $\frac{R}{D}$ within given bounds. The latter is further pointing towards another relevant aspect when developing a questionnaire; namely numbers. It is highly recommended to abandon absolute numbers, at least wherever possible. By doing so, the level of generality of the later deduced knowledge base is elevated. In addition to that, experts working in different fields of application–but yet with the same field of expertise–do not face difficulties answering questions, because otherwise, if numbers are involved, they are reasonable for one field of application and may be totally off for others.

Example 1: Which parameters or parameter constillation effect the braid quality?

Example 2: What is the limit of curvature radius R in depence on the structure's diameter D?

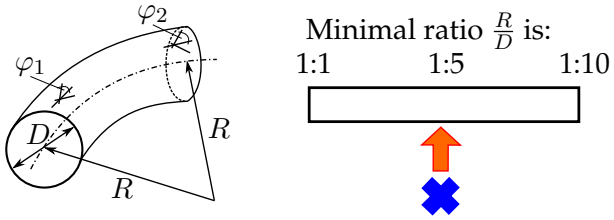

Figure 4.4.: Two examples taken from the developed questionnaire sheet: open (Example 1) and closed (Example 2) question

With figure 4.5, an extract of an interview record is given. The interview took place on the 4th of October 2014. For making it more readable, this extract, including the writings, have been vectorized via the image tool *Inkscape*, wherefore the handwriting has slightly been altered by doing so. Nonetheless, this figure marks the transition from conducting interviews towards the definition of a knowledge base. This knowledge base bridges the knowledge acquisition process (**Level: Knowledge engineering** in figure 4.3) with the program-wise realization, where upon this knowledge base the final implemented inference engine rests. This will then enable the reasoning about certain given inputs (**Level: Soft computing** in figure 4.3). Hence, the knowledge base will actually be implemented as it is, by exploiting soft computing methods; herein, by defining a so called fuzzy inference system with the use of the fuzzy logic arithmetic. For that reason, the more thoroughly the interviews are post-processesed, and, in further consequence, the more detailed the knowledge base is being defined, the more straightforward and intuitively the implementation can be carried out. At this transition stage, there is a latent risk originating from the knowledge engineering in misinterpreting or biasing the definition of the knowledge base. So as to foresee this risk, the documentation of the interview

Example 3: Give a reasonable range for the yarn width of a standard $12k$ CFRP roving!
Please note: Choose such that no braid opening nor over-compacting occurs.

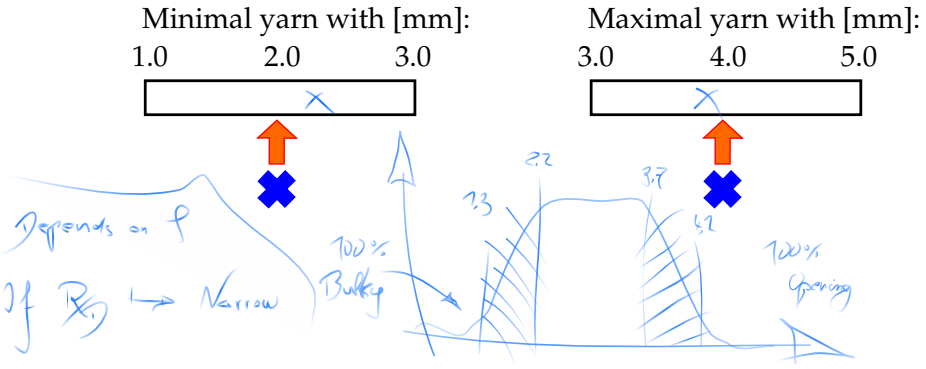

Figure 4.5.: Extract of an expert interview conducted on the 4th of October 2014

shall be as detailed and precise as possible. Notes and other recordings may already be close to the diction used in formulating the knowledge base. In case of the example given with figure 4.5, the knowledge engineer annotates fuzziness expressed by the expert in a form being as close as possible to the later used membership functions as a part of the fuzzy logic arithmetic. This is why, this section of the documented interview can be translated with ease, which can be comprehend with figure 4.6, where the similarity becomes obvious.

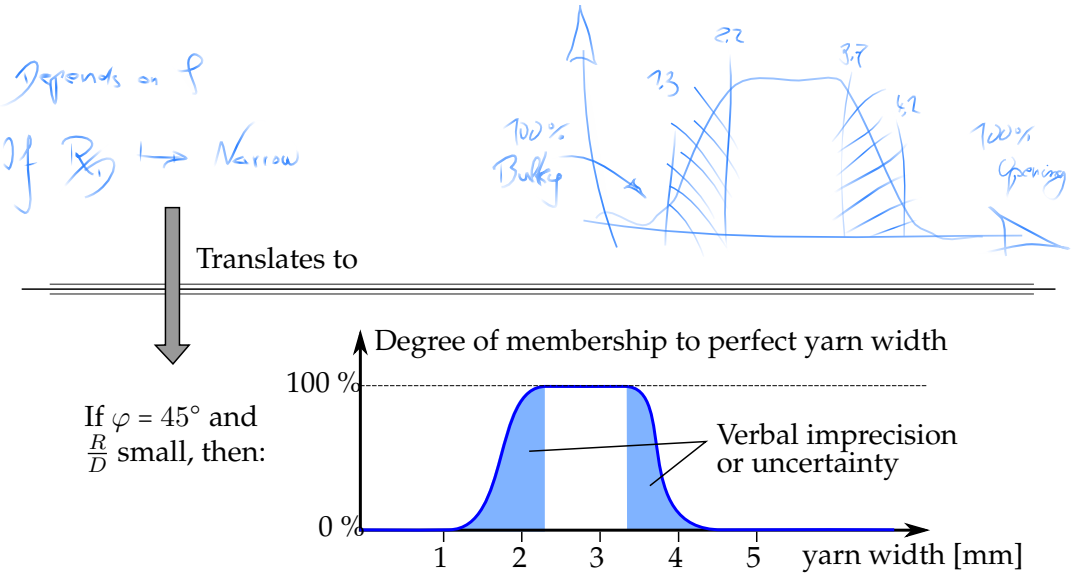

Figure 4.6.: Transition from interview notes towards the final knowledge base

Some details are already anticipated with figure 4.6. So, for instance, it already depicts a membership function, which basically defines the degree of membership of numerical values to a fuzzy number set. By doing so, it conceptualizes one key aspect of the fuzzy logic, where fuzzy number sets are defined and worked with, rather than sharp single numbers. These fuzzy number sets are then compliant to verbal imprecision and/or uncertainty by allowing a vague degree of membership for a certain range of numbers as discussed by Zadeh (1965). In figure 4.6 these ranges are highlighted in marine blue. As a final remark on the interviews, the iterative dialogs in-between the knowledge engineer as an analyst and the expert as the specialist in the knowledge domain of interest, shall obey a open policy, where any bias is kept out, any question can be posed and, most importantly, relevant aspects are not only verbally conceptualized, but also well recorded. This includes remarks on the level of confidence in the discussed numbers and relations, their range of uncertainty et cetera.

Carefully following these points, will help to effectively identify essential parameters and making their interrelations explicit, with a minimal number of interviews needed.

Level: Soft computing

The translation of the priorly acquired expert knowledge into an inference engine, capable of making evaluations, reasoning about made decisions and providing hints for optimal parameter improvements is based on the afore defined knowledge base. This translation and the involved soft computing methods will be discussed in the following. The arithmetic used to form such an inference engine (as illustrated in figure 4.2) will be the fuzzy logic. Here, the author desists from discussing the fuzzy arithmetic at great detail. For more insight into the basics see Huber (2010) and Wehrle (2015). Instead, the features explicitly utilized to model manufacturing effort and the extensions, made by this thesis, will be discussed in the following. Fuzzy inference system (FIS) will henceforth refer to the inference engine realized with the help of the fuzzy logic arithmetic. With figure 4.7 a general form of a Mamdani fuzzy inference system is given as introduced by Mamdani and Assilian (1975). $\mu^j_{x_i}$ therein refers to a membership function, defining the fuzzy number set associated with rule j and the input variable x_i. Coming from bottom left, the crisp input values of x_i are first fuzzified, i.e. translated to a fuzzy number set (antecedent - black horizontal lines over the input variables). Thereafter, their antecedent is evaluated rule-wise such that the rule output membership function μ^j_r can be defined (implication - red fill of output fuzzy membership functions). All rule output membership functions μ^j_r are cumulated into the aggregated output function μ_r (aggregation - green fill of final output fuzzy membership function). Finally, a crisp response r as one output of the Mamdani FIS is computed (defuzzification - black dot in green fill). This process is discussed at length in section 4.3.1.

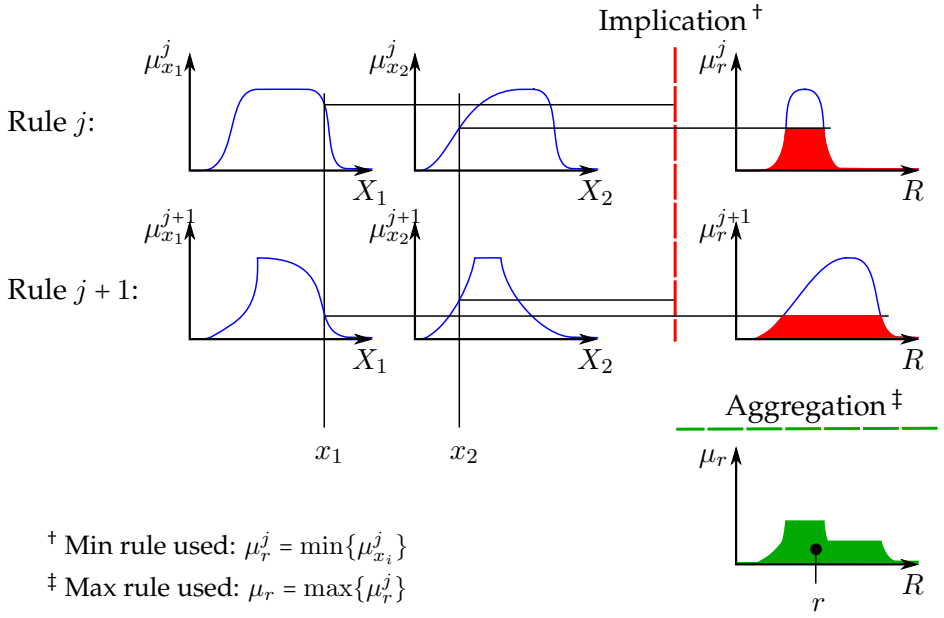

Figure 4.7.: General definition of a Mamdani fuzzy inference system

The implication can either represent an *AND* or *OR* rule. In figure 4.7 the implication is illustrated via a minimum rule, whereas a maximum rule is used to aggregate. Thus the implication here represents an *OR* rule. Further rule definitions are possible, yet, only one alternative is frequently used as well; the product rule for implication and summation rule for the aggregation respectively. Defuzzification is most commonly conducted by computing the center of gravity of the aggregated membership function μ_r as given with the following equation:

$$r_{\mathrm{CoG}} = \frac{\int_R \mu_r r \mathrm{d}r}{\int_R \mu_r \mathrm{d}r} \tag{4.1}$$

In this thesis, an extension to the Mamdani FIS will be made, by not only using the direct output of such a Mamdani fuzzy inference system, but also the weights and circumstances which did lead to that specific outcome. Hence, the arguments which mainly influence the implication or aggregation process are fetched as well. This can be realized by explicitly asking for argument values causing a minimal or respectively maximal rule output. But before coming to this, the involved mathematics for finding an argument causing a function to be minimal will be defined by

$$x^{\min} := \arg\min_x f(x) = \{x' | f(x') = \min_x f(x)\}, \tag{4.2}$$

with f being a given function and $x^{\min}$ the argument, where f is minimal. Translating this for the aggregation and implication rule leads to the following equations (4.3) and (4.4), where j_{Active} indicates the active rule during aggregation and i_{Active} the indices of the active input variable associated with the active rule in the implication.

$$j_{\mathrm{Active}} := \arg\max_j \{\mu_r^j\} \tag{4.3}$$

$$i_{\mathrm{Active}} := \arg\min_i \{\mu_{x_i}^{j_{\mathrm{Active}}}\} \tag{4.4}$$

For rules different to the ones discussed here, the idea is still transferable, even though, the criteria for identifying the active–or most contributing rule or input variable–may be changed. To further illuminating this idea, first the actual manufacturing effort models will be derived and discussed in the following two sections. Comparisons and examples how these general statements are actually implemented will be made and by doing so, the idea will become more clear. So for instance, in section 4.3.1 this process will be demonstrated in detail.

4.2.4. Validating and verifying manufacturing effort models

Once, the knowledge base has been translated into rules and is being implemented in a fuzzy inference system, the knowledge engineer needs to probe the derived system with the help of test queries. These test queries may already been acquired during the interviewing phase, but sure must not been used for defining the knowledge base. In case these test queries reveal inconsistencies, wrong estimates or provide wrong reasoning, a revisal needs to be initiated. This revisal then leads to a re-entering into the loop of updating the questionnaire, re-conducting interviews and re-defining or adding rules in the knowledge base until a certain level of validity is reached. A general validation process, as common in software development or other disciplines, is hard to realize, since it would also imply, that the knowledge engineer needs to set-up that many test queries that all implemented relations and possible interactions are probed. However, this is not viable within this thesis for two reasons. First, the soft computing approach is that mighty, since it evolves human-like capabilities in interpolating or inferring knowledge within a topic-specific field. By doing so, the final knowledge-based system is thus cable of evaluating information, which has not explicitly been implemented by the software engineer, but is covered by the formulation of the knowledge base overall. Moreover, the knowledge engineer would rather implement all of these rules, in case he would be able to make all interactions and possible variations explicit, instead of just using it for testing. Secondly and ultimately, this would also result in an unrealistically high number of expert interviews hindering an efficient usage in the early design phase.

4.3. Developed manufacturing effort models

In this section, two manufacturing effort models (braiding and prepreg laying) will be presented. Huber (2010) presented a FIS capturing soft aspects of another production technique and should be mentioned as an additional reference and source of inspiration here.

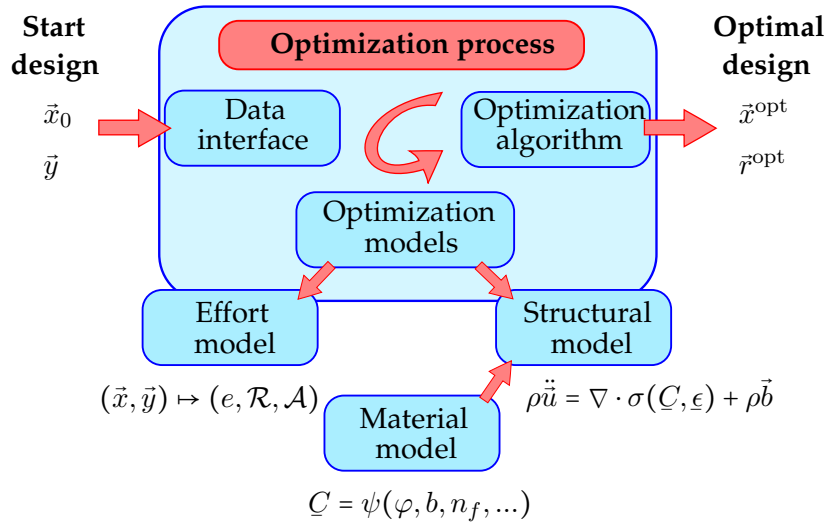

Figure 4.8.: The optimization process including the interface to the optimization models

Figure 4.8 depicts, how each effort model can be incorporated into the general optimization process. This figure has been inspired by Baier et al. (1994), where the term optimization process system have been introduced already. In this figure, $\vec{x}_0$ represents the starting vector and $\vec{y}$ the vector of parameters. Both are passed to the data interface provided by EOS. EOS is an *Environment for optimization and simulation* developed by da Rocha-Schmidt and the author, both working at the Institute of Lightweight Structures. The optimization algorithms and alike modules are imported from the python package pyOpt (Perez et al. (2012)), which represents a gathering of up-to-date optimization algorithms. The optimization as depicted in figure 4.8, then updates the design variable vector $\vec{x}$ until convergence has been reached and the optimal design can be outputted in form of an optimal design variable vector $\vec{x}^{\text{opt}}$ and the associated design responses at the optima $\vec{r}^{\text{opt}}$. For each determination of the objective functions $\vec{f}$ and the constraint vector $\vec{g}$, both optimization models need to be evaluated. On right hand side, the structural responses $\vec{r}_{\text{FEM}}$, as given by the implementation of continuum mechanical system equations with the use of finite element software (FEA), are computed. It shall already be noted, that for doing so, another model, namely a parametrized material model, is needed. This material model will be addressed in chapter 5. On the other side, the *soft* responses $\vec{r}_{\text{MEM}}$ will be determined, by conducting an manufacturing effort analysis (MEA), where the level of effort e, the reason $\mathcal{R}$ for that level and a designing advice $\mathcal{A}$ are computed.

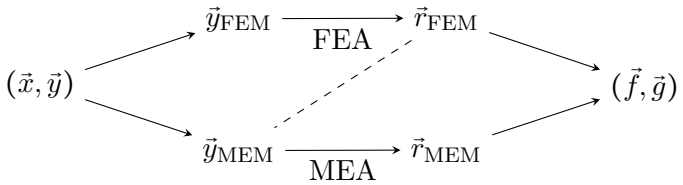

Figure 4.9.: Embedding both models–effort and structural–in the chain from design variables and parameters to optimization responses

Figure 4.9 illustrates the flow for one single evaluation of the optimization model, where the set of design variables and parameters $(\vec{x}, \vec{y})$ are the input values and the optimization response set $(\vec{f}, \vec{g})$ is

to be determined. Since, a sub-set of the MEM input parameter vector $\vec{y}_{\mathrm{MEM}}$ is computed through the pre-processing of the FEA, the FEA response vector $\vec{r}_{\mathrm{FEM}}$ is linked with the input of the MMEA. An example for this would be the braider yarn width $w^{(b)}$, which is needed for the material model as a part of the FEA pre-processing, wherefore it is already computed there, but yet, of course, also needed as an fuzzy variable in the fuzzy inference system of the MEM. For this reason, the braider yarn width is in some cases already computed in the FEA and thereafter passed to MEA. This is depicted with the dashed line in figure 4.9.

4.3.1. Braid manufacturing effort model

The manufacturing effort model (MEM), describing the efforts associated with the braiding technique is derived based on a Mamdani fuzzy inference system as already generally defined and discussed, as for instance given with figure 4.7. The rules are defined using *product*, *max* and *sum*, where the first two define the *AND* and *OR* rule for the implication and the last the aggregation. This is summarized with table 4.1.

Table 4.1.: Used implication and aggreation rules for braid MEM

Mamdani step	Rule	Realization
Implication	*AND*	Product
Implication	*OR*	Max
Aggregation	-	Sum

The knowledge base is derived based on multiple conducted interviews with braiding experts from the Institute of Carbon Composites (*LCC* - TU Munich), Institute of Aircraft Design (*IFB* - TU Stuttgart), the company Munich Composites (*MC: Braid*) and further partners from the MAI-Carbon project MAI-Design. From these interviews, a knowledge base has iteratively formed, on which basis the following depictive representation (figure 4.10) has been generated. It is illustrated there, how the two dimensions of lengthwise geometry and profile geometry do imprint on the expectable manufacturing effort level (ordinate axis). Moreover, the coloring represents the level of severity; hence, red reflects an effort level close to not producible and blue translates into producible with ease. It is evident, that altering the lengthwise geometry from being straight and non-conical towards curved and conical in shape leads to an upward trend in the manufacturing effort level. The same holds for the profile geometry, where a deviation from the perfect cylinder shape towards shapes displaying high aspect ratios Λ, sharp edges $r \to 0$, undercuts et cetera results in higher associated efforts. The situation even worsens, in case both geometric deviations from a simple tubular braid mandrel occur simultaneously. This is also depicted in figure 4.10, where the worst combination accumulate in the greatest level of manufacturing effort. Before the discussion of the braid manufacturing effort model is deepened, the used terminology of the response manufacturing effort shall be put in light of the discussion. This abstract terminology of *effort* is chosen deliberately; basically because of its general validity. More specifically, it is independent of peculiarities being immanent to different engineering disciplines. An example of a measure being dependent on characteristics of the discipline in light, is costs. This is because it is an absolute and quantitative measure, where peculiarities, such as existing machinery, financial situation in terms of obtainable interest rates and regional positioning of the firm, do have a clear and distinctive imprint onto the measure costs. It is further due to the fact, that manufacturing effort basically embraces multiple sources including costs, complexity or poor product quality in a qualitative manner. It can hence be classified as a superordinate measure, unifying the demands for being company and discipline independent, as well as not being affected by regional or similar peculiarities. Table 4.2 gives a brief overview on the sources embraced by the term effort, at least, as it is being comprehended and considered herein.

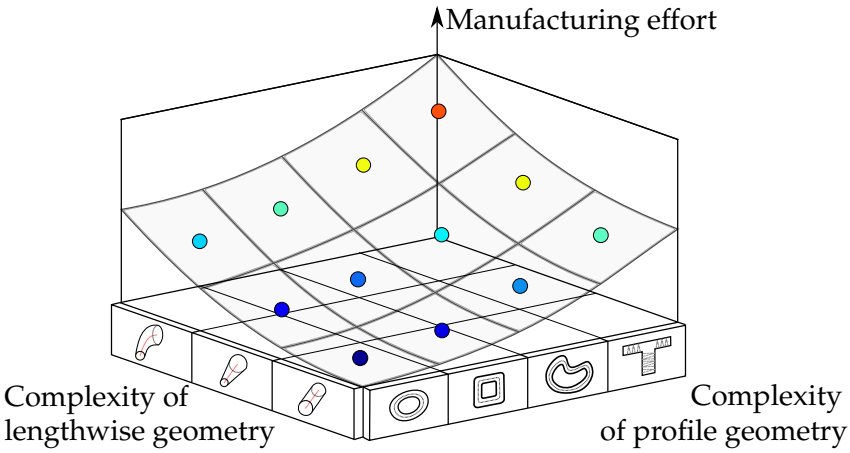

Figure 4.10.: Manufacturing effortover complexity of profile and lengthwise geometry (Schatz and Baier (2014))

Table 4.2.: Sources of manufacturing effort

Source	Examples
costs	production time
	man power
complexity	additional devices
	special machinery
environmentalism	wastage of preform material
product quality	unusable semi-finished product
	scrap rates
...	...

So far, geometric parameters, which mainly influence the shape of the braid mandrel have been discussed and illustrated in figure 4.10. Beside those geometric parameters, braid sizing parameters such as braiding angle or number of over-braidings–or discrete braid layer thickness–as well as process and machine parameters such as number of bobbins and ultimately material parameters, i.e. number of filaments per yarn or fiber material, are considered too, since they contribute to the level of manufacturing effort as well. The whole fuzzy inference system as the core of the braiding manufacturing effort model (BMEM) is depicted with figure 4.11. As illustrated there, the input variables of the BMEM are the braiding angle φ, the mandrel's circumference U, fiber data such as fiber material and number of filaments, lengthwise normalized curvature $\frac{R}{D}$, i.e. curvature of the mandrel axis, the profile's or respectively mandrel's aspect ratio Λ, edge radii r of the profile and the number of layers. A subset of these input variables, namely the braiding angle, the circumference and fiber data, are first condensed by taking advantage of analytical formulas such that the generalized parameters yarn width w and its range w' along with braiding angle φ are obtained and thereafter passed to the appropriate sub-FIS modules. With equation (4.5) the forumla for computing the braider yarn width $w^{(b)}$ as part of the analytical condensation is being given,

$$w^{(b)} = \frac{2U}{n_{\text{Bobbin}}} \cos(\varphi). \tag{4.5}$$

Next, an extract of the whole BMEM will be serve as an illustrative example of how the derived knowledge base has been transfered to the final BMEM. Figure 4.12 shows four rules of the φ-w-FIS, which itself is a sub-FIS module of the main FIS as illustrated in figure 4.11.

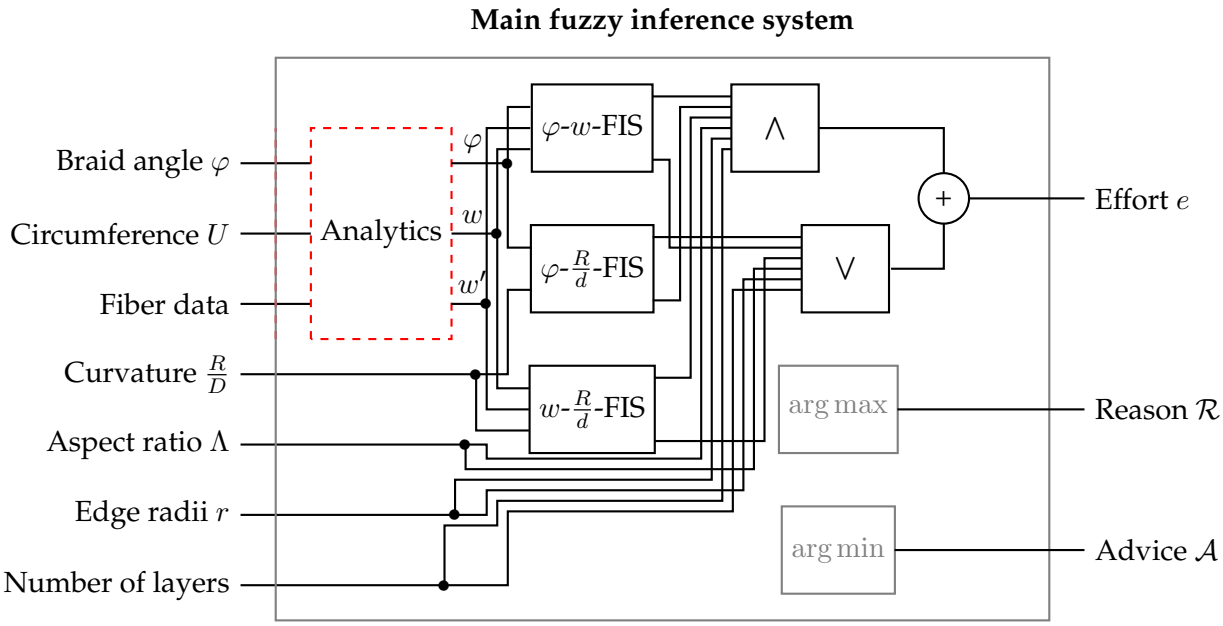

Figure 4.11.: Illustration of the fuzzy inference system for the braiding manufacturing effort model

As illustrated in figure 4.12, the two input variables braiding angle and yarn width are processed such that their contribution to the level of manufacturing effort is computed. For the sake of simplicity, the following discussion is focusing on the interaction of those two input variables and their influence on the final manufacturing effort. This represents a simplification, since more input variable do interact with those two variables and thereby contribute to the final outcome: manufacturing effort. Moreover, the outcome of the sub-FIS φ-w-FIS is contrasted and processed together with the outputs of the sub modules φ-$\frac{R}{d}$-FIS and w-$\frac{R}{d}$-FIS, along with the direct inputs aspect ratio Λ, edge radii r and number of layers via *AND* and *OR* rules in the main FIS as given with figure 4.11. This is way the rules given with figure 4.12 represent a subset of the BMEM, but yet highlight the underlying idea of capturing and reasoning about expert knowledge. The black lines in the gray boxes of figure 4.12 represent the afore discussed membership functions μ, which define the affiliation of sharp values to the fuzzy or, here, verbal variables. This, for instance, defines the link of the sharp input variable braiding angle of $\varphi = 35°$ to the verbal variable *small* braiding angle. This link is hence illustrated by an $100\ \%$ yellow fill of the membership function in rule three. The advantageous feature of being compliant to verbal imprecision and vagueness is also illustrated in that figure, by the partially fill of the two verbal variables *very small* and *moderate* braiding angle. This is respecting the verbal imprecision inhering to each expert interview, where the knowledge engineer needs to decide whether $\varphi = 35°$ is a *small* or rather a *moderate* braiding angle. Of course, this decision is finalized after re-consultation. This feature of the underlying fuzzy logic set theory, empowers the effort model with human-like capabilities in problem solving, involving variables comprising some sort of uncertainty and imprecision. This outlined translation of sharp variables to verbal ones is referred to as fuzzification and the degree of fill of this membership functions is marking the antecedent being passed to the subsequent step; the evaluation of all rules via implication. Implication is realized here by product rule for *AND* network modules and by a maximum for *OR*s (see table 4.1). Each rule is reflecting parts of the knowledge base and to some extend the knowledge of an expert. Rule one for instance, has been translated from the intelligible expertise, that either a *too small* braiding angle or a *too big* yarn width results in the highest possible effort level. In that case *high* manufacturing effort, because either of those leads to a design being in-producible. Rule two, three and four vary in the associated effort level to mirror the difference in the braiding angle, which itself is defined as a ratio of horn gear revolutions and take-up speed of the mandrel and, in that consequence, being proportional to the machine time

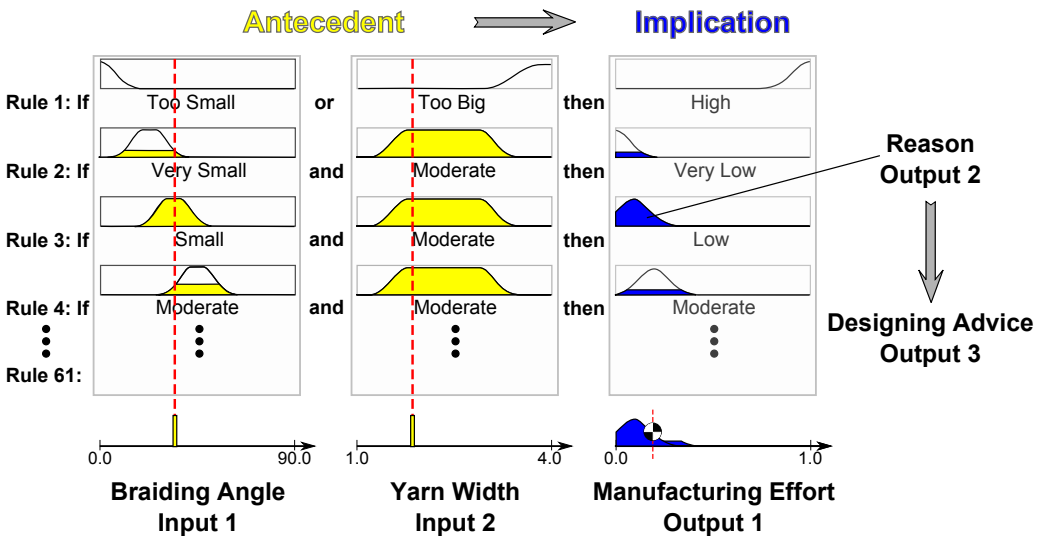

Figure 4.12.: Extract of the sub-FIS φ-w-FIS as part of the whole MEM as given with figure 4.11

and in turn costs. Hence, smaller braiding angles regularly means less braiding time and less effort as well. Once the implication has been computed, which is depicted by the blue fills of the output membership functions in figure 4.12, the final outcome can be computed. This is achieved by the process called aggregation. In the implemented effort model, aggregation has been realized by the summation rule. Summation is generally realized by simply adding all membership functions of each rule according to their implication value or, in other words, according to the degree of fulfillment of each membership function. This is illustrated with the output membership function on the right bottom side of figure 4.12. Finally, a sharp value for the output variable manufacturing effort can be computed by determining the center of gravity, which is computed via the first moment of area herein (see equation (4.1)). This last step is referred to as defuzzification. It has previously been discussed, how the general Mamdani FIS as illustrated with figure 4.7 has been expanded by the feature of deriving the critical rules and therein, the critical design variables, which lead to the computed outcome. This has been achieved by fetching the arguments of the maximal rule of the aggregation by equation (4.3) or the minimal rule in case of an AND during implication by equation (4.4). Now, this generally defined concept is transfered into practice by showing its realization for the BMEM. It is the case, that the knowledge engineer, as the one who implemented all fuzzy rules derived from assessed knowledge domain, can depose a reason for each rule, as long this reason has also been queried from the experts during the interview phase. So by computing the critical rule j_{Active} via equation (4.3), the deposited reason $\mathcal{R}$ can be passed back. Table 4.3 shows an overview of some reasons $\mathcal{R}$, which have been priorly linked to implemented rules. So, in case rule ten can be identified to be the critical one, the reason $\mathcal{R}$: *Braid opening* is passed back, indicating, that the braid does not cover whole of the mandrel and in that consequence, the final product's quality in terms of stiffness is way below an acceptable level.

In addition, the Mamdani FIS has been enhanced such that the critical input variable i_{Active} can be identified by equation (4.4). Prior to that, the critical rule j_{Active} has to be determined as well, but this is obviously realizable. Once, the critical variable and rule have been identified, the effort model can further pass back an elaboration advice $\mathcal{A}$ along with the level of effort and reason $\mathcal{R}$. This advice then gives insight on how to further reduce the computed level of effort. As an example, if variable *braid angle* in rule four has been identified to be critical in a sense, that it dominated the computed manufacturing effort level, the BMEM passes back the advice $\mathcal{A}$: *Increase take-up speed or reduce horn gear speed*. This advice then helps to resolve the problem of an *over-compacting* braid, which can also be provided as the reason $\mathcal{R}$ for the associated effort level. More examples are given with the following

Table 4.3.: Some deposited reasons $\mathcal{R}$ and specific elaboration advices $\mathcal{A}$

Rule	Variable	Reason $\mathcal{R}$	Elaboration advice $\mathcal{A}$
...	...	...	...
4	Yarn width	High production time	$\Leftrightarrow$ [a]
4	Braid angle	High production time	$\Uparrow$ [b] take-up speed {1}
	...	...	...
10	Braid angle	Braid opening	$\Downarrow$ [c] take-up speed {1}; $\Uparrow$ horn gear speed {2}
	...	...	...
16	Curvature	Over-compacting	$\Uparrow$ curvature's radius {1}; $\Downarrow$ mandrel's diameter {2}
	Yarn width	Over-compacting	$\Downarrow$ filaments per yarn {1}; $\Downarrow$ bobbin number {2}
	Braid angle	Over-compacting	$\Uparrow$ take-up speed {1}; $\Downarrow$ horn gear speed {2}
...	...	...	...

[a] Check subsequent rule
[b] Increase
[c] Decrease

table 4.3. Both the provided reason $\mathcal{R}$ and elaboration advice $\mathcal{A}$ are leveraging the significance of the manufacturing effort model to a whole new level for multiple reasons. First of all, it does increase the trust-ability for the users, since effort computations can be made plausible by studying the provided reason and advice. Moreover, this transparency not only increases the trust-ability in a direct fashion, but also equips the verification process with a helpful tool, with which the knowledge engineer can discuss the validity with experts more thoroughly and thereby raising the trust level indirectly. This is mainly because a given reason makes it transparent to the expert, whether or not the underlying rules are reasonable and meaningful. Secondly, the information gain by the supply of a reasons $\mathcal{R}$ and elaboration advices $\mathcal{A}$ make the manufacturing effort model more interesting to be used as an augmented tool, even in the designing process. A realization of this idea, would be the embedding in the computer aided design environment framework, where the effort model could work in tandem with a construction tool, giving the designer a live feed-back on associated effort levels, including reasoning and advices for possible improvements. Clearly, this would propagate the concept of concurrent product development processes beyond all criticism.

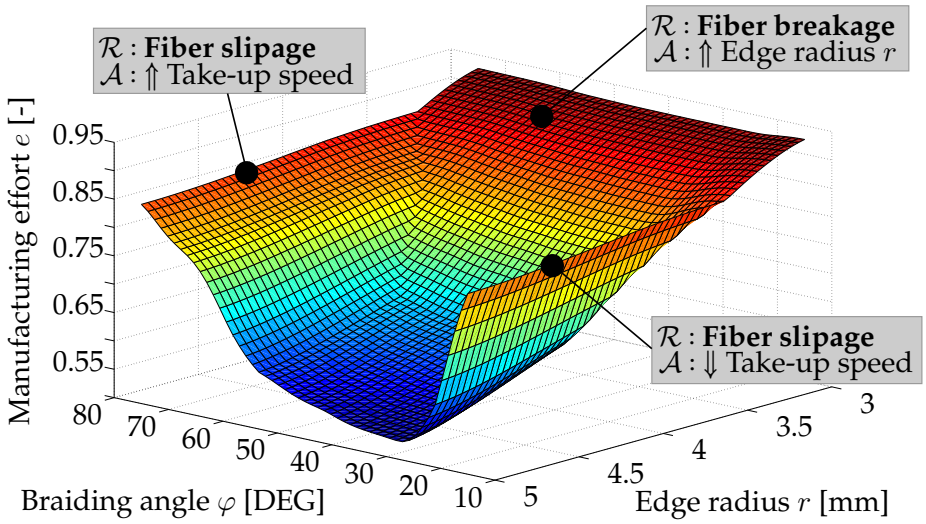

Figure 4.13.: Manufacturing effort response surface over braiding angle and edge radius (Schatz and Baier (2014))

For bringing this section to closure, the final response surfaces defined by the priorly developed

and described braiding manufacturing effort model will be presented. Figure 4.13 depicts the response surface plotted over the braiding angle φ and the smallest edge radius r of the mandrel or respectively the profile. In addition to the direction output, the manufacturing effort e, the reason $\mathcal{R}$ and the first advice of list of advices $\mathcal{A}$ is given as well. With figure 4.14 a gathering of response surface plots is provided, so as to give insight how the input parameters define the level of manufacturing effort.

4.3.2. Prepreg manufacturing effort model

As many aspects of braid manufacturing effort model (BMEM) apply to the prepreg manufacturing effort model (PMEM) in a similar fashion, solely unique features of the PMEM will be discussed at length in the following. This is also why, the reader is advised to read the section 4.3.1 addressing the BMEM first. Table 4.4 depicts the used rules for defining the implication rules *AND* and *OR*, as well as the implication of the PMEM. Some of the underlying rules differ in contrast to the BMEM. This is owned to the uniqueness of some features of the PMEM, such as the embedding of a wastage algorithm or the circumstance, that more sub-FIS modules have used, so as to define the overall main FIS capturing the knowledge assessed for the prepreg lamination technique.

Table 4.4.: Used implication and aggreation methods for prepreg MEM

Mamdani step	Rule	Realization
Implication	*AND*	Min
Implication	*OR*	Sum
Aggregation	-	Sum

The main sources of manufacturing effort covered by the PMEM are: ply wastage, ply continuity requirements, ply drop-offs and drapability of prepreg plies. Figure 4.15 illustrates how prepreg ply wastage is defined. In addition, it schematically depicts how ply wastage has been computed numerically. At first, ply wastage is defined as the leftover, thus the rest of the prepreg roll remaining unused, once each and every prepreg patch has been cut out. In figure 4.15, the gray areas mark the wastage and the differently colored rectangles represent patches, where each color represent a certain prepreg roll (see legend). So for instance, red is representing a prepreg roll of ninety degrees orientation.

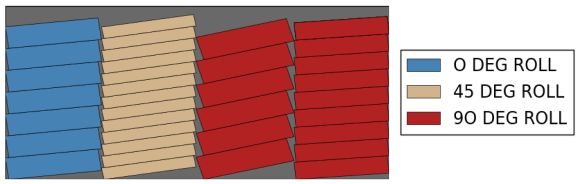

Figure 4.15.: Ply wastage algorithm (wastage is highlighted in gray)

The developed algorithm tries to minimize the wastage, by filling up each column, until no further patch fits in. However, this can lead to discrete jumps in the resulting wastage rate, when for instance a slight change in the patch orientation allows the placing of another patch in a column, thereby drastically reducing total ply wastage. This effect is shown with figure 4.16, where a slight change in the ply orientation α_1 leads to jumps in the wastage rate ψ. A solution described and analyzed by Köhler (2014) is meta-modeling, which flattens this jumps out, by echoing the overall trend determined by the wastage algorithm. This flattening facilitates the usage of gradient-based algorithms, which would not have been applicable in case the PMEM has been build up on the original wastage algorithm. The next aspect determining the level of manufacturing effort, is the fulfillment of the continuity requirement. This continuity requirement ensures structural integrity, by requiring a

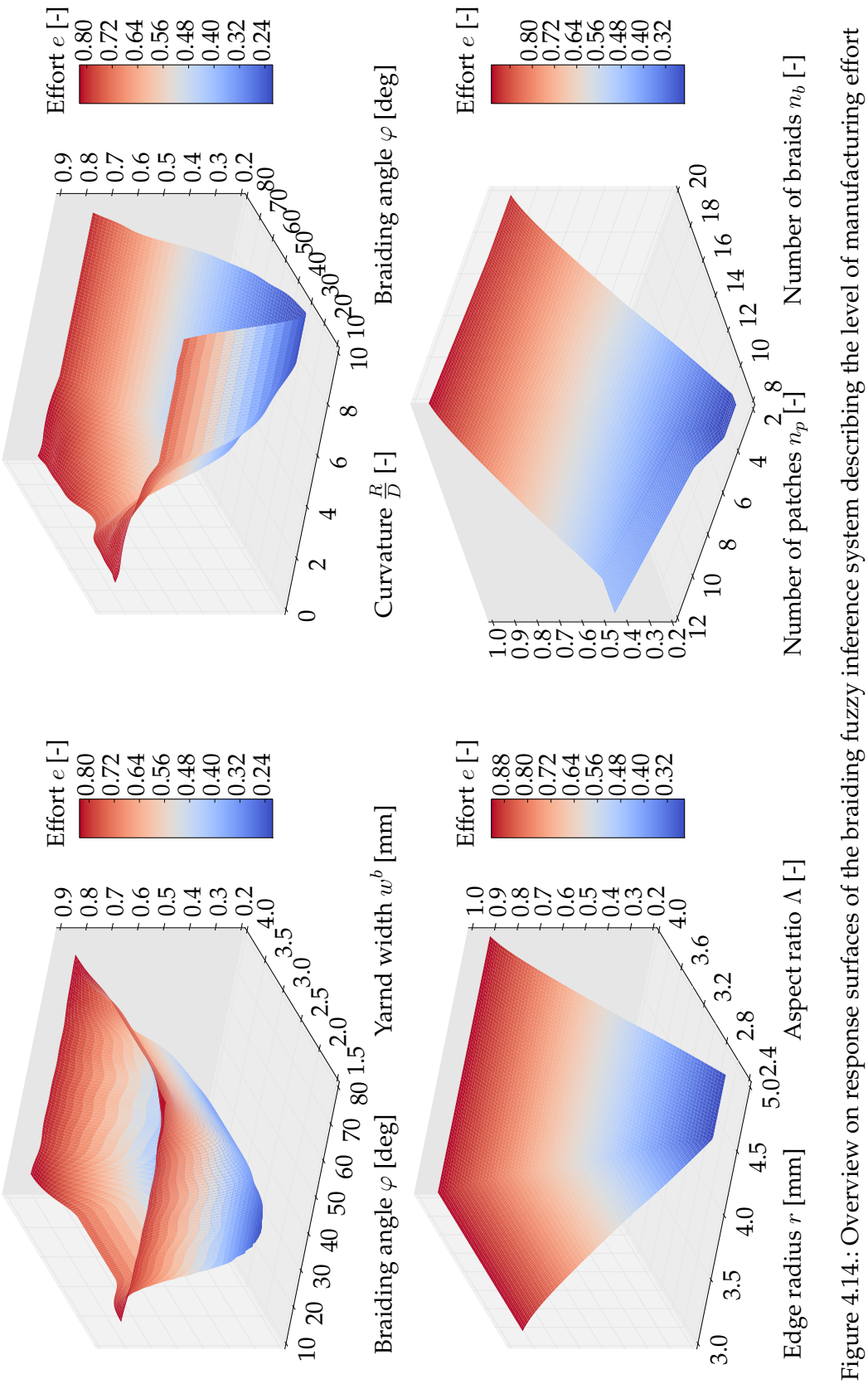

Figure 4.14.: Overview on response surfaces of the braiding fuzzy inference system describing the level of manufacturing effort

certain fraction of a given ply stack to continue into adjacent ply stacks. The check, whether or not a ply continuous into the neighboring region can be realized straight forward, but yet also brings forth discontinuities. Thus, in case of *regular* check, continuity C is only verified or, here, identified to be one, in case the angle difference $\Delta\alpha$ of two neighboring plies is equal to zero and is hence evidently discontinuous, as it basically is a Dirac delta function $\delta(\Delta\alpha)$:

$$C = \delta(\Delta\alpha) = \begin{cases} 1 & \text{if } \Delta\alpha = 0 \\ 0 & \text{otherwise.} \end{cases} \tag{4.6}$$

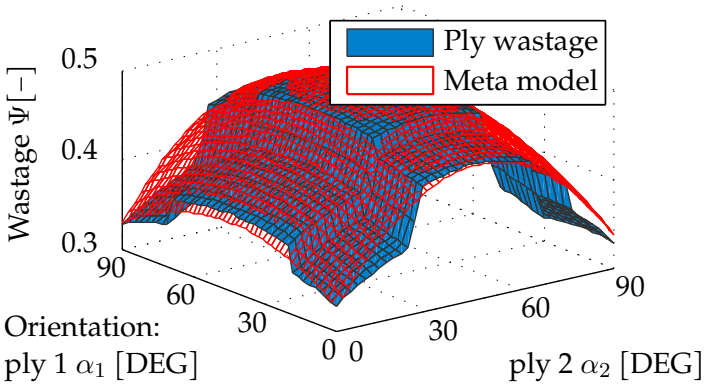

Figure 4.16.: Response surface approximation of the clipping ψ as realized by Köhler (2014): α_1 and α_2 represent patch orientations

This is being illustrated by figure 4.17, where this *regular* check is highlighted in red. Since implementing the continuity check as proposed by equation (4.6) leads to a similar limitation in terms of choice of optimization algorithm, as discussed earlier for the discontinuous clipping response of the wastage algorithm, a continualization is seeked instead. This continualization is given with equation (4.7) and illustrated with the blue curve in figure 4.17 and enables the use of gradient-based algorithms even when the PMEM is embedded.

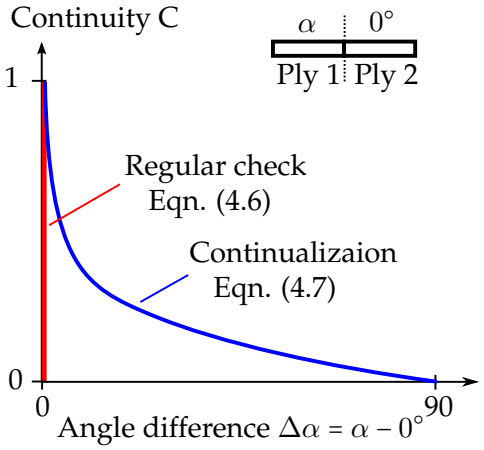

Figure 4.17.: Demonstration of the continualization of the continuity requirement

$$C = 1 - \left(\frac{\Delta\alpha}{90}\right)^{0.2} \tag{4.7}$$

Lastly, ply drop-offs and their steepness have also been considered. Figure 4.18 illustrates how such a ply drop-off is defined. The slope of such is defined via the drop-off length l_D and the drop hight t_D. They need to be considered here as well, because a very steep ply drop-off leads to great

stiffness jumps and in that consequence to three dimensional stress states including peeling stresses, which in turn then increase the risk of possible delaminations. A design displaying a low tendency towards delaminations is desirable and thus pursued by the manufacturing effort model as well.

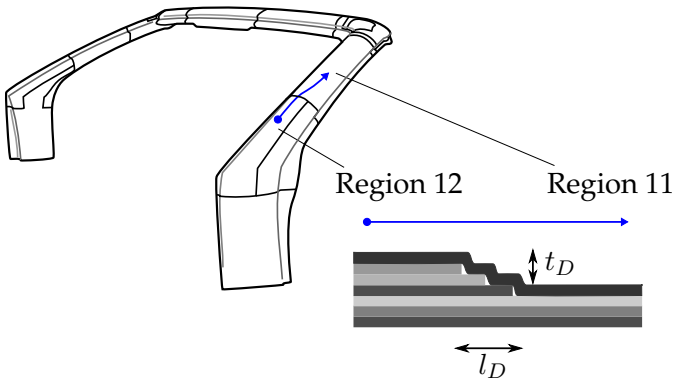

Figure 4.18.: Illustration of a drop-off with its drop height t_D and length l_D

All the afore mentioned parameters are comprehended in the circuit-like illustration of the FIS via figure 4.19, where the evaluation of the individual contributors such as the continuity requirement are illustrated via sub-FIS modules, e.g. C-FIS. Due to the massive extend of parameters, which need to be passed into PMEM, a general interface querying all needed parameters directly from the mesh data being generated by the pre-processing for the FEA has been developed. By doing so, the parametrization in terms of the variable mapping from the structural model to the manufacturing effort model is now obsolete and the MEM can therefore basically be plugged into any given optimization model, once the finite element model is defined already. The two red dashed boxes in figure 4.19 represent interfaces to external scripts. The wastage algorithm is being called here from within the PMEM, such that the wastage ψ for a given patch geometry (l, b) and orientation α can be computed. For the sake of completeness, several response surfaces of the PMEM are given with figure 4.21. As can be seen there, all response surfaces are smooth, continuous and unimodal, which is why, no issues are to be expected in case gradient-based algorithms are chosen to solve optimization problems involving such soft computing models.

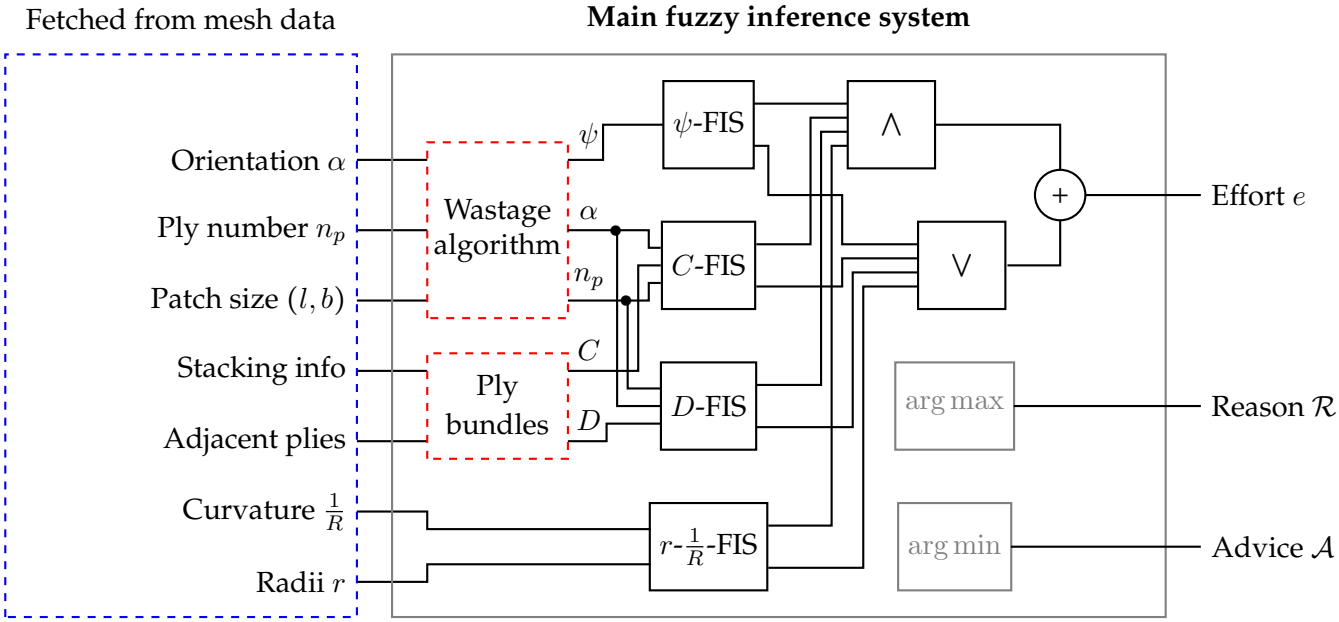

Figure 4.19.: The fuzzy inference system for the prepreg manufacturing effort model

4.3.3. Implementation details

It shall be highlighted here, how the implementation of such manufacturing effort models is compliant to generalization, thereby leveraging the applicability of the underlying method. Once a general soft computing base has been set up, deriving multiple manufacturing effort models founded on different knowledge bases is rather straight forward to realize.

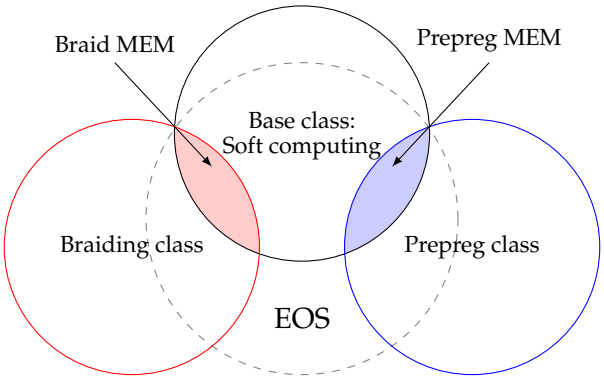

Figure 4.20.: Overview on base and derived classes used to implement both manufacturing effort models

This is already observable in figure 4.3, where the programming-wise realization was basically sketched via the soft computing level, which itself can in most regards be separated from the knowledge engineering. The link connecting both levels is the knowledge base, which is obviously not common to distinct effort models as well as the revision process of the same is not. Both effort models, as priorly discussed, have been implemented in the programming language Python using its object-orientated scheme. Therefore, a general base class has been defined for all general methods associated with soft computing. Examples would be the setting-up of a Mamdani fuzzy inference system as given with figure 4.7, including the programming-wise realization of the equations (4.1), (4.3), (4.4), et cetera. Further, the post-processing in terms of reasoning and advising, also for plotting response surfaces and similar has been generalized and defined in that base class. All methods have then been inherited by the derivative classes from the base class. These derivative classes, such as the one defining the braiding manufacturing effort model, are for instance unique because of its own knowledge base covering acquired and formalized expertise regarding the braiding technique. This is illustrated with figure 4.20, where the black circle represents the base class *Soft computing* and the red one respectively the *Braiding class*. Things become interesting, once another effort model needs to be defined, since, this can be achieved by simply inherit it with the general methodolgies being defined in the *Base class* and focusing on the determination of the knowledge base. Finally, it should be noted, that all of this has been added to the simulation platform EOS as a library called FuzzyLibrary. This is sketched by the dashed gray circle in figure 4.20. Again, EOS as an *Environment for Optimization and Simulation* has been developed by da Rocha-Schmidt and the author. It is currently licensed such that no fees or costs need to be paid to use it.

4.4. Final remarks on the soft computing of manufacturing effort

It has been shown that soft computing represents a powerful methodology. This is mainly because of its capability to model and capture imprecise and uncertain information, so as to solve problems being not solvable or hard to solve with conventional methods. Of similar significance; one can address the demand of replacing highly sophisticated analyses being numerically expensive and elaborately to be build up, by this modeling scheme being straight forward to be developed and displaying efficiency in terms of numerics. In addition, it is because of its ease of implementation, that the derived approach

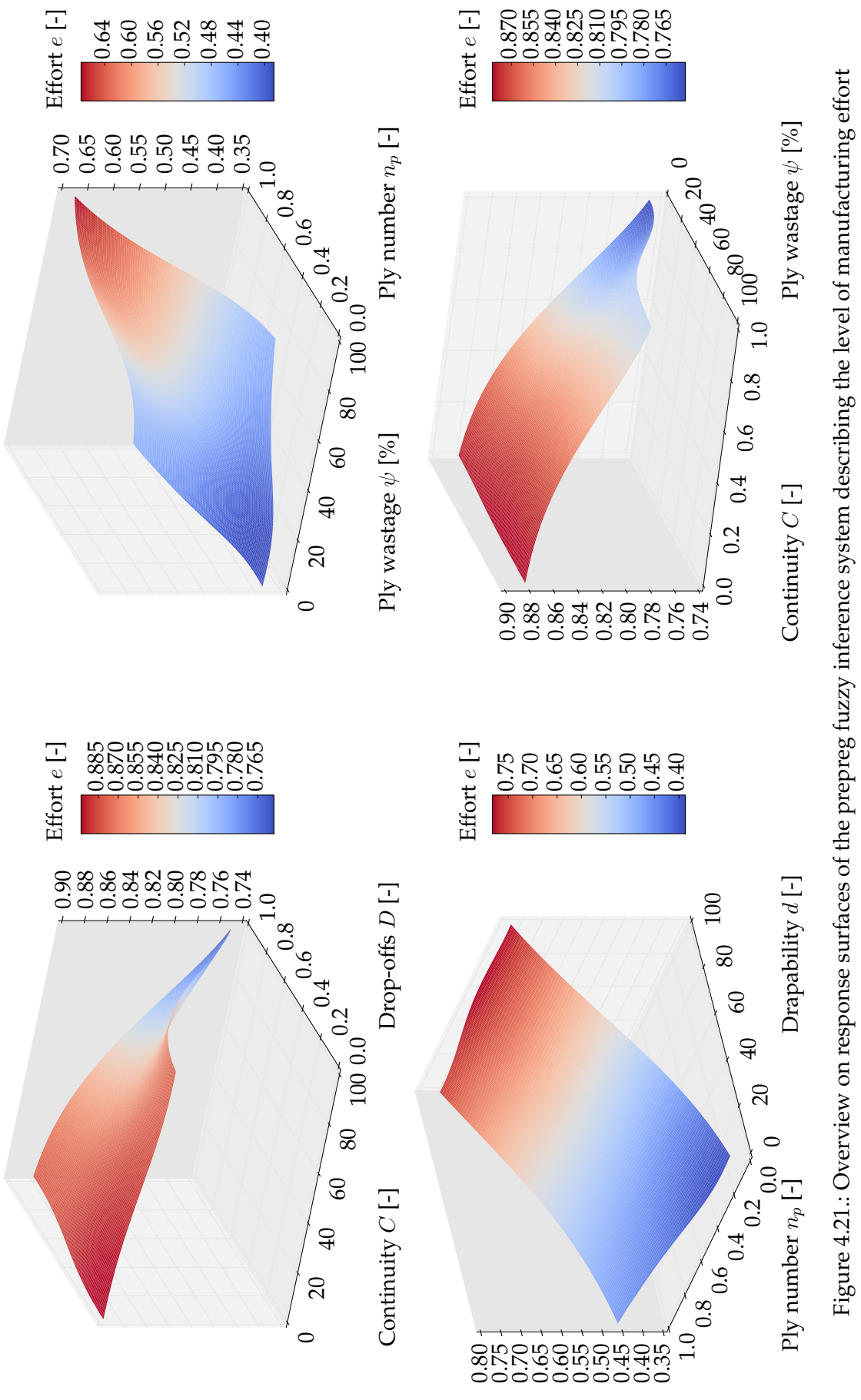

Figure 4.21.: Overview on response surfaces of the prepreg fuzzy inference system describing the level of manufacturing effort

can be employed even in early design phases, where information is brought in most potently. All of this, can be lead back to the analogy of the underlying methodologies to the human mind, making it intuitive to form such soft models for the developer, or in this context, the knowledge engineer. The capability to cope with impression, being inherently involved in verbal expert knowledge and thus qualitative information in an expedient fashion underpins this analogy.

The fertile coping with fuzziness, gives access to the modeling and handling of verbal knowledge. This further facilitates the definition of effort models, founded on knowledge bases, which essentially capture verbal knowledge, being priorly acquired from appropriate experts. Reasoning about this captured qualitative expertise concerning a manufacturing technique in hand, leads to the ability to compute associated levels of manufacturing effort for distinct designs. This has been realized by translating the described expert knowledge into Mamdani fuzzy inference systems (FIS). It has moreover been shown, that this Mamdani FIS could be extended, such that the critical argument primarily determining the final output can be identified. Utilizing the arguments of both evaluation steps of the inference engine–the implication and aggregation–and contrasting them with the knowledge base reveals the reason of why a certain output level has been computed and, further, which parameters need to be altered such that an optimal improvement is realized.

Summing up, the impact of the manufacturing effort models reaches beyond the question: whether or not a certain design is producible. This is not only because of its capability to rank design proposals based on the linked effort levels in dependence on the chosen production technique, but also since these models do provide reasoning and return elaboration advices. The latter facilitates–similar to a sensitivity study–the identification of critical design parameters and thereby the most effective design improvement in terms of reducing the level of manufacturing effort. The priorly mentioned reasoning increases the significance of these models, since this reasoning makes the determination of the effort level transparent to the knowledge engineer, such that it can made plausible and verified with ease.

5 Efficient meta modeling of composite materials

In this chapter, a novel approach for incorporating complex composite material models–those demanding multi scale homogenization–into the composite optimization process, is being presented. Before the details of this approach are given, a brief review on micro mechanics will be given. For the purpose of demonstrating the developed approach, braiding has been chosen throughout the following chapter, as it evinces a complex fiber architecture, thereby making experimental and/or numerical homogenization indispensable. Please note, that the scope of this chapter is rather lying on the surrogate-based decoupling of the homogenization chain, such that a given complex composite material model can be considered efficiently, than on the homogenization model, theory or technique itself.

Contents

5.1. General concepts in micro mechanics

Composites in general evince at least two different scales; one where the material can be regarded to be homogeneous and scales were multiple constituent phases do exist. Most frequently, these multiple phases display some sort of repetitive pattern and further influence the material properties. In micro mechanical engineering, homogenization is used to model material quantities in an effective and thus representative fashion. In principal, there are four different types of homogenization methods researcher generally distinguish in: analytical, semi-empirical, empirical and numerical. Analytical homogenization methods commonly take advantage of the repetitive geometric pattern or of dilute distributions of phases and abstract effective material quantities in analytic formulas. Examples of analytical homogenization methods are the rule of mixture, Hashin-Shtrikman bounds introduced by Hashin and Shtrikman (1963), mean field approximations based on Eshelby (1957) and many more. UD composites may be described sufficiently accurate with such analytical homogenization

formulas. This is due to the presence of one predominant material scale, the micro scale, i.e. the length scale proportional to the fiber's diameter. However, when considering textiles with complex fiber architectures, as is the case for braids, another scale becomes relevant; the so called meso scale.

All three scales are illustrated in figure 5.1 for the case of an automotive A-pillar structure. For the composite material in that figure, braiding has been chosen as the manufacturing technique. The meso scale is thus characterized by fiber-matrix tows and the surrounding matrix. These braided composites demonstrate all three scales: micro, meso and macro. Analytical approaches may also lack precision especially for strength quantities. Byun (2000) has for instance been able to derive an efficient analytical approach for the stiffness modeling of triaxial braids. But there are only few investigations regarding effective strength of braid composites, as was done by Swanson and Smith (1996). A remedy addressing these inaccuracies, is to enhance analytical formulas by embedding results from experimental investigations leading to so called semi-empirical homogenization methods, as discussed by Daniel and O.Ishai (2010). Nevertheless, labor intense and time consuming test campaigns must be performed in order to do so. This is also why, the third approach empirical of simply describing the material via excessive test campaigns is not being pursuit herein. For more details regarding homogenization methods consult Kanouté et al. (2009) as well as Daniel and O.Ishai (2010). Finally, performing numerical homogenizations to determine effective properties can result in accurate predictions in stiffness as well as strength properties, but are also computationally expensive due to the involved FEA. One key idea pursued within this chapter is to mitigate computational costs, while still preserving numerical accuracy, by decoupling the homogenization chain in-between the macro and meso scale. The decoupling is realized by surrogate modeling as discussed in section 2.5.4. This surrogate modeling leverages several numerical analyses to a complete material model, capturing the response behavior over the whole parameter space via approximations.

5.2. The developed decoupled homogenization approach

5.2.1. Underlying idea

The basic idea is to separate the homogenization chain between the meso and macro scale as depicted with figure 5.1.

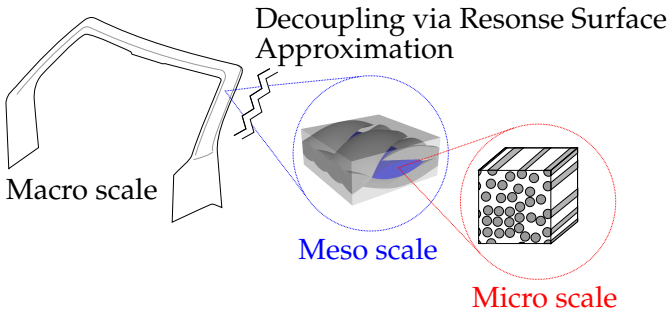

Figure 5.1.: The multi-scale homogenization via RSA-based decoupling

This is promising for multiple reasons. First and foremost, the computation times of the structural model are in the same order as to conduct the homogenization based on a meso scale model. Moreover, slight parameter changes in the macro scale would generally require an update of the material properties, hence, further homogenization runs. Finally, it can be the case, that on the macro scale parameters such as for instance the braiding angle, just change slightly in their magnitude, but still demand corresponding material properties, which however do only slightly vary. All of these mentioned aspects are especially visible in the case of structural optimization. This is mainly because the optimization process per se alters parameters, which would require re-homogenization at the meso

scale or even micro scale. The separation or decoupling of the homogenization chain is herein realized by taking advantage of surrogate modeling. Surrogate modeling–or also referred to as meta-modeling and response surface approximation (RSA)–has been introduced in section 2.5.4. By using surrogate models, the effective responses of the meso unit cell model, e.g. homogenized stiffness in fiber direction, can be leveraged to a fully parametrized and general material model. This parametrized model can be embedded in most finite element tools or in CLT analyses software packages as well. This is due to the fact, that the surrogate model is in the following formed by a polynomial regression and is therefore expressible via rather simple equations. NASTRAN for instance offers users the possibility to define the material card entries via a sum of coefficients and variables, which are later also considered in the computation of analytical derivatives during the analytical design sensitivity analysis (see (2.14) in section 2.4).

5.2.2. Overview of the developed decoupling process

Figure 5.2 depicts the decoupled process. The process as illustrated there, has been developed and sucessfully been implemented by taking advantage of the Python programming language and by the help of Flach (2014).

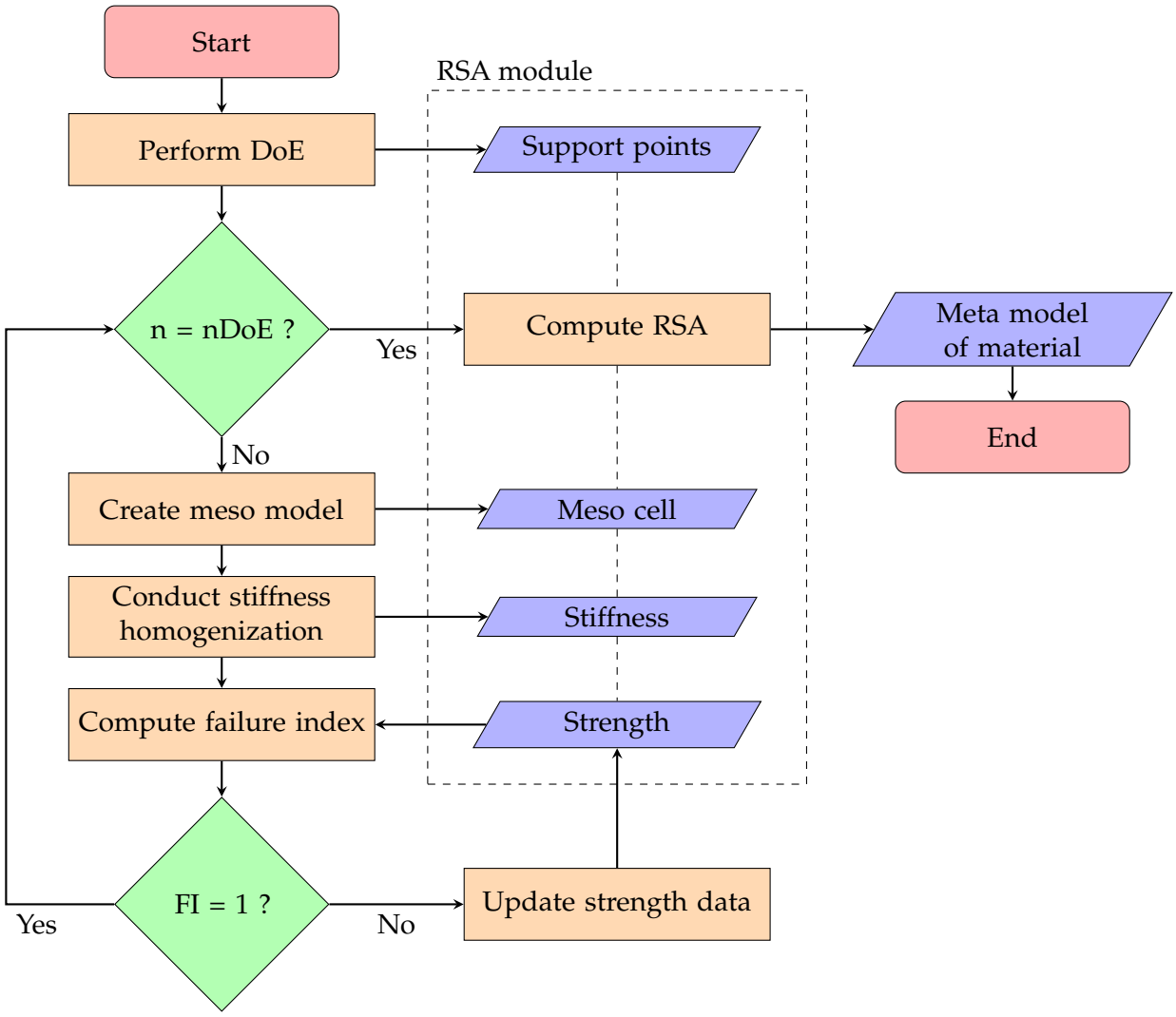

Figure 5.2.: Flow chart of developed homogenization approach

5.3. Application of the approach on triax-braid materials

The realization of the decoupled homogenization approach will be shown next. Again, braiding has been chosen to be the composite manufacturing technique, but can however be substituted by similar ones while the approach remains the same.

5.3.1. Derived meso scale model

Parametrized of the meso scale model

As already shown with figure 5.1, the key idea is to decouple the multi-scale homogenization chain in-between the macro and meso scale. Because the surrogate material model, once it has been computed, will be used for parametric investigations and within structural design optimizations, the homogenization of the meso scale model needs to be parametrized in all relevant parameters. The superscripts $\blacksquare^{(a)}$ and $\blacksquare^{(b)}$ declare whether the quantity $\blacksquare$ is associated with the axial or braider yarn.

The meso cell and independent parameters of the meso model are:

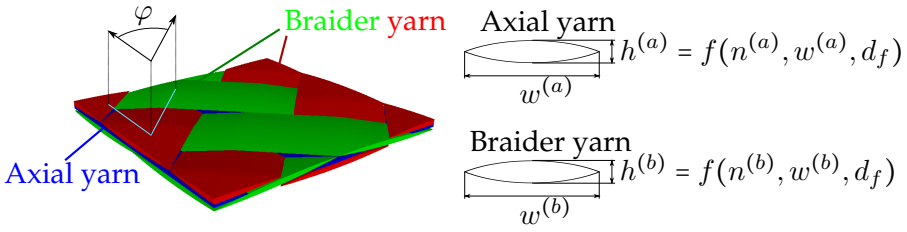

Figure 5.3.: Parametrized meso model derived via TexGen

- braiding angle: φ
- filament number for axial and braider yarn (a, b): $n^{(a,b)}$
- fiber volume in percent for both yarns (a, b): $\xi^{(a,b)}$
- width of axia (a) and braider (b) yarn: $w^{(a,b)}$
- stiffness properties of yarns (a, b): $E_{11}^{(a,b)}, E_{33}^{(a,b)}, \nu_{12}^{(a,b)}, \nu_{13}^{(a,b)}, G_{13}^{(a,b)}$
- stiffness properties of matrix (m): $E^{(m)}, \nu^{(m)}$
- CTEs[†] of yarns (a, b) and matrix (m): $\alpha_1^{(a,b,m)}, \alpha_2^{(a,b,m)}, \alpha_3^{(a,b,m)}$
- strength quantities of yarns (a, b): $R_{11}^t, R_{11}^c, R_{22}^t, R_{22}^c, R_{12}$
- strength quantities of matrix (m): $\epsilon_{max}^{(m)}$
- curvature of meso braid architecture: $\kappa = \frac{1}{R}$

The meso model and especially the parametrization has been realized by using the dynamic link libraries (*dll*) of TexGen. TexGen has been developed by Long and Brown (2011) from the University of Nottingham Textile Composites Research group. It is a license-free software. An example of how TexGen can be used to compute the textile's mechanics is given with Lin et al. (2011). In this thesis, the libraries have been imported via Python so that all functionalities of TexGen could be used to generate

[†]CTE ... Coefficient of thermal expansion

parametrized meso models, which are then passed to the Abaqus standard solver. Figure 5.3 gives an example of how such an meso model looks like, with φ being the braiding angle, $h^{(a,b)}$ yarn height, $w^{(a,b)}$ yarn width and d_f the fibers' diameter. The specific fiber architecture defined by the braiding process also imposes some geometric dependencies onto the parameters $w^{(b)}$ and $w^{(a)}$ and further on $h^{(b)}$ and $h^{(a)}$. The first dependency is given by the architecture itself and is illustrated with figure 5.4. The latter, between $w^{(a,b)}$ and $h^{(a,b)}$, is given by the fact, that both parameter pairs are defined by the corresponding surface $A^{(a,b)}$ of the yarns.

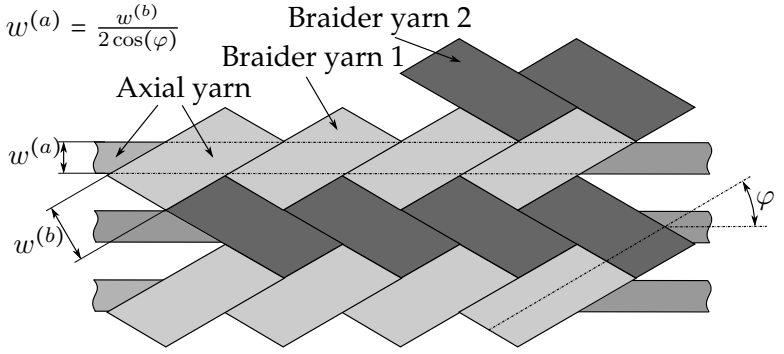

Figure 5.4.: Relationship in-between axial yarn width $w^{(a)}$, braider yarn width $w^{(b)}$ and braiding angle φ

In this work the surface of each yarn is assumed to be of lenticular shape and can therefore be defined as,

$$A = 2r^2 \arccos\left(1 - \frac{h}{2r}\right) - \sqrt{rh - \frac{h^2}{4}}\,(2r - h)\,, \tag{5.1}$$

with r being

$$r = \frac{h^2 + w^2}{4h}. \tag{5.2}$$

So for instance, the axial yarn's hight $h^{(a)}$ is determined based on the axial yarn's width $w^{(a)}$ and the desired area $A^{(a)}$. Prior to this computation, the width $w^{(a)}$ needs to be resolved via $w^{(a)} = w^{(b)}/(2\cos(\varphi))$, as illustrated in figure 5.4. Using the independent parameters; number of filaments $n^{(a)}$ and fiber volume $\xi^{(a)}$ together with the constant fiber diameter d_f one can define the following equation (5.3).

$$A^{(a)} = \frac{\pi n^{(a)}}{4\xi^{(a)}} d_f^2 \tag{5.3}$$

Together with equation (5.1), which defines $A(h^{(a)}, w^{(a)})$, one can then define the nonlinear and implicit equation (5.4), which is here given in residual form with $\mathcal{R}_A$ being the residual.

$$\mathcal{R}_A = \frac{\pi n^{(a)}}{4\xi^{(a)}} d_f^2 - A(h^{(a)}, w^{(a)}) = 0. \tag{5.4}$$

An appropriate and efficient way to solve this equation, is by taking advantage of the Newton-Raphson method, which basically linearizes the residuum $\mathcal{R}_A$ and solves it iteratively, where i represents the iterator. Convergence is achieved once $\mathcal{R}_A$ falls below an afore defined tolerance. The solution is then, the needed $h^{(a)}$ for the given parameters $w^{(a)}$, $n^{(a)}$ and $\xi^{(a)}$.

$$\begin{aligned} \mathrm{Lin}(\mathcal{R}_A) = \mathcal{R}_A(h^{(a),i}) + \frac{\partial \mathcal{R}_A}{\partial h}\Big|_{h^{(a),i}} \Delta h^{(a),i} = \frac{\pi n^{(a)}}{4\xi^{(a)}} d_f^2 - A(h^{(a)}, w^{(a)}) - \frac{\partial A}{\partial h}\Big|_{h^{(a),i}} \Delta h^{(a),i} = 0 \\ h^{(a),i+1} = h^{(a),i} + \Delta h^{(a),i} \end{aligned} \tag{5.5}$$

After all dependent parameters have been determined via equations (5.5) and $w^{(a)} = w^{(b)}/(2\cos(\varphi))$, the meso model can be build up using TexGen. Once the geometry has been defined within the TexGen module, the mesh and all associated transformed element rotations for the yarns will be determined and returned.

Computing the effective stiffness

In this work, the numerical homogenization is being realized by imposing an uniform strain field and inversely computing the effective stiffness of fictitious material, such that it would display equal strain energy for this applied loading. Hashin and Shtrikman (1963) and Sun and Vaidya (1996), did show, that doing so, solely the upper bound of the effective material property in light is being computed. In the appendix A.1, the reason for this given, by deriving equation (A.1), which illustratively depicts the incompatibility originating from the uniform strain loading. For the sake of completeness, the lower bound on material properties can be computed by imposing a uniform stress field. Both bounds are most frequently referred to as variational bounds and sometimes as the Reuss (upper) and Voigt (lower) bound. In the diploma thesis of the author (Schatz (2012)) a homogenization scheme for directly resolving the viso-elastic material properties is being presented, where the asymptotic expansion homogenization scheme has been used to compute the effective visco-elastic material properties. Yu and Fish (2002) also discussed the asymptotic expansion homogenization for spatial and temporal scales. Further homogenization theories can also be found in Lukkassen et al. (1995). Nonetheless, since both bounds are quite narrow for the given fiber-architecture, namely the triaxial braid, and strength properties can be computed accordingly, the homogenization is conducted based on the variational bounds approach. Figure 5.5a depicts the realized loading state, which in tandem with the periodic boundary conditions resolve in a uniform strain field, such as $u_{i,0} = x_j \bar{\epsilon}_{ij}$ (Sun and Vaidya (1996)). The periodic boundary conditions are given with equation (5.6) for the strain and with (5.7) for the stresses. In those equations $\Gamma_{Y,\bar{k}}$ denotes the opposite boundary surface of $\Gamma_{Y,k}$.

(a) Applied uniform load (b) Periodic boundary condition

Figure 5.5.: Unit cell loading and boundary condition (Schatz (2012))

$$\epsilon_{ij}|_{\Gamma_{Y,k}} = \epsilon_{ij}|_{\Gamma_{Y,\bar{k}}} \tag{5.6}$$

$$(\sigma_{ij} n_j)|_{\Gamma_{Y,k}} = -(\sigma_{ij} n_j)|_{\Gamma_{Y,\bar{k}}} \tag{5.7}$$

These periodic boundary conditions can be set by using a reference boundary node and is being depicted in figure 5.5b, where the blue d represent the reference or also called dummy node.

Strength computation

For computing effective strength properties of the meso cell model–hence, the strength of the representative and so to say fictitious homogeneous braid-like material–the meso cell model is incrementally loaded until initial failure can be observed. During that loading, the same periodic boundary conditions as priorly defined are used, such that periodicity and therefore repeatability of the unit cell in each direction can be assured. The thereby derived effective strength quantities mark the onset of failure, thus initial failure. It has been desisted from computing progressive or even fatal failure quantities numerically based on the unit cell, since linear homogenization theory, as assumed up to this point, would then not hold any more. Moreover, the thereby caused numerical efforts would burst the frame of this thesis (see Wegmann (2015)). Failure of the meso cell model has been evaluated based on the Puck failure criteria for the fiber tows and max strain failure for the matrix phase surrounding the fiber tows. The Puck failure theory has been introduced in section 3.3 and are embedded here based on equation (3.8) and (3.9). In order to enhance the numerical performance of the homogenization approach, the computation of the strength properties have been accelerated by utilizing the Newton-Raphson scheme to solve for the critical loading forces $F_{\mathrm{crit},i}$, such that initial failure occurs, i.e.

$$\mathcal{FI}(F_{\mathrm{crit},i}) \overset{!}{=} 1 \tag{5.8}$$

The residuum $\mathcal{R}_{F_i}$ for determining the critical force $F_{\mathrm{crit},i}$ and its linearization as an intermediate stage towards the iterative solving procedure are given with the following equations (5.9) and (5.10).

$$\mathcal{R}_{F_i} = \mathcal{FI}(F_i) - 1 = 0. \tag{5.9}$$

$$\mathrm{Lin}(\mathcal{R}_{F_i}) = \mathcal{R}_{F_i}(F_i) + \left.\frac{\partial \mathcal{R}_{F_i}}{\partial F_i}\right|_{F_i} \Delta F_i \overset{!}{=} 0 \tag{5.10}$$

The linearized equation (5.10) is then iteratively solved via (5.11) and (5.12) until convergence has been reached. Converge is again assumed to be achieved, once the residuum $\mathcal{R}_{F_i}(F_i^{j+1})$ is smaller than a given tolerance. At this point, initial failure strength as stated with (5.8) has been computed.

$$F_i^{j+1} = F_i^{j+1} + \Delta F_i^j \tag{5.11}$$

$$\Delta F_i^j = -\mathcal{R}_{F_i}(F_i^j) \left(\left.\frac{\partial \mathcal{R}_{F_i}}{\partial F_i}\right|_{F_i^j} \right)^{-1} \tag{5.12}$$

5.3.2. Results for stiffness and strength

Next, the results of the homogenization approach will be shown and discussed. The parameters and their values used to conduct the homogenizations are given with the following table 5.1. Both variables, braiding angle φ and braider yarn width $w^{(b)}$ will be varied in the following but are given here as parameter as well, since these values are defined to be the reference values for one-dimensional plots. For instance, if any result is plotted over the braiding angle φ, $w^{(b)}$ is set to $2.7\mathrm{mm}$.

Table 5.1.: Used material parameter for the mirco and meso scale model

Entity	Value	Unit
φ	40	DEG
$w^{(b)}$	2.7	mm
E_{Matrix}	3.8	GPa
ν_{Matrix}	.3	-
$\epsilon_{\text{max,Matrix}}$	.8	%
$E_{xx,\text{Fiber}}$	239	GPa
$E_{yy,\text{Fiber}}$	15	GPa
$E_{zz,\text{Fiber}}$	15	GPa
$G_{xy,\text{Fiber}}$	5.8	GPa
$G_{xz,\text{Fiber}}$	6	GPa
$G_{yz,\text{Fiber}}$	6	GPa
$\nu_{yz,\text{Fiber}}$	.3	-
$\nu_{yz,\text{Fiber}}$	.3	-
$\nu_{yz,\text{Fiber}}$	.3	-
ψ_{Fiber}	68	%
n_{Fiber}	12k	-
$R_{11,t,\text{Tow}}$	2142	MPa
$R_{11,c,\text{Tow}}$	1083	MPa
$R_{22,t,\text{Tow}}$	40	MPa
$R_{22,c,\text{Tow}}$	104	MPa
$R_{12,\text{Tow}}$	117	MPa

Stiffness responses

Before the stiffness responses of the surrogate model are presented, a generalized appearance of the response surface plots will be defined. This definition is given with figure 5.6, where the red grid is depicting the response of the meta-model and the blue points represent the support points on which basis the meta-model has been computed. Since the meta-model represents an approximation of the original model and a polynomial regression has been used to compute it, approximation errors for each support point can be computed and will therefore also be given with error bars.

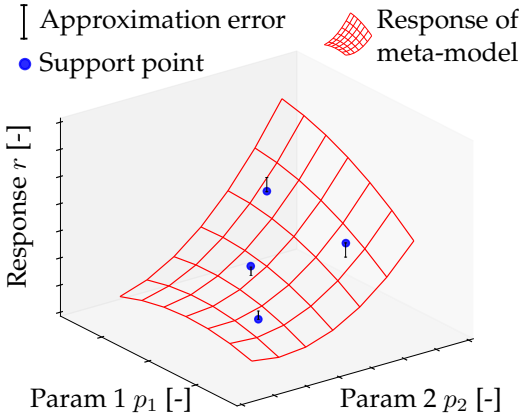

Figure 5.6.: Definition of the general illustration

In the following, the responses of the meta-model, which approximates all stiffness and strength properties of the triaxial braid (table 5.1) in dependence on the two parameters braiding angle φ and

yarn width $w^{(b)}$ will be presented and discussed. Together with the equation for the minimal number of coefficients $n_\beta = \frac{1}{2}(1 + n_{\mathrm{DV}})(2 + n_{\mathrm{DV}})$ the minimal sampling size can be computed to be six (also see table 2.1). However, a certain oversampling is always advisable, for which reason the number of samples has been set to nine. These samples have been distributed over the design space by taking advantage of the Latin Hypercube Sampling method.

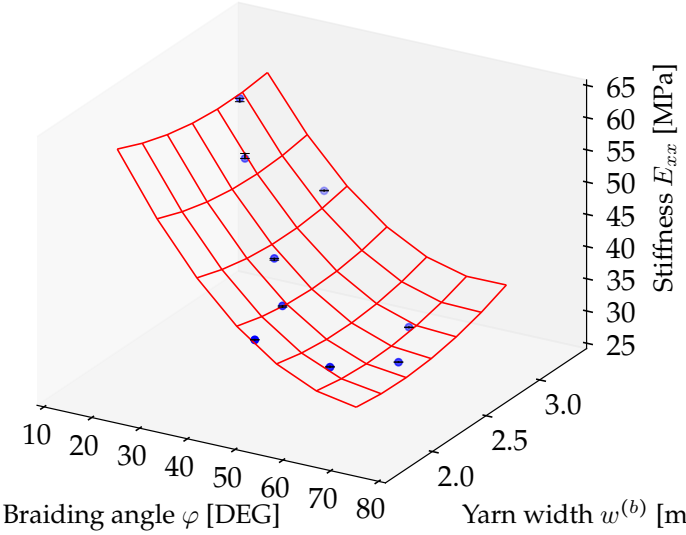

Figure 5.7.: Stiffness E_{xx} computed by the material meta-model

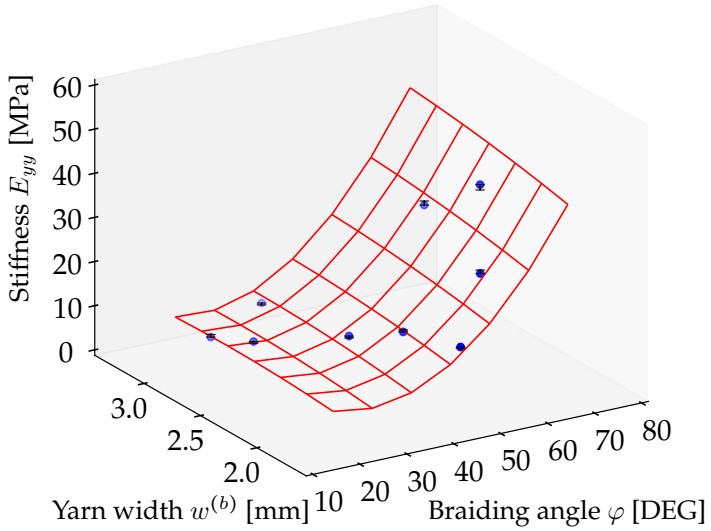

Figure 5.8.: Stiffness E_{yy} computed by the material meta-model

With figure 5.7 the response surface plot of the stiffness E_{xx}, thus in axial fiber direction is given. As defined with figure 5.6, the red represents the derived polynomial regression, whereas the blue points mark the support points. The support points are determined via the DoE and the corresponding stiffness and strength responses are computed by evaluating the meso homogenization model. Beside the computed response values, the distance to the response grid of the meta-model–or response surface approximation–is given, which basically displays the approximation error made by the conducted curve fitting. By studying the error bars in figure 5.7, one can convince oneself, that the approximation error made is less then two percent at the support points. Despite this obviously good fitting agreement, one cannot deduce a good approximation quality of the meta-model, since these points, where the error has been computed have also been considered during the curve fitting and are thus likely to be approximated well. To gain more insight on whether or not the meta-model is able

to bring forth credible and resilient surrogate response values over the whole design space several verification studies have been made. The verification study for E_{xx} will be discussed next. Before the quality of the meta-model is being assessed by verifying and studying approximation errors, the surrogate response for the transversal stiffness E_{yy} will be discussed briefly. The response surface of the meta-model for that stiffness E_{yy}, probed perpendicular to the axial yarn direction, is depicted in figure 5.8. Similarly to the axial stiffness E_{xx}, the surrogate response displayed there evinces small approximation errors at the support points, which again have been used to set up the meta-model. They actually are less then five percent. As afore mentioned, in order to gain sharp impression on the quality of the surrogate responses of the meta-model the error should not be evaluated at the DoE points, which have been used as support points. This is because of the fact, that a polynomial regression inherently intends to minimize the sum of squared errors (least squares). It is thereby actually realizing curve fitting to a polynomial of priorly defined order. Knowing that, verification can solely be established by studying the approximation at sample points, being randomly scattered over the whole parameter space spanned by the lower and upper bound of each parameter and contrasting surrogate responses with the responses of the original model. This is herein done for the stiffness response E_{xx} by randomly scatter sample points; four hundred points in total for this verification case. Figure 5.9 depicts the result of this verification by plotting the surrogate stiffness provided by the meta-model $E_{xx,\mathrm{meta}}$ on the coordinate axis and the stiffness result determined by the original model on the ordinate axis $E_{xx,\mathrm{org}}$.

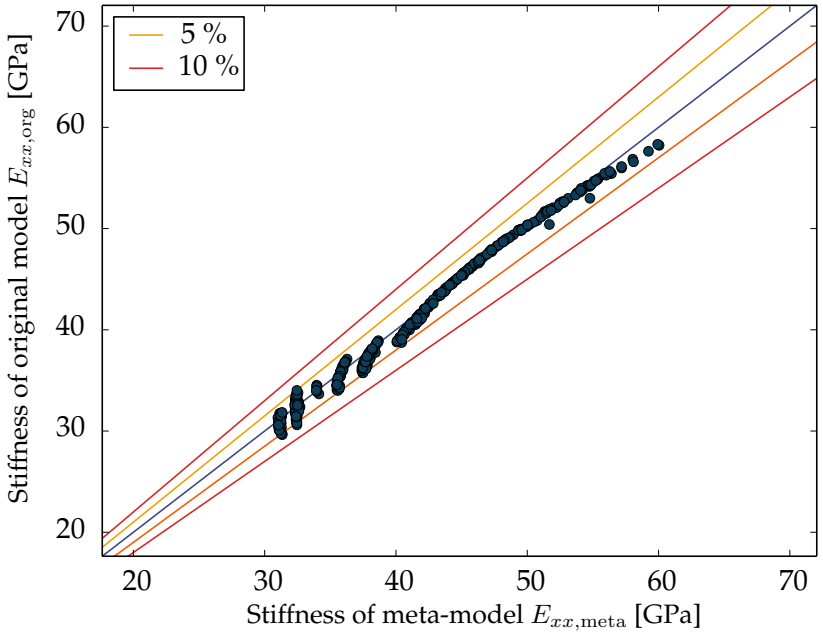

Figure 5.9.: The approximation quality for the responsel stiffness E_{xx}

The maximal approximation error identified by this verification study can be numbered to be six percent and the mean approximation error can be computed to three percent. In the thesis of Flach (2014) these errors and the small–but still present–jumps can be traced back to mesh-size dependent geometrical approximations of the braider yarns geometry. This is the reason for these jumps to especially turn up at high braiding angles φ and hence great geometric changes. They are regarded to be small, since the maximal detected change in stiffness is less then five percent. Considering all of this, the meta-model can be regarded to be verified for all stiffness responses.

Strength responses

Beside the stiffness responses, the meta-model further comprises the strength quantities of the triaxial braid based on initial failure decided based on Puck's failure criteria for the yarn tows and max strain for the pure matrix phase. At this point, it shall be noted, that these strength quantities are surely conservative and that the braid sustains greater loads (see Wegmann (2015)). Figure 5.10 depicts the initial failure strength in axial yarn direction R_{11}. The transversal strength R_{22} of the triaxial braid is illustrated in figure 5.11. As before, the response surface of the meta-model is given by the red grid and the blue points highlight the support points.

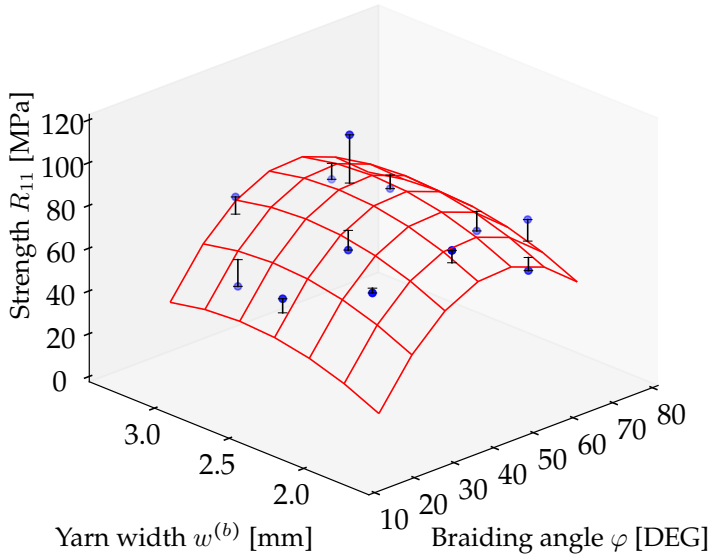

Figure 5.10.: Strength R_{11} computed by the material meta-model

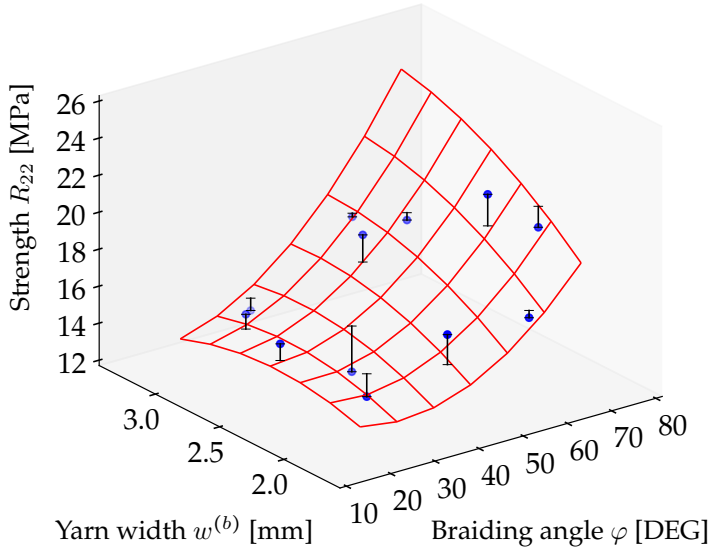

Figure 5.11.: Strength R_{22} computed by the material meta-model

For both strength responses, the approximation error at the support points are higher then for the stiffness case. For instance, the maximal approximation error can be identified to be eight percent for the approximated transversal strength R_{22} and even goes up to nine percent for the approximated axial strength R_{11}. This can be explained by the voxel finite element discretization of the meso geometry, where great stiffness discontinuities over element boundaries in tandem with the rectangular approximation of curved geometries–especially critical, where the braider yarns

dive underneath the axial yarns–leads to a greater mesh dependence. Two possible approaches for further reducing the approximation error have been identified for this case: either drastically reduce element size or change discretization type. However, since the developed material model neglects aspects, which influence the strength behavior more dominantly on a detailed level, such as nesting or geometrical deviations from the idealized sinusoidal path of the braider yarns. And, moreover, the material model is not indented to be used in detailed analyses of progressive damage evolution of one single given braid structure, but instead for the effective and efficient incorporation into a structural design optimization model for optimizing braid structures at early design phases, it has been abstained from further detailing the homogenization model. This particularly holds in light of the fact, that the derived meta-model is able to predict general trends and parameter relations and their impact on the strength properties of the braid material correctly and in a conservative fashion.

5.3.3. Comparison with experimental investigations

The experimental comparison shall just briefly be mentioned here, but has been studied by Siroky (2014) more thoroughly, where also a comparison with the analytical modeling approach proposed by Byun (2000) has been made. Table 5.2 summarizes experimental investigations made by *AUDI* and *IFB Stuttgart*, who studied the material within the MAI-Carbon project MAI-Design. These test have been conducted to the specifications of the standard AITM 1-0007 in case of tensile testing and AITM 1-0008 respectively for compression testing. In table 5.2 it has been differentiated in-between tension and compression testing and transversal (E_{yy}) and longitudinal stiffness (E_{xx}).

Table 5.2.: Meassured stiffness via two specimen configurations:
Triax30 (φ = 30°) and Triax55 (φ = 55°)
Thomas (2014)

	Tension		Compression	
Specimen	E_{xx} [GPa]	E_{yy} [GPa]	E_{xx} [GPa]	E_{yy} [GPa]
Triax30	63.6	10.2	61.0	9.2
Triax55	33.5	35.2	30.7	30.8

For drawing a comparison, the results, in terms of longitudinal E_{xx} and transversal stiffness E_{yy}, generated by the derived meta-material model are given with table 5.3. Evidently, the meta-model does not differentiate in-between tension and compression.

Table 5.3.: Computed stiffness responses by the meta-model

Braiding angle φ[DEG]	E_{xx} [GPa]	E_{yy} [GPa]
30.	53.5	8.5
55.	34.2	23.5

Comparing the results from experiments (table 5.2) with the those given by the meta-model (table 5.3) leads to the insight, that the meta-model rather underestimates the stiffness, which makes it conservative. Further, some stiffness values differ considerably, which may also be traced back to the experimental test procedure, which is currently under revision. This is the case, because during the production of the specimens, alteration of the braid architecture in terms of braider angle φ and yarn widths could yet not be avoided. This certainly influences the test outcome, since changing the braider angle by just five degrees brings forth a deviation in stiffness of eleven percent. This deviation has been computed by changing the braider angle at $\varphi = 30 \pm 5°$ and studying the output of the meta-model. Next, the geometric representation of the braid architecture as presented earlier is compared. For that purpose, several micrographs have been made by Siroky (2014). Three of these

are shown in figure 5.12. In this figure the actual fiber architecture is depicted. The micrograph in die middle cuts the axial yarn perpendicularly, while the one right next to it cuts the axial yarns lengthwise and the left one cuts the braider yarns lengthwise. Several of those micrographs have been made and evaluated leading to the results as given with tables 5.4 and 5.5.

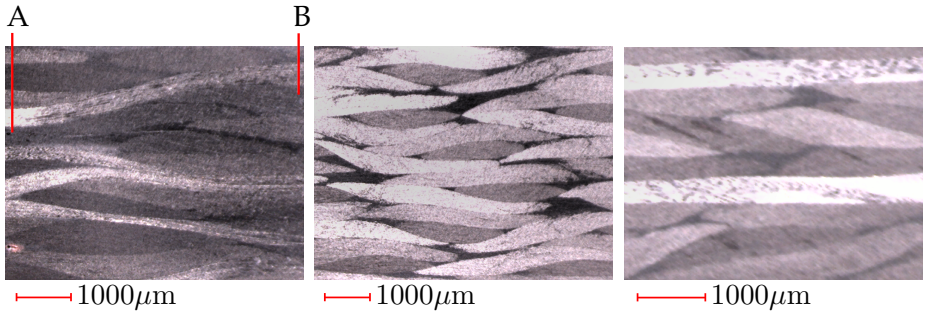

Figure 5.12.: Different micrographs for verifying the made geometrical abstraction

Table 5.4.: Meassured geometric properties of Triax30

Entity	Mean value [μm]	Error band [%]
$h^{(a)}$	424.3	±5
$h^{(b)}$	375.7	±12
$w^{(a)}$	2260.3	±3

Table 5.5.: Meassured geometric properties of Triax55

Entity	Mean value [μm]	Error band [%]
$h^{(a)}$	397.3	±4
$h^{(b)}$	379.7	±18
$w^{(a)}$	2963.7	±3

5.3.4. Hybrid homogenization - experimental and numerical

In this subsection, a possible extension of the introduced idea will be sketched. So far, it has been shown, that the surrogate modeling approach can be used to approximate the stiffness and strength responses of the meso unit cell model and, thereby, decouple the homogenization chain in-between macro and meso scale. In principal, the underlying nature of the "original model" does therein not matter. Hence, the approach works for numerically determined responses as well as for those based on experiments. This is why, the material model could have been formed by solely conducting a polynomial regression on the experimental data. Or, and this is discussed in the following, by pursuing a hybrid approach, where responses from both disciplines, i.e. numerics and experiments, are considered simultaneously, so as to form a common unified material model via hybrid meta modeling. This hybrid homogenization approach has been carried out, by simply embedding two additional support points right before the polynomial coefficients are determined via the least squares approach. Figure 5.13 depicts the response surface for the case of nine numerically determined support points and two experimental ones. As displayed there, they successfully form one unified material meta-model capable of predicting the effective longitudinal stiffness E_{xx} based on a basis formed by simulations and experiments.

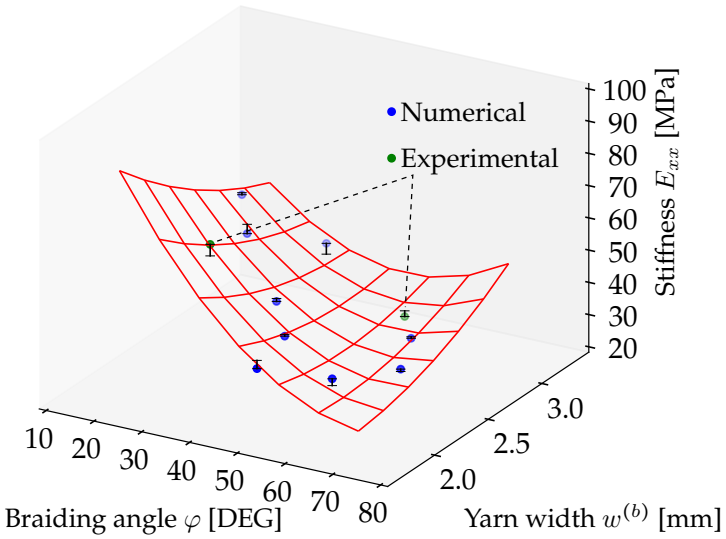

Figure 5.13.: Stiffness E_{xx} response by the hybrid material meta-model

5.4. Summary on the decoupled homogenization

By taking advantage of surrogate modeling techniques, an efficient material model has been developed. It is regarded efficient, since once all effective properties, such as longitudinal stiffness or transversal strength for a certain kind of composite material are homogenized, the meta-model comprising most relevant aspects can be formed, which then predicts effective properties for any other parameter configuration in no time. This especially holds, since the meta-model–owing to its polynomial basis for the polynomial regression–is orders of magnitudes less numerically expensive than full simulations, which are needed throughout the numerical homogenization.

The decoupling in-between the macro and meso scale of the homogenization chain, enables detailed investigation of the material meta-model in terms of sensitivity studies of the considered material parameters. Further, the decoupled material model can be re-used for multiple structural problems. This will actually be demonstrated later, by showing how straight forward the material meta-model can be incorporated into the analyses of an A-pillar, via the FEA tool Abaqus, and a propeller, where NASTRAN has been used for solving the underlying mechanical system equations. As already indicated with this software independence, the polynomial coefficients, which basically determine the meta model, can be passed to most FEA tools without the necessity of any complex mapping or similar obstacles.

Moreover, it has been shown, how the homogenization approach can be hybridized, so that effective material properties are determined based on numerics as well as experiments. This can leverage the trust level by unlocking the potential of mutual enrichment from both disciplines, which may also result in higher model accuracy and generality.

As a final remark, the surrogate modeling in form of a polynomial regression can equalize errors originating from simulation or experiments. This was already postulated by Gauss, who realized, that the underlying least square approach equalizes errors in the observation of planets and thus helps to describe and predict their pathways. And ultimately, most material models–as they involve curve fitting for some of their parameters–can be regarded to be surrogate models, at least to some extend, as well.

6 General insights and anticipated findings

This chapter generalizes and presents core aspects of the conducted research of this thesis. The concepts, ideas and insights gained presented throughout this chapter will later be discussed based on technically relevant design tasks involving structural analyses. They are presented before and separately, to underpin their general validity. For the sake of understanding, a small analytical design task–specifically a pipeline optimization based on the classical laminate theory–will be used as a vehicle to illustrate the concept or idea. This small academic example will be highlighted in gray, such that the focal point solely lies on the general statements made throughout this chapter.

Contents

6.1. Introduction to multi-criteria optimization

6.1.1. A brief overview

In everyday life, we face situation demanding some sort of decision making, where each individual needs to weight up, possibly contradicting, decision criteria, so to make the most appropriate choice. An example reflecting this, can be found in the variety of bicycles ranging from mountain bikes over racing to folding bicycles, each of those representing an optimal choice depending on individual preferences on criteria such as flotation, max speed, price, size variety et cetera. These sort of *"decision-making"* problems are within the frame of optimization addressed by the discipline of vector optimization; also being referred to as multi-criteria, multi-objective and in some literature Pareto optimization. Historically, one of the first discussions addressing the handling of conflicting objectives is given by Edgeworth (1881). In this book, the optimal settlement in-between parties, e.g. consumers, with conflicting interest is described to be achieved, once for any infinitesimal change in the decision variables each consumer's utility does not increase simultaneously. Further it has been stated: "In case

the utility of one party increases, the utilities of the remaining must decrease". This early statement of optimality of multi-criteria problems has been profoundly elaborated by Pareto (1906). Pareto studied in this context, conflicts in societies and how optimal compromises can be characterized. He for instance came to the following conclusion:

> The optimum allocation of the resources of a society is not attained so long as it is possible to make at least one individual better off in his own estimation, while keeping others as well off as before in their own estimation
>
> Vilfredo Pareto (1848 – 1923)

This conclusion did lead to a general definition of optimality in vector optimization. The terms dedicated to this early optimality definition are Pareto efficiency and optimality, which basically both characterize optimal solutions of a given multi-criteria optimization problem. In the following decades, mathematical debates dominated the vector optimization discipline. Kuhn and Tucker (1951) for instance contributed to the generalization of the efficiency definition in case multiple objectives are to be considered. Further contributions to the proper and mathematically profound understanding of optimality and the solution space of general vector optimization problems have for instance been made by Cunha and Polak (1967). In engineering, optimization problems involving multiple objective where extensively discussed by Baier (1977), Leitmann (1977) and Stadler (1984) at first. Baier (1978) especially pioneered by not only discussing the peculiarities of vector optimization in structural design, but further showed its realization and added value–by for instance depicting post-processing possibilities in analogy to the well-known shadow price concept–on structural problems derived from engineering practice.

A side example is given next, but yet is introduced within a gray box, so as to highlight, that this example is not of superior importance for the understanding of this part. However, these framed and colored sections intend to provide an intuitive and comprehensive illustration of the rather abstract discussions of this thesis part and shall thus be regarded as supplementary information.

Side example: Structural aspects and the system responses

For the sake of illustration, a side example–specifically the structural optimization of a composite pipeline–will be defined next. As depicted below, a pipeline segment is abstracted towards a non-curved plate. As illustrated there, the pipeline will be loaded with a certain internal pressure p_i. Moreover an axial stress loading and a simple supported bending load case are considered as well (see Häußler (2014), Häußler et al. (2015), Harnischfeger (2015)). The laminate itself is parametrized in such a way, that the thickness t_i and ply ortientations α_i of the outer (i = 1) and inner (i = 2) layer can be varied. The responses are the pipeline mass m, structural failure indices according to Tsai-Hill $\mathcal{FI}_S$, function failure index determined by a leakage criteria $\mathcal{FI}_F$, coefficient of thermal expansion α_{CTE} and bending stiffness K_b are computed via the classical laminate theory.

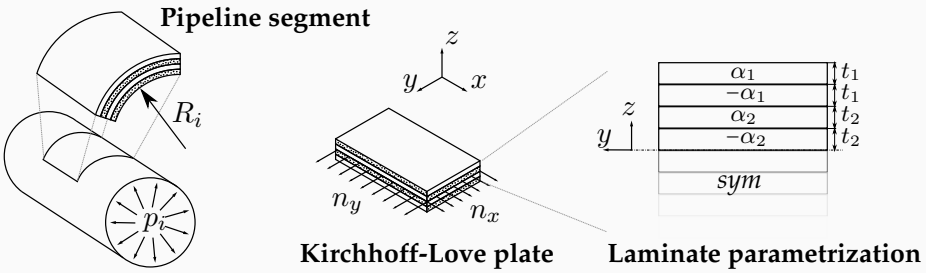

6.1.2. Fundamentals in vector optimization

At first, the general statement of a vector optimization problem is given as,

$$\begin{array}{lll} \underset{\vec{x}\in\chi}{\text{minimize}} & f_i(x_j), & i = 1,\ldots,n_{\mathrm{O}},\ j = 1,\ldots,n_{\mathrm{DV}} \\ \text{subject to} & g_l(x_j) \le 0, & l = 1,\ldots,n_{\mathrm{IC}} \\ \text{with} & \chi = \{x_j \in \mathbb{R}^{n_{\mathrm{DV}}} : 0. \le x_j \le 5.\}, & \end{array} \tag{6.1}$$

where,

$\vec{f}$ vector of objectives,
$\vec{g}$ vector of inequality constraints,
$\vec{x}$ design variable vector.

In this posed optimization problem (6.1), n_{O} represents the number of objectives. The following three cases are of practical relevance and can thus be regarded as a common classification of multi-criteria optimization problems,

$$n_{\mathrm{O}} = \begin{cases} 1: & \text{Single objective problem} \\ 2: & \text{Bi-objective problem} \\ > 2: & \text{Multi-objective problem} \end{cases} \tag{6.2}$$

In this thesis, most of the multi-criteria optimization problems are bi-objective. The following general discussion will focus on this case. Figure 6.1 illustratively depicts such an bi-objective problem, where criteria one f_1 is plotted over the coordinate axis and the second respectively over the ordinate axis.

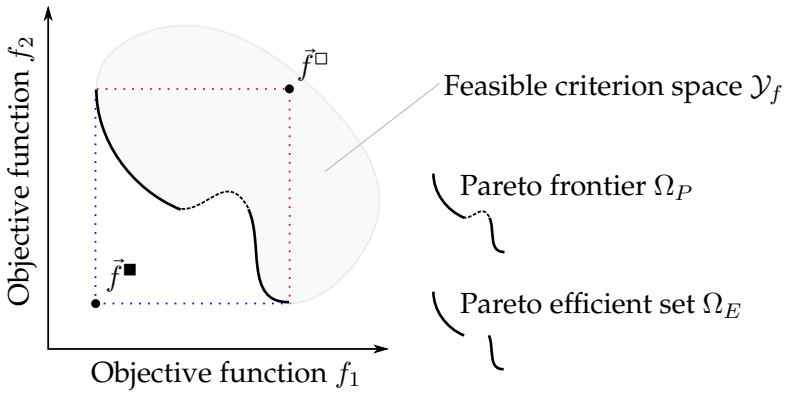

Figure 6.1.: Exemplary illustration of bi-objective criterion space

The gray area reflects the feasible criterion space $\mathcal{Y}_f$, which is the space, gathering all criteria, i.e. objective function values, where the inequality constraints as well as the side constraints are fulfilled (see Marler and Arora (2004) and Stadler (1988)). Mathematically stated, the feasible criterion space $\mathcal{Y}_f$ is spanned by mapping each decision variable $\vec{x}$ as element of the feasible decision space χ_f via the objective functions, as given with the following set of equations (6.3).

$$\begin{array}{ll} \mathcal{Y}_f & := \left\{\vec{f}(\vec{x}) \mid \vec{x} \in \chi_f\right\} \\ \chi_f & := \{\vec{x} \in \chi \mid \vec{g}(\vec{x}) \le 0\} \end{array} \tag{6.3}$$

Side example: The definition of the optimization task

Now, an exemplary vector optimization problem will be stated, based on the priorly introduced side example; the pipeline. This example will later serve as a vehicle to illustrate abstract concepts and findings.

$$\begin{aligned} \underset{x\in\chi}{\text{minimize}} \quad & \vec{f} = f_i(x_j), && i = 1,2,\ j = 1,\dots,4 \\ \text{subject to} \quad & g_l(x_j) \le 0, && l = 1,\dots,5 \\ \text{with} \quad & \chi = \{x_j \in \mathbb{R}^{n_{\mathrm{DV}}} : 0. \le x_j \le 5.\}, \\ \text{where,} \quad & \end{aligned} \tag{6.4}$$

f_1	$= m$	mass of pipeline,
f_2	$= K_b$	bending stiffness,
g_1	$= \mathcal{FI}_S\,\mathrm{FoS}_S - 1$	no structural failure,
g_2	$= \mathcal{FI}_F\,\mathrm{FoS}_F - 1$	no functional failure,
g_3	$= K_{b,\min} - K_b$	minimal bending stiffness,
g_4	$= \alpha_{\mathrm{CTE}} - \alpha_{\mathrm{CTE,max}}$	maximal allowable CTE,
g_5	$= m - m_{\max}$	maximal tolarable mass,
x_1	$= \alpha_1$	ply orientation of outer layer,
x_2	$= \alpha_2$	ply orientation of inner layer,
x_3	$= t_1$	ply thickness of outer layer,
x_4	$= t_2$	ply thickness of inner layer.

The following figure depicts the decision space, where x_3 and x_4 are set constant to mass optimal values including the isolines for both objectives and all constraints (colored regions are infeasible).

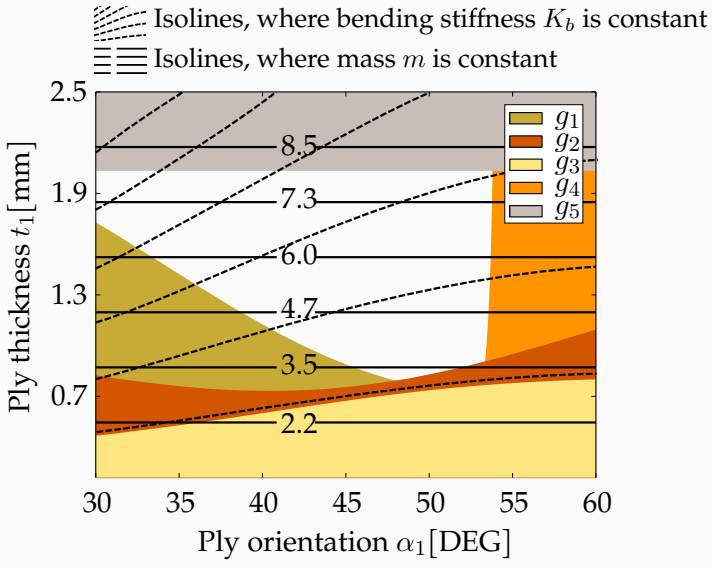

Once the feasible criterion space is spanned, the question of which criteria are optimal and how to measure optimality arises. However, there is no distinct generally accepted definition for this. Marler and Arora (2004) suggest in their work, that the reason for this can be found in the multitude of optimal solutions of a multi-criteria problem. This is opposed to the presence of one unique global solution in case of single objective problems. After reading Ehrgott (2005), Stadler (1988) and further publications, the author of this thesis came to the same conclusion as Marler and Arora (2004); specifically, that

optimality will be measured by the concept of dominance or Pareto efficiency, being, by the way, the most frequently used concept anyhow. In the fundamentals part of this thesis, this concept for determining Pareto efficiency has already been given (see section 2.2.3 and (2.6)). Pareto efficient criteria will henceforth gathered in the set Ω_E, being highlighted by the bold black line in figure 6.1. It shall be noted that for most structural design problems, this set contains infinite many solutions due to the presence of continuous decision variables, see (6.3). In addition to this set, another well-established concept of optimality will be used throughout this thesis, namely, the concept of a Pareto frontier. A Pareto frontier Ω_P bounds the feasible criterion space $\mathcal{Y}_f$ and locally fulfills the Pareto efficiency, but may contain criteria, being not Pareto efficient over the whole criterion space $\mathcal{Y}$. Thus,

$$\Omega_E \subseteq \Omega_P. \tag{6.5}$$

Most literature also add the following terms to the afore mentioned terminologies: anchor points, point of utopia and nadir point. The first, refers to the extremal of the Pareto frontier Ω_F, i.e. minimizing to solely one criteria e.g. $f = f_2$. Combining the best criteria values of each anchor point, yields the point of utopia $\vec{f}^{\blacksquare}$, which is evidently a fictitious solution being far from being obtainable in general.

$$f_i^{\blacksquare} = \min_{x \in \chi} \{ f_i(\vec{x}) | \vec{g}(\vec{x}) \leq 0 \} \qquad\qquad i = 1, \ldots, n_{\mathrm{O}} \tag{6.6}$$

The vice versa evaluation of the anchor points–thus crapping only the worst solutions–leads to the nadir point $\vec{f}^{\square}$. These points are relevant for many algorithms, e.g. internal normalizing or for spanning hyperplanes. They are also depicted in figure 6.1.

6.2. Solving and post-processing of vector optimizations

6.2.1. Common solving techniques in multi-criteria optimization

Approaches based on zeroth order algorithms

Optimization problems can in general be solved by algorithms exploiting gradient information and those that do not. Obviously, both classes gradient-based and zeroth order algorithms, do therefore differ considerable in computational performance, treatment of discrete variables, ease of implementation et cetera. When it comes to multi-criteria optimization problems, zeroth order algorithms, and especially those being biologically inspired, frequently allow a straight forward solving of such. This is mainly due to the fact, that some sort of fitness function, evaluating and contrasting each member of the population, is embedded already, where a slight modification in terms of considering the dominance rank, vector metrics or some sort of Pareto filter as an additional for evaluating fitness can be incorporated with ease. This is also reflected by the flood of literature solving multi-criteria via biologically-inspired algorithms. Schaffer (1985) implemented a vector evaluated genetic algorithm, whereas Fonseca and Fleming (1993) used a ranking procedure and Cheng and Li (1997) used Pareto filters within a genetic algorithm framework. Summing up, there is a great variety of biologically-inspired algorithms being able to cope with multiple objectives. Despite their pronounced advantages, the associated computational effort can be considerably high and due to the lack of gradient information there is no possibility for evaluating optimality for a determined solution.

Approaches founded on gradient information

The by far most frequently used approach is the simple scalarization approach, where the multi-objective problem is condensed to one single objective $\tilde{f}$ with the use of an objective weighting parameter, here κ, as follows,

$$\tilde{f} = \tilde{f}_1 + \tilde{f}_2 = \kappa f_1 + (1-\kappa) f_2. \tag{6.7}$$

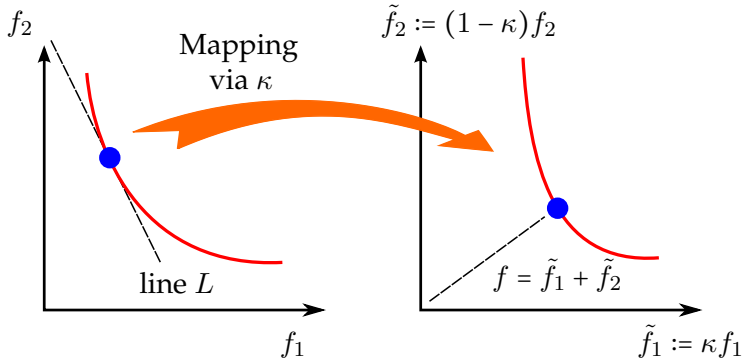

Figure 6.2.: Interpretation of the objective weight κ as a mapping or as in Sobieszczanksi-Sobieski et al. (2015) by an intersection with line $L := \{(f_1, f_2) | \text{const.} = \kappa f_1 + (1-\kappa) f_2\}$

In most cases, the substitutive single objective optimization problem $\min\{\tilde{f} | \vec{g} \leq 0\}$ is solved once for one given weighting parameter κ. In literature, $\tilde{f}$ is sometimes also referred to as the utility function. Interpreting equation (6.2), leads to the idea of κ being some sort of mapping, with which–once κ is being fixed–the single objective $\tilde{f}$ can be understood as a measure of the minimal distance from the origin of the criterion space to the mapped Pareto frontier. This interpretation is illustrated in figure 6.2. This mapping is especially usefully when all objective functions are normalized, for instance, with their ideal or extremal value. A similar geometric interpretation of this scalarization is given by Sobieszczanksi-Sobieski et al. (2015), where the condensed optimization problem is understood as finding the intersection of the Pareto frontier with the line L given by const $= \kappa f_1 + (1-\kappa) f_2$, as also depicted in figure 6.2. As a remark, for finding a reasonable compromise, one should normalize with the help of the vector of utopia $\vec{f}^{\blacksquare}$, as follows,

$$\hat{f}_i = \frac{f_i - f_i^{\blacksquare}}{f_i^{\blacksquare}}. \tag{6.8}$$

Optimizing on these normalized objectives, i.e. $\tilde{f} = .5\hat{f}_1 + .5\hat{f}_2$, is quite likely to lead to an optimal compromise, lying in the middle of the Pareto frontier, in case it is convex and symmetric. This will also been shown in this thesis. In section 8.2, for instance, a reasonable compromise solution is found by normalizing the individual objectives mass and effort–as given by equation (8.13)–such that an optimal compromise for the structural optimization of the A-pillar can be found.

$$\tilde{f} = \left\{ \sum_i \alpha_i \hat{f}_i^q \right\}^{-q} = \left\{ \sum_i \alpha_i \left(\frac{f_i - f_i^{\blacksquare}}{f_i^{\blacksquare}} \right)^q \right\}^{-q} \tag{6.9}$$

Therefore, for the use of gradient-based approaches, some sort of condensation to one single objective problem needs to be conducted and, obviously, each single objective problem solely reveals one solution of the whole set of Pareto efficient solutions Ω_E (see figure 6.1). However, in some situations, for identifying the most suitable compromise it would be expedient to get some insight

on how the objectives do compete and, thus, how the Pareto efficient solutions actually deploy in a Pareto frontier. For efficiently approximating the whole Pareto frontier, an approach as suggested by Pereyra et al. (2013) has been implemented and applied in this thesis as well.

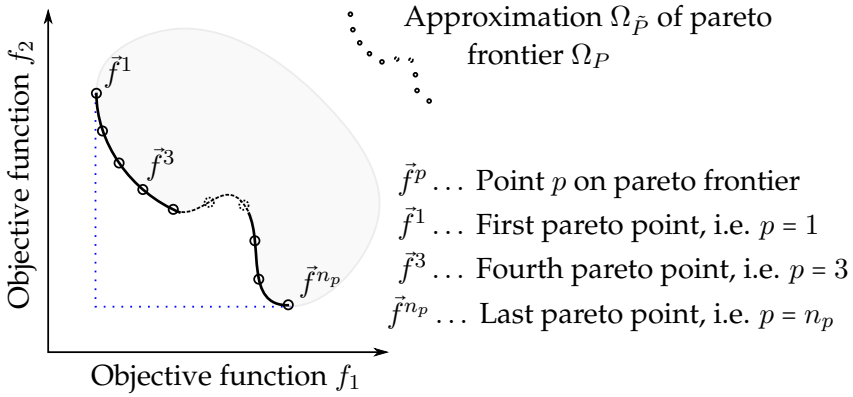

Figure 6.3.: Approximation $\Omega_{\tilde{P}}$ of the whole Pareto frontier Ω_P

Figure 6.3 outlines the underlying idea of approximating the whole Pareto frontier Ω_P as a superset of Pareto efficient solutions Ω_E by a pre-defined number of solution points, here denoted as n_P. As a consequence, the approximation $\Omega_{\tilde{P}}$ can be regarded as a subset of Ω_P and thus $\Omega_{\tilde{P}} \subsetneqq \Omega_P$. The approximation $\Omega_{\tilde{P}}$ shall thereby ideally be equispaced, thus display equal distances in-between different solutions, such that this approximation reveals most of the Pareto frontier in the criterion space.

6.2.2. Implemented and realized approach in this thesis

Now, the approach of solving vector optimization for an equispaced set of Pareto efficient criteria will be presented. The general multi-criteria optimization problem, as posed with equation set (6.1), will therefore be substituted by a sequence of scalarized and, hence, single objective optimization problems, as given next

$$\begin{aligned} \underset{x,\kappa}{\text{minimize}} \quad & \tilde{f} = \kappa f_1 + (1-\kappa) f_2 \\ \text{subject to} \quad & \vec{g} \leq 0, \\ & g_{\text{BS}} \leq 0, \\ \text{and} \quad & h_\gamma = \gamma^2, \\ \text{with} \quad & \vec{x} \in \chi \text{ and } \kappa \in [0, ..., 1] \end{aligned} \tag{6.10}$$

Studying this optimization formulation reveals two major aspects of this approach. First, the vector of objective functions is condensed to a scalar objective $\tilde{f}$ by weighting them with κ. Opposed to most approaches, the objective weight κ is not set constant, but instead optimized as well and thus part of the decision variable vector. Secondly, two constraints have been added: the back-stepping g_{BS} and the equidistance h_γ constraint. The first ensures, that priorly computed criteria vectors $\vec{f}^{p-1}, \vec{f}^{p-2}$ are not re-solved (no back-stepping), while the second imposes, that the distance in-between the current criteria vector $\vec{f}$ and the prior one $\vec{f}^{p-1}$ is constant, namely γ (equidistance). Both constraints are given with the following equations and also sketched in figure 6.4.

$$\begin{aligned} g_{\text{BS}}(\vec{x}) &= \|(\vec{f}^{p-1} - \vec{f}^{p-2})(\vec{f}(\vec{x}) - \vec{f}^{p-1})\|_{\text{L2}} \leq 0, \\ h_\gamma(\vec{x}) &= \|\vec{f} - \vec{f}^{p-1}\|_{\text{L2}}^2 = \gamma^2 \end{aligned} \tag{6.11}$$

g_{BS}, the first constraint, is an inequality constraint and added to exclude solutions which already have been found. These undesirable situations occur, when the algorithm is not properly climbing from one side to the other of the Pareto frontier. This is also why, the constraint has been called *back-stepping* (BS) constraint.This constraint is further illustrated in figure 7.1 on the right side. There, the red arrows visualize a geometric interpretation g_{BS}, where the angle α_{BS} between the red arrows is restricted such that it needs to be greater than ninety degrees. The following equation provides more insight

$$\begin{aligned} g_{\text{BS}}(\vec{x}) &= \|(\vec{f}^{p-1} - \vec{f}^{p-2})(\vec{f}(\vec{x}) - \vec{f}^{p-1})\|_{\text{L2}} \\ &= \|(\vec{f}^{p-1} - \vec{f}^{p-2})\|_{\text{L2}} \|(\vec{f}(\vec{x}) - \vec{f}^{p-1})\|_{\text{L2}} \cos(\alpha_{\text{BS}}) - \cos(\pi). \end{aligned} \tag{6.12}$$

The second constraint h_γ is imposed so as to obtain an equidistant approximation $\Omega_{\tilde{P}}$ of the Pareto frontier Ω_P. To do so, an a priori estimate of the distance in-between successive Pareto solutions $\vec{f}^p$ and $\vec{f}^{p-1}$ needs to be made such that the desired distance in-between successive solutions γ can be computed. In this work, this estimate is made by computing extremal solutions first, thus for fixing κ to zero and one. Then, the length of the Pareto frontier is approximated by computing the distance between both extremal solutions and multiplying it with a chord factor c accounting for the possible bend of the frontier. This chord factor has in most cases been set to be 1.2 and is, aside from the desired number of Pareto solutions n_p, the only parameter of the approach. Lastly, the desired distance in-between Pareto optimal solutions γ is computed by dividing the scaled distance between both extremal solutions by the desired number of Pareto optimal n_P.

$$\gamma = \frac{c}{n_P} \left\| \vec{f}^1 - \vec{f}^{n_p} \right\|_2 \tag{6.13}$$

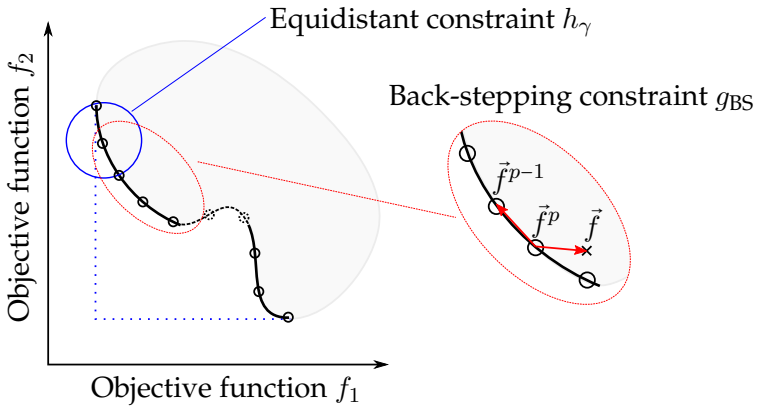

Figure 6.4.: Depiction of the added equidistant and back-stepping constraints

The added constraints do in tandem with the expansion of the design space by the objective function weight κ facilitate the computation of an equidistant approximation of the Pareto frontier. Obviously, the optimization problem as given with equation set (7.3) is solved multiple times, i.e. $p = 1, ..., n_p$. Maier (2015) has implemented and validated this approach extensively. He moreover showed its general applicability. With figure 6.5, an overview of the implemented approach is given. This figure is followed by a parenthesis, where the solution of the priorly defined side-example is given. At this point, it shall also be highlighted, that this approach is also applicable to multi-criteria optimization problems with more than two objectives. This is for instance demonstrated for a small academic example in the appendix section A.3. As can be seen in figure A.2, the approach can also provide a reasonable approximation for such a tri-objective optimization problem. However, the interpretation of the outcome is by far more challenging (surface instead of intuitive curve), which makes the definition of such problems in practice rather unrealistic.

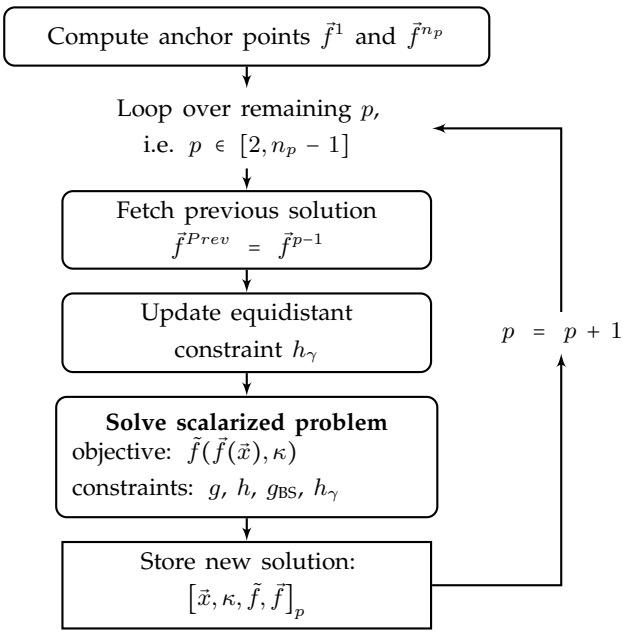

Figure 6.5.: Flow chart of the implemented algorithm by Maier (2015)

Side example: Solving the vector optimization task

The following plot depicts multiple solutions of the bi-objective optimization problem, as posed with equation set (6.4), where the pipeline's mass m was set as one objective and the maximization of bending stiffness K_b as the contradicting one. The dashed black line represents the solution determined by the implemented gradient-based Pareto frontier approximation. On the contrary, the colored dots reflect vector optimizations accomplished by a zeroth order algorithm; here, by the well renowned genetic algorithm NSGA-II by Deb et al. (2002). In the legend, #eval., #pop. and #gen. stand for the number of needed total function evaluations, size of population and respectively number of generations. Contrasting these results, the gradient-based approach performed superior in terms of number of function evaluations. Moreover, the gradient-based optimization outperformed the genetic algorithm in the exploitation of the individual optima, therefore, the gradient-based optimization found Pareto efficient solutions where most dominate those obtained by the genetic ones. This indicates, the genetic algorithm did not completely "converge", which could be improved by increasing the number of generations and in that turn, the number of functions evaluations. Despite this, it shall be noted, that zeroth order algorithms do not demand that sophisticated optimization models regarding convexity, variable type (discrete, integer etc.), numerical robustness and alike.

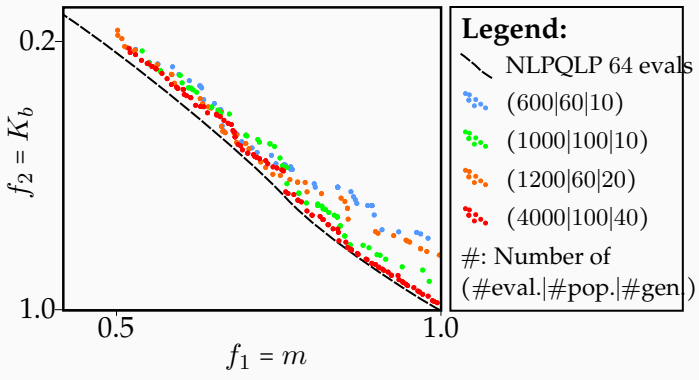

6.2.3. Post-processing

Evaluating optimality for a given set of Pareto optimal solutions

A measure for evaluating, whether or not optimality is given, the Karush-Kuhn-Tucker condidtions–being mentioned first in the fundamentals part in section 2.2 by equation (2.3)–can be used. This measure can evidently be applied here as well, since a gradient-based algorithm is used and sensitivities are therefore evidently available at each derived optima. Yet, the fulfillment of this measure does not guarantee, that the best, i.e. global, optima has been found. Nonetheless, it provides insight on the quality of the found solutions. Such that the KKT conditions can be properly plotted, a definition being compliant to numerics and the associated inaccuracies, a scalar measure needs to be defined. One of the most established scalar measures is the so called first order optimality, which basically is the norm of a vector embracing the stationary of the Lagrangian function $\mathcal{L}$ and the complementary slackness. This first oder optimality measure is given by,

$$\mathcal{O} = \left\| \begin{Bmatrix} \frac{\partial \mathcal{L}}{x_1}\Big|_{x_1^{\mathrm{Opt}}} \\ \vdots \\ \frac{\partial \mathcal{L}}{x_{n_{\mathrm{DV}}}}\Big|_{x_{n_{\mathrm{DV}}}^{\mathrm{Opt}}} \\ \lambda_1 g_1(x') \\ \vdots \\ \lambda_{n_{\mathrm{IC}}} g_{n_{\mathrm{IC}}}(x') \end{Bmatrix} \right\|_2 \tag{6.14}$$

where $\frac{\partial \mathcal{L}}{x_1}\Big|_{x_1^{\mathrm{Opt}}} = \frac{\partial f}{\partial x_1}\Big|_{x_1^{\mathrm{Opt}}} + \sum_k \mu_k \frac{\partial h_k}{\partial x_1}\Big|_{x_1^{\mathrm{Opt}}} + \sum_l \lambda_l \frac{\partial g_l}{\partial x_1}\Big|_{x_1^{\mathrm{Opt}}}$. The evaluation of this optimality criteria is highly advisable and will for instance be shown for the propeller structure in section 9.2, where the optimality can be stated for the whole approximation of the Pareto frontier for two distinct multi-criteria optimizations; the simultaneous optimization of mass and frequency, and additionally for the case where frequency and braiding time are considered.

Choosing the most appropriate Pareto efficient solution

In literature, there are multiple suggestions on how to chose the most suitable solution from the set of computed Pareto efficient solutions. Marler and Arora (2004) for instance provide multiple variations in their survey, where one is being picked and discussed in brevity herein, namely the notion of maximal utility. One can for instance define utility such that it quantifies the degree of individual benefit or gain by putting the current criteria value $f_i^\star$ into context with the best and worst possible outcome. This definition is given next,

$$U = \sum_{i=1}^{n_o} \bar{f}_i = \sum_{i=1}^{n_o} 1 - \frac{f_i^\star - f_i^\square}{f_i^\square - f_i^\blacksquare}, \tag{6.15}$$

where $f_i^\square$ and $f_i^\blacksquare$ represent the worst (nadir) solution and respectively the best (utopia). Once, the utility is computed for each optimum, the one displaying the maximum utility could be chosen. Even though, this approach is appealing due to its mathematical basis, it is not generally viable in practice, since the engineer or responsible project managing director will re-evaluate the whole situation by bringing in new preferences and thus weights, which could point into a totally other direction where a situation-dependent optimal compromise is lying. Knowing that, it is hence beneficial to rely on an efficient approach capable of robustly approximating most of Pareto frontier, such that the decision maker's information is being maximized. This utility definition has also been applied on the propeller example yielding the outcome depicted in figure A.12.

Sensitivities of the criteria and associated shadow prices

In this thesis, the concept of shadow prices is used quite extensively for almost every structural example. This is mainly because of they illuminate much of the design-dominating restrictions and how those imprint onto the releasable utilities or vice versa, the price being payed in the hidden by imposing certain constraint levels. In section 2.2.2 they were introduced for single-objective problems first via equation (2.4). Now, this concept will be transfered to a general multi-objective optimization problem being scalarized to $\tilde{f}$ as given with equation (6.7). The linearization of one objective f_i with respect to the constraint level c of the response r associated with the constraint $g_l = \frac{r}{c} - 1 \leq 0$ can be made explicit via the following equation

$$\begin{aligned} \mathrm{Lin}(f_i(c + \Delta c)) &= f_i|_{x_j^{\mathrm{opt}}} + \frac{\partial f_i}{\partial c}\Delta c \\ &= f_i|_{x_j^{\mathrm{opt}}} + \frac{\partial f_i}{\partial \tilde{f}}\frac{\partial \tilde{f}}{\partial g_l}\frac{\partial g_l}{\partial r}\frac{\partial r}{\partial c}\Delta c, \end{aligned} \tag{6.16}$$

where the partial derivatives $\frac{\partial \tilde{f}}{\partial g_l}$, $\frac{\partial g_l}{\partial r}$ and $\frac{\partial r}{\partial c}$ can be determined to be $-\lambda_l$, c^{-1} and 1, respectively. The sole component asking for determination is the partial derivative $\frac{\partial f_i}{\partial \tilde{f}}$, which can be obtained by differentiating the scalarization. Hence, for the simplest scalarziation, given by equation (6.7), the derivative can be computed to be $\frac{\partial f_1}{\partial \tilde{f}} = \kappa^{-1}$ and $\frac{\partial f_2}{\partial \tilde{f}} = (1-\kappa)^{-1}$. This linearization is for instance done for the A-pillar example in section 8.2, where the equations (8.18) and (8.19) provide the partial derivative of the scalarized objective, there f_d, and the linearization of one objective, effort e. An extension of this linearization can be made by not linearizing with respect to the constraint level, but instead to any given relevant parameter Υ of the model, such as fiber stiffness, number of filaments or even process parameters such number of bobbins. Obviously, for doing so, the linearization as introduced by (6.16) simply needs to be extended by all partial derivatives with respect to the parameter Υ of interest. It shall be highlighted, that all partial derivatives means, that all constraints comprising responses which are being influenced by Υ need be considered, such that a meaningful linearization can be realized. The following equation (6.17) states this, with Λ representing a set of indicies l of all constraints with direct or indirect dependency on Υ, i.e. $g_l = g_l(\Upsilon, r_l(\Upsilon), x, c)$.

$$\begin{aligned} \mathrm{Lin}(f_i(\Upsilon + \Delta\Upsilon)) &= f_i|_{x_j^{\mathrm{opt}}} + \frac{\partial f_i}{\partial \Upsilon}\Delta\Upsilon \\ &= f_i|_{x_j^{\mathrm{opt}}} + \frac{\partial f_i}{\partial \tilde{f}}\left\{\sum_{l\in\Lambda}\frac{\partial \tilde{f}}{\partial g_l}\left(\frac{\partial g_l}{\partial r_l}\frac{\partial r_l}{\partial \Upsilon} + \frac{\partial g_l}{\partial \Upsilon}\right)\right\}\Delta\Upsilon, \end{aligned} \tag{6.17}$$

The afore mentioned A-pillar linearlization of the objective effort e with respect to the constraint level will also be extended by a sensitivity study yielding equation (8.20). This partial derivative can be utilized so as to extrapolate the influence of the used fiber material, i.e. how the objective effort e would change in case the fiber is being substituted (see equation (8.21) and table 8.8). Before the discussion on post-processing is closed, the sensitivity of one objective to another $\frac{\partial f_2}{\partial f_1}$ is being discussed briefly. This will be applied and discussed at length in section 9.2.2, where this derivative is elaborated based on the computed approximations of the Pareto frontier. As mentioned before, the optimization of the scalarized vector optimization problem, can also be understood, as finding the intersection of of line L–being defined as $L := \{(f_1, f_2)|\text{const.} = \kappa f_1 + (1-\kappa)f_2\}$ for a given objective weight κ–with the boundary curve C on the region of feasible design criteria $\mathcal{Y}$. Again, the Pareto frontier is evidently a subset of this boundary $\partial\mathcal{Y}$. This abstract interpretation is illustrated in the following figure, where the line L is shifted until it touches the boundary $\partial\mathcal{Y}$. Analytically, one can derive, that at the optimum or geometrically speaking at the intersection of L and C, the derivative $\frac{\partial f_2}{\partial f_1}$ of the Pareto frontier is equal to the one defined by the line L. This is because they are tangent (minimization) at this point. Thus the derivative can be expressed via,

$$\frac{\partial f_2}{\partial f_1} = \frac{\kappa}{\kappa - 1} \tag{6.18}$$

Obviously, this though only works for the convex hull of $\partial\mathcal{Y}$. Moreover, it will be shown in section 9.2.2, by following a different derivation of this partial derivative, that this statement holds. However, the application within industrial problems revealed, that computing the slope of the Pareto frontier via equation (6.18) is susceptible to small numerical deviations in the used objective weights κ and thus may yield derivative information being correct in direction but displaying considerable large errors in magnitude. For this reason, an alternative approach will be derived and applied, being less sensitive to numerical imperfections and being in that consequence more robust and reliable in practice.

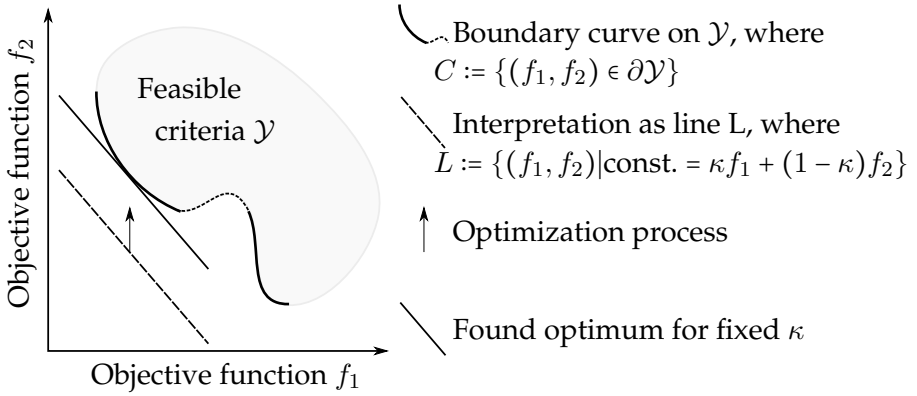

Figure 6.6.: Exploiting the line interpretation for deriving the sensitivity at a given point of the Pareto frontier Ω_P

6.3. General aspects of composite optimization

This section addresses all gained insights particularly associated with the structural design optimization of composites. In spite of this, these insights may also apply for further fields and applications of multi-criteria optimizations as well.

6.3.1. Possible design conflicts in composite optimization

The afore lead discussions mainly focused on vector optimizations, i.e., the simultaneous optimization of multiple criteria, which typically emerge in the design process. The focal point of the discussion was the involved theory and mathematical fundamentals in terms of solving, post-processing, stating optimality et cetera; yet the question how these most-likely conflicting design goals determining the optimization criteria do form, remained unanswered. Figure 6.7 provides the most prominent fields in composite design, possibly yielding those conflicting optimization criteria. So obviously, the ecological perspective can point into directions being opposed to the economical one, when for instance the decision on a certain matrix material shall be made. Or, as being more related to this thesis, the technical mindset, which may mainly focuses on technical feasibility and production-wise realization of the structure. On the contrary, the mechanical viewpoint observes structural efficient by designing as light as possible. This can, however, bring forth issues in producibility and associated manufacturing cost, which in that consequence translates to designing conflicts with the technical and economical perspective towards optimal composite design. Within this thesis, several multi-criteria optimization tasks will be posed and solved, thereby illustrating how to capture relevant aspects forming the distinct objectives and then solving methodologies facilitating the efficient treatment of

those design tasks. Obviously, a profound framework for dissolving those conflicts in optimal design of composites can unleash most of the light weight potential of composites.

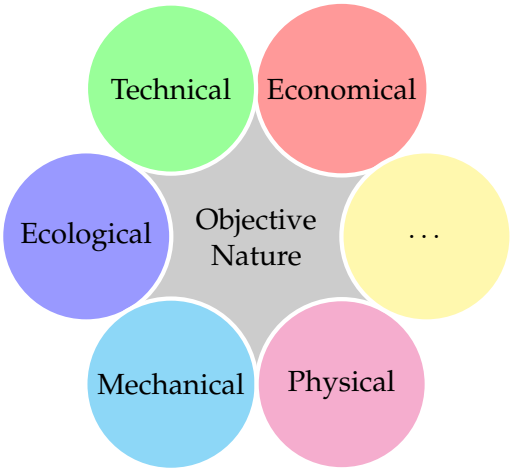

Figure 6.7.: Possible design goals in structural design optimization

6.3.2. Pecularities of gradient-based composite optimization

Multi-modality and the developed global search strategy

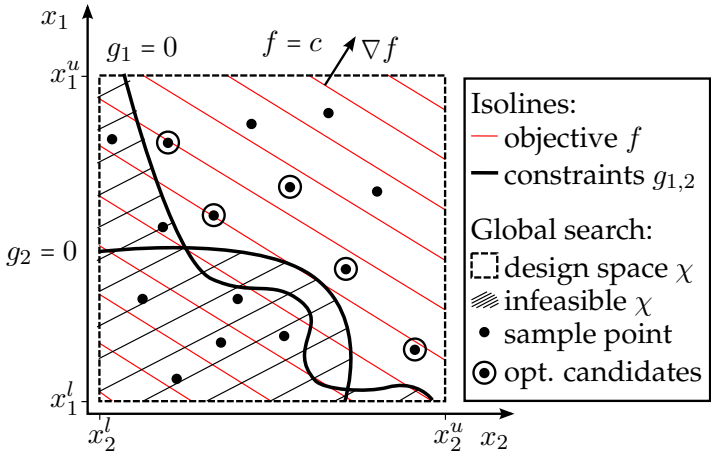

Figure 6.8.: Illustration of the global search strategy

The differentiation between local and global optima has already been introduced in section 2.2, where the optimality was in light of the discussion (see figure 2.1, where ①represents a local and ③a global optimum). Later, the system equations in tandem with the gradient-based optimization strategy have been identified to possibly lead to local optimization results, in case the underlying optimization responses are non-convex with respect to the design variables. This can for instance be the case for strongly non-linear or oscillating system equations. In the subsequent chapter 3, composite have been introduced. Since the mechanical description of those determines the underlying system equations, they are of particular interest. It has further been show in section 3.1, how the ply-wise transformation of the stiffness tensors $\underline{Q}$ to $\underline{\bar{Q}}$ introduced a trigonometric dependency on the orientation of the plies, e.g. $\sin(\theta)^4$ (see equation (3.2)). Obviously, this may lead to a pronounced non-convexity of an optimization response with respect to the orientation θ, once the response is to some extend characterized by the composites stiffness, e.g. maximal allowable failure index of 0.9:

$g(\theta) = \mathcal{FI}(\theta) - 0.9$. Figure 6.8 depicts the same design as in figure 2.1, but in addition to the isolines of the objectives in red and constraints in bold black lines, the side constraint–hence, the bounds x_i^l and x_i^u on the design variables–are given as well (dashed black box). As can be comprehend, the feasible design space is basically situated in the upper-right half of the design space.

Side example: Post-processing of the vector optimization

In the following, the post-processing as discussed earlier is carried out for the posed and solved optimization problem (6.4). At first, the first oder optimality $\mathcal{O}$ as introduced via equation (6.14) is plotted. It can be comprehended by the help of the following figure, that optimality can be stated for each derived solution with ease.

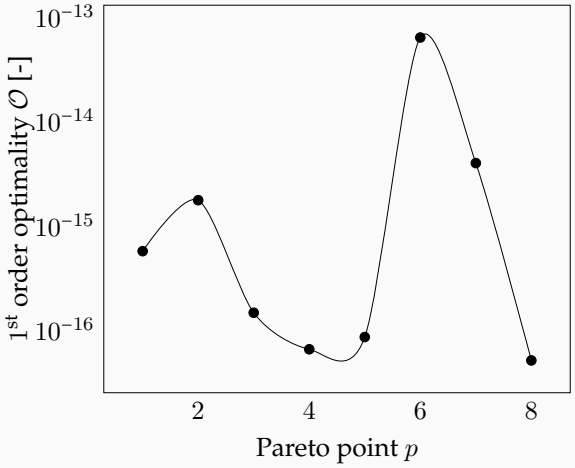

Next, the utility u as defined with equation (6.15) is given as well. As can be seen in the following plot, Pareto efficient solution four has the greatest utility. However, it shall also be noticed that the utility values are all rather small indicating that the Pareto frontier itself has a rather flat convexity, rendering each solution a reasonable compromise.

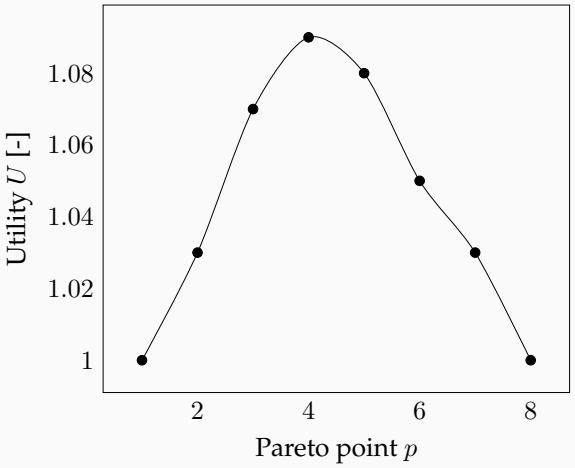

As afore mentioned, the issue of converging to a local optimum can arise, once gradient-based optimization strategies are chosen, which, by the way, will be the choice of strategy for multiple reasons in this thesis. A strategy mitigating this drawback of multi-modality to some extend, herein referred to as *global search strategy*, is introduced next. First, sample points are generated via a Latin Hypercube

Sampling (see section 2.5.4) over the whole design space. Thereafter, the optimization responses, i.e. objective f and inequality constraints $\vec{g}$, are being evaluated for each sample points. Then, the thereby obtained results are ranked and sorted, such that infeasible solutions are highly penalized and sample points are arranged in ascending order starting from the lowest feasible objective function value. Based on this order, a small subset–the optimization candidates with the lowest objective function value, while still being feasible–is chosen to be used as starting points for the subsequent optimizations. Once each optimization run has converged, they are post-processed collectively, whereby additional insight into the optimization task is provided by the evaluation of the scatter of optimal objective function values, scatter in the optima et cetera. This global search strategy is also visualized in figure 6.8, where the sample points are given by the five-teen bullets •, being distributed over the whole design space χ. As further can be seen, the five most promising candidates–thus the ones being feasible $g_i \leq 0$ and evincing the lowest objective function values f–are selected and highlighted by a surrounded circle $\odot$. Despite this additional sampling, requiring additional function evaluations, this strategy proved itself to be highly computationally efficient. This is because of multiple reasons. First of all, the number of sample points is rather small. Secondly, the optimizations themselves not only require less function evaluations due to the efficient sampling, but further are already efficient in their-selves, since gradient information was accessible and used in each and every design. Last but not least, this strategy also enriched the understanding of the composite optimization tasks, by exposing more of the complex design spaces and supplying additional information about the scatter of $\vec{f}$ and $\vec{x}$, thereby allowing some sort of inference on the level of multi-modality of the design task.

Discrete variables

Stating optimization tasks in composite design often yields a special sub-class of optimization problems, the so-called mixed integer nonlinear problems as discrete or integer design variables are present. Examples for those variable types are number of plies, choice of fiber, number of bobbins in braiding and alike. For coping with those class of problems while still exploiting gradient information, Schatz et al. (2014) developed a novel algorithm: APSIS (**A**lgorithm-based **P**roperty **S**election **I**ncluding **S**izing). This algorithm was inspired by Bendsœand Sigmund (1999), where various material interpolation are discussed, Ashby (2011), who discusses concepts for material selection and Stegmann and Lund (2004), who relaxed integer variables in Topology optimization. The foundation for this, was set by the work of Ehrmann (2013), where the first outline of APSIS was defined. Adam (2014) successfully deepened the understanding and added value to the engineering examples. Finally, Eiperle (2014) showed the numerical performance by studying academic examples as well as engineering examples and moreover added a new discrete variable type, the beam's profile shape, i.e. square, I-beam et cetera.

Zero objective function sensitivities

An possible issue also being associated with composite optimization problems, is the presence of the zero design sensitivities. These sensitivities can for instance arise, once the mass of a composite structure m shall be minimized, which is most frequently the case, and in addition to that, ply orientations θ_i are a subset of the design variables $\vec{x}$. Clearly, the mass is not affected by a change in the orientation of a ply and consequently $\frac{\partial m}{\partial \theta_i} \stackrel{!}{=} 0$. In case, gradient-based optimization approaches are used and the response displaying zero design sensitivities is set as an objective, this may lead to convergence issues, where the algorithms may need more iterations and, thus, more function evaluations. This has been observed in several composite optimizations, e.g. in the work of Köhler (2014). This will also be discussed later in section 8.2.1, where the optimization of the prepreg laminated A-pillar is discussed. To underpin this, a survey has also been made for the side example, the optimization of the pipeline and will be given next.

Side example: Studying zero design sensitivities

To illuminate how zero design sensitivities can negatively affect the condition of the optimization problem, the posed pipeline optimization (see (6.4)) has been optimized twice, once minimizing the mass of the pipeline m and thereafter, minimizing the compliance of the structure K_b, whereby the first objective includes zero design sensitivities. Three different algorithms, SLSQP, NLPQLP and CONMIN have been used.
The following bar plot illustrates the outcome of this, where the difference in function evaluations between both runs $\Delta\text{Eval} = (\text{Eval}_m - \text{Eval}_{K_b})/\text{Eval}_m$ is used as the measure. Thus, $\Delta\text{Eval} = 49$ basically means, that minimizing on the objective mass leads to an average increase in function evaluations of 49%. So, considering all three studies, one can see, that the number of function evaluations is considerably higher for the mass optimization using SLSQP or NLPQLP and a bit less for CONMIN. This reflects the made experiences quite well.

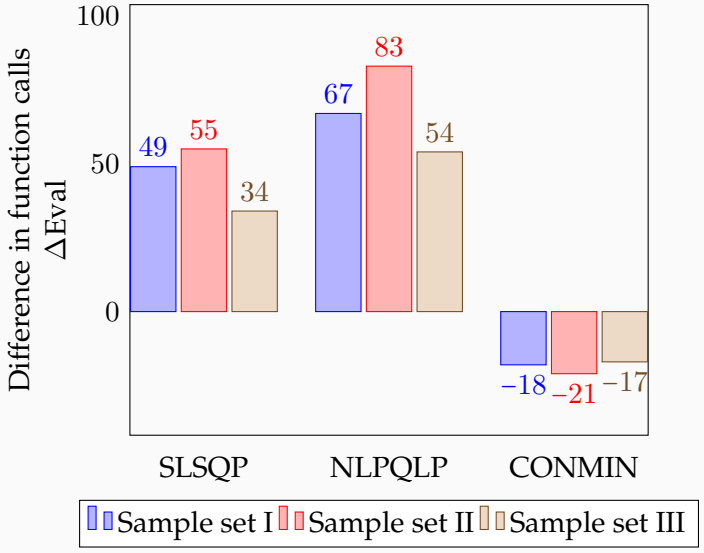

7 | Academic demonstration examples

The interaction of structural efficiency, manufacturing effort and complex material models is especially of interest in the following chapters. For that purpose, several numerical demonstration examples will be defined, with which these interactions will be highlighted and studied for two given manufacturing techniques: prepreg laying and braiding. The used demonstration examples are adopted from practice. But before the two large structural examples–the A-pillar and propeller structure–some academic examples shall be given first. The fist example is intended to give an insight into the general gradient-based multi-criteria optimization. This example is then followed by an academic structure, a cantilever beam, for which the simultaneous gradient-based optimization of structural efficiency and technical effort, particularly, the effort originating from the composite manufacturing, is being demonstrated.

Contents

7.1. Analytical test example

This first analytical example is pointing towards the issue of approaching multi-criteria optimization problems with gradient-based algorithms. The use of gradient-based algorithms is desirable in this thesis, because the structural design problems addressed within the following two chapters are involving not only sophisticated finite element analyses, but also a great number of design variables. Next, the analytical test example is defined first. Thereafter, the optimization problem is transformed such that the set of optimal solutions–thus the set of Pareto efficient criteria of the multi-objective optimization problem–can iteratively be obtained. Then, the multi-criteria optimization problem is solved, where the solution process is in the focus of the ensuing discussion. Lastly, the gained insights are briefly discussed.

7.1.1. Problem definition

With the following set of equations (7.1) the analytical multi-criteria optimization problem is being defined.

$$\begin{aligned} \underset{x\in\chi}{\text{minimize}} \quad & f_i(x_j), && i \in \{1,2\},\ j \in \{1,2\} \\ \text{subject to} \quad & g_l(x_j) \leq 0, && l \in \{1,2,3\} \\ \text{with} \quad & \chi = \{x_j \in \mathbb{R}^{n_{\mathrm{DV}}} : 0. \leq x_j \leq 5.\}, \\ \text{where} \quad & \end{aligned} \tag{7.1}$$

$$\vec{f}: \quad \begin{aligned} f_1 &= x_1 \\ f_2 &= x_2 \end{aligned} \qquad \vec{g}: \quad \begin{aligned} g_1 &= (x_1-5)^2 + (x_2-5)^2 - 4^2 \leq 0 \\ g_2 &= x_1 - 4 \leq 0 \\ g_3 &= x_2 - 4 \leq 0 \end{aligned}$$

As given therewith, the optimization task is, to find values for the two design variables x_1 and x_2 such that the objective function vector composed of f_1 and f_2 is minimal, while all three inequality constraints g_1, g_2 and g_3 are fulfilled. Studying this problem reveals, that there is in general not only one single optimal solution, but rather a set of optima instead, the Pareto frontier as given with,

$$\Omega_P := \min_x \{\vec{f}(\vec{x}) | \vec{g}(\vec{x}) \leq \vec{0}\} \tag{7.2}$$

In the following, an approach for computing discrete Pareto optimal points $\vec{f}^p$ approximating the whole Pareto frontier Ω_P, being composed of infinitely many Pareto efficient solutions, is being presented. Clearly, the challenge in hand is to find this set of Pareto efficient solutions, or a subset representing a good approximation of the whole set, such that it uncovers most of the Pareto frontier's course while requiring as few optimization runs as possible.

7.1.2. Condensing the optimization problem

In the prologue part, more specifically in section 6.2, a gradient-based approach for solving multi-objective optimization problems has been introduced. This approach is now applied, such that the original vector optimization problem stated by the equation set (7.1) can be condensed to

$$\begin{aligned} \underset{x,\kappa}{\text{minimize}} \quad & f_\kappa = \kappa x_1 + (1-\kappa)x_2, \\ \text{subject to} \quad & g_{1,2,3} \leq 0, \\ & g_{\mathrm{BS}} \leq 0, \\ \text{and} \quad & h_\gamma = \gamma^2, \\ \text{with} \quad & \vec{x} \in \chi \text{ and } \kappa \in [0, ..., 1] \end{aligned} \tag{7.3}$$

As already given in section 6.2, the two additional constraints g_{BS} and h_γ are defined as follows,

$$\begin{aligned} g_{\mathrm{BS}} &:= \|(\vec{f}^{p-1} - \vec{f}^{p-2})(\vec{f}(\vec{x}) - \vec{f}^{p-1})\|_{\mathrm{L2}} \leq 0, \\ h_\gamma &:= \|\vec{f}(\vec{x}) - \vec{f}^{p-1}\|_{\mathrm{L2}}^2 = \gamma^2. \end{aligned} \tag{7.4}$$

The following figure 7.1 recapitulates the introduction of the approach in brief, by illustrating the equidistant constraint h_γ in blue and the back-stepping constraint g_{BS} in red.

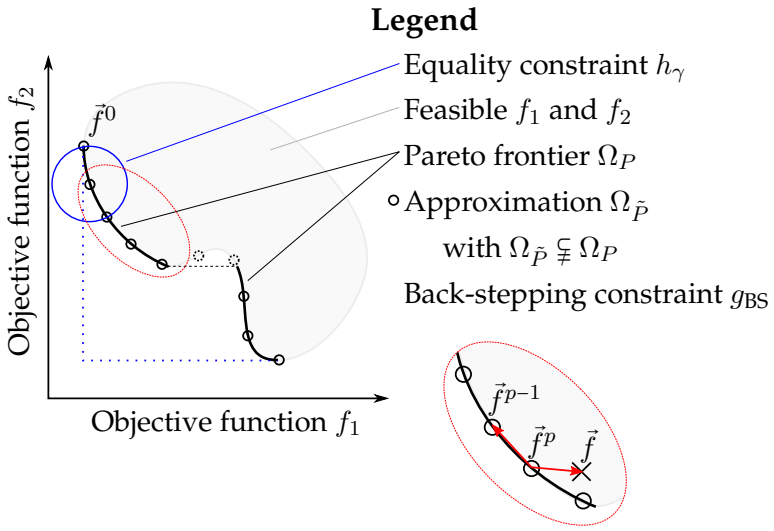

Figure 7.1.: Sketch of the vector optimization approach

7.1.3. Pareto efficient criteria

For this analytical vector optimization problem the set of Pareto optimal solutions, can be given analytically with

$$\Omega_P = \Omega_E := \left\{ (f_1 \ , \ f_2) = \left(t \ , \ 5 - \sqrt{16 - (t-5)^2} \right) \ \middle| \ t \in \mathbb{R} : 5 - \sqrt{15} \leq t \leq 4 \right\}, \tag{7.5}$$

where Ω_E denotes the set of Pareto efficient or optimal solutions, Ω_P the Pareto frontier and t the parameter defining the frontier. For this example, the whole Pareto frontier is Pareto efficient, hence, there are no local optima due to a non-convexity of the frontier. Next, the numerical solution is presented by solving the condensed optimization problem (7.3) for eight Pareto optima n_P, hence, eight optimizations needed to be conducted sequentially. Figure 7.2 depicts this numerical approximation of the frontier, where the red points highlight Pareto optimal solutions, the green line represents the distance between the extremal solutions, i.e. $\left\| \vec{f}|_{\kappa=0} - \vec{f}|_{\kappa=1} \right\|_2$ the blue circles with radius γ visualize the equality constraint h_γ and finally the black lines the approximation of the Pareto frontier. Besides, the discrete scatter of points and the resulting multi-linear frontier representation, makes it comprehendable why the numerical vector optimization utilizing gradient-based methods has to be regarded as an approximation $\Omega_{\tilde{P}}$ or at least as a subset of all Pareto optimal solutions as given here with Ω_P. In addition to these directly derived results, two interesting points–utopia and nadir design point–are given in figure 7.2 as well. Combining the best objective function values of both extremal solutions leads to utopia, but as the name already reflects, that this design is clearly fictitious in most cases. The nadir is defined vice versa and thus theoretically represents the worst fictitious optima.

7.1.4. Brief summary on the general vector optimization

Before stepping into the discussion, a comparison of the computed Pareto efficient solutions $(\tilde{f}_1, \tilde{f}_2)$, which approximate the analytical Pareto frontier given by Ω_P in equation (7.5) will be made, by evaluating the following error measure,

$$\Delta \vec{f} := \frac{f_2(\tilde{f}_1) - \tilde{f}_2}{f_2(\tilde{f}_1)}, \tag{7.6}$$

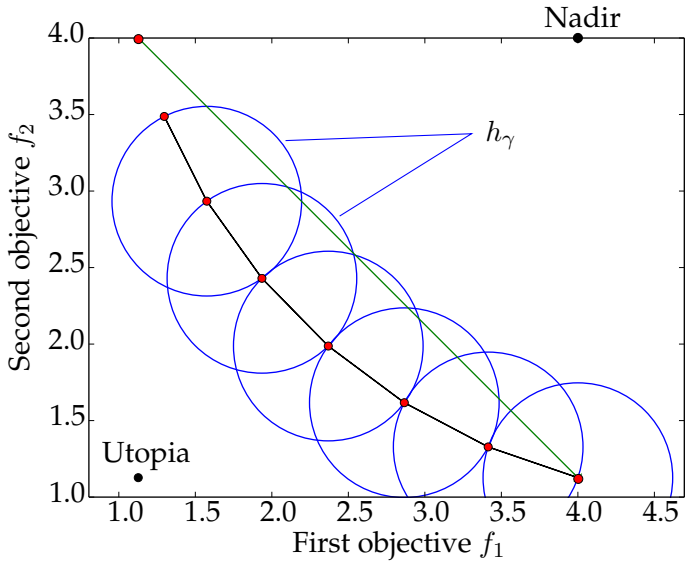

Figure 7.2.: Solution of the analytical vector optimization problem

where f_2 is determined by the analytical solution. As can be comprehended by studying the optimization result as given with figure 7.2 in tandem with the errors listed in table 7.1, the gradient-based vector optimization scheme is capable of computing Pareto frontier approximations with high quality, i.e. equidistant, and of high accuracy. Ultimately, the approach can be identified to be advantageous for the following reasons. First and foremost, the mathematical frame ensures an equidistant approximation of the Pareto frontier, where the number of support points of the frontier can be given afore by n_P as well. Secondly, the sensitivities–being inherently computed within the gradient-based algorithms–can be used for profoundly inquiring optimality via the KKT conditions (see equation set (2.3)). And lastly, the approach did prove to be numerically efficient in terms of number of function evaluations compared to zero-order algorithms. This superiority in efficiency even magnifies for large design space and efficient design sensitivity analyses. This becomes more evident after comparing the performance of this approach with the one of zero-order algorithms. Some of these results are given in appendix section A.4, where the genetic algorithm NSGA-II needed more function evaluations, while still not being able to resolve the Pareto frontier in good quality and in addition to that yielding sub-optimal solutions, since dominated by the analytical solutions, which is not the case for the ones obtained by the implemented approach (see table 7.1).

Table 7.1.: Listing of the errors $\Delta\vec{f}$ for each Pareto efficient solution p

p	0	1	2	3	4	5	6	7
$\Delta\vec{f}$	$-1.2E-13$	$1.9E-08$	$1.3E-09$	$1.8E-10$	$7.1E-11$	$2.9E-14$	$1.2E-11$	$-1.2E-13$

7.2. Cantilever beam

Now, an academic demonstration example shall further underpin the general multi-criteria optimization approach. In contrast to the analytical example, the technical significance will drastically be lifted, since structural mechanics will be considered along side with manufacturing aspects. However, the core discussion of how the developed manufacturing effort model enriches the optimization process will be shifted into the two subsequent chapters.

7.2.1. Model definition

The structural design problem is given by the following figure 7.3. As can be seen there, a beam of square shape is clamped on one side and loaded with three different loads on the opposite side. Two of the loads, F_{LC1} and F_{LC2}, are determined by bending forces causing the deflections u_{LC1} and u_{LC2} respectively. The torsional moment M_{LC3} defines the last load, twisting the beam by ϑ_{LC3}. Height H, width B, edge radius r and the fiber architecture, i.e. φ, of the square beam are fully parametrized and will thus later serve as design variables. Priorly, in chapter 4 and 5, the manufacturing effort model and the involved multi-scale homogenization approach have been introduced. Both models are now combined to one optimization model as illustrated in figure 4.8.

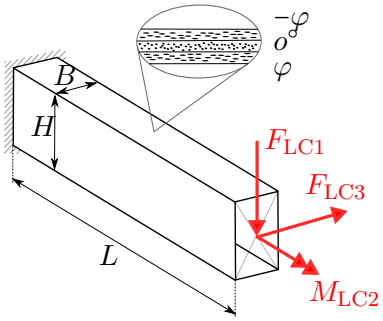

Figure 7.3.: Schematic sketch of the beam problem

7.2.2. Setting up the optimization problem

With the following equation set (7.7), the optimization task is defined. As stated, H, B, r and φ of the square beam form the design variable vector $\vec{x}$. The mass m and associated manufacturing effort e determine the objective vector $\vec{f}$. Imposing certain stiffness requirements and requiring no failure, results in the constraint vector $\vec{g}$.

$$\begin{aligned} \underset{x\in\chi}{\text{minimize}} \quad & f_i(x_j), && i \in \{1,2\},\ j \in \{1,\dots,4\} \\ \text{subject to} \quad & g_l(x_j) \le 0, && l \in \{1,\dots,3n_{\mathrm{sec}}+3\} \\ \text{with} \quad & \chi = \{x_j \in \mathbb{R}^{n_{\mathrm{DV}}} : x_j^l \le x_j \le x_j^u\}, \\ \text{where} \quad & \end{aligned} \tag{7.7}$$

$$\vec{x}: \begin{aligned} x_1 &= H \\ x_2 &= B \\ x_3 &= r \\ x_4 &= \varphi \end{aligned} \qquad \vec{f}: \begin{aligned} f_1 &= m \\ f_2 &= e \end{aligned} \qquad \vec{g}: \begin{aligned} g_1 &= \tfrac{u_{\mathrm{LC1}}}{u_{\mathrm{max},1}} - 1 \le 0 \\ g_{k+1} &= \mathcal{FI}_{\mathrm{LC1}} - 0.9 \le 0 \quad k = 1,\dots,n_{\mathrm{sec}} \\ g_{n_{\mathrm{sec}}+2} &= \tfrac{u_{\mathrm{LC2}}}{u_{\mathrm{max},2}} - 1 \le 0 \\ g_{k+n_{\mathrm{sec}}+2} &= \mathcal{FI}_{\mathrm{LC2}} - 0.9 \le 0 \quad k = 1,\dots,n_{\mathrm{sec}} \\ g_{2n_{\mathrm{sec}}+3} &= \tfrac{\vartheta_{\mathrm{LC3}}}{\vartheta_{\mathrm{max},3}} - 1 \le 0 \\ g_{k+2n_{\mathrm{sec}}+3} &= \mathcal{FI}_{\mathrm{LC3}} - 0.9 \le 0 \quad k = 1,\dots,n_{\mathrm{sec}} \end{aligned}$$

This optimization task is then iteratively solved, by solving the following condensed–or also called scalarized–optimization problem (7.8). Again, the scalarized optimization problem (7.8) is solved n_P-times, where n_P is the number of Pareto points for the approximation $\Omega_{\tilde{P}}$ of the whole Pareto frontier Ω_P. g_{BS} and h_γ further ensure a proper equidistant arrangement of those points. See equation set (6.11) and the illustrations in section 7.1 for more information.

$$\begin{aligned} \underset{x,\kappa}{\text{minimize}} \quad & f_\kappa = \kappa m + (1-\kappa)e \\ \text{subject to} \quad & g_{1,\dots,3(n_{\text{sec}}+1)} \leq 0, \\ & g_{\text{BS}} \leq 0, \\ \text{and} \quad & h_\gamma = \gamma^2, \\ \text{with} \quad & \vec{x} \in \chi \text{ and } \kappa \in [0,\dots,1] \end{aligned} \tag{7.8}$$

7.2.3. Pareto frontier of the cantilever beam

With figure 7.4 the solution of the original vector optimization problem (7.7) is given. As mentioned earlier, the Pareto frontier has been iteratively been solved by solving the problem in scalarized form as stated (7.8) for $n_P = 7$ times. In figure 7.4, the green line represents the direct connection between the extrema, minimal effort and minimal mass and thus highlights the non-convexity of the problem once being contrasted with the computed n_P Pareto optimal solutions in red.

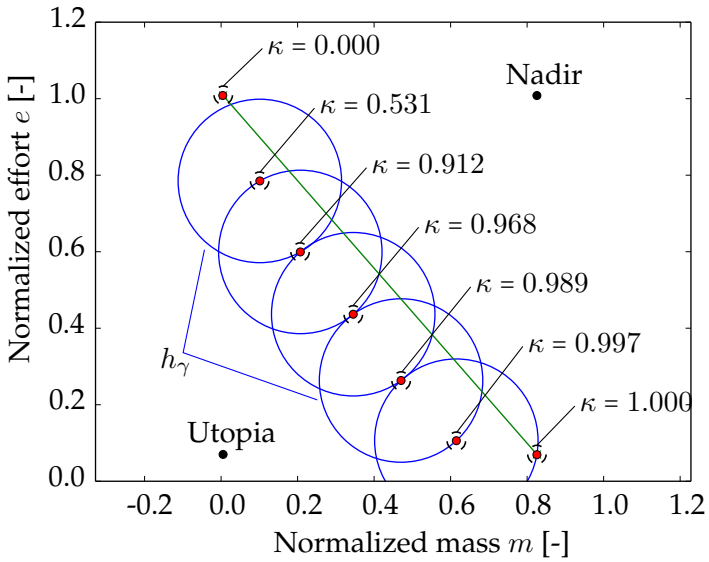

Figure 7.4.: Approximated Pareto frontier of the vector cantilever optimization

Moreover, the objective function weights κ are here given in figure 7.4 as well, so as to underpin the generality of the approach, since those weights are not distributed linearly, but instead rather grow exponentially. This can be comprehended by considering figure 7.5b, where those objective function weights κ are plotted over the number of Pareto point, thus $p = [1, \dots, n_P]$. As can be seen there, they are far from being linear as highlighted by the dashed black line. Last but not least, the approximated Pareto frontier is given with figure 7.5a. As a side mark, due to the fact, that a Pareto frontier actually did form, it can be stated at this point, that manufacturing effort and structural efficiency in terms of mass can be competitive. Later it will be shown, that this is the case for most structural design problems. For this case, the aspects influencing the outcome of the manufacturing effort model the most are:

- $\frac{H}{B} \to 5.0$: High aspect ratio, thus fiber slipage, breakage or braid opening
- $\varphi \to 0.0°$: Take-up speed to infinity
- $w^{(b)} \to 4.0\ \text{mm}$: Braid opening
- $r \to 0.0\ \text{mm}$: Fiber breakage at sharp corners

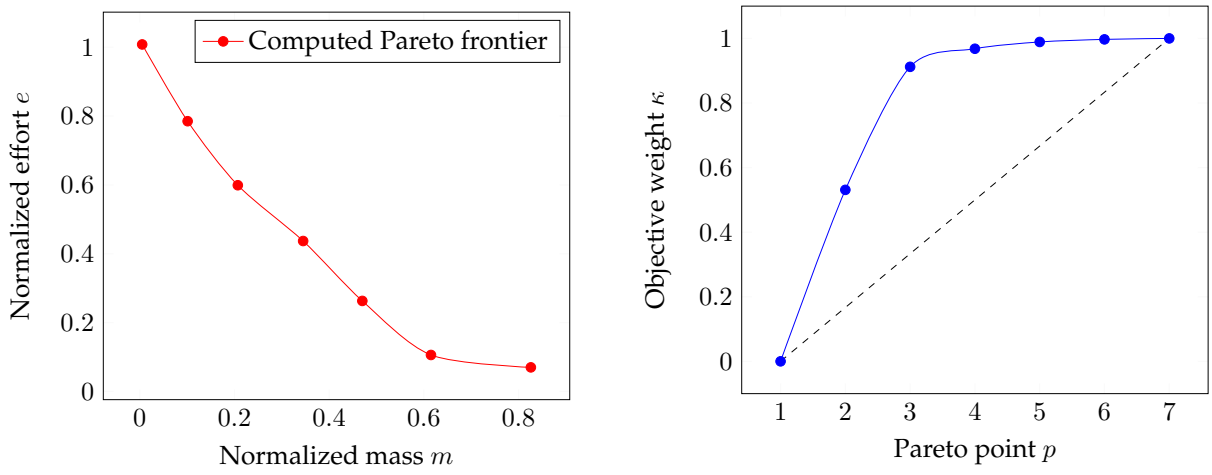

(a) Approximation of Pareto frontier

(b) Plot of objective weights κ

Figure 7.5.: Approxmiated Pareto frontier and objective weight plot for cantilever beam example

7.2.4. Brief summary on multidisciplinary vector optimization

Even so, the example is conceivable simple from a structural optimization point of view, the multi-criteria optimization task is rather challenging to be solve gradient-based. This is mainly because of the fact that simple scalarizing the multi-criteria optimization task via $f = .5e + .5m$ would lead to a Pareto optimal solution being far from being an optimal compromise. However, the outlined approach, where the objective weight κ is also being considered as a decision variable yields an equidistant and in that sense accurate approximation of the whole Pareto frontier. By this approach, an optimal compromise–here, minimal distance to utopia, being the combination of the both minima–could be identified to be around $\kappa = 0.968$. This weight is actually quite far away from any intuition, which would normally yield 0.5.

Morever, the discussed multi-criteria optimization problem included structural and technical responses, which did display a pronounced competitiveness. The investigation of this will be further deepened by studying industry relevant design tasks, an A-pillar and a propeller structure.

8 Optimizing an automotive A-pillar

In this section, an A-pillar of a roadster shall serve as a demonstrator. For this automotive structure the simultaneous optimization of structural and technical aspects, namely, the associated manufacturing efforts will be shown. The two considered manufacturing techniques are: braiding and prepreg laying. Manufacturing effort will thereby be modeled via the introduced soft computing approach, hence, by capturing and emulating expert knowledge regarding those two manufacturing techniques. With figure 8.1, the A-pillar as situated in the convertible *Roadster R1* produced by Roding is being illustrated. The picture on the left is taken from the official Roding homepage. On the right, the A-pillar structure itself is depicted. In the following subsections, the optimization problem is first stated, then solved for the case of prepreg laying and braiding as the manufacturing technique. Finally a brief summary is given for this automotive optimization example.

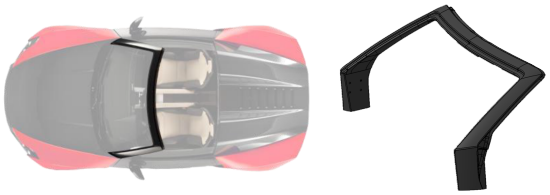

Figure 8.1.: The installation circumstances of the investigated A-pillar
Left picture: ©Roding Automobile GmbH

> "Saving even a few pounds of a vehicle's weight could mean that they would also go faster and consume less fuel. Reducing weight involves reducing materials, which in turn, means reducing cost as well!"
>
> Henry Ford (1863 – 1947)

Contents

8.1. Problem definition

Concerning the designing of an automotive A-pillar, multiple disciplines do imprint restrictions and requirements onto the designing process. However, in this thesis, the design-determining requirements are to be derived from basically two disciplines: driving dynamics and crash-worthiness. By doing so, the purview in terms of technical detailing and maturity may be inchoate. Nevertheless, the study of influences and interactions with the associated manufacturing effort for both manufacturing techniques–which is in any case the main focus of this thesis–is not affected.

8.1.1. Relevant load cases for the A-pillar

The first load case is determined by the most critical crash load case for the A-pillar structure, the roof crush occurring once the vehicle overturns. Figure 8.2a illustrates the laboratory test set up as for instance given with DOT (2006) according to the *Federal Motor Vehicle Safety Standard* FMVSS 216a. Based on this standard, the roof crush force F_{LC1} is defined to be one and a half times as big as the vehicle's weight force, thus, $F_{\mathrm{LC1}} = 1.5mg \approx 15.5\mathrm{kN}$ for the considered case. After the load is being applied the structure shall retain structural integrity and may not deflect more than $u_{\mathrm{LC1},max} = 127\mathrm{mm}$.

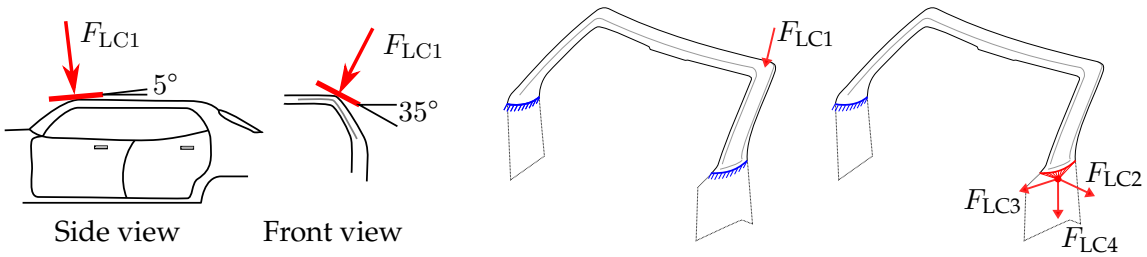

(a) Roof crush test set-up (b) Considered load cases

Figure 8.2.: Laboratory roof crush resistance test and load cases for the A-pillar design task

For ensuring a high level driving dynamic performance of the roadster, the car body needs display a certain stiffness for a bending and torsional load. For that reason, the three load cases characterized by F_{LC2}, F_{LC3} and F_{LC4} are defined. They mainly probe the stiffness in three different directions, by computing the displacement for unit forces, such that those stiffness responses can be used and regarded throughout the optimization process. Figure 8.2b summarized all four considered load cases in one figure.

8.1.2. Modeling the A-pillar via finite elements

At the beginning, the A-pillar has been fully modeled using a MatLab routine defining the mesh in a direct fashion. In the thesis of Jörg (2014), the general approach of directly generating the mesh for tubular structures is presented and discussed at length. Exploiting this approach of defining the model directly via nodal coordinates and element connectivity is especially advantageous in terms of analytical sensitivities. This is mainly because they are accessible in a straight forward fashion, in case NASTRAN is being used as the FEA. This has for instance, successfully be done by Köhler (2014). However, considering the fact, that geometric information such as profile radii and circumferences are needed as a subset of the parameter input vector for the manufacturing effort model (as already discussed and illustrated in figure 4.9: $\vec{y}_{\mathrm{MEM}}$) leads to the idea of actually modeling and parameterizing the A-pillar based on geometric information. This has been initiated by the thesis of Rödl (2014), where the A-pillar is geometrically parametrized utilizing Abaqus CAE with the help of multiple scripts written in Python. In the following this A-pillar model including its parametrization

will be presented. Figure 8.3 not only provides an overview by illustrating different modeling levels, for instance the surface model including the partitions or the line model, where the different profile types are already sketched. Figure 8.3 further shows, how the final FE model is actually derived; namely, starting from profiles, the surfaces are defined with the help of the line model. After they are partitioned, a neat mesh can be generated. In addition to the clear decomposition of the geometry, enabling a robust and euclidean meshing, these partitions facilitate a variable definition of braiding sections and, in that consequence, braiding angle. The extrude axis is defined via supporting points and radii, which are taken from the initial geometry given by Roding. Due to strong geometric restrictions imposed from other disciplines such as design or other parts such as the door, the only variable parameter is considered to be the curvature R at the tip corner of the A-pillar. This is being illustrated in figure 8.4a, where the extrude axis is given in blue. Moreover, a coordinate s, which basically follows the extrude axis, is defined, witch which the braid angle will later be determined if braiding is chosen as the manufacturing technique.

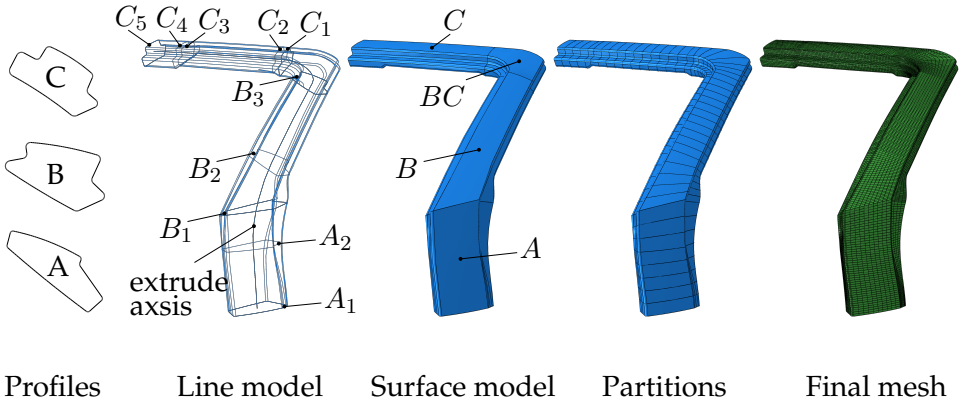

Figure 8.3.: Different parametrization levels for the A-pillar model by Rödl (2014)

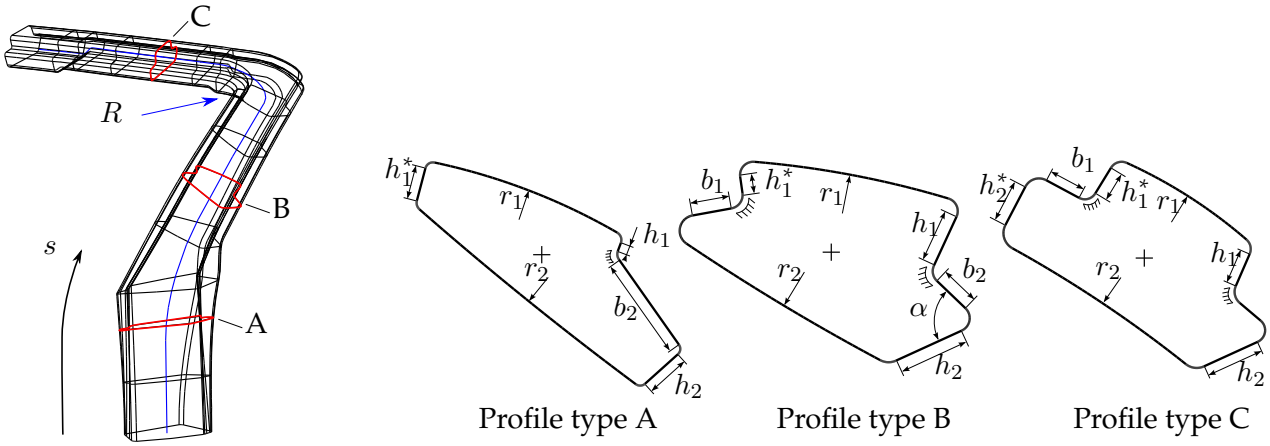

(a) Extrusion axis

(b) Profile types by Rödl (2014)

Figure 8.4.: Extrusion axis and associated profile types A, B and C of the A-pillar

As also shown in figure 8.4a, the profiles vary along the extrude axis. To account that, three different profile types, A, B and C have been defined. They mainly differ in the base shape shape, hence, radii, the rounding off at the corners and number of corners (A six, B seven and C nine corners). All three different profile types are given with figure 8.4b. By this parametrization, the generation of basis vectors was made possible with which analytical design sensitivities can be computed. In the two following subsections, the material parametrization and further peculiarities for the two different manufacturing techniques–braiding and prepreg laying–will be discussed. But for the sake

of completeness, the sequence of analyses and available responses shall be presented. As given in table 8.1, first the roof crush is simulated by imposing the crush force F_{LC1} onto the tip of the A-pillar (see figure 8.2b). Responses for this load case are failure indices for all composite layers and intrusion at tip. This step is followed by a set load cases, which probe the stiffness of the A-pillar, hence, the unit forces from F_{LC2} to F_{LC4} trial the stiffnesses ranging from K_{xx} to K_{zz}.

Table 8.1.: The analysis steps as implemented in the parametrized model

Step	Load case	Loading	Remarks
(Buckling)	-	F_{LC1}	Optional step
Roof crush	LC1	F_{LC1}	Evaluate failure and deflection
Static stiffness	LC2	F_{LC2}	Probing stiffness K_{xx}
Static stiffness	LC3	F_{LC3}	Probing stiffness K_{yy}
Static stiffness	LC4	F_{LC4}	Probing stiffness K_{zz}

8.1.3. Material modeling in case of braiding

Now, the FEM of the braided A-pillar is being discussed. Since, both FEM–prepreg layered and braided–mainly differ in the material model definition and parametrization, the focus shall lie on those two aspects. At first, a variation of the braiding angle $\varphi(s)$ along the extrude axis s (as depicted in figure 8.4a) needs to be enabled, such that this angle distribution can be optimized in the subsequent structural design optimization. Equation (8.1) states how the braiding angle $\varphi(s)$ is defined based on the coordinate s, by taking advantage of several support points i. Each support point i is characterized by an angle φ_i and a coordinate s_i and in-between two, i.e. s_i and s_{i+1}, a linear angle variation is set.

$$\varphi(s) = \varphi_i + \frac{\varphi_{i+1} - \varphi_i}{s_{i+1} - s_i}(s - s_i) \Longleftrightarrow s_i < s \leq s_{i+1}, \qquad i \in \{1, 2, 3, 4\}, \tag{8.1}$$

Through this variation of the braiding angle $\varphi(s)$ multiple braid configuration can be considered. For the sake of further increasing the degrees of freedom for design optimization, the thickness of the braids can be varied and, thus, be optimized as well. This is shown in figure 8.5, where the three braid layer sections $k \in \{1, 2, 3\}$ with their corresponding section thickness t_k is given.

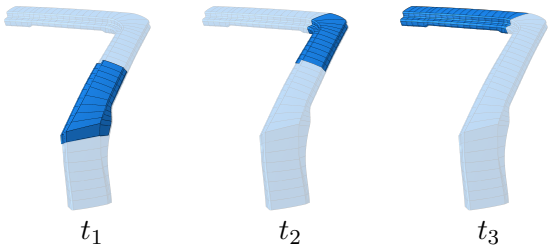

Figure 8.5.: Illustration of the three different braid section regions Rödl (2014)

As mentioned earlier, the stiffness and strength properties of a braided structure are highly dependent on the given fiber architecture in regard of braiding angle, braider yarn width, axial yarn width and many more, since undulations and similar effects have a strong imprint on these properties. To account that, a decoupled homogenization approach based on surrogate modeling (as discussed earlier in chapter 5) has been developed and actually conducted. Now, it will be shown, how this material meta-model can be embedded into the FEA. First the constitutive law will be given, followed by the failure criteria. Both will be discussed for the Abaqus CAE, but it is self-evident, that this

procedure holds in similar form for other tools as well. A general anisotropic elastic material can be defined as follows,

$$\begin{Bmatrix}\sigma_{11}\\ \sigma_{22}\\ \sigma_{12}\end{Bmatrix} = \begin{bmatrix}C_{11} & C_{12} & C_{13}\\ & C_{22} & C_{23}\\ \text{sym} & & D_{1212}\end{bmatrix}\begin{Bmatrix}\varepsilon_{11}\\ \varepsilon_{22}\\ \gamma_{12}\end{Bmatrix}. \tag{8.2}$$

Please note, that in equation (8.2) the in-plane shear γ_{12} is equal to $\gamma_{12} = 2\varepsilon_{12}$ and that it has further been exploited, that the Mindlin-Reissner plate theory, i.e. plane stress, will later be used for describing the A-pillar, being a tubular shell structure. Each component of the stiffness tensor, or matrix in Voigt notation, is defined as given as depicted with the next equation for C_{11},

$$C_{11}(\varphi(s), w^{(b)}(s,\varphi)) = a_5\varphi^2 + a_4\left(w^{(b)}\right)^2 + a_3\varphi w^{(b)} + a_2\varphi + a_1 w^{(b)} + a_0 \tag{8.3}$$

As given with this equation (8.3), the entry C_{11} of the stiffness tensor $\underline{C}$ is approximated via a polynomial regression based on the two parameters braiding angle φ and braider yarn width $w^{(b)}$. Because sensitivities massively accelerate gradient-based optimization runs and gradient-based methods shall mainly be applied herein, available derivatives of each and every response will be computed. For the entry C_{11} of the stiffness tensor, the derivative with respect to φ at $s' = 0.5(s_3 - s_2) + s_2$ can directly be stated to be

$$\begin{aligned}\left.\frac{\mathrm{d}C_{11}}{\mathrm{d}\varphi}\right|_{s'} &= \left.\frac{\partial C_{11}}{\partial\varphi}\right|_{s'} + \left.\frac{\partial C_{11}}{\partial w^{(b)}}\frac{\mathrm{d}w^{(b)}}{\mathrm{d}\varphi}\right|_{s'}\\ &= 2a_5\frac{\varphi_3-\varphi_2}{2} + a_3 w^{(b)}|_{s'} + a_2 + \left(2a_4 w^{(b)}|_{s'} + a_3\frac{\varphi_3-\varphi_2}{2} + a_1\right)\left.\frac{\mathrm{d}w^{(b)}}{\mathrm{d}\varphi}\right|_{s'}.\end{aligned} \tag{8.4}$$

Failure has been considered as based on first ply failure. To implement the computed and approximated failure strength values R_k the following elliptic failure body has been used.

$$\begin{aligned}\mathcal{FI}(\sigma_k, R_k) &= \sqrt{\sum_k\left(\frac{\sigma_k}{R_k}\right)^2}, \qquad k \in \{11, 22, 12, 13, 23\}\\ R_k &= a_{5,k}\varphi^2 + a_{4,k}\left(w^{(b)}\right)^2 + a_{3,k}\varphi w^{(b)} + a_{2,k}\varphi + a_{1,k}w^{(b)} + a_{0,k}\end{aligned} \tag{8.5}$$

As given with (8.5), the strength values R_k are also given via polynomial regressions, where the six coefficients, thus from $a_{0,k}$ to $a_{5,k}$, have been determined via the decoupled homogenization scheme. In that scheme, the meso-cell model has been incrementally loaded in multiple directions until failure according to Puck for the fiber tows or Max Strain for the matrix did occur. With figure 8.6 a visualization of the failure is being given. This shown failure body is computed for a braiding angle φ of twenty degrees. The shape of the elliptical failure body is plausible, since the braid layer can take more load in axial direction than in shear or in transversal direction.

Again, the derivatives can be defined beforehand in the following fashion,

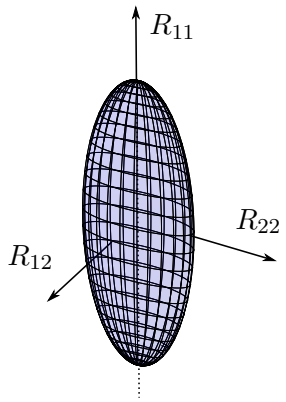

Figure 8.6.: Failure body spanned by the material meta-model for braiding

$$\left.\frac{\mathrm{d}\mathcal{FI}}{\mathrm{d}\varphi}\right|_{s'} = \underbrace{\left.\frac{\partial \mathcal{FI}}{\partial \varphi}\right|_{s'}}_{\text{Zero}} + \sum_k \left(\frac{\partial \mathcal{FI}}{\partial \sigma_k} \underbrace{\left.\frac{\mathrm{d}\sigma_k}{\mathrm{d}\varphi}\right|_{s'}}_{\text{Given by DSA}} + \frac{\partial \mathcal{FI}}{\partial R_k} \underbrace{\left.\frac{\mathrm{d}R_k}{\mathrm{d}\varphi}\right|_{s'}}_{\text{Similar to (8.4)}} \right), \tag{8.6}$$

$$\frac{\partial \mathcal{FI}}{\partial \sigma_k} = \mathcal{FI}^{-1} \frac{\sigma_k}{R_k^2}$$

$$\frac{\partial \mathcal{FI}}{\partial R_k} = -\mathcal{FI}^{-1} \frac{\sigma_k^2}{R_k^3}$$

where DSA is referring to the analytical design sensitivity analysis (see equation (2.14)). The derivatives and implementation of both, the stiffness tensor and strength quantities, have been studied extensively by Rödl (2014). In his work, all sensitivities are implemented and used throughout every optimization.

8.1.4. The prepreg material definition

For the optimization of the A-pillar considering prepreg laying as the manufacturing technique, NASTRAN has been used for the FEA. This has been done for essentially two reasons. First and foremost, it should be shown that the incorporation of soft computing models, especially the manufacturing effort models, can be accomplished for any FEA tool and is in that consequence generally applicable and realizable in a technical environment with moderate to low implementation effort. Secondly, NASTRAN does, as opposed to Abaqus, provide analytical design sensitvities (see equation (2.14)), which overweight the disadvantages of lacking geometrical information in the considered case, since the linked manufacturing effort model fetches all needed inputs directly from raw mesh data. The material is defined to be linear elastic and shows transversal isotropy for each ply. Because of the fact, that undulations are negligible for most prepreg lay-ups–at least within early design phases–a standard material definition provided by the FEA tool NASTRAN is used. The same accounts for the failure criteria, which has been chosen to be the Tsai-Wu criteria. Each material card is defined for a given region or, speaking more precisely, a given element set. Figure 8.7 depicts a possible region definition.

In the master thesis of Köhler (2014), the consideration of discrete variables via APSIS within the structural optimization of the A-pillar is studied comprehensively. An example for discrete variable would be the thickness of plies, which can only be draped in integer steps. Köhler (2014) did shown,

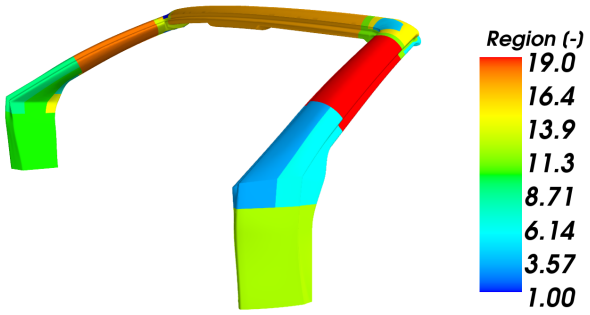

Figure 8.7.: Prepreg regions given in different colors for the A-pillar

that discrete variables can have a certain impact onto the optima, but, however, shall be studied for a reduced set of discrete choices. He therefore concluded, that one shall first conduct fully continuous optimizations, thereafter reduce the number of choices for discrete variables and optimize again using APSIS. Withing the overall scope of this thesis, it is reasonable to conduct all optimizations continuously, while focusing on the incorporation of manufacturing effort and restrictions first. As a final remark, all prepreg optimization results shown later, have been derived based on an A-pillar model in which analytical gradients are exploited. Hence, the following gradients (equation (8.7)) have been computed and passed back by NASTRAN. They namely are, intrusion u_{LC1} and failure index $\mathcal{FI}_{\mathrm{LC1}}$ for the roof crush case and all stiffness responses $K_{\mathrm{xx,\ldots,zz}}$ of load case two to four.

$$\frac{\mathrm{d}u_{\mathrm{LC1}}}{\mathrm{d}x_i} \qquad \frac{\mathrm{d}\mathcal{FI}_{\mathrm{LC1}}}{\mathrm{d}x_i} \qquad \frac{\mathrm{d}K_{\mathrm{xx,\ldots,zz}}}{\mathrm{d}x_i} \tag{8.7}$$

8.1.5. Design responses of the initial design

Roding designs and manufactures the A-pillar using the braiding technology for manufacturing. This is why, the initial design is being evaluated for the braided A-pillar. Rödl (2014) studied that initial design. The results brought forth by his thesis are presented next. First, the deflections are presented for all four load cases in figure 8.8. Load case number one, the roof crush load case, is depicted on the left top side of the figure and the stiffness load cases start from right top side for K_{xx} and go over the left bottom side for K_{yy} to the right bottom side for K_{zz}. Highlighted in red, right below of the roof crush results, one can find the monitored intrusion value of $u_{\mathrm{LC1}}^{max} = 28.9\mathrm{mm}$. Due to the fact, that similar forces have been used for all stiffness load cases, it can be stated that the A-pillar structure shows the greatest stiffness in y direction for that initial design. In figure 8.9 information regarding failure for the roof crush case is given. On the far left top, the failure index for that load case is illustrated. As depicted, the maximal failure index is computed to be 0.69 and is near the clamp point of the A-pillar. The A-pillar is installed and fixed at this clamp point with the help of bracket, which in reality might be softer and in that consequence raise smaller stress peaks. Nevertheless, stress peaks will be present in this area anyhow due the chiseled design in terms of radii and profile geometry. Owned to the fact, that conservative values for the stiffness and strength properties of the braid layers have been used and that the failure index is markedly below one, it can be stated that no failure is to expected for the imposed load F_{LC1}. If failure occurs, albeit not likely, the initial design of the A-pillar will fail first near the clamping.

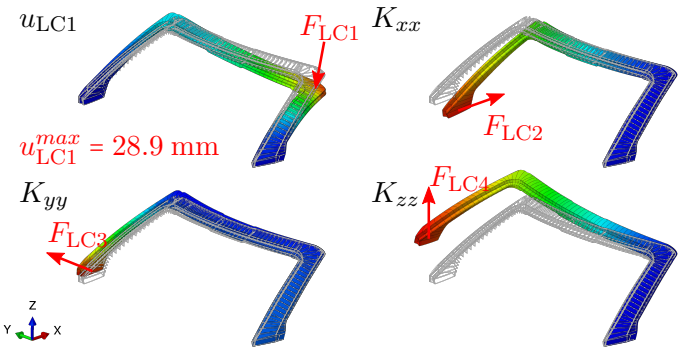

Figure 8.8.: Deformation and deflections for all four load cases by Rödl (2014)

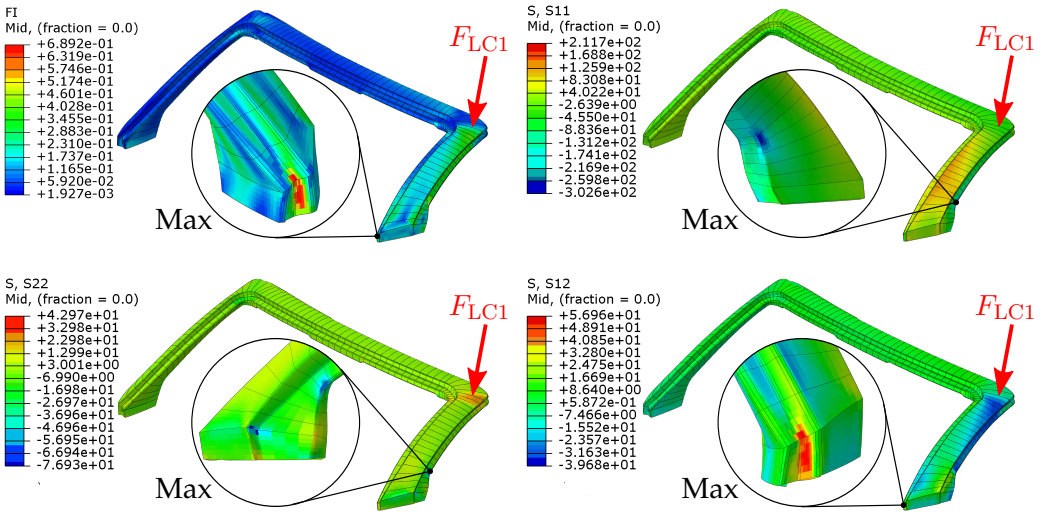

Figure 8.9.: Stress and failure index distribution by Rödl (2014)

8.1.6. Definition of the optimization task

The optimization task for the braided as well as the prepreg manufactured A-pillar can be stated as follows,

$$\begin{aligned} \underset{x\in\chi}{\text{minimize}} \quad & f, \\ \text{subject to} \quad & g_l \le 0, && l = 1,\dots,n_{\mathrm{IC}} \\ \text{with} \quad & \chi = \{x_j \in \mathbb{R}^{n_{\mathrm{DV}}} : x_j^l \le x_j \le x_j^u\}. && j = 1,\dots,n_{\mathrm{DV}} \end{aligned} \tag{8.8}$$

$$g_1(\vec{x}) = 1 - \frac{K_{xx}}{K_{xx,\min}} \quad \text{Stiffness requirement in } x \text{ direction}$$

$$g_2(\vec{x}) = 1 - \frac{K_{yy}}{K_{yy,\min}} \quad \text{Stiffness requirement in } y \text{ direction}$$

$$g_3(\vec{x}) = 1 - \frac{K_{zz}}{K_{zz,\min}} \quad \text{Stiffness requirement in } z \text{ direction}$$

$$g_4(\vec{x}) = \frac{u_{\mathrm{LC1}}}{u_{\mathrm{LC1,max}}} - 1 \quad \text{Limit on intrusion for roof crush case}$$

$$g_{5+s}(\vec{x}) = \frac{\mathcal{FI}_{\mathrm{LC1},s}}{0.9} - 1 \quad \text{No failure for the roof crush case } \forall s \in \{1,\dots,n_{\mathrm{Sec}}\}$$

The objective function vector will be defined right before each optimization result. As defined with the set of equations (8.8), the constraints ensure that all technical requirements are fulfilled. One

set of requirements is originating from the driving dynamics and is imposing a lower threshold onto the A-pillars stiffness in each direction, thus x, y and z direction. These stiffness requirements are considered via the constraints $g_1(\vec{x})$ to $g_3(\vec{x})$. The constraint $g_4(\vec{x})$ limits the intrusion of the A-pillar tip, such that no passenger is harmed for a roof crush. To further enforce structural integrity in this given case $g_{5,\dots,5+n_{\text{Sec}}}(\vec{x})$ are imposed as well. In the following table 8.2 the design space is given. The subtable 8.2a lists all shape design variables with their bounds. Subtables 8.2b and 8.2c provide the design space of the sizing variables for the prepreg and braiding case. In addition, all optimization tasks of this section are solved by taking advantage of gradient-based algorithms, more precisely, either NLPQLP by Schitttkowski (2010), SLSQP by Kraft (1988), KSOPT by Wrenn (1989), MMA by Svanberg (2005) and CONMIN by Vanderplaats (1973).

Table 8.2.: Definition of the design space for both A-pillar optimization tasks: prepreg and braiding

(a) Shape variables

$\vec{x}$	$\vec{x}^l$	$\vec{x}^u$	Unit	ID
$b_1^{(B)}$	-10.	20.	mm	1
$b_2^{(B_1)}$	-5.	15.	mm	2
$b_2^{(B_2)}$	-5.	30.	mm	3
$b_2^{(B_3)}$	-5.	10.	mm	4
$h_1^{(B_1)}$	-3.	20.	mm	5
$h_1^{(B_2)}$	-2.	20.	mm	6
$h_1^{(B_3)}$	-3.	20.	mm	7
$h_2^{(B_1)}$	-10.	15.	mm	8
$h_2^{(B_2)}$	-10.	15.	mm	9
$h_2^{(B_3)}$	-10.	20.	mm	10
$\alpha^{(B_1)}$	-10.	20.	DEG	11
$\alpha^{(B_2)}$	-10.	50.	DEG	12
$\alpha^{(B_3)}$	-10.	20.	DEG	13
$r_1^{(B_2)}$	-2000.	2000.	mm	14
$r_1^{(B_3)}$	-2000.	2000.	mm	15
$r_2^{(B_2)}$	-4000.	4000.	mm	16
$r_2^{(B_3)}$	-1000.	1000.	mm	17
$b_1^{(C)}$	-10.	20.	mm	18
$h_1^{(C)}$	-7.	10.	mm	19
$h_2^{(C)}$	-7.	10.	mm	20
$r_1^{(C)}$	-1000.	1000.	mm	21
$r_2^{(C_1)}$	-4000.	2000.	mm	22
$r_2^{(C_2)}$	-4000.	3000.	mm	23
R	-1.	0.5	-	24

(b) Prepreg sizing variables

$\vec{x}$	$\vec{x}^l$	$\vec{x}^u$	Unit	ID
$n_0^{(1)}$	1.	9.	-	25
$n_\alpha^{(1)}$	0.	9.	-	26
$n_0^{(2)}$	1.	9.	-	27
$n_\alpha^{(2)}$	0.	9.	-	28
$n_0^{(3)}$	1.	9.	-	29
$n_\alpha^{(3)}$	0.	9.	-	30
$n_0^{(4)}$	1.	9.	-	31
$n_\alpha^{(4)}$	0.	9.	-	32
$\alpha^{(1)}$	0.	90.	DEG	33
$\alpha^{(2)}$	0.	90.	DEG	34
$\alpha^{(3)}$	0.	90.	DEG	35
$\alpha^{(4)}$	0.	90.	DEG	36
$n_{P,\alpha}^{(1)}$	0.	9.	-	37
$n_{P,\alpha}^{(2)}$	0.	9.	-	38
$n_{P,\alpha}^{(3)}$	0.	9.	-	39
$n_{P,\alpha}^{(4)}$	0.	9.	-	40
$\alpha_P^{(1)}$	0.	90.	DEG	41
$\alpha_P^{(2)}$	0.	90.	DEG	42
$\alpha_P^{(3)}$	0.	90.	DEG	43
$\alpha_P^{(4)}$	0.	90.	DEG	44

(c) Braiding sizing variables

$\vec{x}$	$\vec{x}^l$	$\vec{x}^u$	Unit	ID
t_1	2.	8.	mm	25
t_2	2.	8.	mm	26
t_3	2.	8.	mm	27
$t_{P,1}$	0.001	0.6	mm	28
$t_{P,2}$	0.001	0.6	mm	29
$t_{P,3}$	0.001	0.6	mm	30
$t_{P,4}$	0.001	0.6	mm	31
φ_1	15.	75.	DEG	32
φ_2	15.	75.	DEG	33
φ_3	15.	75.	DEG	34
φ_4	15.	75.	DEG	35
φ_5	15.	75.	DEG	36

8.2. Optimization of the A-pillar

8.2.1. Optimizing the prepreg laminated A-pillar

At first, the optimization task as defined with the equation set (8.8) will be solved and studied considering the prepreg laying technology. To gain some insight; first, the mass of the A-pillar will be minimized, followed by a minimization of the associated manufacturing effort. All constraints will be monitored and regarded in all subsequent optimizations. At first, the objective f of (8.8) is

set to the mass m as highlighted with equation (8.9). Several optimizations have been conduced, which converged quite robustly, albeit they in average needed more iterations than expected. This is exemplary illustrated in the following figure 8.10.

$$f_m = m \qquad \text{(mass objective)} \tag{8.9}$$

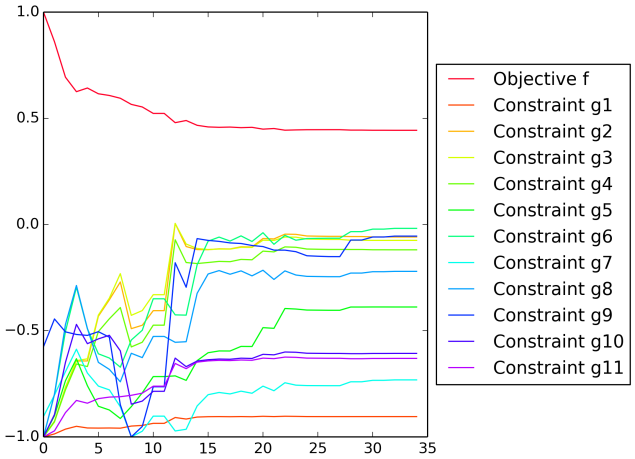

Figure 8.10.: Convergence plot of the prepreg A-pillar mass minimization

One reason the rather slow convergence, i.e. great number of needed iterations, can be found in the fact, that some derivatives of the objective are exactly equal to zero, but yet have a huge imprint onto the constraints. For instance, the derivative of f_m and some of the defined constraints g_l with respect to the orientation of the prepreg unidirectional layer one α_1 can evidently be stated to be,

$$\frac{\mathrm{d}f_m}{\mathrm{d}\alpha_1} \overset{!}{=} 0, \qquad \frac{\mathrm{d}g_l}{\mathrm{d}\alpha_1} \neq 0. \tag{8.10}$$

The difference in the gradients as given with the equation set (8.10) is considered to be the explanation, because the objective can solely be reduced each time a constraint is released. For this to happen, the constraint needs to be active first. Hence, an iterative pattern of constraints becoming active and projecting the influence of specific design variables, such as orientation α, onto the cost function in an indirect fashion forms. This finally yields an increase in iterations. This has also been observed and studied in the thesis of Köhler (2014).

With figure 8.11 the optimum for solely minimizing mass is given. In the left sub-figure 8.11a, the thickness distribution is given. This optimum is characterized by great thickness jumps; which, nevertheless, are plausible considering the fact that they actually stiffen and reinforce the structure at areas, where either high strain energy densities or stress peaks are to be expected. It can further been seen, that the A-pillar's root is enlarged, or graphically-spoken blown up. This leads to a higher second moment of area and in that turn increases the bending stiffness of the overall structure. Nonetheless, this optimum is critical in terms of technical feasibility, since multiple manufacturing restrictions are even violated, thereby hindering a straight forward technical realization. One restriction, which is totally disregarded here, is the continuity requirement. This requirement states, that a certain fraction of plies needs to continue through several patch regions, such that structural integrity after curing can be assured. For this and other reasons, such as wastage rates, the manufacturing effort model predicted a very high effort level of 65 for this design (see sub-figure 8.11b). Please note, that sub-figure

8.11b is plotting the manufacturing effort density, which is being computed for each ply region. The final effort level is cumulated through the following integration scheme,

$$e = \frac{\int_{A_{\mathrm{APillar}}} \dot{e} \mathrm{d}A}{\int_{A_{\mathrm{APillar}}} \mathrm{d}A}, \tag{8.11}$$

with $\dot{e}$ being the effort density and $\Omega_{\mathrm{APillar}}$ respectively the domain defined by the surface of the A-pillar. After minimizing solely the mass of the structure, now, the associated manufacturing effort shall be minimized as well. Therefore, the effort e, as a direct response of the manufacturing effort model and being cumulated via equation (8.12), is minimized. For doing so, the objective is set to be,

$$f_e = e. \qquad \text{(effort objective)} \tag{8.12}$$

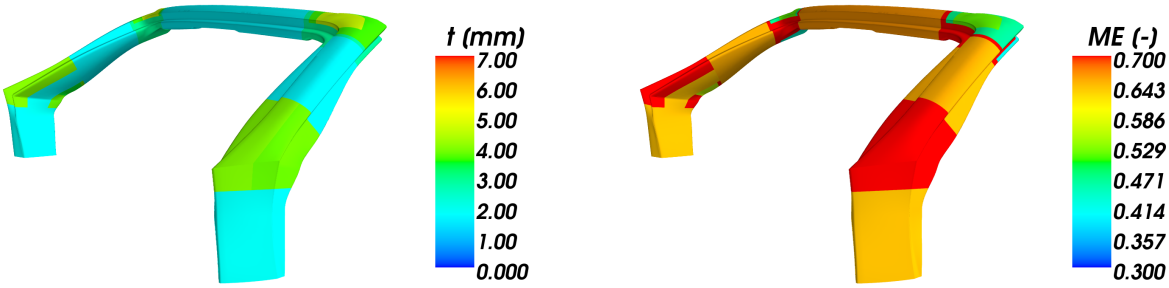

(a) Thickness distribution (b) Manufacturing effort density

Figure 8.11.: Thickness and manufacturing effort shown for the mass optimal solution

The effort optimal solution is shown in both sub-figures of figure 8.12, where sub-figure 8.12a depicts the thickness distribution, whereas sub-figure 8.12b shows the manufacturing effort distribution $\dot{e}$.

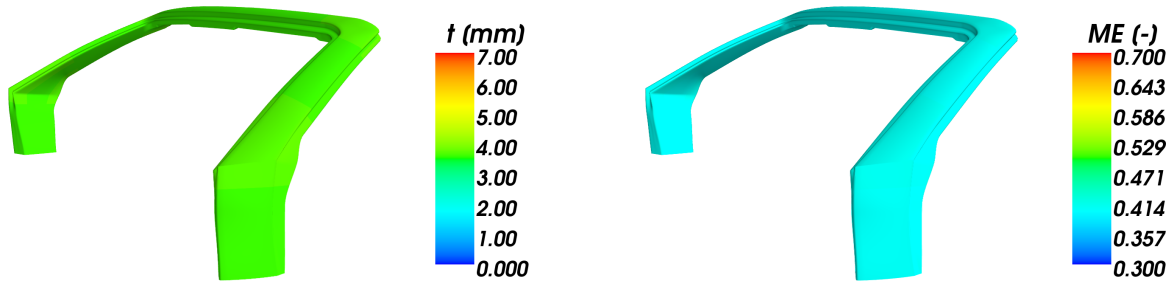

(a) Thickness distribution (b) Manufacturing effort density

Figure 8.12.: Thickness and manufacturing effort shown for the effort optimal solution

As can be seen in sub-figure 8.12a, the thickness distribution is uniform in a sense that the thicknesses of each region is chosen equally. In addition to that, the geometry of the A-pillar has converged to a state, where neat and sharp outlines result in rectangularly shaped patch geometries for most ply regions. These rectangular shapes do in tandem with angles being almost equal to the ones of the available rolls lead to minimal ply wastage.

Both presented optimizations evidently represent extrema, i.e. one is very lightweight, but yet also associated with very high manufacturing efforts and the second optimization displays reverse

relations. Despite their individual advantages, in engineering practice, a design striking an optimal compromise of these obviously conflicting goals of being lightweight and at the same time producible at a low effort level is highly desirable. In chapter 2 and 6.2, the simultaneous optimization of multiple objectives has been introduced as a vector optimization task. Moreover, it has been briefly shown, that with (2.7) and (6.9), an originally vector problem can be condensed to a single objective optimization task by defining a norm. This will now be applied such that a optimal compromise can be met in-between the objectives mass m and manufacturing effort e. As discussed in chapter 6.2, the following scalarization of the objective function vector is likely to perform well, since both criteria are normalized with their best possible outcome or in other words, by the utopia vector:

$$f_d = d(m, e) \qquad \text{(compromise objective)} \tag{8.13}$$

$$\begin{aligned} \text{with} \quad d(m,e) &= \|(\hat{m}, \hat{e})\|_2 \\ \hat{m} &= \frac{\alpha_m (m - m^{\text{opt}})}{m^{\text{opt}}} \\ \hat{e} &= \frac{\alpha_e (e - e^{\text{opt}})}{e^{\text{opt}}} \end{aligned}$$

At the exact same moment, the analytical design sensitivities need to be defined as well. As an example, the partial derivative of the compromise objective $f_d(x)$ with respect to the thickness t_1 is given next. $\frac{\mathrm{d}m}{\mathrm{d}t_1}$ is given analytically by the FEA and $\frac{\mathrm{d}e}{\mathrm{d}t_1}$ will be computed via finite difference. Equation (8.14) represents the partial derivative in general metric form, whereas equation (8.15) only holds for the euclidean norm, i.e. $q == 2$:

$$\begin{aligned} \frac{\partial f_d}{\partial t_1} &= \frac{\partial f_d}{\partial \hat{e}} \frac{\partial \hat{e}}{\partial e} \frac{\mathrm{d}e}{\mathrm{d}t_1} + \frac{\partial f_d}{\partial \hat{m}} \frac{\partial \hat{m}}{\partial m} \frac{\mathrm{d}m}{\mathrm{d}t_1} \\ &= f_d^{1-q} \left\{ \left(\frac{\alpha_e (e - e^{\text{opt}})}{e^{\text{opt}}} \right)^{q-1} \frac{\alpha_e}{e^{\text{opt}}} \frac{\mathrm{d}e}{\mathrm{d}t_1} + \left(\frac{\alpha_m (m - m^{\text{opt}})}{m^{\text{opt}}} \right)^{q-1} \frac{\alpha_m}{m^{\text{opt}}} \frac{\mathrm{d}m}{\mathrm{d}t_1} \right\} \qquad (8.14) \\ &\overset{q=2}{=} \frac{1}{f_d} \left(\frac{\alpha_e^2 (e - e^{\text{opt}})}{{e^{\text{opt}}}^2} \frac{\mathrm{d}e}{\mathrm{d}t_1} + \frac{\alpha_m^2 (m - m^{\text{opt}})}{{m^{\text{opt}}}^2} \frac{\mathrm{d}m}{\mathrm{d}t_1} \right). \qquad (8.15) \end{aligned}$$

Setting f_d given by equation (8.13) as the objective function, basically leads to a minimization of the distance from the current criteria values, here mass m and effort e to a fictitious utopia configuration, being assembled from both extremal solutions, i.e. minimal mass m^{opt} and minimal effort e^{opt}. Table 8.3 provides the result of the compromise optimization $d(m, e)$. Moreover it contrasts this outcome with the extremal solutions, i.e. sole minimization of mass m and effort e. As depicted there, the compromise is met equitable in a sense, that the conflicting goals mass and effort settled almost evenly. That the compromise is made equitable, can also be comprehended by plotting each optimum in a normalized space, adding the utopia point and an angle bisector. This is given with figure 8.13, where the red star reflects for the found compromise design. As illustrated, this compromise is almost lying on the angle bisector and, thus, situated between both extremal solutions represented via the yellow stars.

With figure 8.14, the manufacturing effort distribution of the optimal compromise solution is given. The minimal effort solution is characterized by an optimal design in light of manufacturing. For achieving this, the optimization algorithm did strictly follow the MEM's responses such that no drop-offs where realized, minimal clipping or ply wastage, almost every ply was continued, i.e. no jumps in ply orientation et cetera. Opposed to that extremal design–truly being too radical for practical applications in terms of structural efficiency or light weight design–the optimal compromise allows

Table 8.3.: Pareto efficient solutions of the prepreg optimization task

Objective	Mass m [kg]	Effort e [-]	Remarks
m	3.5	64.7	Pure minimization of mass
e	5.3	39.0	Pure minimization of effort
$d(m,e)$	3.9	54	Optimal compromise

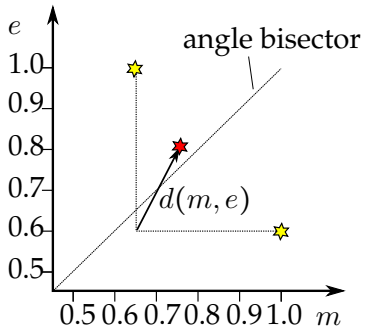

Figure 8.13.: Found Pareto optimal solutions for laminated A-pillar

for some increase in effort, thereby striking a reasonable and technically attractive compromise. This compromise is hence realized by tolerating some clipping, certain ply drop-offs and by accepting that multiple plies do not continue as long as they do not exceed a critical fraction. All of the mentioned aspects are obviously plausible and tenable for a practical stance. Beside those technical insights, the conducted optimization runs revealed, that the mathematical condition in terms of numerical performance did not decrease, but instead actually got lifted once the MEM has been incorporated into the optimization process. This has been studied by varying the starting point, optimization algorithms, e.g. MMA, NLPQLP etc., optimization tolerances and similar facets of the optimization process. Of course, this not only provides insight into the mathematical condition and especially whether or not the optimization is well posed, but also whether the problem is multi-modal and in that consequence local optima can lead to sub-optimal performance. Nonetheless, the following table 8.4 has been condensed from all those conducted optimization runs. As given therewith, the MEM apparently alleviates the scatter in optimal responses and optima.

Table 8.4.: Evaluation of the optimization problems' condition

Measured entity	Optimization Objective		
	Mass f_m	Effort f_e	Compromise f_d
Scatter in f_{opt}	◇◇	◇	◇
Scatter in $\vec{x}_{\text{opt}}$	◇◇◇	◇◇	◇◇
Scatter in $\vec{g}_{\text{opt}}$	◇◇	◇	◇◇

◇ Low
◇◇ Moderate
◇◇◇ Strong

An explanation for the elevation in the optimization model's condition can be found in the sensitivities of the objective. As stated earlier, for the mass objective f_m there are several sensitivities being exactly zero, but yet their associated design variable show a major impact on certain constraints. With equation (8.10), an example has been given by discussing the derivative with respect to a ply orientation α_1. These so to say unbalanced circumstances in the sensitivities did lead to a considerably slower convergence and may also be the cause for the mal-conditioned optimization problem. For the case, that the MEM is being incorporated, the sensitivities are in all circumstances throughout the whole design space non-zero as given with equation (8.16). This can be verified by either studying the response surface plots or by conducting sensitivity studies; both of which have been done. Ultimately, the non-zero sensitivities lead to proper and robust convergences, thus in optimizations converging

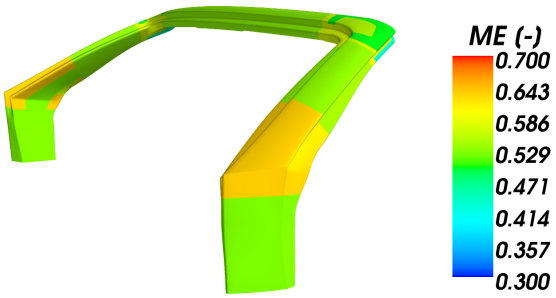

Figure 8.14.: Optimal compromise

within less than twenty iterations in average and displaying view till moderate scattering in the objective function value f_{opt}, constraint value $\vec{g}_{\text{opt}}$ and the corresponding designs $\vec{x}_{\text{opt}}$.

$$\frac{\mathrm{d}f_d}{\mathrm{d}\alpha_1} = \frac{\mathrm{d}f_e}{\mathrm{d}\alpha_1} \neq 0, \qquad \frac{\mathrm{d}g_l}{\mathrm{d}\alpha_1} \neq 0. \tag{8.16}$$

8.2.2. Optimization considering braiding as the manufacturing technique

The structural design optimization of the braided A-pillar will shown in the three subsequent subsections. First the an optimal compromise will be derived and discussed. Thereafter, the post-processing possibilities of the gradient-based approach will be shown. This braid optimization section will then be closed by highlighting the CAE capabilities of the effort model, i.e. the stand-alone features and, hence, the significance in designing based on the responses of the braid manufacturing effort model.

Simple scalarization and post processing of multi-criteria optimizations

With equation (8.17), the objective function for solving the stated optimization task (8.8) for the optimal compromise is given. Besides, it shall be noted at this point, that an optimal compromise can vary from industry to industry and for different applications. It is here defined as the shortest distance from the Pareto frontier to the fictitious combination of extremal solutions, the point of utopia. It is hence assumed that an optimal compromise outbalances both objects equally. For achieving this, $d(m,e)$ has been defined via normalized mass m and effort e responses, whereby each of those is normalized by its extremal solution.

$$f_d = d(m,e) \qquad \text{(compromise objective)} \tag{8.17}$$

$$\begin{aligned} \text{with} \quad d(m,e) &= \|(\hat{m},\hat{e})\|_2 \\ \hat{m} &= \frac{\alpha_m(m - m^{\text{opt}})}{m^{\text{opt}}} \\ \hat{e} &= \frac{\alpha_e(e - e^{\text{opt}})}{e^{\text{opt}}} \end{aligned}$$

After conducting several optimizations, the following solutions, as given via table 8.5, are obtained. It can be observed that an optimal compromise between both objectives–similarly to the priorly conducted prepreg optimizations–could be found. However, the objective weights leading to this

Table 8.5.: Optima of the braid optimization task of the A-pillar

Weight α_m [-]	Weight α_e [-]	Mass m [kg]	Effort e [-]	Remarks
1.0	0.	5.2	70.3	Pure minimization of mass
0.	1.0	6.7	33.4	Pure minimization of effort
0.167	0.833	5.9	41.2	Optimal compromise

optimal compromise, took values deviating a lot from the intuitive guess of an equal weighting, i.e. $\alpha_m = \alpha_e = 0.5$. They actually were $\alpha_m = \frac{1}{6} \approx 0.167$ and $\alpha_e = \frac{5}{6} \approx 0.833$.

Obviously, the found compromise solution for the braided A-pillar is heavier as the one derived for the prepreg optimization, where the optimal compromise weight only 3.9kg (see table 8.3). Two major reasons can be identified being response for that significant difference. First, different carbon materials have been used. So, the carbon fibers for the braided A-Pillar case are less stiff and display lower strength values, but are way easier to handle during the preform production. Secondly, the stiffness of the cured braided material is further reduced by undulations. In section 5, it has already been shown, that the braid material shows great stiffness sensitivities towards the braider yarn orientation, but also towards the thickness of each yarn, since different amplitudes of these undulations are brought forward. It has further been shown by figure 5.12 how those undulations appear in technical specimens.

With figure 8.15 the lengthwise geometry and an examplary profile section (profile section 19) of the optimal compromise design is illustrated. Several design requirements for the A-pillar require a certain section modulus, e.g. minimal bending stiffness, which is, however, achieved in concert with the material model and thus the braiding parameters, braiding angle and yarn width. Nonetheless, at this point, the discussion is reduced on the profile's cross section. As can be seen in figure 8.15, the optimization increased the section modulus by blowing it up. This is highlighted by the red dashed circle A. For accounting the associated manufacturing effort, the profile's edge radii have been increase to their limit (see green dashed circle C). Last but not least, the lengthwise curvature radius at the region B has been increase a lot as well.

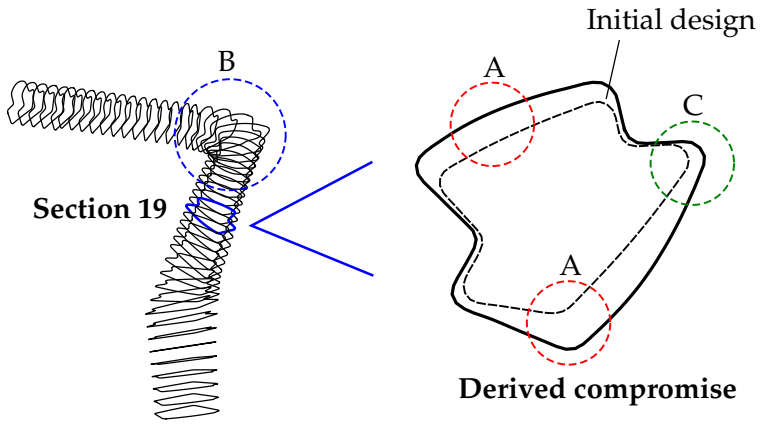

Figure 8.15.: Illustration of the optimal compromise for the braided A-pillar

The distribution of the braiding angle φ for the first braid layer is given with subfigure 8.16a. The following subfigure 8.16b depicts the corresponding effort density $\dot{e}$ of the same first braid layer. It can be comprehended, that the overall associated effort level is low, even though one region shows a slight increase due to the lengthwise conical change of the A-pillar at this point. Noteworthy, is the fact that the manufacturing effort level could be retained at such a low level, since the braiding angle distribution is perfectly in concert with the corresponding yarn widths and associated geometry quantities such as circumference. This is comprehend-able, when studying subfigure 8.16c, where

local changes of the yarn width in areas of high curvature (region B in figure 8.15) get ahead of any braid opening due to unrealistically high yarn widths. More plots, such as the ones for the braid layers two and three, are given in the appendix section A.5.

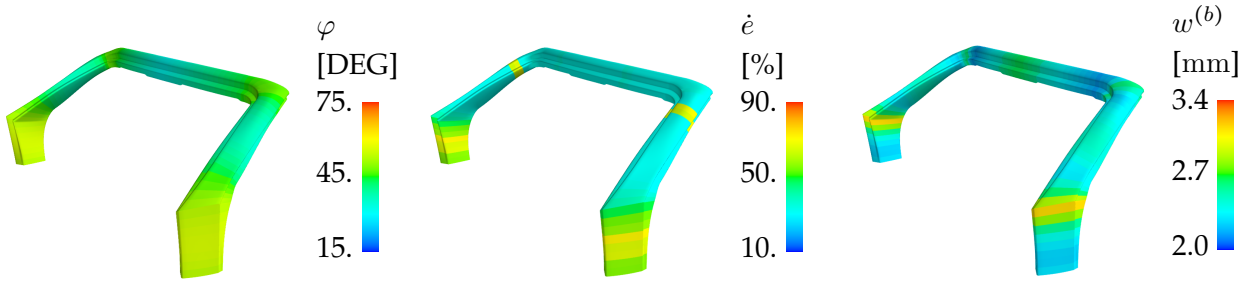

(a) Braiding angle $\varphi(s)$ (b) Effort density $\dot{e}(s)$ (c) Braider yarn width $w^{(b)}(s)$

Figure 8.16.: Response and design variable distributions for the optimal compromise of the braided A-pillar given for the first braid layer

Post processing of vector optimizations

In the fundamentals section 2.2 optimality was introduced. This optimality evaluation given by the Karuh-Kuhn-Tucker conditions, involved the so called Lagrangian parameters λ_i for each constraint i. These parameters are obtainable with ease and do not require any re-evaluation of the underlying system equations, i.e. finite element analyses. In section 6.2.3, the extrapolation at a found optima was based on those Lagrangian parameters λ_i, which were then referred to as shadow prices (see equation (2.4), (6.16) and (6.17)). Now, this theoretically demonstrated concept is applied for the structural A-pillar design task and specifically for the optimal compromise design, discussed priorly. Before the extrapolation based on a linearization can be conducted, the partial derivative of the aggregated objective f_d with respect to each contributing objective, i.e. mass m and effort e needs to be defined. This is given by the following equation,

$$\frac{\partial e}{\partial f_d} = \frac{f_d {e^{\text{opt}}}^2}{\alpha_e^2 (e - e^{\text{opt}})}. \tag{8.18}$$

Exploiting this equation and linearizing at the found optima $\vec{x}^{\text{opt}}$ leads to the following expression, where the linearization is conducted for the objective manufacturing effort e and relaxed over the constraint number one, which imposes a minimal stiffness $K_{xx,\min}$ onto the design.

$$\begin{aligned} \text{Lin}(e)(\Delta K_{xx,\min}) &= e|_{\vec{x}^{\text{opt}}} + \frac{\partial e}{\partial u_{\text{LC1,max}}} \Delta K_{xx,\min}. \\ &= e|_{\vec{x}^{\text{opt}}} + \underbrace{\frac{\partial e}{\partial f_d}}_{(8.18)} \underbrace{\frac{\partial f_d}{\partial g_1}}_{-\lambda_1} \underbrace{\frac{\partial g_1}{\partial K_{xx}}}_{\frac{-1}{K_{xx,\min}}} \underbrace{\frac{\partial K_{xx}}{\partial K_{xx,\min}}}_{1} \Delta K_{xx,\min} \\ &= e|_{\vec{x}^{\text{opt}}} + \frac{f_d {e^{\text{opt}}}^2}{\alpha_e^2 (e - e^{\text{opt}})} \lambda_1 \frac{\Delta K_{xx,\min}}{K_{xx,\min}}. \end{aligned} \tag{8.19}$$

Equation (8.19) thus illuminates, how a change in the restriction limit–therein, a decrease in the required minimal stiffness $K_{xx,\min}$–would imprint onto the objective effort e. Or in other words, the shadow prices reveal possible objective improvements in case constraints are loosened and, hence, the price the optimizer paid by imposing that constraint level in hand. This has similarly been conducted

for every constraint of the optimization task as given with equation set (8.8). The results of this is listed in table 8.6. In this table, the values of each Lagrangian parameter λ_i is given. This column already reveals, that the constraint of $K_{zz,\min}$ appears to be dominating for this optimum and further, that the constraint based on the limit for the roof crush intrusion $u_{\mathrm{LC1,max}}$ is not active, i.e. $\lambda = 0$. The two outer right columns depicts the change in the corresponding objectives mass m and manufacturing effort e. Again, the constraint for requiring a minimal stiffness $K_{zz,\min}$ demanded for the highest price in terms of possible objective improvements, which has already been perceptible by studying the shadow prices. For this case, the extrapolated improvements for a ten percent relaxation of the constraint level are computed to be almost six hundred gram for mass and twelve units for the effort level.

Table 8.6.: Post processing of compromise optimum as of table 8.5

Shadow price		Constraint	Linearized changes	
Constraint	Lagrange value λ [-]	change [%]	Mass Δm [g]	Effort Δe [-]
$K_{xx,\min}$	−2.3	−10.0	−50	−0.9
$K_{yy,\min}$	−3.6	−10.0	−70	−1.5
$K_{zz,\min}$	−28.6	−10.0	−570	−11.4
$u_{\mathrm{LC1,max}}$	0.0	10.0	0	0.0
$\mathcal{FI}_{\mathrm{LC1,max}}$	0.4	10.0	−8	−0.2

Beside the useful feature of linearly extrapolating based on these Lagrangian parameters λ_i, they also allow the contrasting of different derived optima in terms of robustness. This is because, they reflect the sensitivity of the objective function with respect to the constraint limits and thus how sensitive an optimum regarding changes in the constraint responses or uncertainties–from a practical perspective–is. Table 8.7 illustrates this, by portraying the maximal Lagrangian parameters $\max\{\lambda_i\}$ along with the objective function values for the manufacturing effort e and the mass m. The third row provides the optimal compromise design with the lowest manufacturing effort level, but yet also the most sensitive one. It is regarded to be the most sensitive one, since its shadow prices is the highest. In comparison to the shadow prices of the first design, which have been studied afore and listed in table 8.6, the change in the objectives would be 53% greater.

Table 8.7.: Contrasting three found optimal compromises with respect to robustness

Effort e [-]	Mass m [kg]	$\max\{\|\lambda_i\|\}$ [-]	Remark
41.2	5.9	28.6	Most robust optimum
40.6	5.9	32.4	Moderate robust design
39.5	5.8	43.7	Minimal effort but most sensitive

In addition to the sole extrapolation of the how the objective function evolves for changes in constraint limits, the linearization can be extended by further exploiting sensitivities of design parameters. Here, it has for instance been shown, that the stiffness requirement demanding a certain stiffness for K_{zz} is the most limiting constraint. Obviously, beside all design variables, parameters such as those of the material model do also influence the stiffness performance of the A-pillar. One parameter chiefly determining the stiffness responses of the material model clearly is the used fiber material and more specifically the fiber's stiffness $E_{11,f}$ in longitudinal direction. The question to be answered next is: how would a substitution of the used fiber material by a more stiffer one affect the optimizations outcome? For answering this, a sensitivity study was additionally conducted. In this sensitivity study, the influence of the fiber's stiffness $E_{11,f}$ onto all optimization responses, such as the stiffness responses K_{xx}, K_{yy} and K_{zz}, has been revealed, by varying the stiffness for the axial yarn and the stiffness of the braider yarn. This is illustrated with equation (8.20), where $E_{11,f}^{(a)}$ represent the

fiber stiffness of the axial yarn and $E_{11,f}^{(b)}$ respective the one of the braider yarn.

$$\frac{\partial K_{zz}}{\partial E_{11,f}} = \frac{\partial K_{zz}}{\partial E_{11}^{(a)}} \frac{\partial E_{11}^{(a)}}{\partial E_{11,f}^{(a)}} + \frac{\partial K_{zz}}{\partial E_{11}^{(b)}} \frac{\partial E_{11,f}^{(b)}}{\partial E_{11,f}} \tag{8.20}$$

Once this partial derivative (8.20) is computed via the sensitivity study, the linearization at the optimal compromise design as already outlined by equation (8.19) can be expanded as follows. As a side mark, the derivatives $\frac{\partial e}{\partial u_{\mathrm{LC1}}}$ are not listed, since those constraints are not active (see table 8.6).

$$\begin{aligned}\mathrm{Lin}(e) &= e|_{\vec{x}^{\mathrm{opt}}} + \left\{ \frac{\partial e}{\partial K_{xx}} \frac{\partial K_{xx}}{\partial E_{11,f}} + \frac{\partial e}{\partial K_{yy}} \frac{\partial K_{yy}}{\partial E_{11,f}} + \frac{\partial e}{\partial K_{zz}} \frac{\partial K_{zz}}{\partial E_{11,f}} + \frac{\partial e}{\partial \mathcal{FI}_{\mathrm{LC1}}} \frac{\partial \mathcal{FI}_{\mathrm{LC1}}}{\partial E_{11,f}} \right\} \Delta E_{11,f} \\ &= e|_{\vec{x}^{\mathrm{opt}}} + \left\{ \frac{\lambda_1}{K_{xx,\min}} \frac{\partial K_{xx}}{\partial E_{11,f}} + \frac{\lambda_2}{K_{yy,\min}} \frac{\partial K_{yy}}{\partial E_{11,f}} + \frac{\lambda_3}{K_{zz,\min}} \frac{\partial K_{zz}}{\partial E_{11,f}} - \frac{\lambda_5}{\mathcal{FI}_{\mathrm{LC1,max}}} \frac{\partial \mathcal{FI}_{\mathrm{LC1}}}{\partial E_{11,f}} \right\} \frac{f_d {e^{\mathrm{opt}}}^2}{\alpha_e^2 (e - e^{\mathrm{opt}})} \Delta E_{11,f}.\end{aligned} \tag{8.21}$$

Now, assuming a substitution of the so far used Toho Tenax HTA ($E_{11,f} \approx 240\mathrm{GPa}^{\dagger}$) carbon fibers with SGL SIGRAFIL CT24-5 fiber ($E_{11,f} \approx 270\mathrm{GPa}^{\dagger}$) leads to the changes in effort e and mass m as listed with 8.8. It is illustrated there, that both objectives, as must be the case, can be reduced; effort by 6.3 and mass by $406.7g$.

Table 8.8.: Substitution of fiber material

Change of fiber stiffness $\Delta E_{11,f}$[GPa]	Resulting change in Effort Δe [-]	Mass Δm [g]
+30.0	−6.3	−406.7

CAE capabilities of the developed soft computing approach

So far, the manufacturing effort model (MEM) has solely been studied in concert with the structural design optimization. However, the approach is that mature, that it shall be considered as a stand-alone computer-aided engineering (CAE) tool. This will be pinned in the following discussion. First and foremost, the developed MEM is independent of any other software tool. So, the fuzzy logic arithmetic, knowledge base, post-processing and miscellaneous are implemented via Python in an object-orientated fashion and do not rely on any other software. Moreover, the inputs of the MEM are automatically fetched from mere mesh data, which can be generated by almost any finite element tool, since it only relies on nodal coordinates and connectivity information. This fetching of geometrical information is realized exploiting B-splines as given with the following equation, where $\vec{\Psi}(s)$ represents the coordates of the spline curve at parameter value s, $\vec{P}_i$ being the nodal coordinate values and $\vec{N_{i,p,\tau}}$ the B-spline basis functions ($\odot$ denotes the pointwise Hadamard product).

$$\vec{\Psi}(s) = \sum_{i=1}^{n-p} \vec{P}_i \odot \vec{N}_{i,p,\tau}(s) \tag{8.22}$$

The B-Spline interpolation scheme yields the following representation as depited with figure 8.17. Once all splines are computed, the MEM inputs can be computed as well. For instance the curvature radius R along the profile curve coordinate s can be computed to be

[†]Material properties are taken from data sheets provided by the corresponding company

$$R(s) = \frac{\|\dot{\vec{\Psi}}\|^3}{\|\dot{\vec{\Psi}} \times \ddot{\vec{\Psi}}\|} \qquad \text{with } \dot{\vec{\Psi}} = \frac{\mathrm{d}\vec{\Psi}}{\mathrm{d}s}. \tag{8.23}$$

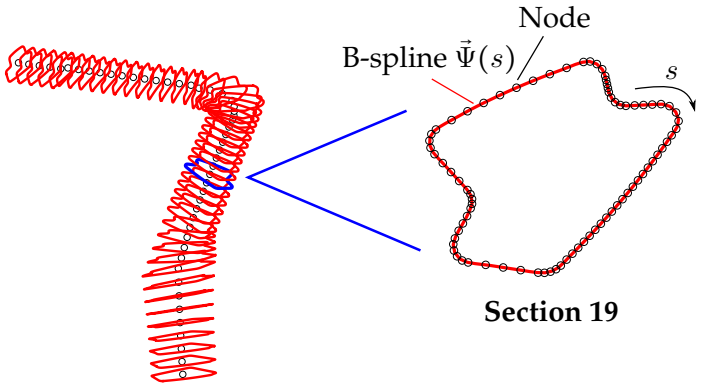

Figure 8.17.: B-spline representation of the A-pillar

As observable, this renders the MEM to an independent CAE tool. Figure 8.18 illustrates how the MEM generates the outputs solely based on the data provided by the B-spline representation. First, it shall be noted, that a small legend is given in the lower right. Secondly, the outputs have been computed for the initial design to display the significance of the MEM in terms of pointing out design directions. Last but not least, the outputs of the MEM have not been modified, which is why the outputs are of rather stenographic nature. In figure 8.18, three exemplary profiles have been highlighted along with the associated manufacturing effort level e computed by the MEM. Below each effort level, a reason $\mathcal{R}$ why that specific manufacturing effort level has been computed, is passed as well. Lastly, the engineer obtains an elaboration advice $\mathcal{A}$ as the last output. All three outputs equip the engineer, such that he can alter the design in an optimal fashion. For instance, for the second profile the MEM did compute the effort level to be $e = 0.805$, which is close to one and, hence, rather high in that context. Further, the engineer can comprehend this computation by studying the reason $\mathcal{R}$, with which he can put things into context. In this case, the MEM identified the combination of very small braiding angles (*"Angle" is "VerySmall"*) and curvature (*Rule "TakeUpCurvature"*) to be the reason. If the engineer agrees with that, he can update the design according to the elaboration advice $\mathcal{A}$ given next.

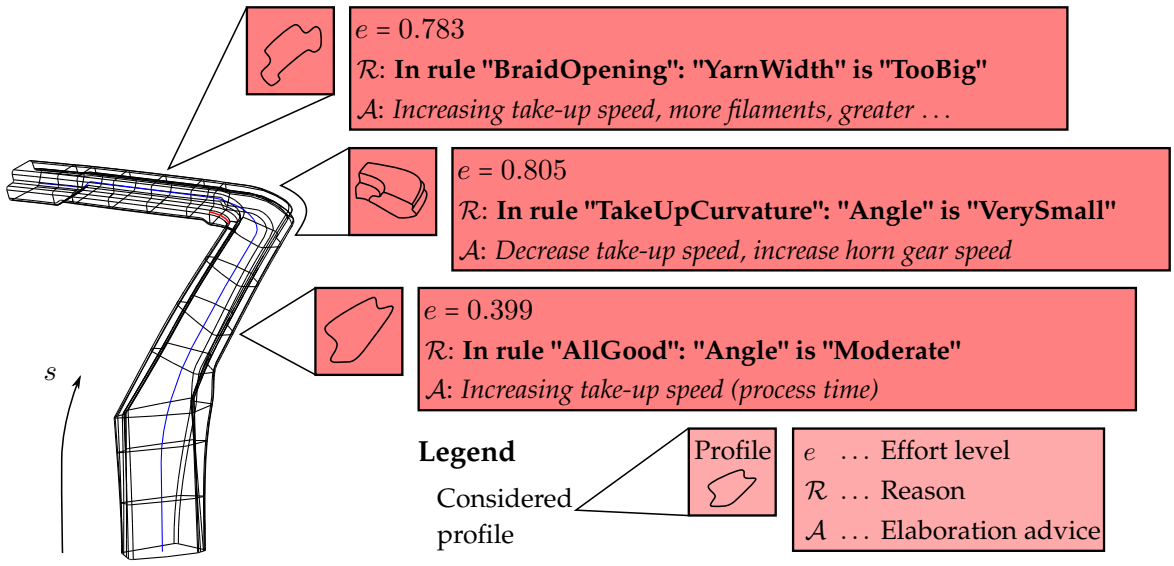

Figure 8.18.: CAE capabilities of effort model shown for the initial design

At this point, it is conceivable that the engineer not only gains insight for one manufacturing technique and updates the design on those insights, but also effort levels and reasons for multiple manufacturing techniques. By doing that, the CAE process would be enriched a lot, since an engineer could not only design concurrent to manufacturing, but also take influence on the optimal choice of a manufacturing technique. This is mainly because of the general nature of the developed approach and the fact that different MEMs share common rationals such as the fuzzy logic arithmetic and solely differ in the knowledge base, which is obviously exchangeable (see figure 4.20).

8.3. Summary of the optimization including a soft computing model

The A-pillar served as the first structural design problem of industrial scale. It has been shown how the multi-scale model as developed and motivated in section 5 can be incorporated into such a structural optimization model. Particular attention was turned to the preservation of the analytical design sensitivities, which have been made available for any conducted analysis kind and moreover for every design variable, no matter which nature, i.e. sizing and shape variables. The associated implementation effort amortized multiple times. Through this analytical design sensitivity analysis, the high dimensional optimization tasks, could be solved with less than seventy system equation evaluations in average for all considered cases. This is especially noteworthy, since each evaluation of system equations involves sophisticated finite element analysis, which cause most of the computation time throughout the optimization process. In addition to this numerical efficiency, the meta modeling of the homogenization model made any complex mapping or alike unnecessary, while still preserving most of the braiding material characteristics.

Concerning the manufacturing effort modeling through soft computing, the A-pillar design task revealed its general validity and applicability. This can be stated, since manufacturing effort caused by braiding, has been considered with ease, as the ones for prepreg laying. For both cases, the manufacturing effort model considerably influenced the course of the optimization, resulting into designs being closer to technical reality. In that consequence, the manufacturing effort models leveraged the optimization process to a whole new level of technical significance, by making the underlying optimization model more holistic. In addition to the enrichment of the optimization process, it has been discussed, how the developed braiding manufacturing effort model can be used as an independent CAE tool in designing. One major reason for regarding the effort model as an independent tool, is the general data acquisition, being independent of any other finite element or CAD tool. Hence, both effort models are implemented as stand-alone tools, capable of pointing into the most goal orientated design direction in terms of technical manufacturing. Both effort models underpin these directions, by providing reasons for its evaluation. Moreover, the designing direction is supported by instructions on how to alter the current design, namely, by providing elaboration advices.

Last but not least, it has been shown, that the objectives of structural efficiency, here, mass and the associated manufacturing effort are strongly competitive and thus ultimately lead to a multi-criteria optimization problem. In this section, all bi-objective optimizations, thus optimization problems with two objectives, have been scalarized by using different types of norms. However, two major questions remained unanswered. First, the difficulty of how to weight both objectives in general cases and how the whole set of Pareto efficient solutions–or the gathering of those, the Pareto frontier–can be obtained in one single shot. This will be analyzed, resolved for general cases and demonstrated for the following structural design task: the braided propeller.

9 Optimizing a propeller structure

Within this chapter, a propeller will serve as an example for the structural multi-criteria optimization considering manufacturing effort. The manufacturing effort will be computed by the afore discussed manufacturing effort model, being facilitated through the soft computing based on verbal expert knowledge. Despite further interesting aspects originating for instance from aerodynamics (optimization of thrust and drag) or aeroelasticity (flutter and similar effects), the interaction of manufacturing effort and structural mechanics shall have priority in the following discussion. Moreover, the general multi-criteria optimization approach, as already introduced and applied for the academic examples, will be extensively studied. Figure 9.1 depicts the two bladed propeller from which one blade will serve as a technical demonstrator.

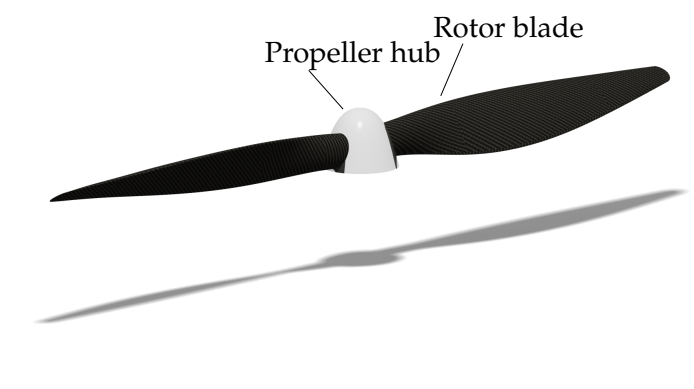

Figure 9.1.: Braided CFRP propeller

Contents

9.1. Problem definition

During the designing of the propeller of a piston engine driven airplane, engineers need to face two design-determining load cases. One is derived from climbing at the maximal climbing rate, here referred to as max thrust load case, and the other of maximal descent, whereby the propeller is operated with almost no thrust or in worst case even with a negative thrust, resulting in a so-called windmill effect. Both load cases will be discussed next.

9.1.1. Description of the load cases

First, the load case of maximal thrust will be discussed. For an airplane climbing at a constant ascent speed and climb angle of γ, figure 9.2 depicts the acting forces: thrust T, drag D, lift L and gravitational force W. The airplane of the figure is inspired by illustrations of Curtiss-Wright-Corporation (1944), from where the outer sketch has been taken. For this flight configuration, the following equations do hold,

$$\begin{aligned} T - D - W\sin(\gamma) &= 0 \\ L - W\cos(\gamma) &= 0. \end{aligned} \tag{9.1}$$

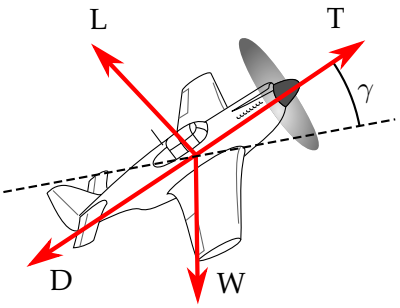

Figure 9.2.: Forces acting on an airplane in steady ascent

Re-arranging and exploiting that the ratio of drag to lift can be expressed via $\epsilon = \frac{D}{L} = \frac{1}{\mathrm{GR}}$ (*german: Gleitzahl*) or the inverse of the glide ratio GR leads to

$$T = W(\sin(\gamma) + \epsilon) = m_{\mathrm{Plane}} g(\sin(\gamma) + \epsilon). \tag{9.2}$$

Computing the climb angle γ via the rate of climb $\dot{h}$ and max climb speed $V_{\dot{h}}$ and inserting it into (9.2) leads to the final equation

$$T = m_{\mathrm{Plane}} g\left[\sin\left(\arctan\left(\frac{\dot{h}}{V_{\dot{h}}}\right)\right) + \epsilon\right]. \tag{9.3}$$

Assuming a mass m_{Plane} of $1089\mathrm{kg}$, a climb rate of $\dot{h}$ of $220\frac{\mathrm{m}}{\mathrm{min}}$ at a speed $V_{\dot{h}}$ of $60\mathrm{kn}$ and a moderate ϵ of 0.14, the thrust T can be computed to be $2.8\mathrm{kN}$. In that consequence, each blade of a two-bladed propeller needs to bring forth $1.4\mathrm{kN}$ thrust. Contrary, for a stationary straight flight the thrust can be computed to be $0.7\mathrm{kN}$ by simple using (9.2), where the climb angle γ of (9.2) is simply set to zero, i.e. $T = W\epsilon = m_{\mathrm{Plane}} g\epsilon$. So, in that consequence, one can see, that the load case of climbing at the highest climbing rate is design-driving in terms of maximal twist and bending forces acting on the propeller. Further considering, that the propeller is rotating at the highest rotation speed, translating into great centrifugal forces, underlines the design-determining character of this load case. The second load

case basically represents an inversion of the forces acting on the propeller and, thus, in a sense the opposite loading situation as of load case one. This inversion is caused by a negative pitch angle for the relative wind along the propeller blade. This relative wind is depicted in figure 9.3, where V_W is the superposed velocity of wind and forward velocity of the airplane, V_P the velocity of propeller defined by the rotational speed and blade radius and V_A as the aerodynamic velocity or relative wind speed. Further illustrations of the relative wind for propellers can be found in Curtiss-Wright-Corporation (1944). The angle at which the relative wind attacks the propeller blade's profile is called pitch. In case of a positive pitch angle, thrust is being generated by translating the moment of the engine into aerodynamic lift. Hence, for the windmilling case, the negative pitch angles along the blade axis results in inverse forces, where the propeller does not generate thrust, but instead behaves similar to a wind turbine.

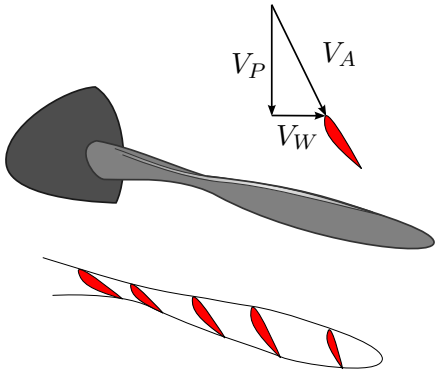

Figure 9.3.: Pitch angle distribution along the propeller

Another aspect, which is being illustrated in figure 9.3 is the geometrical twist of the aerodynamic profiles along the propeller blade axis. This twist (*german: Schränkung*) is necessary to compensate for the varying velocity of the propeller V_P along the blade axis r (see equation (9.4)).

$$V_P(r) = \frac{n_P 2\pi}{60} r \tag{9.4}$$

9.1.2. Computing the pressure distribution for both load cases

Prior to the computation of the structural responses in terms of stiffness, modal properties and strength, the pressure distribution needs to be computed first, such that they can be imposed as loads in the structural simulation. In this work, ANSYS Fluent has been used as it is a computational fluid dynamic simulation (CFD) tool, since it is capable to resolve all relevant physical aspects of the flow around the propeller. Extensions of the potential theory such as the blade element momentum theory have been considered as computational approaches for this kind of problem. However, in the investigated case the velocities–especially at the tip of propeller blade–are rather high, which is why incompressibility of the flow may not be assumed. This assumption is commonly made until a Mach number of $\mathrm{Ma} \approx 0.3$, see Oertel (2003). For the considered case the velocities even reach up to $\mathrm{Ma} \approx 0.85$, rendering the assumption of incompressibility impossible. Further aspects, which can be considered by Fluent are friction due to the viscosity of the fluid and turbulence.

For determining the flow and its quantities, the Reynolds-averaged Navier-Stokes equations have to be solved in tandem with the energy equation. The latter is necessary to account for the fluid's compressibility. Within the fluid simulations, the k-ϵ turbulence model has been used to close the closure problem. For more information regarding turbulence and the Reynolds-averaged Navier-Stokes equations see Tu et al. (2008). With figure 9.4, the solution of the CFD simulation for the max thrust load case is given. In the left sub-figure 9.4a, the resulting pressure distribution is being plotted

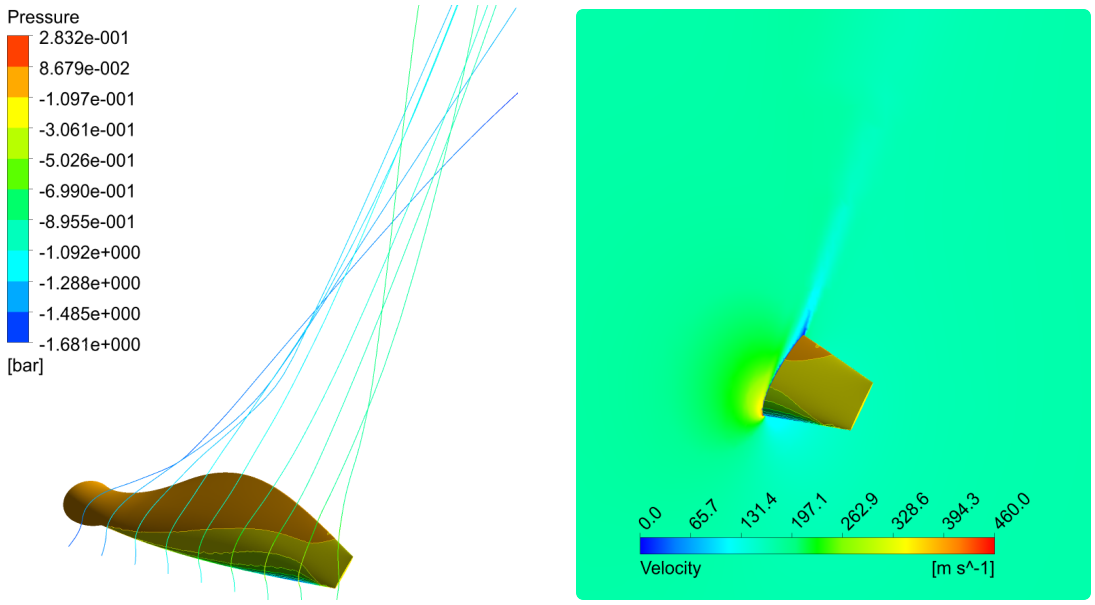

(a) Streamlines and pressure distribution (b) Velocity at 85% of the propeller's length

Figure 9.4.: Velocity and pressure results of the maximal thrust case

onto the propeller. Furthermore, some stream lines originating right before the propeller blade are displayed. As can be seen, the flow is deflected by the propeller blade resulting in lift and in that consequence translates into thrust, due to Bernoulli's principle, where pressure drops for an increasing flow speed on the top and vice versa underneath the propeller blade. In the right sub-figure 9.4b the velocity distribution is plotted on a plane at 85% of the propeller's length. Once the pressure fields are computed for both load cases the information is passed to Abaqus, where an existing mapping routine is used to map the pressure fields based on the fluid mesh to the structural shell mesh of the propeller's surface.

9.1.3. The structural model

With figure 9.5 the structural model of the propeller is given. As illustrated there, the blade profile geometry (highlighted in red) varies in profile depth (chord length), camber and profile thickness. Beside those geometric profile variations, the profiles are twisted along the blade axis, so as to realize an optimal pitch angle distribution while in operation; as the propeller speed varies along the blade axis r (see equation (9.4)).

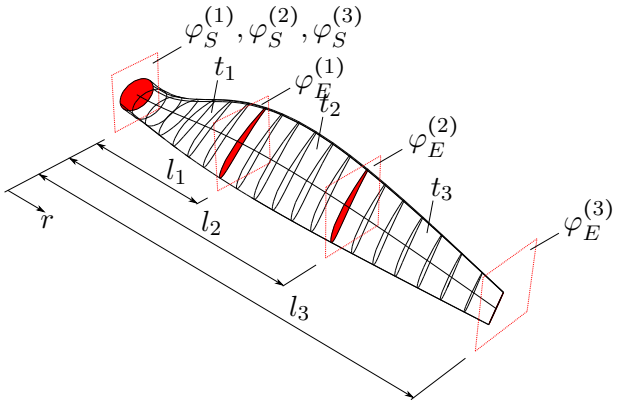

Figure 9.5.: Structural model of the propeller

The propeller has a length l_P of one meter. The greatest chord length amounts to 180mm, which drops down to 85mm at $.9l_P$ and 60mm at l_P. For accounting multiple over-braidings, the model is defined by three braid layer sections, where each braid section i is defined by a starting braiding angle $\varphi_S^{(i)}$, an ending braiding angle $\varphi_E^{(i)}$ and a braiding layer thickness t_i. In addition to that, the first and second of the braid sections are parametrized in their length $l_{1,2}$. Therefore, the third braid section has a length of $l_3 = l_P$, whereas the remaining can vary according to the following equation,

$$l_i = \xi_{b,i} l_P, \qquad \{\xi_{b,i} \in \mathbb{R} | 0 < \xi_{b,i} < 1\}, \qquad i \in \{1, 2\}. \tag{9.5}$$

For the braid angles, the following equation has been implemented

$$\varphi_i(r) = \varphi_S^{(i)} + \alpha^{(i)} r + \left(\frac{\varphi_E^{(i)} - \varphi_S^{(i)}}{l_i^2} - \frac{\alpha^{(i)}}{l_i} \right) r^2, \qquad i \in \{1, 2, 3\}, \tag{9.6}$$

where r is a coordinate axis aligned with the blade axis as illustrated in figure 9.5 and α parametrizes the slope at $r = 0$, hence:

$$\left. \frac{\mathrm{d}\varphi_i}{\mathrm{d}r} \right|_{r=0} = \alpha^{(i)}, \qquad i \in \{1, 2, 3\}. \tag{9.7}$$

Again–as shown in section 8.1.3–the braid material model is embedded within the structural simulation as well. Here, it is being determined within the Abaqus CAE preprocessing by reading in the meta-model of the homogenized meso scale. This model is parametrized in the braiding angle, yarn width and thickness of the braid. With table 9.1, the solution sequence as implemented in the FEA is given. As illustrated there, first mechanical stability, i.e. buckling analysis, is evaluated for both load cases: maximal thrust and windmilling. This first step, is however an optional step, meaning it is only being evaluated in verification runs and not throughout the entire optimization, since instabilities do in most cases not occur. This is mainly because of the high centrifugal forces acting in both load cases. Subsequent to this step, a static analysis for both load cases is conducted. These steps aim towards the evaluation of failure and the determination of the deflection at the propeller's tip together with the rotational deflection along the propeller blade. These deflections will later be used to obtain insight on whether or not aeroelastic effects are likely to interfere in a negative fashion. Failure is evaluated based on a failure envelope determined by strength characteristica determined through the meso scale model, where Puck has been used as the failure criteria for the fiber tows and max strain respectively for the matrix. Lastly, a frequency analysis is conducted, where all modal properties of the propeller are computed. It is worth mentioning, that the rotary stiffening caused by the high rotation speeds are taken into account therein.

Table 9.1.: Overview on the solution sequence as implemented

Step	Pressure field	Remarks
(Buckling LC1)	Maximal thrust	Optional step
(Buckling LC2)	Windmill	Optional step
Static LC2	Windmill	Evaluation of failure and stiffness
Static LC1	Maximal thrust	Evaluation of failure and stiffness
Frequency step	-	Rotary stiffening is considered

For all steps, the propeller is properly clamped at $r = 0$, where an widening of the propeller's root at that clamp is of course not suppressed. The revolution is either set to 2100rpm for the max thrust case or to 955rpm for the windmilling. So summing up, available optimization responses–thus, responses passed from the structural simulation to the optimization model–are:

- tip deflection for static loading of both LCs
- torsional deflection for static loading of both LCs
- failure indices for static loading of both LCs
- first ten eigenfrequencies
- critical buckling factors of both LCs (optional)

Beside those listed optimization responses, several parameters and geometric quantities are further defined as responses, since they are needed for the computation of the manufacturing effort and are therefore piped to the manufacturing effort model (see figure 4.9).

9.1.4. Evaluating the initial design

With figure 9.6a and figure 9.6b, the braiding angles $\varphi_i(r)$ and thickness $t(r)$ distribution of the initial design is given.

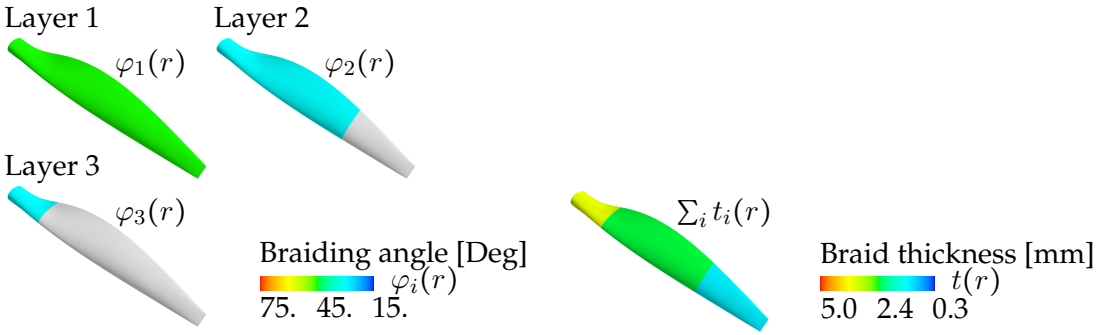

(a) Braiding angle $\varphi_i(r)$ of layer i (b) Total braid thickness $t(r)$

Figure 9.6.: Initial design of the propeller

Note, individual braid thickness of each braid layer $t_i(r)$ are summed up, such that the total braid thickness is obtained, i.e. $t(r) = \sum_i t_i(r)$. Conducting a modal analysis for this first design reveals the natural frequencies as given with table 9.2 and the modal shapes as illustrated with figure 9.7. The modal shapes as illustrated in figure 9.7 appear to be plausible. However, to get a precise insight on whether or not the modal characteristics are properly computed they are here put into context with the help of a so called Campbell diagram. This diagram, which is also referred to as inference diagram, supports engineers in finding resonance frequencies. The Campbell diagram of the initial design is plotted with figure 9.8, where the first and second eigenfrequency of the propeller are given in red and blue and the citation frequencies–here originating from the shaft's revolutions–of first order in black and the one of second order with the dashed black line. As can be seen in figure 9.8, the initial design has a resonance of second order at roughly 1600rpm. This is not as severe as if it would display resonance of first order, since the amplitude and hence the energy of the citation is way smaller, but is still somewhat less than perfect.

Table 9.2.: Eigenfrequencies of the first three modes

Mode 1	Mode 2	Mode 3
57Hz	114Hz	220Hz

Last but not least, the response of the manufacturing effort model is evaluated for this initial design as well. The total manufacturing effort e is computed via equation (9.8), with $\dot{e}_i$ being the effort density of braid layer i and $A_{\mathrm{P},i}$ the corresponding propeller surface. The manufacturing effort

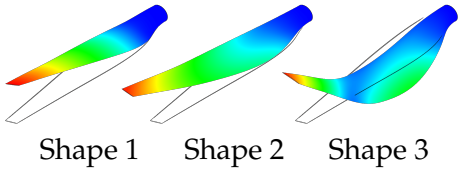

Figure 9.7.: The first three modal virbration shapes

e has been computed to be 49.6 for this case. Figure 9.9 depicts the individual contributions via the effort densities $\dot{e}_i$. This illustration reveals, that this initial design also offers huge potential in terms of reducing associated manufacturing effort. This especially holds for layer one and two, where for instance an unrealistic ratio of take-up and angular horn gear speed–in tandem with the yarn's geometric quantities–cause the braid to open and ultimately to an unserviceable propeller.

$$e = \sum_i \frac{\int_{A_{\mathrm{P},i}} \dot{e}_i \mathrm{d}A}{\int_{A_{\mathrm{P},i}} \mathrm{d}A} \tag{9.8}$$

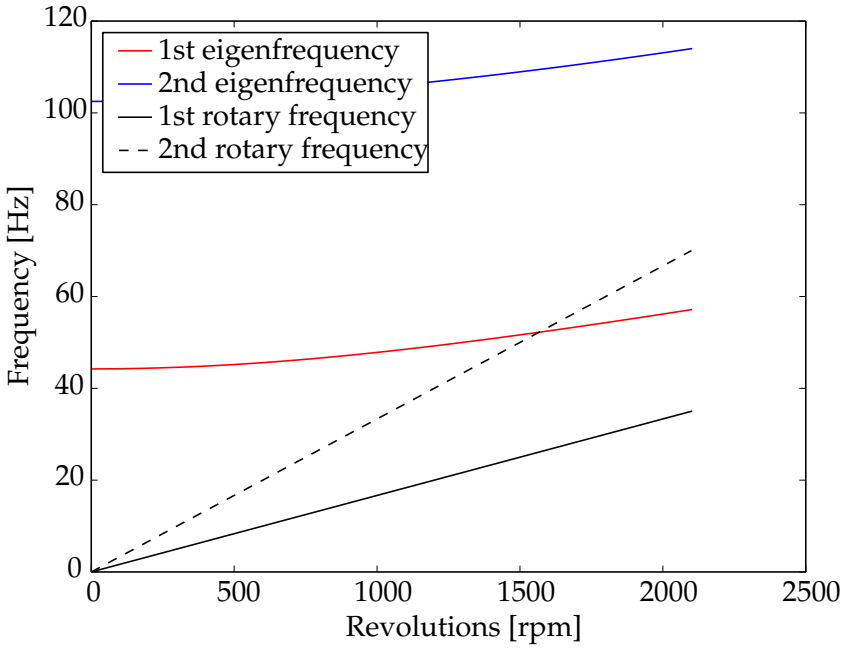

Figure 9.8.: Campbell diagram for the initial design of the propeller

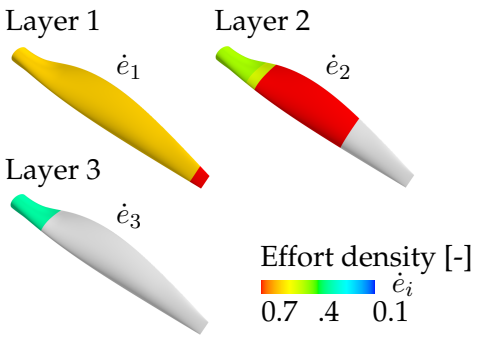

Figure 9.9.: Manufacturing effort density $\dot{e}_i$ for each layer i

9.1.5. Definition of the optimization task

The vector optimization task for the propeller demonstration example can be defined as follows,

$$\begin{aligned} \underset{x\in\chi}{\text{minimize}} \quad & f_i(x_j), && i = 1,\dots,n_{\mathrm{O}}, j = 1,\dots,n_{\mathrm{DV}} \\ \text{subject to} \quad & g_l(x_j) \le 0, && l = 1,\dots,n_{\mathrm{IC}} \\ \text{with} \quad & \chi = \{x_j \in \mathbb{R}^{n_{\mathrm{DV}}} : x_j^l \le x_j \le x_j^u\}. \end{aligned} \tag{9.9}$$

$$g_1(\vec{x}) = \frac{F_h}{F_{h,\mathrm{Max}}} - 1 \qquad \text{Hub force}$$

$$g_{2,\dots,11}(\vec{x}) = 1 - \frac{60\omega_{1,\dots,10}}{2\pi n_{\mathrm{P,Max}}} \qquad \text{Resonance behavior}$$

$$g_{12,\dots,14}(\vec{x}) = \frac{u_{\mathrm{Tip,LC1}}}{u_{\mathrm{Tip,LC1,Max}}} - 1 \qquad \text{Aeroelastic interactions}$$

$$g_{15,\dots,14+n_{\mathrm{Sec}}}(\vec{x}) = \frac{\mathcal{FI}_{\mathrm{LC1},s}}{0.9} - 1 \qquad \text{Failure for max thrust load case } \forall s \in \{1,\dots,n_{\mathrm{Sec}}\}$$

$$g_{15+n_{\mathrm{Sec}},\dots,14+2n_{\mathrm{Sec}}}(\vec{x}) = \frac{\mathcal{FI}_{\mathrm{LC2},s}}{0.9} - 1 \qquad \text{Failure for windmill load case } \forall s \in \{1,\dots,n_{\mathrm{Sec}}\}$$

g_1 simply imposes an upper bound onto the hub force F_h and thus restricts the maximal clamp force which is solely influenced by the mass of the propeller. The constraints two to eleven ensure that the propeller is not excited by the rotary frequency while in operation. This is realized by restricting the first ten eigenfrequencies of the propeller. For the accurate computation of these eigenfrequencies, it is important, to take the centrifugal stiffening caused by the rotation into consideration. The rotary frequency f_R can be computed based on given revolution n_P in rounds per minute of the propeller with equation (9.10), where ω_P is the angular frequency.

$$f_R = \frac{\omega_P}{2\pi} = \frac{n_P}{60} \tag{9.10}$$

These resonance constraints are followed by constraints ensuring that the deflection of the propeller blade's tip is small enough, such that negative aeroelastic interactions are likely to not occur. Last but not least, structural integrity is ensured by the constraints $g_{15,\dots,14+n_{\mathrm{Sec}}}(\vec{x})$ for the maximal thrust load case and $g_{15+n_{\mathrm{Sec}},\dots,14+2n_{\mathrm{Sec}}}(\vec{x})$ for the windmill load case. It is important to note, that failure has been evaluated for several sections along the propeller blade axis to ensure proper convergence of the optimization. Thus, for each load case, failure indicies $\mathcal{FI}_{\mathrm{LC1/2,s}}$ are computed and monitored for each section s, i.e. $\forall s \in \{1,\dots,n_{\mathrm{Sec}}\}$. The objective functions f_i will be defined right before each optimization outcome in the following subsection. Design variables and the design space they span are given with the next table. In this table, $\vec{x}$, $\vec{x}^l$, $\vec{x}^u$ and ID refer to the vector of design variables, the lower and upper bound for the design variables and the associated identification number.

9.2. Design optimization of the braided propeller

In this section, multiple variations and post-processing possibilities for multi-criteria optimizations– especially with focus on the introduced gradient-based approach of section 6.2–will be realized and studied on the sophisticated structural design problem: the braided propeller.

Table 9.3.: Definition of the design space for the propeller problem

$\vec{x}$	$\vec{x}^l$	$\vec{x}^u$	Unit	ID
$\varphi_S^{(3)}$	15.	75.	DEG	1
$\varphi_E^{(3)}$	15.	75.	DEG	2
$\alpha^{(3)}$	-100.	-100.	DEG/mm	3
t_3	1.	8.	mm	4
$\varphi_S^{(2)}$	15.	75.	DEG	5
$\varphi_E^{(2)}$	15.	75.	DEG	6
$\alpha^{(2)}$	-100.	-100.	DEG/mm	7
t_2	1.	8.	mm	8
$\xi_{b,2}$	.5	.75	-	9
$\varphi_S^{(1)}$	15.	75.	DEG	10
$\varphi_E^{(1)}$	15.	75.	DEG	11
$\alpha^{(1)}$	-100.	-100.	DEG/mm	12
t_1	1.	8.	mm	13
$\xi_{b,1}$	.2	.5	-	14

9.2.1. Multi-criterial optimization of manufacturing effort, mass and frequency

Gradient-based vector optimization on the criteria mass and eigenfrequency

The first structural design problem is defined by the two competing objectives: propeller's mass m and smallest eigenfrequency ω_1, where mass is obviously minimized whereas the eigenfrequency will be maximized. The following set of equations (9.11) represent the gradient-based vector optimization approach, with κ being the objective weight and also a decision variable, g_{BS} the back-stepping constraint and h_γ the equidistant constraint. Aside, both additional constraints are discussed in section 6.2 and 7.1, illustrated in figure 7.1 and stated with equation (6.11) already. The constraints and the design space are retained as priorly defined in section 9.1.5. With the following figure 9.10, the iteratively obtained solution of the condensed vector optimization task (9.11) is given. As depicted there, the Pareto frontier has been approximated by nine points, i.e. $n_P = 9$. Moreover, it is now evident, that both objectives are competing, since a pronounced convex Pareto frontier forms, being, here approximated by the nine Pareto efficient solutions. Specifically, the change in mass from one extremal solution to the other numbers $\Delta m = 1.7\text{kg}$ or 36 % and respectively for the frequency $\Delta\omega_1 = 34\text{Hz}$ or 97 %. The following sub-figure 9.11a is given to illustrate the approximated Pareto frontier in the physical space, by plotting the first natural frequency ω_1 over the propeller's mass m. Physically speaking, the fact that both criteria are competing can be made plausible by the fact, that adding mass at the root of the propeller blade enhances its performance in terms of dynamics, even though it might not be needed in terms of strength. Figure A.9b in the appendix provides insight on the frequency optimal thickness distribution of the braid layers. In addition to the computed Pareto frontier, figure 9.11 provides insight how the objective function weights κ evolve over the discretely computed Pareto optimal solutions $\vec{f}^p$ with sub-figure 9.11b. This plot shows, how the weights erratically change near the extremal solutions and how they become almost constant in-between. The constant level is thereby roughly 0.7. This again highlights, how difficult it can be to set most suitable objective weights a priori.

$$\begin{aligned} \underset{x,\kappa}{\text{minimize}} \quad & \tilde{f} = \kappa m - (1-\kappa)\omega_1 \\ \text{subject to} \quad & g_{1,\dots,14+2n_{\text{Sec}}} \leq 0, \\ & g_{\text{BS}} \leq 0, \\ \text{and} \quad & h_\gamma = \gamma^2, \\ \text{with} \quad & \vec{x} \in \chi \text{ and } \kappa \in [0,\dots,1] \end{aligned} \tag{9.11}$$

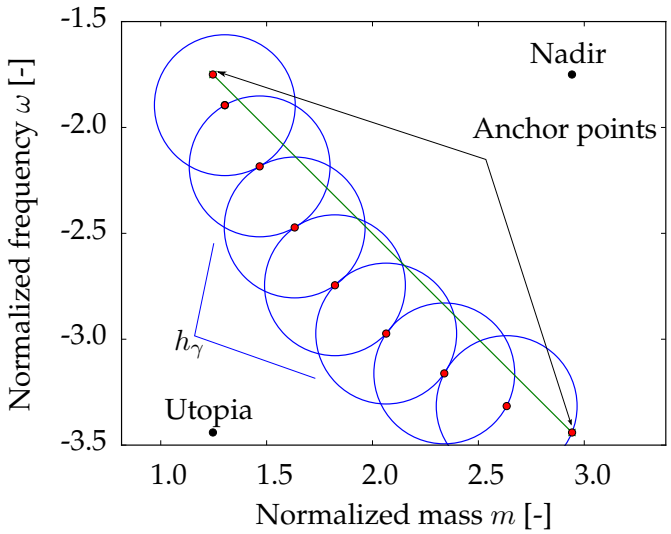

Figure 9.10.: Direct result of the Pareto computation via equation set (9.11)

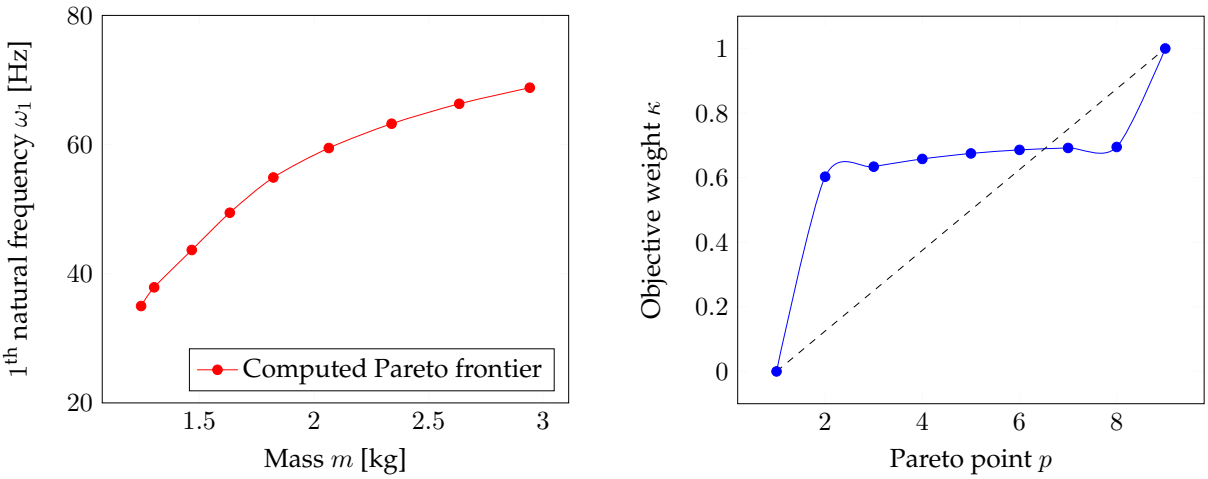

(a) Approximation of Pareto frontier

(b) Plot of objective weights κ

Figure 9.11.: Pareto frontier (a) and weights (b) for mass m and frequency ω

Since it has been shown via the first Campbell diagram (see figure 9.8), that the first natural frequency could be excited by the second shaft rotary frequency, the dynamical performance is solely being discussed for the maximum natural frequency design. Besides, the mass is here considered to be a less relevant design criteria, because it mainly contributes to the magnitude of the reaction forces at the hub, which are however for almost any design tolerable and furthermore no other gains are observable when minimizing the mass. Before the dynamics of the maximum frequency design are discussed, the braiding angle distributions for this design are given with the following figure 9.12. For this design, evincing a maximal natural frequency ω_1–thus being on the outer upper right of the

Pareto frontier in sub-figure 9.11a–more information is being given in the the appendix A.6. In this appendix section, figure A.9a depicts the braider yarn width $w_i^{(b)}(r)$ and figure A.9b the thickness distribution $t_i(r)$.

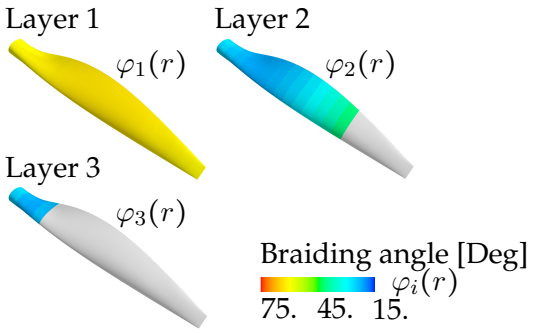

Figure 9.12.: Braiding angle $\varphi_i(r)$ for each layer i of the maximum natural frequency design

Modal performance and Imprint of the braider yarn onto the optimal propeller design

Figure 9.13 provides the Campbell diagram for this design. As can be seen there, the situation improved significantly, because the first and evidently also the second natural frequency do not anymore intersect with any of the rotary frequencies–hence, not the first nor the second rotary frequency given in black–over the whole revolutions range.

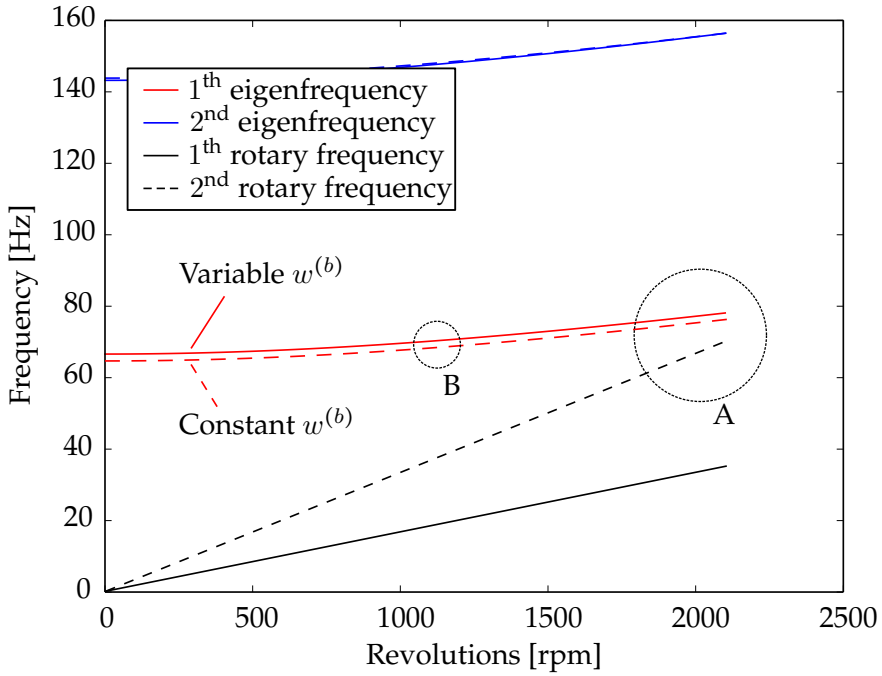

Figure 9.13.: Campbell diagram for the maximum frequency design; depicting the influence of the braider yarn width $w^{(b)}$

So, the afore critical area, highlighted by an A in figure 9.13, has been mitigated by elevating the first natural frequencies through the conducted design optimization. Beside this information, figure 9.13 also provides insights on the influence of the braider yarn width $w^{(b)}$ and especially its computation via the directly integrated material meta-model. As a side mark, the material model has been defined via equation (8.2) and for each entry via equations according to (8.3). Each of those entries

are thereby determined by the meta-model of the meso cell homogenization (see figure 5.3). By default, the model has been set up in such a fashion, that it automatically computes the corresponding braid parameters, such as braider yarn width $w^{(b)}$, for a given geometry situation. However, to underpin the influence arising from the fact, that the braid parameters are interwoven with the geometry of the current design, the braider yarn width $w^{(b)}$ is set constant for once. The outcome of this, is given by the red dashed line in figure 9.13. Despite the fact, that $w^{(b)}$ has only been set to be constant to a technically reasonable value, one can clearly observe the difference. This difference would become even more distinct, once the braider yarn width would go to extremer values.

The numerical performance of the gradient-based vector optimization approach

Now, the numerical performance of the used approach shall be assessed. For doing so, the result obtained via the gradient-based vector optimization approach have been compared with a widely used alternative: the genetic algorithm NSGA-II. This genetic algorithm has a tournament selection-based fitness evaluation, enabling it with the capability of solving multi-objective optimization problems. The population size n_{pop} and the number of generations n_{gen} has been varied so as to leverage the comparability. In figure 9.14, one can find the plots of the obtained results. Before the results are actually compared, the optimality of the outcomes will be assessed first. In section 6.2.3, a measure for determining optimality being compliant to numerical imprecision has been introduced, the first oder optimality $\mathcal{O}$. It was basically defined as the norm of the stationary of the Lagrangian function and complementary slackness.

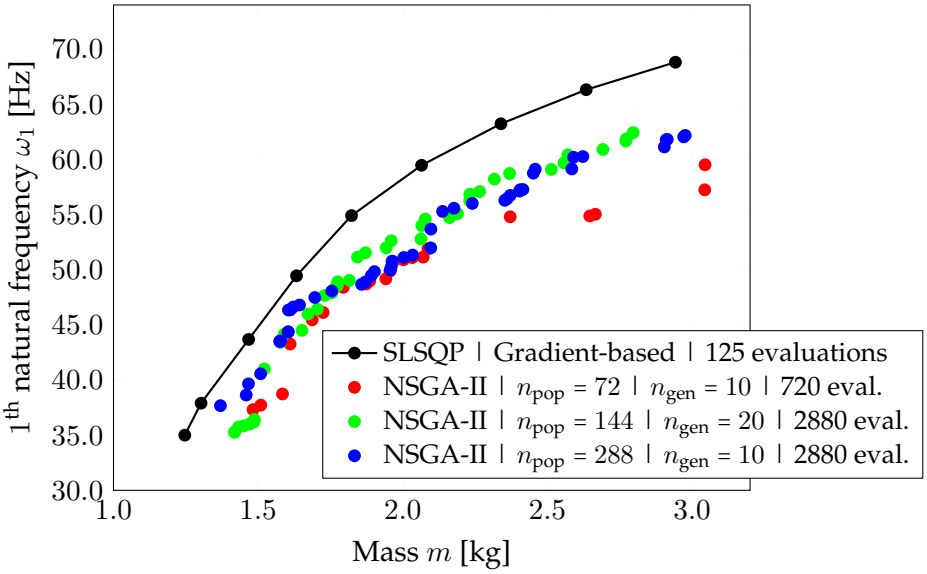

Figure 9.14.: Contrasting the gradient-based approach with a genetic algorithm
Maier (2015)

In the following figure 9.15, this first order optimality $\mathcal{O}$ is plotted for every computed Pareto efficient solution p. As can be observed with ease, the first order optimality $\mathcal{O}$ takes throughout the whole set of solutions small values. Coming back to the comparison of the outcomes, the black line in figure 9.14 highlights the results computed via SLSQP, thus second order gradient-based. Knowing that for each computed Pareto point p optimality can be stated ($\mathcal{O}$ is numerically zero as in figure 9.15) each computed point p is a Pareto efficient solution and can hence collectively be regarded to be a reasonable good approximation of the Pareto frontier. For the sake of comparison, several optimal populations obtained by the NSGA-II algorithm are plotted in the same figure, where the colors refer to different settings. At the first glance, the genetic algorithm lead to a denser approximation of the frontier. However, the approximation is considerably inferior, because each of the derived optima

is being dominated. In addition to that, for the NSGA-II algorithm to *converge* (strictly speaking no convergence observable!), significantly more system evaluations are needed, e.g. the blue frontier did need more than twenty three times the system evaluations and thus numerical analyses than the gradient-based approach. This leveraged the computation times from a couple of hours (3h : 47min) to days (3d : 14h : 17min). This becomes even worse for a large design space. This has, by the way, been the reason, why the genetic algorithm has not been applicable with reasonable computational effort for the A-pillar example. Further it has been observed, that a certain population size is needed such that the individuals of the optimal population representatively approximate the Pareto frontier. This becomes evident, when studying the outcome of the smallest population (72 individuals and red dots in plot), where the approximation of the frontier is rather dilute.

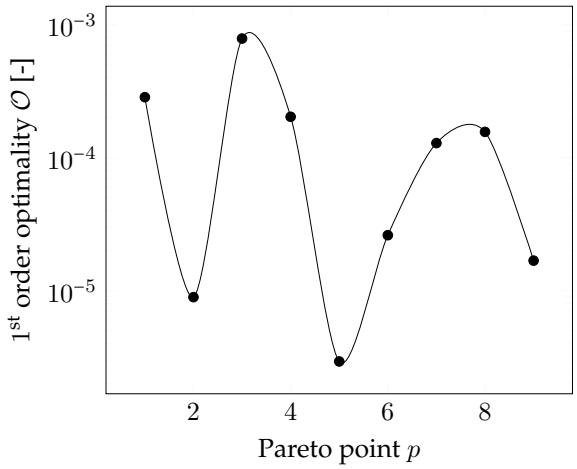

Figure 9.15.: First oder optimality $\mathcal{O}$ as introduced via equation (6.14) and associated with the vector optimization problem (9.11)

Despite all these mentioned shortcomings it should be mentioned as well, that for the genetic algorithm to work, almost no effort in terms of modeling has to be made, which is definitely expedient in many industrial applications. Besides, in the appendix section A.7 the utility U is evaluated for both, the gradient-based approach and the genetic algorithm. By studying the different utility curves in figure A.12 and the pronounced oscillations, again confirms that the genetic algorithm approach performs inferior in providing information for the necessary decision making. This is because, the gradient-based approach points to a distinct Pareto efficient solution (roughly in the middle), whereas the genetic algorithm identifies a whole range of maximal utility.

Incorporating manufacturing effort into the vector optimization

For the derived design almost every structural aspect has improved, e.g. maximal eigenfrequency, while still fulfilling all structural requirements. On the contrary, studying the technical aspects of this design in terms of manufacturing reveals a high associated effort. This is described by the developed manufacturing effort model (MEM), whose responses are given by figure 9.16. The individual effort levels turn out that high, since the MEM did predict a braid opening for the current configuration. Therefore the braider yarn width is going beyond $3.5\mathrm{mm}$ in some regions and in others way underneath the threshold of $2.0\mathrm{mm}$ (figure A.9a). To address this high level of effort while still maintaining the satisfying dynamical performance, the multi-criteria optimization problem is redefined to (9.11). There, the first objective is substituted by the MEM's response effort e, so as to compensate for the high associated manufacturing effort of the prior design. This objective is of course minimized while the smallest eigenfrequency ω_1 is still maximized.

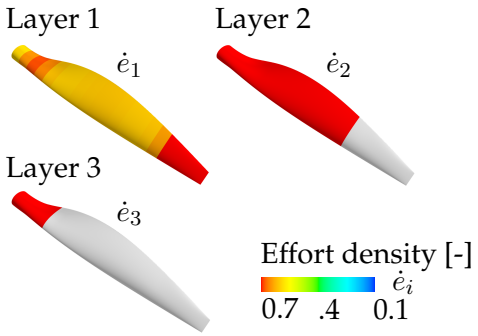

Figure 9.16.: Effort densities $\dot{e}_i(r)$ for each layer i of the maximum natural frequency design

$$\begin{aligned} \underset{x,\kappa}{\text{minimize}} \quad & \tilde{f} = \kappa e - (1-\kappa)\omega_1 \\ \text{subject to} \quad & g_{1,\dots,14+2n_{\text{Sec}}} \leq 0, \\ & g_{\text{BS}} \leq 0, \\ \text{and} \quad & h_\gamma = \gamma^2, \\ \text{with} \quad & \vec{x} \in \chi \text{ and } \kappa \in [0,\dots,1] \end{aligned} \tag{9.12}$$

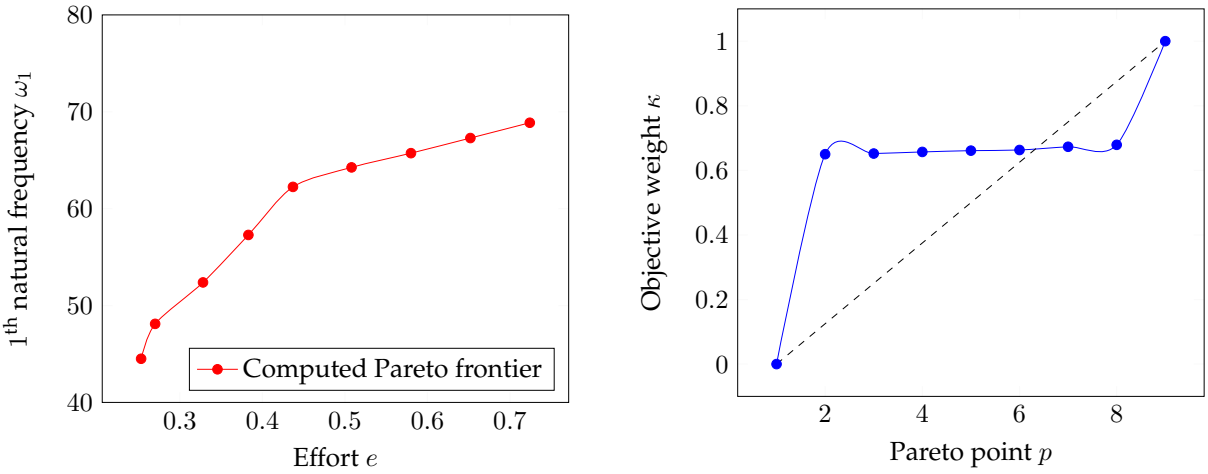

(a) Approximation of Pareto frontier

(b) Plot of objective weights κ

Figure 9.17.: Pareto frontier (a) and weights (b) for effort e and frequency ω

Figure 9.17 depicts the solution of the re-conducted optimizations, where again the continuous Pareto frontier has been approximated by nine $n_P = 9$ Pareto efficient solutions. The thereby computed Pareto frontier approximation is illustrated with sub-figure 9.17a. As can be observed, both objectives, ω_1 and e are competing as well, wherefore substantial differences between both extremal solutions or ends of the Pareto frontier can be observed. Analogously to before, a plot, providing insight on the distribution of the objective weight $\kappa(p)$ over the Pareto points is given by sub-figure 9.17b. Once more, the distribution of those weights is far from being intuitive and thus predictable a priori. One design of the derived nine design has been identified to represent an optimal compromise. This design is given by the following figure 9.18, where its braiding angle distribution $\varphi_i(r)$ for each braid layer i is given. In the appendix section A.6, figures A.10a, A.11 and A.10b reveal more detail by plotting the braider yarn width distribution $w^{(b)}(r)$, braid thickness distribution $t(r)$ and the corresponding effort densities $\dot{e}_i$. Next, the precise and profound post-processing of the so far conducted vector optimization is presented.

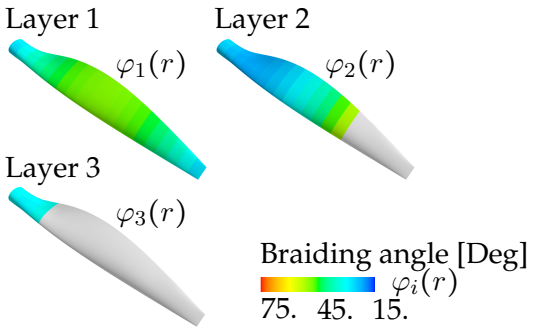

Figure 9.18.: Braiding angle $\varphi_i(r)$ for each layer i of the effort-frequency-compromise design

9.2.2. Post-processing of vector optimizations

First, the sensitivity of one entry of the objective vector to another entry, i.e. $\frac{\partial f_2}{\partial f_1}$ will be derived and discussed. Thereafter, the linearizion based on the available shadow prices will be shown for a general vector optimization problem statement. In section 2.2, optimality has been mentioned first. There, the optimality has been discussed via the Karush-Kuhn-Tucker conditions, which are in principle founded on the stationarity condition of the Lagrangian function, thus $\delta\mathcal{L} \stackrel{!}{=} 0$ (equation 2.2 and following). In general, this can analogously be applied to any of the priorly defined multi-criteria optimization problems. However, to leverage the discussion on a general level, the following abstract definition of a scalarized objective $\tilde{f}$ with the two objective f_1 and f_2 is made,

$$\tilde{f} = \kappa f_1 + (1-\kappa) f_2. \tag{9.13}$$

Using this and further requiring the Lagrangian function $\mathcal{L}$ to be stationary, leads to the following expression:

$$\delta\mathcal{L} \stackrel{!}{=} 0 = \kappa\delta f_1 + (1-\kappa)\delta f_2 + (f_1 - f_2)\delta\kappa + \mu\delta h_\gamma + \sum_l \lambda_l \delta g_l \tag{9.14}$$

Rearranging this, such that the desired partial derivative of f_2 with respect to f_1 can be determined, results in the following equation (9.15). It appears, that the partial derivative is directly defined via the objective weight variable κ. This has already been discussed by Baier (1978).

$$\frac{\delta f_2}{\delta f_1} \stackrel{\delta\to 0}{=} \frac{\partial f_2}{\partial f_1} = \frac{\kappa}{\kappa - 1} \quad \text{while} \quad \delta\kappa = \delta h_\gamma = \delta g_l \stackrel{!}{=} 0 \tag{9.15}$$

However, it should kept in mind, that this only holds in case neither of the constraints nor the objective weight variable κ itself is changed, i.e. $\delta\kappa = \delta h_\gamma = \delta g_l$=0. This basically means, that the sensitivity of one objective to another competing objective can only be computed by κ, if no change in the constraints and objective weights is expected. Or in other words, using equation (9.15) to extrapolate solutions on the Pareto frontier is only valid if none of the constraint levels is being altered, thus $\delta h_\gamma = \delta g_l$=0 and if the change in the objective weight is neglect-able $\delta\kappa$0. This will now be discussed for the analytical vector optimization problem as given via equation set (7.3) in section 7.1, where figure 7.2 did reveal the accurate approximation of the Pareto frontier. The fact that the Pareto frontier is given analytically by equation (7.5), also enables the analytical computation of the derivative $\frac{\mathrm{d}f_2}{\mathrm{d}f_1}$. This derivative is given in the following figure 9.19 by the red dashed line. In this figure, the approximation based on the objective function weights κ, as suggested by the statement

(9.15), is given by the blue dashed line. Obviously, the direction and the magnitude of both derivatives are quite alike, which is why, their error in percent, in figure 9.19 illustrated via the black line plot, is rather small. For the sake of completeness, the plot of objective function weights is given in the appendix section A.4.

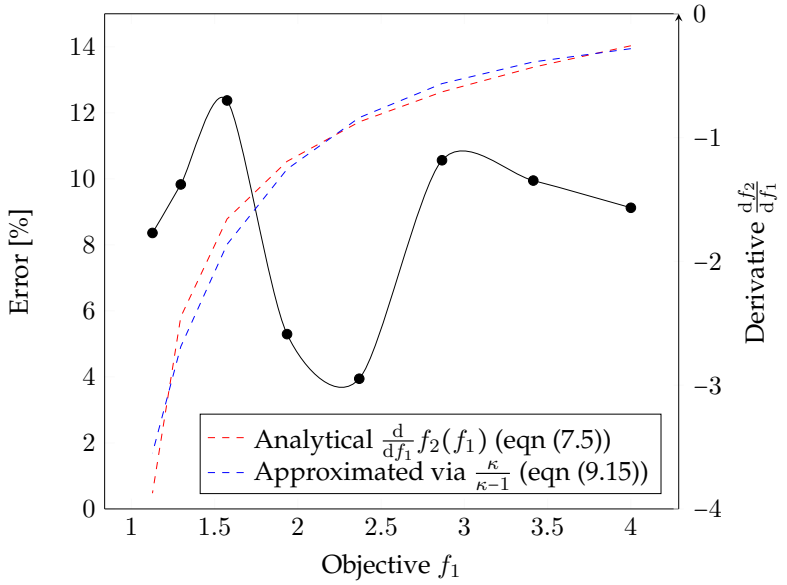

Figure 9.19.: Comparison of the two methods for computing $\frac{df_2}{df_1}$ for the analytical example

Despite this promising rendering of the derivative in direction and magnitude, this approach can result in an insignificant prognosis, because the approximation did show to be quite sensitive towards the underlying numerics, by being mal-conditioned. Thus, a small change in the used algorithm settings aggregates in huge and almost erratic changes in the prediction, even though, the objective function values do not change much. For this reason, another approach for determining the whole Pareto frontier and for extrapolating additional solutions will be presented next. As already illustrated for the simple analytical test, the set of all Pareto efficient solutions Ω_E, or in this case as well the Pareto frontier Ω_P, can be accurately approximated by the outlined gradient-based approach, by iteratively solving for the n_P Pareto efficient solutions. This cumulated in negligible approximation errors as given with table 7.1. Further, for the structural vector design optimization the computed Pareto frontier did display a pronounced strict convexity of almost quadratic shape. Accumulating these mentioned properties of high approximation accuracy and convex shape, clearly points to the direction of utilizing a polynomial regression to describe the Pareto frontier, thus to solve for the coefficients a_i in the following equation,

$$f_2(f_1) \simeq a_2 f_1^2 + a_1 f_1 + a_0. \tag{9.16}$$

This will here be done for the multi-criteria optimization problem given by (9.11), hence, where mass and natural frequency did serve as the optimization criteria. The red points in figure 9.20 show the computed Pareto efficient solutions and the blue line represents the polynomial regression. For this representation of the Pareto frontier, partial derivatives can be computed, as given with equation set (9.17), where the derivative is computed for the Pareto point A as depicted in figure 9.20.

$$\begin{aligned} f_2(f_1) &\simeq \left(-11.369 f_1^2 + 66.713 f_1 - 29.782\right) \mathrm{Hz} \\ \left.\frac{\partial f_2}{\partial f_1}\right|_A &= \left(66.713 - 22.738 f_1\right)|_{f_1=1.8} \frac{\mathrm{Hz}}{\mathrm{kg}} = 25.785 \frac{\mathrm{Hz}}{\mathrm{kg}} \end{aligned} \tag{9.17}$$

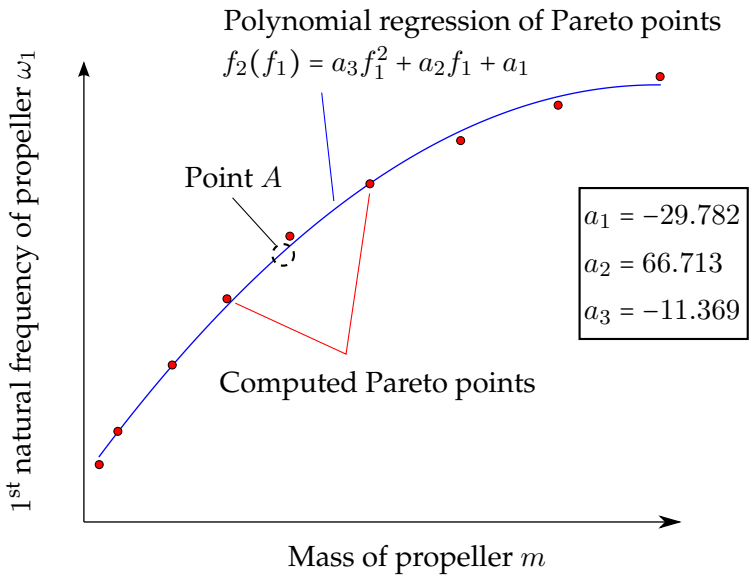

Figure 9.20.: Response surface approximation of the Pareto front

This derivative $\frac{\partial f_2}{\partial f_1}\Big|_A$ reveals at this point, that adding half a kilogram more to the propeller design will further increase the first natural frequency by roughly thirteen Hertz. This approach for determining the derivative or extrapolating via meta modeling is by far more effective. This can also be comprehended by considering the following figure 9.21, where the derivative given by the meta model is contrasted to the derivative approximated by equation (9.15). As observable, despite the fact, that the directions of the derivatives point into the same direction, they are of no use, since, the error is now way beyond an acceptable level. Through multiple optimization runs, it has been observed, that the objective function weights κ are quite sensitive with respect to the choice of optimization algorithm, e.g. NLPQLP or MMA, to the convergence tolerances and alike. For these reasons, the estimation of the Pareto derivative $\frac{\mathrm{d}f_2}{\mathrm{d}f_1}$ based on equation (9.15) is not advisable for structural design problems as discussed herein. Instead, the surrogate modeling of Pareto frontiers–as for instance via equation (9.16)–is recommended.

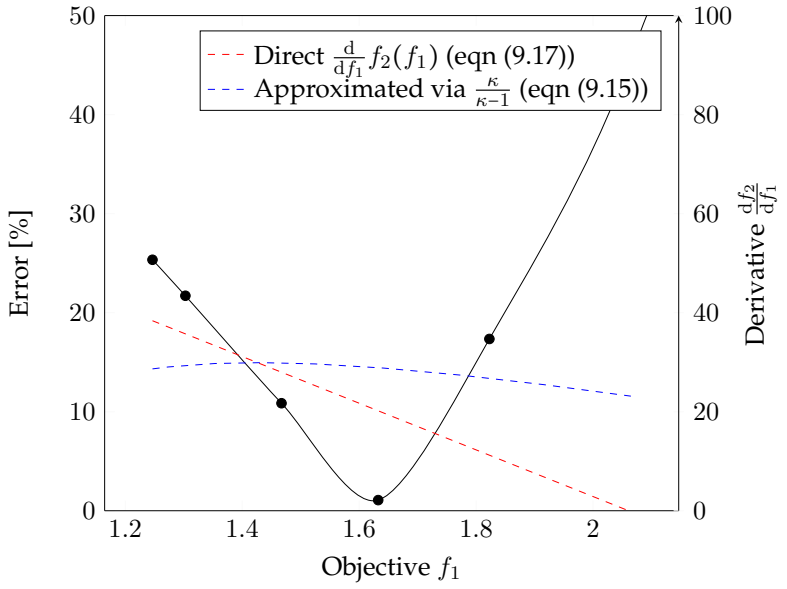

Figure 9.21.: Comparison of the two methods for computing $\frac{\mathrm{df}_2}{\mathrm{d}f_1}$ for the scalarized propeller vector optimization, i.e. $f = \kappa m - (1-\kappa)\omega_1$

Now, two further advantageous features of the gradient-based approach for computing the equidistant Pareto frontier are discussed: the accessibility of optimality and the possibility to linearize at an optima based on shadow prices. The first is self-evident, since all gradients are computed and also due to that the vector optimization problem is scalarized to one single objective. This is why, the Karush-Kuhn-Tucker conditions can be applied and probed for every Pareto optimal point. The optimality has already been given by figure 9.15, where the first order optimality as a norm of all equations (2.3) is plotted over the Pareto optimal points p. As can be seen, each of the Pareto optimal points can be regarded to be optimal because all norms are numerically zero. The second feature, the linearization of one optimization response at the optimum with respect to one active constraint level is discussed next. For doing so, the Pareto optimal solution $\vec{f}^4$ is picked. At this Pareto point, the first natural frequency ω_1 is linearized with respect to the constraint level $u_{\text{Tip,LC1,Max}}$ of constraint g_{13}, which restricts the displacement of the rotor blade's tip. The following equations show the conducted linearization. As can be computed, loosen the constraint level for the tip displacement by five perfect would result in an additional gain of seven Hertz.

$$\begin{aligned}
\text{Lin}(\omega_1)(\Delta u_{\text{Tip,LC1,Max}}) &= \omega_1\big|_{\vec{x}^{\text{opt}}} + \frac{\partial \omega_1}{\partial u_{\text{Tip,LC1,Max}}} \Delta u_{\text{Tip,LC1,Max}}. \\
&= \underbrace{\omega_1\big|_{\vec{x}^{\text{opt}}}}_{54.9\text{Hz}} + \underbrace{\frac{\partial \omega_1}{\partial \tilde{f}}}_{(\kappa-1)^{-1}} \underbrace{\frac{\partial \tilde{f}}{\partial g_{13}}}_{-\lambda_{13}} \underbrace{\frac{\partial g_{13}}{\partial u_{\text{Tip,LC1}}}}_{\frac{1}{u_{\text{Tip,LC1,Max}}}} \underbrace{\frac{\partial u_{\text{Tip,LC1}}}{\partial u_{\text{Tip,LC1,Max}}}}_{1} \Delta u_{\text{Tip,LC1,Max}} \\
&= 54.9\text{Hz} + 1.4 \tfrac{\text{Hz}}{\%} \Delta u_{\text{Tip,LC1,Max}}
\end{aligned} \tag{9.18}$$

9.2.3. Considering braiding time as a bridge towards costs

In this subsection, a progression towards the incorporation of a cost model into the multi-criteria design optimization process will be discussed. The canonical basis for achieving this progression, is in the context of braiding, the manufacturing time. And one huge fraction of the overall manufacturing time, is influenced by the take-up speed of the mandrel V_T^i and can thus be expressed for each braid layer i as follows,

$$T_\varphi^i = \int \frac{1}{V_T^i} \mathrm{d}s. \tag{9.19}$$

Since the braiding angle is defined by the ratio of take-up speed and horn gear speed, this braiding time T_φ^i for braid layer i is therefore ascertainable by the braiding angle φ as well. Equation (9.20) depicts the quadrature, thus the numerical integration, of equation (9.19), where the Gaussian quadrature has been chosen as the numerical integration scheme. For the integration of a linear braid angle section one Gauss point ($\varphi \sim s: \; n_{Gauss} = 1$) has been used. Otherwise n_{Gauss} has been set to two and, hence, $\xi_1 = -\sqrt{3^{-1}}$, $\xi_1 = \sqrt{3^{-1}}$ and $w_1 = w_2 = 1$.

$$\begin{aligned}
T_\varphi^i &= \int_{s_1}^{s_{n^i}} \frac{1}{V(\varphi(s))} \mathrm{d}s = \int_{s_1}^{s_{n^i}} \frac{\tan(\varphi(s)) N_h}{2\pi\omega_h r(s)} \mathrm{d}s \\
&= \int_{-1}^{1} \frac{\tan(\varphi(s(\xi)))N_h}{2\pi\omega_h r(s(\xi))} \frac{\mathrm{d}s}{\mathrm{d}\xi} d\xi \approx \sum_{j=1}^{n_{Gauss}} \frac{\tan(\varphi(s(\xi_j)))N_h}{2\pi\omega_h r(s(\xi_j))} \frac{s_{n^i}+s_1}{2} w_j \\
T_\varphi &= \sum_{i=1}^{n_{Layer}} T_\varphi^i
\end{aligned} \tag{9.20}$$

Just for the sake of completeness, an exemplary and frequently used cost model in the context of braiding will be outlined. However, in the subsequent optimization the braiding time T_φ will be set as one objective in the objective vector to preserve general validity. As mentioned earlier, the manufacturing time can be regarded as the canonical basis in the context of braiding. This is why, the manufacturing cost for one single preform can be estimated with equation (9.21), with T_m being the sole machine time, T_w the time of a worker and the constants a_m and a_w. The machine time T_m is composed of the braiding time T_φ and an offset T_0 accounting for the turn-overs, which are necessary after each braid layer. The constants are determined by multiple aspects and do vary from company to company. For instance, aspects determining a_m–amongst further ones–are: possible shift pattern, production period, plant surface costs and capital costs for financing including depreciation methods et cetera.

$$C_\varphi = T_m a_m + T_w a_w = (T_\varphi + T_0) a_m + T_w a_w \tag{9.21}$$

As before, the vector optimization task can be stated as follows, where the eigenfrequency ω_1 is maximized and the braiding time T_φ is minimized, while all structural constraints are still honored.

$$\begin{aligned} \underset{x,\kappa}{\text{minimize}} \quad & \tilde{f} = -\kappa\omega_1 + (1-\kappa)T_\varphi \\ \text{subject to} \quad & g_{1,\dots,14+2n_{\text{Sec}}} \leq 0, \\ & g_{\text{BS}} \leq 0, \\ \text{and} \quad & h_\gamma = \gamma^2, \\ \text{with} \quad & \vec{x} \in \chi \text{ and } \kappa \in [0, \dots, 1] \end{aligned} \tag{9.22}$$

Similarly to before, this vector optimization has been solved nine times ($n_P = 9$), such that the following approximation of the Pareto frontier is yielded. Sub-figure 9.22a depicts the approximated Pareto frontier, whereas sub-figure 9.22b provides the plot of the objective weights κ over the identification number p of each Pareto optimal solution. It has been noted before, that the curve $\kappa(p)$ is far from being intuitive and thus challenging to be defined a priori. This applies for this vector optimization task (9.22) as well. With figure 9.23 a plot showing the first order optimality for each Pareto optimal point p of the approximated Pareto frontier is given.

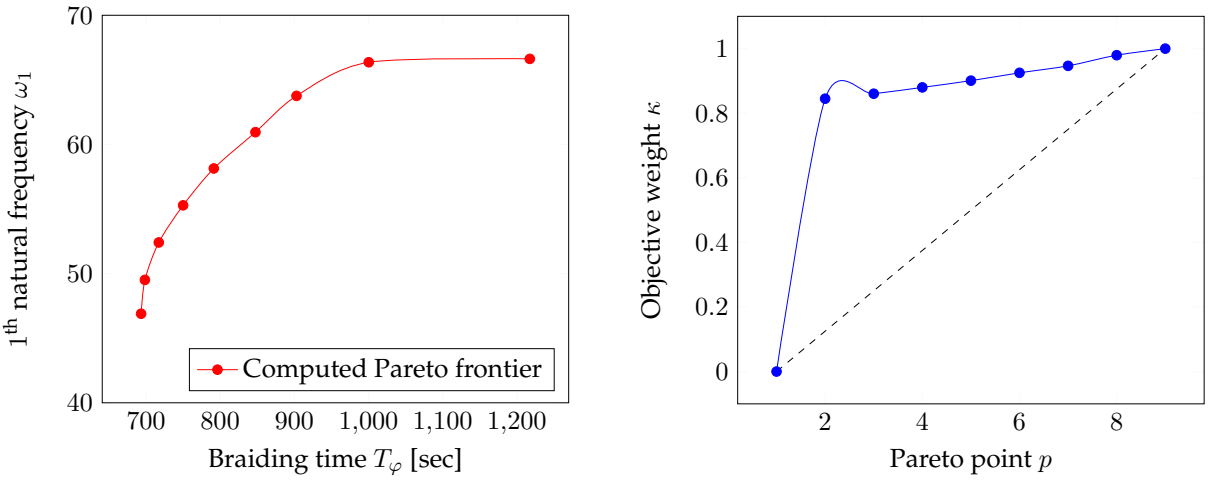

(a) Approximation of Pareto frontier

(b) Plot of objective weights κ

Figure 9.22.: Pareto frontier (a) and objective weights (b) for the criteria braiding time T_φ and frequency ω

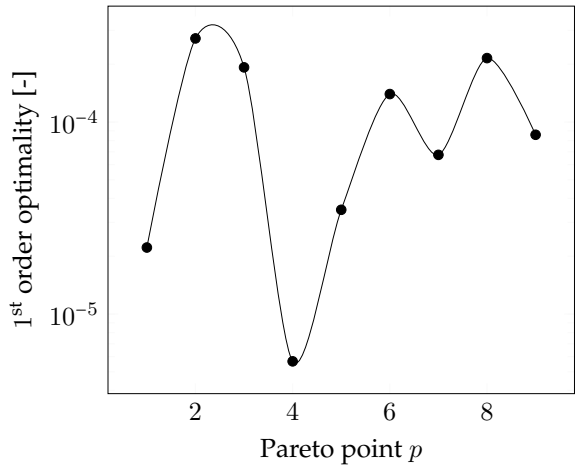

Figure 9.23.: Evaluation of the first oder optimality for the vector optimization problem (9.22)

9.2.4. Tri-objective optimization

Next the propeller optimization task, as posed with equation set (9.9), shall be solved considering three criteria simultaneously. The criteria shall be mass m, effort e and frequency ω. Thus, the optimization task can be stated as follows.

$$\begin{aligned} \underset{\vec{x}}{\text{minimize}} \quad & \vec{f} = [m;\ e;\ -\omega]^T \\ \text{subject to} \quad & \vec{g} \leq 0, \\ \text{with} \quad & \vec{x} \in \chi \end{aligned} \tag{9.23}$$

So as to efficiently solve for the approximation of the Pareto frontier $\Omega_{\tilde{P}}$ this optimization task is first scalarized by objective weights $\vec{\kappa}$. Then four additional constraints are added for ensuring no back-stepping to occur $g_{\text{BS},1/2}$ and that found Pareto efficient solutions are equidistant $h_{\gamma,1/2}$ are added to the optimization task. Last but not least, the optimization task is solved, whilst the objective weights $\vec{\kappa}$ are also considered as design variables.

$$\begin{aligned} \underset{\vec{x},\vec{\kappa}}{\text{minimize}} \quad & \tilde{f} = \kappa_1 m + \kappa_2 e - (1 - \kappa_1 - \kappa_2)\omega_1 \\ \text{subject to} \quad & \vec{g} \leq 0, \\ & g_{\text{BS},1} \leq 0, \\ & g_{\text{BS},2} \leq 0, \\ & h_{\gamma,1} = \gamma_1^2, \\ \text{and} \quad & h_{\gamma,2} = \gamma_2^2, \\ \text{with} \quad & \vec{x} \in \chi \text{ and } \kappa_{1,2} \in [0, ..., 1] \end{aligned} \tag{9.24}$$

The obtained three-dimensional Pareto frontier–or more precisely its approximation–is given by figure 9.24. As observable, all three criteria are highly competitive, wherefore a clear and convex Pareto frontier forms. For this frontier, five-teen Pareto efficient criteria, each displaying equal spacing in the criterion space, have been computed. The optimization algorithm needed 351 system response evaluations (FEA and MEA). This underlines the applicability and effectiveness of the gradient-based vector optimization approach.

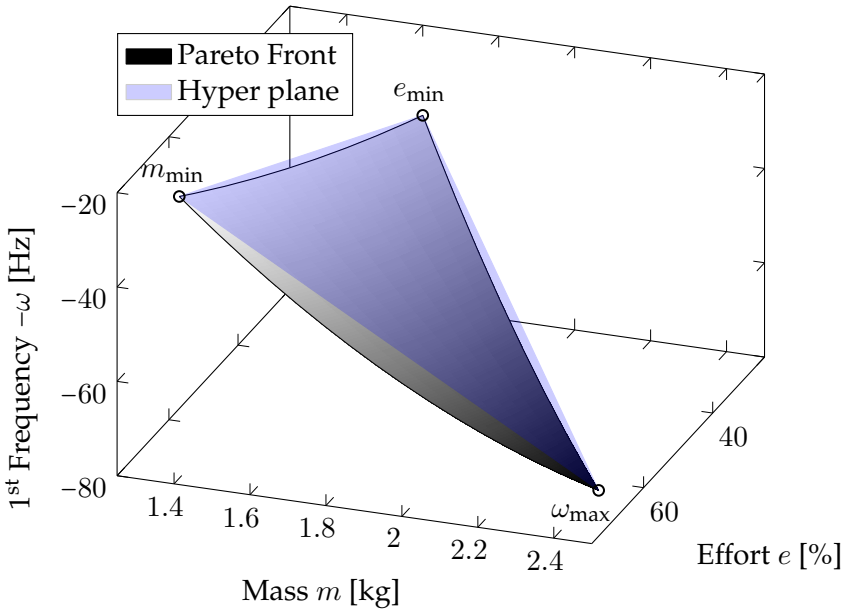

Figure 9.24.: Illustration of the obtained 3D Pareto frontier for the criteria mass m, effort e and frequency ω

9.3. Summary on the conducted vector optimizations

In this chapter, the focal point was lying on multi-criteria optimizations and their post-processing. One major outcome certainly is, that the implemented and deployed gradient-based multi-criteria optimization approach is of general applicability and that it is not solely limited to academic analytical multi-criteria optimization tasks. The approach did further facilitate the investigation of how certain objectives do interact for the investigated propeller, itself representing a sophisticated structural design task. In this regard, the analytical design sensitivities and the efficient exploitation of those, released the full potential of the approach. This has also been reflected by the average number of function calls, which have been way less than two hundred for most of the multi-criteria optimizations. The superior efficiency was also underpinned by contrasting the approach with a state of the art genetic algorithm, which did require more than twenty times the number of function evaluations while still not yielding the same approximation quality of the Pareto frontier. In addition to the appealing numerical efficiency, further advantageous features like the precise evaluation of optimality (KKT conditions for each solution) or the extrapolation at any optimum–either via shadow prices or via sensitivity study at Pareto efficient solutions–could have been identified. Moreover, the approach also revealed how the objective function weights κ can vary over the Pareto frontier making an a priori guess almost impossible for most cases. Nonetheless, if only an optimal compromise is of interest, the geometric interpretation–gained via the conducted investigations–as already being introduced in section 6.2 may help. As discussed there, the scalarization via κ can either be interpreted as a mapping or by a line, for which the intersection with the Pareto frontier shall be found through the optimization.

Lastly, the conducted optimizations gave insight on how the different objectives frequency, mass, manufacturing effort and braiding time lead to distinct designs. This is mainly due to the fact, that the objectives are strongly competing with each other. The following table 9.4 highlights this, by providing the extremal solution of each objective. So, for instance, solely minimizing manufacturing effort results in a design displaying a really low first eigenfrequency of roughly forty Hertz and a moderate mass and braiding time. Trying to resolve this, by maximizing the first eigenfrequency in turn, yields a design evincing really high associated manufacturing efforts in tandem with a high

structural mass and long braiding times, which ultimately also translate into high production costs. Studying this table hence underlines the potential of Pareto frontiers, which do form a great basis for engineers to find most suitable compromises for given design tasks, while simultaneously considering the industrial situation and available means.

Table 9.4.: Extremal optima of the vector optimization task

Objective $\tilde{f}$	Eigenfrequency ω_1 [Hz]	Effort e [-]	Mass m [kg]	Braiding time T_φ [s]
$-\omega_1$	68.8	72.5	2.9	1478
m	35.0	55.1	1.2	1823
e	39.1	25.0	1.6	1116
T_φ	47.2	51.1	2.1	695

Part III.

Postlude

10 | Discussion and findings

This chapter summarizes the conducted research first. Then, the presented research work will be condensed to the gained insights. Finally, an outlook for perspective research work will be given.

Contents

10.1. Summary of the conducted research work

Next a summary on the three core aspects of the conducted research work will be given: incorporation of manufacturing effort, gradient-based vector optimization and optimization of composite structures.

The incorporation of manufacturing effort through soft computing forms one pillar of this thesis. First and foremost, the developed approach of capturing expert knowledge, so as to describe soft aspects via soft computing is applicable to a wide variety of processes. Herein, the manufacturing effort associated with the braiding technology have been captured as well as those, associated with the prepreg lamination. Even though, each manufacturing process has its distinct peculiarities, the developed approach displayed great generality, while still being adaptable to specific demands. It further showed great flexibility in terms of its utilization. As has been investigated with the A-pillar design problem, the manufacturing effort model could be used independently. This is mainly due to the b-spline-based representation of the underlying geometry, where the model fetched all necessary data fully automated. This leveraged the effort model to an independent CAE tool. In this regard, the novel output capability of providing reason $\mathcal{R}$ and elaboration advices $\mathcal{A}$, augmented its CAE capabilities tremendously. This is mainly because, an engineer can precisely comprehend, what lead to the effort level and, moreover, which had the greatest imprint on it and how to optimally re-design. Both responses have only been accessible, because the effort models have been implemented from sketch via object orientation Python scripts. This implementation also revealed that most effort models share a common basis, which can hence be gathered in a base class, which then inherits further classes. Furthermore, the developed approach is appealing within any structural design optimization process, since it has been shown, that the mathematical condition is rather affected in a positive fashion. In addition to that, soft computing relaxes discrete variables, such that they can be considered in gradient-based optimization and the computational effort is neglect-able. Despite of these mentioned advantages, the approach is also subjected to certain limitations. One being, that the approach always relies on the derived knowledge basis and thus only considers knowledge covered throughout the acquisition and derivation of that basis. In that consequence, the approach is not capable of extrapolating knowledge. Another drawback, may be the fact, that the technical

interpretation of the used measure effort could be tedious due to its qualitative nature. Nevertheless, it shall be noted here, that the approach gains most of its advantages out of this qualitative and thus generally valid measure. Moreover, it was shown, how measures such as costs are to be computed by data provided by the effort model.

Another strong pillar of the thesis is given by the developed gradient-based vector optimization approach, which yields equidistantly distributed Pareto optimal solutions. These solutions thereby approximate the continuous Pareto frontier, which in general gathers an infinite number of Pareto efficient solutions. Expanding the design variable vector by the objective function weights, made the afore intricate necessity of defining those a priori redundant. This can specifically regarded as an advantage, because most multi-criteria optimizations, such as those conducted on the propeller, revealed, that those objective weights distribute far from any intuition and can change erratically near the extrema. Beside this, the approach is further controllable in terms of the number of derived Pareto efficient solutions, with which the optimizer can strike a compromise in-between computational effort and the accuracy of the Pareto frontier approximation. In addition to this, the approach showed to be numerically efficient, because of few function evaluations needed. This got immensely amplified by the embedded analytical design sensitivities. These sensitivities in concert with the gradient-based optimization algorithms, also rendered the profound evaluation of optimality and shadow prices possible, which equipped the approach with a sophisticated mathematical basis. Lastly, the thereby computed Pareto frontiers facilitated the decision making on a firm basis. This is pre-eminently due to the visualization of how the individual goals actually compete. On the contrary, two drawbacks could be identified as well. One being the difficulty to interpret Pareto fronts of a higher dimension than three. Obviously, this is because of the impossibility of graphically visualizing hypersurfaces. Further, the general implementation of such a higher dimensional approach can be quite sophisticated, but yet possible. Nonetheless, to draw a conclusion on that, the approach performed superiorly to most alternatives, for the two and three dimensional case.

To close this summary, a general statement concluding the overall general gradient-based optimization of composite structures shall be given. In this thesis two industry relevant composite structures have explicitly been optimized. Both of them had a rather big design space, i.e. the A-pillar structure had almost fifty design variables and involved multiple analysis types ranging from stiffness computation over failure analysis to modal analysis. These aspects did in concert with the multitude of design requirements yield sophisticated and complex composite design tasks. In spite of these challenges, the gradient-based methodology performed more than satisfactory. One fact substantiating this, is the numerical efficiency manifesting in few function evaluations, hence, finite element analyses. This fact has been leveraged by exploiting analytical design sensitivities. These sensitivities where available for each and every analysis type, variable type and model. Despite the upfront implementation effort they caused, they not only amortized the effort spend, but instead reimbursed it multiple times, since most vector optimization would not have been viable without. Beside this, they also enabled a sophisticated post-processing of each and every optima, where optimality could precisely stated, sensitivities and shadow prices utilized to extrapolate further gains and deepen insight. This has for instance been shown for the A-pillar example, where the design sensitivity analysis at the end illuminated the most critical design restrictions and on top pointed out parameters, which influence this situation the most for an optimal design revision.

10.2. Insights gained

This section presents the condensate of the conducted thesis; the gained insights. For the sake of a clear synopsis, the gained insights are grouped and given in itemized format.

Soft computing of manufacturing aspects

Underlying methodology of general applicability: This is because it can be exploited to define models capturing soft aspects of almost any nature, e.g. Klinsiński (1988). Herein, manufacturing effort was described based on verbal expert knowledge base.

Emulates human designing capabilities: Both developed manufacturing effort models (MEMs) compute effort levels upon request. In addition to that, the MEMs provide reason about their evaluations made and return elaboration advices pointing into the direction of optimal design improvement. Owing to all of that, the MEMs shall be regarded as an independent CAE tool, i.e. complementary to classical constructing software.

Soft computing as used is numerically appealing: The approach is numerically efficient in terms of computation times, because of its rather elementary mathematics. This efficiency empowers the fast conduct of sensitivity analyses. It is further appealing, since it can cope with discrete variables, since the fuzzy set theory is inherently compliant to continualization.

Straightforward model development: For a successful MEM development the acquisition and defintion of a knowledge base is essential and this vital step is realizable with only few expert interviews, in case the knowledge engineer pursuits the ideas propagated herein. Adding to this, a object-orientation implementation facilitates the separation of general soft computing methods, such that they only need to be defined and implemented once.

Design optimization of composite structures

Potential of mathematical design optimization: The profound mathematical optimization framework unleashed most of the composite's potential in lightweight design. This is mostly because it handled the multitude of design parameters, different load cases and multiple criteria profoundly.

Soft computing enriches the optimization process: Such that the optimization can yield optimal and significant design proposals, the optimization models need to be as holistic as possible, while still being available at early product development phases and being numerically efficient. Both demands are met by soft computing.

Gradient-based optimization most expedient approach: Based on the experiences made, gradients are less affected by the dimension of the design space, since the computation via analytical approaches is convenient in FEA. The issue of non-convexity was addressed adequately by multiple starting points generated via a DoE. Last but not least, first or second order optimization algorithms share an overwhelming majority in commercial software as well, e.g. `OptiStruct`, `VisualDOC`, `ATOM`, `NASTRAN` and more.

Great flexibility in the formulation of optimization tasks: Studying the optimization on the propeller reveals that not only each response of either the FEM or MEM can be set as an objective or constraint, but further they can be combined or formulated as a multi-criteria optimization task. This underlines the flexibility an engineer has in formulating an optimization task.

Multi-criteria optimization of conflicting goals

Pareto frontiers mitigate issues in decision finding: In industry, engineers seek for optimal compromises in-between many conflicting goals. Since the optimizer may not be familiar with each and every involved discipline and/or the superordinate goals, Pareto frontiers can represent distinguished media for communicating the optimization outcomes to a committee, which then strikes the final design determining compromise.

Forthright formulation of the optimization task: Defining the optimization problem and especially the objective functions is a rather straight forward task, because the optimizer does not face the difficulty of providing weights for objectives a priori; instead, each of the allegedly conflicting goals can be defined as an objective and the post-processing of the multi-criteria optimization then reveals, whether or not these goals have been counteracting and in case yes, where an optimal compromise could lie.

Gradient-based algorithms are applicable as well: Algorithms of higher order can be utilized for computing Pareto optimal solutions by the proposed approach, which then solves for the Pareto optimal solutions efficiently. Moreover, the approximation of the Pareto frontier is of high quality since the computed solutions are equidistantly distributed.

10.3. Outlook

It has been shown, that considering manufacturing effort even in the early design phase–herein realized and discussed via structural design optimization of composites–immensely enriches the significance of the thereby derived designs. Moreover, the developed manufacturing effort models are apparently independent and can thus be regarded as a separate simulation tool within the vast family of CAE tools. This gives room for further investigation of how the effort models are for instance integrable into a CAD software and whether or not they are able to similarly enhance the designing phase. Besides, the underlying soft computing methodology could be applied to other fields as well. Klinsiński (1988) for instance applied it in material modeling, also pointing out an interesting research direction. Another path for extending the conducted research work, is given by leveraging the significance of the optimization process by incorporating more aspects. For instance, the conducted propeller optimization could be augmented by fully coupled structural and fluid simulations, thereby facilitating the investigation of aerodynamics, aeroelasticity and their imprint onto the optimization model's condition and optimization outcomes. Further aspects to be investigated at more detail, are for instance, discrete variables and the optimization considering those. Wehrle and the author have developed a promising approach called APSIS, where the discrete variables are basically relaxed to continuous ones, such that efficient gradient-based approaches (including analytical sensitivity informations) are applicable again (see Schatz et al. (2014)). Integrating APSIS into the outlined optimization process represents another interesting facet of holistic composite design optimization.

A | Appendix

A.1. Homogenization: Incompability in terms of the upper bound

The following equations have already been shown in Schatz (2012). The potential engergy of the composite (heterogenous) for the unit cell Y can be derived to be.

$$U = \int_{\Omega_Y} \frac{1}{2}\sigma_{ij}\epsilon_{ij}\mathrm{d}\Omega$$

This equation can be expanded via pertubating the strain, hence, U is strictly speeking the strain energy.

$$\begin{aligned} U_\epsilon &= \int_{\Omega_Y} \frac{1}{2}\sigma_{ij}(\epsilon_{ij} - \overline{\epsilon}_{ij} + \overline{\epsilon}_{ij})\mathrm{d}\Omega \\ &= \int_{\Omega_Y} \frac{1}{2}\sigma_{ij}(\epsilon_{ij} - \overline{\epsilon}_{ij})\mathrm{d}\Omega + \overline{\epsilon}_{ij}\frac{1}{2}\int_{\Omega_Y} \sigma_{ij}\mathrm{d}d\Omega \end{aligned}$$

Exploiting the fact that rotations are zero, or more precisely, that the antisymmetric part of the gradient is zero $\frac{1}{2}\left(\nabla u - (\nabla u)^T\right) = 0$, yields [Sun and Vaidya (1996)].

$$U_\epsilon = \frac{1}{2}\left\{\int_{\Omega_Y} \sigma_{ij}\left(\frac{\partial u_i}{\partial x_j} - \frac{\partial \overline{u}_i}{\partial x_j}\right)\mathrm{d}\Omega + \overline{\epsilon}_{ij}\int_{\Omega_Y} \sigma_{ij}\mathrm{d}\Omega\right\}$$

Now, assuming that both, $\int_{\Omega_Y} \sigma_{ij}\mathrm{d}\Omega = \overline{\sigma}_{ij}V_Y$ and $\overline{U}_\epsilon = \overline{\sigma}_{ij}\overline{\epsilon}_{ij}V_Y$ hold, further simplifies the equation to;

$$U_\epsilon - \overline{U}_\epsilon = \frac{1}{2}\int_{\Omega_Y} \sigma_{ij}\left(\frac{\partial u_i}{\partial x_j} - \frac{\partial \overline{u}_i}{\partial x_j}\right)\mathrm{d}\Omega$$

With the equilibrium equation $\frac{\partial \sigma_{ij}}{\partial x_j} = 0$ and the Gaussian divergence theorem one can obtain the final identity in which Γ_Y representes the boundary of the unit cell Y. Since Ω_Y covers the volume, Γ_Y accordingly is the surface of the domain [Sun and Vaidya (1996)].

$$U_\epsilon - \overline{U}_\epsilon = \frac{1}{2}\int_{\Omega_Y} \frac{\partial}{\partial x_j}\left\{\sigma_{ij}\left(u_i - \overline{u}_i\right)\right\} \mathrm{d}\Omega$$
$$= \frac{1}{2}\int_{\Gamma_Y} \sigma_{ij}\left(u_i - \overline{u}_i\right) n_j \mathrm{d}\Gamma$$

$$U_\epsilon - \overline{U}_\epsilon = \frac{1}{2}\int_{\Gamma_Y} \sigma_{ij}\left(u_i - \overline{u}_i\right) n_j \mathrm{d}\Gamma \qquad i,j = 1,2,3 \tag{A.1}$$

A.2. Vector optimization: Generalized κ-plots

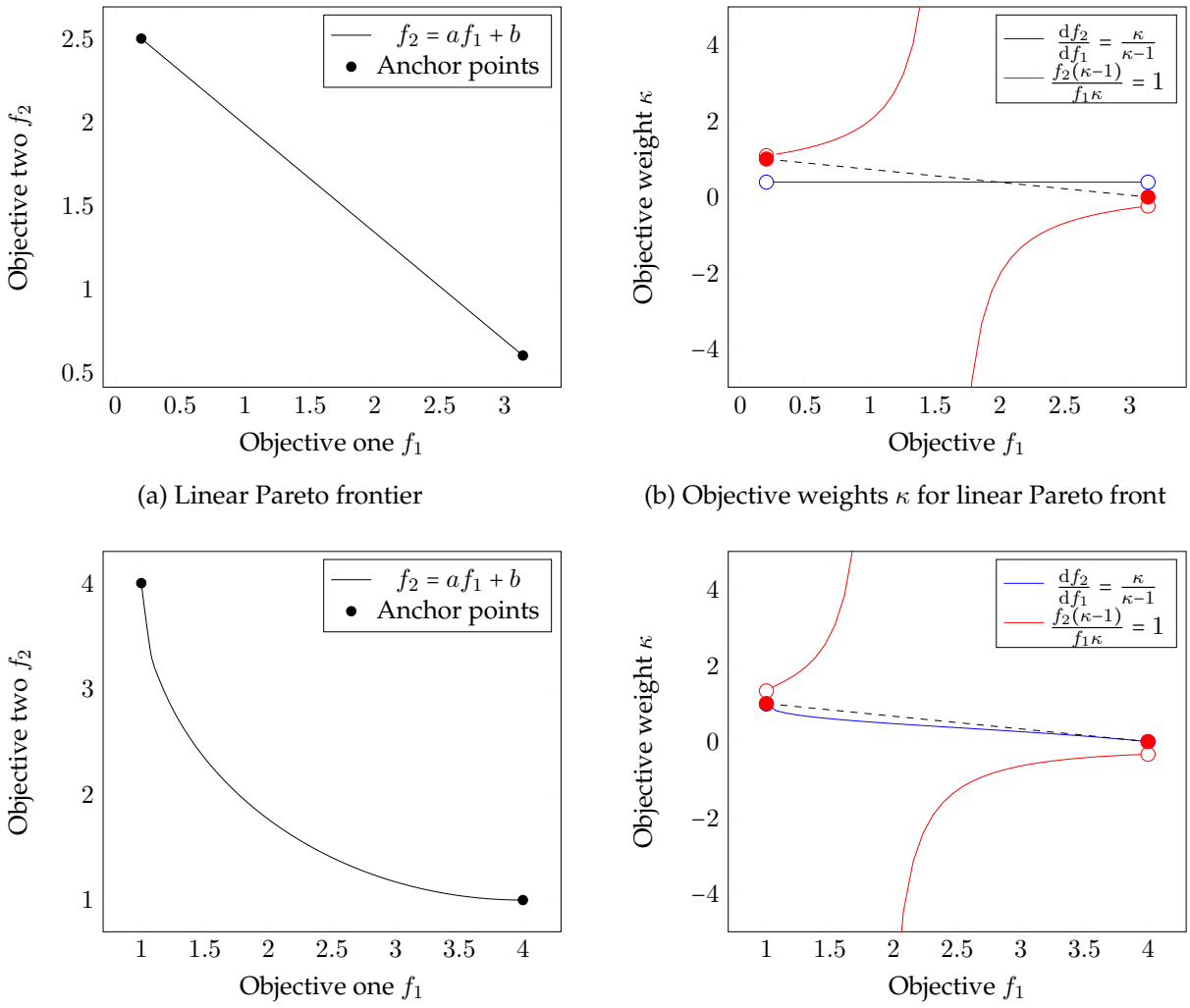

(a) Linear Pareto frontier

(b) Objective weights κ for linear Pareto front

(c) Circular Pareto frontier

(d) Objective weights κ for circular Pareto front

Figure A.1.: Three general abstract Pareto frontiers

A.3. Tri-objective vector optimization example

This analytical example is provided so as to demonstrate the capability of the developed approach for also solving vector optimization problems with more than two objectives. For this sake, the following problem statement is given,

$$
\begin{aligned}
\underset{x\epsilon\chi}{\text{minimize}} \quad & \vec{f} = f_i(x_j), && i = 1,\ldots,3,\ j = 1,\ldots,3 \\
\text{subject to} \quad & g(x_j) \leq 0, \\
\text{with} \quad & \chi = \{x_j \in \mathbb{R}^3 : 0. \leq x_j \leq 5.\}, \\
\text{where,} \quad &
\end{aligned}
\tag{A.2}
$$

$$
\begin{aligned}
f_1 &= x_1 \\
f_2 &= x_2 \\
f_3 &= x_3 \\
\\
g &= (x_1 - 2)^2 + (x_2 - 2)^2 + (x_3 - 2)^2 - 1.5
\end{aligned}
$$

where three objectives have been defined. Because of the analytics, one can determine the set of Pareto efficient solutions, the Pareto frontier Ω_P explicitly. This analytical frontier is being approximated by taking advantage of the implemented vector optimization approach as introduced earlier and plotted next. As can be seen, the approximation $\Omega_{\tilde{P}}$ is almost identical to the analytical one.

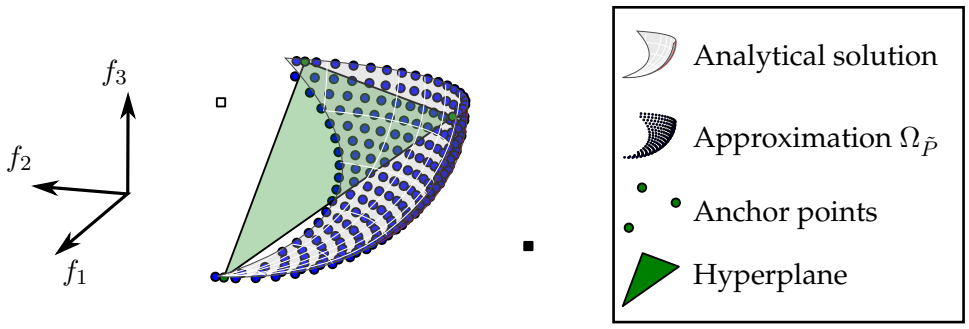

Figure A.2.: Solution of the vector optimization problem given with equation set (A.2)

A.4. Analytical example: Additional Pareto frontiers

Gradient-based Pareto frontier

With figure A.3, the computed approximation of the Pareto frontier of the analytical vector optimization problem of section 7.1 is given. It shall be noted, that the Pareto frontier is analytically determinable via equation (7.5) as well and that both, the computed and the analytical one are almost congruent.

Biologically insprired computation of Pareto optima

In the following, some results computed via the well known and renowned genetic algorithm NSGA-II as implemented in pyOpt by Deb et al. (2002) will be given. The red line in each plot illustrates the analytical solution and the blue points are computed by the GA for a given number of individuals per generation n_I and a total number of generations n_G.

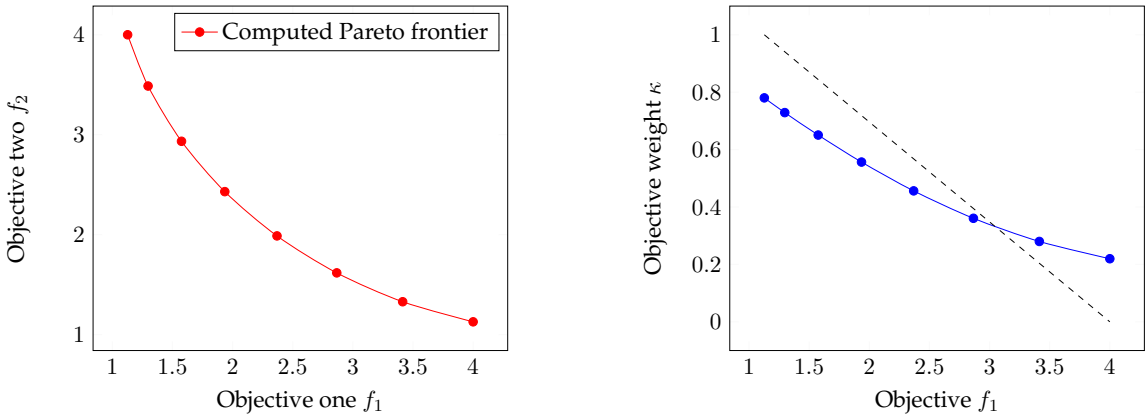

(a) Approximation of Pareto frontier

(b) Plot of objective weights κ

Figure A.3.: Approxmiated Pareto frontier and objective weight plot for the analytical example (see section 7.1)

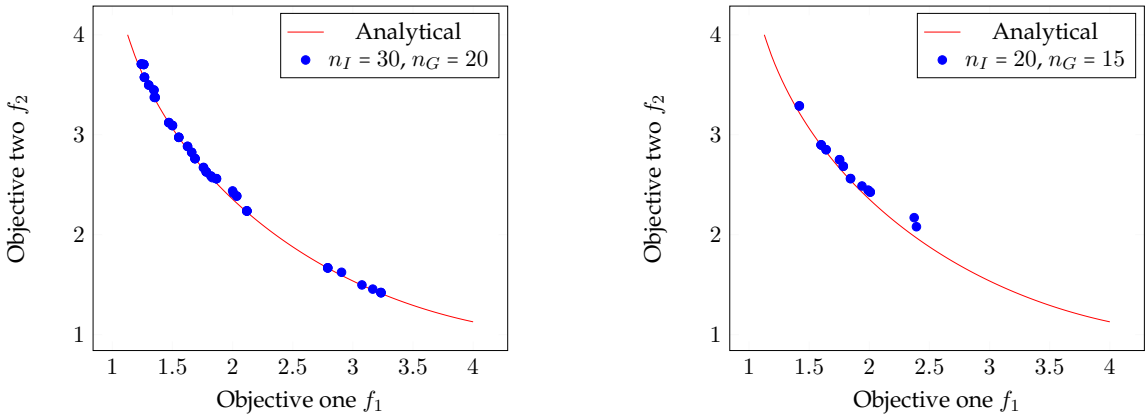

(a) Pareto frontier A

(b) Pareto frontier B

Figure A.4.: Computed Pareto frontiers via NSGA-II: 600 (A) and 300 (B) function calls

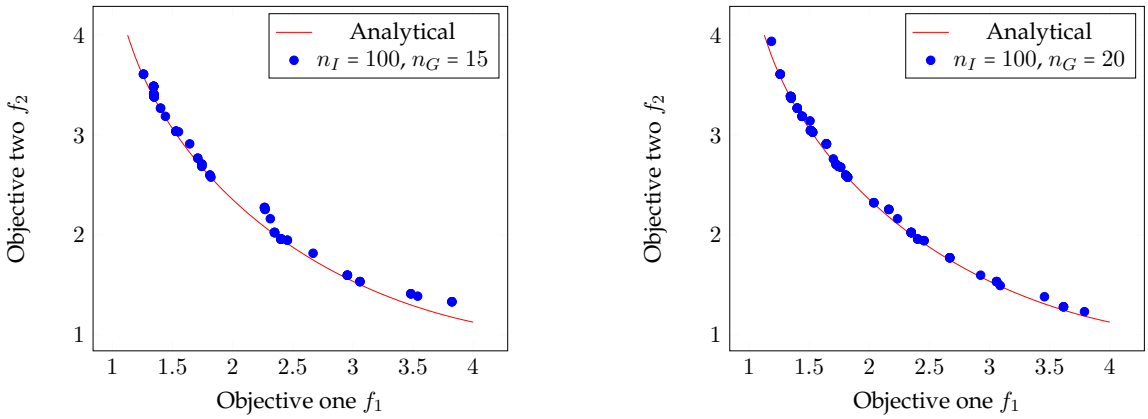

(a) Pareto frontier C

(b) Pareto frontier B

Figure A.5.: Computed Pareto frontiers via NSGA-II: 1500 (A) and 2000 (B) function calls

A.5. A-Pillar example: Supplementary braid results

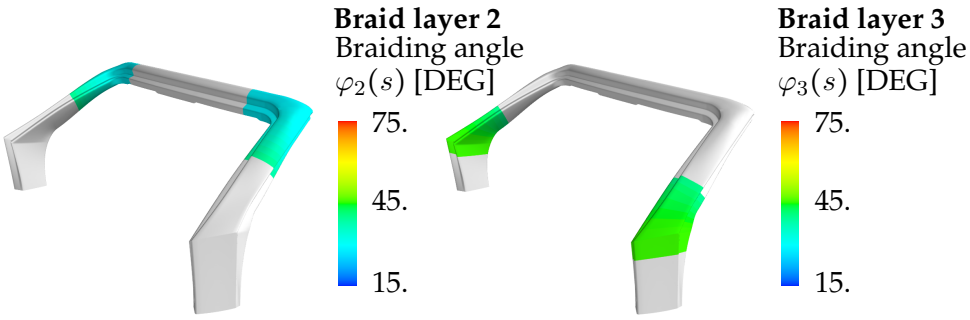

Figure A.6.: Braiding angle distribution $\varphi(s)$ for the second and third braid layer

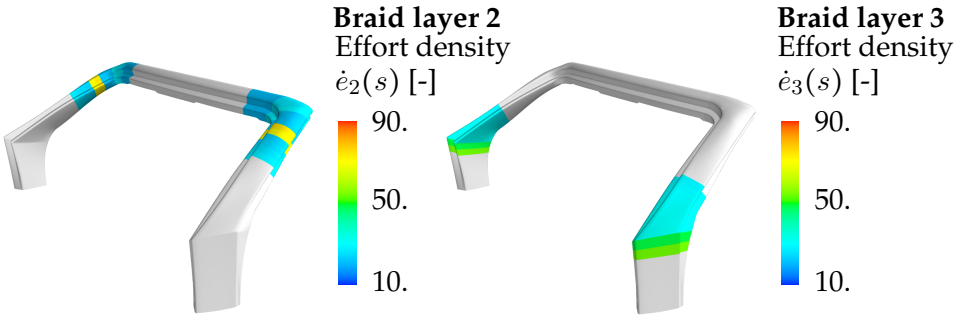

Figure A.7.: Effort density distribution $\dot{e}(s)$ for the second and third braid layer

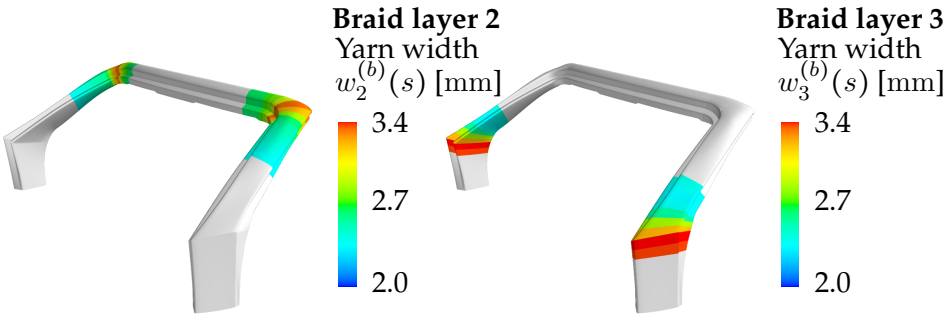

Figure A.8.: Braider yarn width distribution $w^{(b)}(s)$ for the second and third braid layer

A.6. Propeller example: Supplementary plots of the optimal designs

In this section, supplementary propeller results are given. Most of the pictures are discussed in section 9.2 and are therefore referenced from there as well.

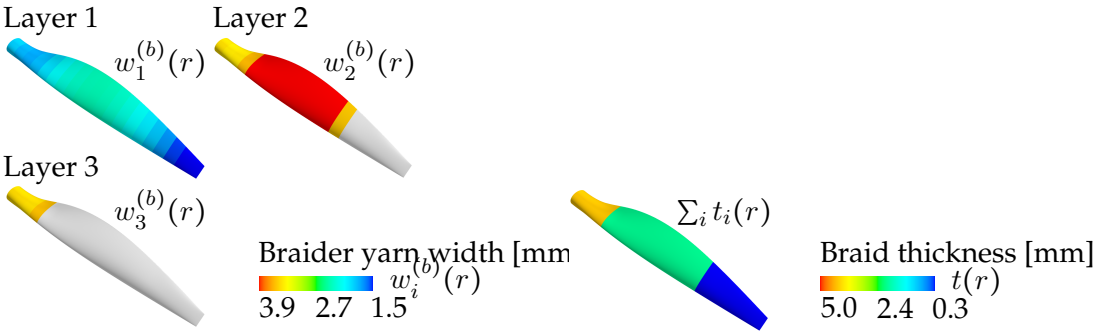

(a) Yarn width $w_i^{(b)}(r)$ of layer i (b) Braid thickness $t(r)$

Figure A.9.: Maximum frequency design of the propeller

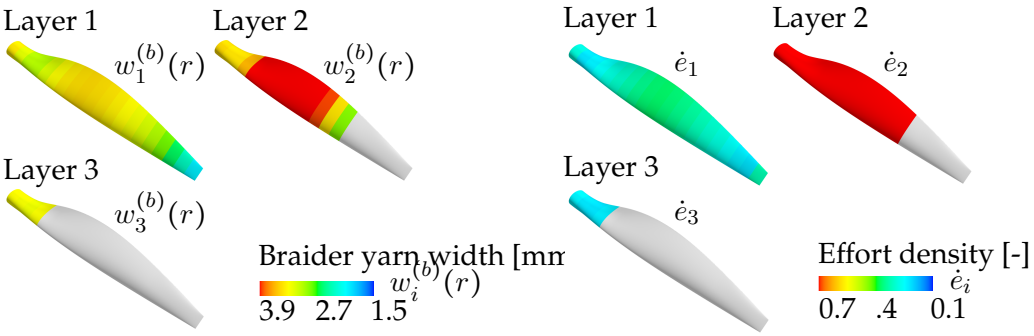

(a) Yarn width $w_i^{(b)}(r)$ of layer i (b) Effort densities $\dot{e}_i(r)$ of layer i

Figure A.10.: Effort-frequency-compromise design of the propeller

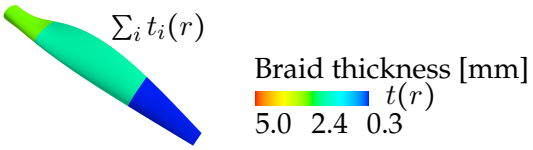

Figure A.11.: Braid thickness $t(r)$ of the effort-frequency-compromise design

A.7. Evaluating utility for the bi-objective optimization mass-frequency of the propeller

The following figure A.12 illustrates the evaluation of the utility U based on the definition in section 6.2.3. However, a slight modification was necessary, since the first natural frequency is maximized, wherefore the utility has to be defined as

$$U = \underbrace{1 - \frac{m^{\text{opt}} - m^{\square}}{m^{\square} - m^{\blacksquare}}}_{\bar{m}} + \underbrace{\frac{\omega_1^{\text{opt}} - \omega_1^{\square}}{\omega_1^{\square} - \omega_1^{\blacksquare}}}_{\bar{\omega_1}}. \tag{A.3}$$

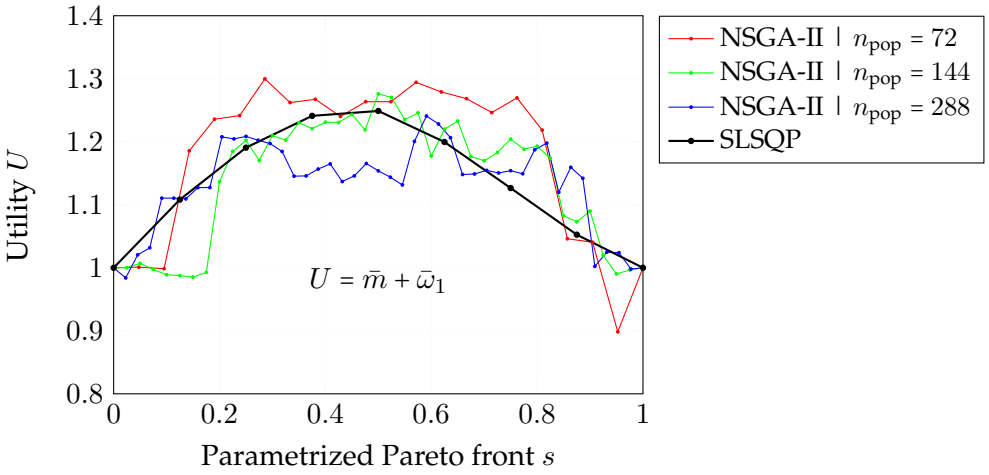

Figure A.12.: Illustration of the utility as defined in section 6.2.3 (more details see Maier (2015))

B | Bibliography

Adam, M. (2014). Study of Optimization Approaches for Mixed-Integer-Nonlinear-Problems. Term thesis, Technical University of Munich, Institute of Lightweight Structures.

Ashby, M. F. (2011). *Material Selection in Mechanical Design*. Elsevier Ltd.

Baier, H. (1977). Über Algorithmen zur Ermittlung und Charakterisierung Pareto-optimaler Lösungen bei Entwurfsaufgaben elastischer Tragwerke. *Zeitschrift für Angewandte Methematik und Mechanik 57*, 318–320.

Baier, H. (1978). *Mathematische Programmierung zur Optimierung von Tragwerken insbesondere bei mehrfachen Zielen*. Doctoral Thesis, Technische Hochschule Darmstadt.

Baier, H., C. Seeßelberg, and B. Specht (1994). *Optimierung in der Strukturmechanik*. Vieweg.

Bendsœ, M. P. and O. Sigmund (1999). Material Interpolation Schemes in Topology Optimization Material Interpolation Schemes in Topology Optimization. *Archive of Applied Mechanics 69*.

Byun, J.-H. (2000). The analytical characterization of 2-D braided textile composites. *Composites Science and Technology 60*, 705–716.

Cheng, F. and D. Li (1997). Multiobjective optimization design with Pareto genetic algorithm. *Journal of Structural Engineering*, 1252–1261.

Cunha, N. O. D. and E. Polak (1967). Constrained minimization under vector-valued criteria in finite dimensional spaces. *Journal of Mathematical Analysis and Applications 19.1*, 103–124.

Curtiss-Wright-Corporation (1944). *Propeller Theory*. Curtiss-Wright corporation, Propeller division.

Daniel, I. and O.Ishai (2010). *Engineering Mechanics of Composite Materials*. Oxford University Press.

Deb, K., A. Pratap, S. Agarwal, and T. Meyarivan (2002). A fast and elitist multiobjective genetic algorithm: NSGA-II. *Evolutionary Computation, IEEE Transactions on 6*, 182–197.

Dimopoulos, C. and A. M. S. Zalzala (2000). Recent Developments in Evolutionary Computation for Manufacturing Optimization: Problems, Solutions and Comparisons. *IEEE Transactions of evolutionary computation 4*, 93–113.

Dolansky, C. (2014). Strukturoptimierung einer CFK-Karosserie unter Berücksichtigung von Fertigungsaspekten. Master's thesis, Technical University of Munich, Institute of Lightweight Structures.

DOT (2006). *Laboratory test procedure for FMVSS 216 roof crush resistance*. U.S. Department of transportation.

Eberhart, R. C. (2014). *Neural network PC tools: a practical guide*. Academic Press.

Edgeworth, F. Y. (1881). *Mathematical physics and other essays*. James & Gordon.

Ehrgott, M. (2005). *Multicriteria Optimization*. Springer.

Ehrmann, M. (2013). Entwicklung, Test und Anwendung eines Algorithmus zur gleichzeitigen Materialwahl und Dimensionierung von Strukturen. Diploma thesis, Technical University of Munich, Institute of Lightweight Structures.

Eiperle, P. (2014). Enhancement and Study of a Gradient-based Optimization Algorithm for Mixed-Integer-Nonlinear-Problems by Consideration of Shape Selection. Termthesis, Technical University of Munich, Institute of Lightweight Structures.

Eshelby, J. (1957). The Determination of the Elastic Field of an Ellipsoidal Inclusion and Related Problems. *Proceedings of the Royal Society A241*, 376–396.

Flach, S. T. (2014). Entkoppelte Mehrskalenhomogenisierung von Flechtstrukturen mittels Metamodellierung unter Berücksichtigung des Puck-Versagenskriteriums. Master's thesis, Technical University of Munich, Institute of Lightweight Structures.

Fonseca, C. M. and P. J. Fleming (1993). Genetic Algorithms for multiobjective optimization: formulation, discussion and generalization. *The fifth International Conference on Genetic Algorithms*, 416–423.

Forrester, A. I., A. Sóbester, and A. J. Keane (2008). *Engineering Design via Surrogate Modelling - A Practical Guide*. Wiley.

Ghiasi, H., L. Lessard, D. Pasini, and M. Thouin (2010). Optimum Structural and Manufacturing Design of a Braided Hollow Composite Part. *Applied Composite Materials 17*, 159–173.

Ghiasi, H., D. Pasini, and L. Lessard (2008). Constraint Globalized Nelder-Mead Method for Simultaneous Structural and Manufacturing Optimization of a Composite Bracket. *Journal of Composite Materials 42*, 717–736.

Gürdal, Z. and R. Haftka (1992). *Elements of structural optimization*. Kluwer.

Hajela, P. (2002). Soft computing in multidisciplinary aerospace design - New directions for research. *Aerospace Sciences 38*, 1–21.

Harnischfeger, M. (2015). Testing of Polymer Composite Piping Components with Multilayer Fiber Architectures. Bachelor thesis, Technical University of Munich, Institute of Lightweight Structures.

Hashin, Z. and S. Shtrikman (1963). A variational approach to the theory of the elastic behaviour of multiphase materials. *Journal of the Mechanics and Physics of Solids 11*, 127–140.

Häußler, M. (2014). Optimal Composite Piping Design Considering Structural Integrity and Leakage Failure. Term thesis, Technical University of Munich, Institute of Lightweight Structures.

Häußler, M., M. Schatz, H. Baier, and P. Mertiny (2015). Optimization of polymer composite pipe under consideration of hybridization. *ASME 2015 Pressure Vessels and Piping Conference*.

Hayes-Roth, F., D. Waterman, and D. Lenat (1984). *Building expert systems*. Addison-Wesley.

Henderson, J. L., Z. Gürdal, and A. C. Loos (1999). Combined Structural and Manufacturing Optimization of Stiffened Composite Panels. *Journal of Aircraft 36*, 246 – 254.

Huang, J., L. Gao, and X. Li (2015). An effective teaching-learning-based cuckoo search algorithm for parameter optimization problems in structure designing and machining processes. *Applied Soft Computing*, 349–356.

Huber, M. (2010). *Structural Design Optimization Including Quantitative Manufacturing Aspects Derived from Fuzzy Knowledge*. Doctoral Thesis, Technical University of Munich.

Iqbal, A., N. He, L. Li, and N. U. Dar (2007). A fuzzy expert system for optimizing parameters and predicting performance measures in hard-milling process. *Expert Systems with Applications 32*.

Irisarri, F.-X., A. Lasseigne, F.-H. Leroy, and R. L. Riche (2014). Optimal design of laminated composite structures with ply drops using stacking sequence tables. *Composite Structures 107*, 559–569.

Jones, R. M. (1999). *Mechanics of Composite Materials*. Taylor & Francis Inc.

Jörg, P. (2014). Development of a method for the creation of a fully parametrized finite element model using the example of an A pillar. Term thesis, Technical University of Munich, Institute of Lightweight Structures.

Kaddour, A. S. and M. J. Hinton (2013). Maturity of 3D failure criteria for fibre-reinforced composites: Comparison between theories and exerpiments: Part B of WWFE-II. *Journal of Composite Materials*.

Kanouté, P., D. Boso, J. Chaboche, and B. Schrefler (2009). Multiscale Methods for Composites: A Review. *Archives of Computational Methods in Engineering 16.1*, 31–75.

Kastner, D. (2014). Structural optimization of the CFRP monocoque of a lightweight vehicle for an efficiency competition. Term thesis, Technical University of Munich, Institute of Lightweight Structures.

Klinsiński, M. (1988). Plasticity Theory Based on Fuzzy Sets. *Journal of Engineering Mechanics 114*(4), 563–582.

Knaier, T. (2015). Entwicklung einer Vorrichtung zum automatischen Schneiden einzelner Lagen einer Flechtpreform. Term thesis, Technical University of Munich, Institute of Lightweight Structures.

Köhler, M.-A. (2014). Gradient-based mixed-integer optimization of prepreg composite structures considering manufacturing effort and restrictions. Master's thesis, Technical University of Munich, Institute of Lightweight Structures.

Kraft, D. (1988). *A software package for sequential quadratic programming*. DLR German Aerospace Cetner - Institute for Flight Mechanics.

Kuhn, H. and A. Tucker (1951). Nonlinear programming. *Proceedings of the Second Berkeley Symposium on Mathematical Statistics and Probability*, 481–492.

Langer, H. (2005). *Extended Evolutionary Algorithms for Multiobjective and Discrete Design Optimization of Structures*. Doctroal thesis, Technical University of Munich.

Langer, H., T. Pühlhofer, and H. Baier (2004). A Multiobjective Evolutionary Algorithm with Integrated Response Surface Functionalities for Configuration Optimization with Discrete Variables. *Proceedings 10th AIAA/ISSMO Multidisciplinary Analysis and Optimization Conference*.

Lee, S. (2014). Konzeptstudie zum Einsatz eines endlosfaserverstärkten thermoplastischen Integralbauteils in Karosseriestrukturen. Master's thesis, Technical University of Munich, Institute of Lightweight Structures.

Leitmann, G. (1977). Some problems of scalar and vector-valued optimization in linear viscoelasticity. *Journal of Optimization Theory and Application 23*, 93–99.

Liao, S.-H. (2004). Expert system methodologies and applications – a decade review from 1995 to 2004. *Expert Systems with Applications*.

Lin, H., L. P. Brown, and A. C. Long (2011). Modelling and Simulating Textile Structures using TexGen. *Advanced Materials Research 331*, 44–47.

Lindsay, R. K., B. G. Buchanan, E. A. Feigenbaum, and J. Lederberg (1993). DENDRAL: A Case Study of the First Expert System for Scientific Hypothesis Formation. *Artificial Intelligence 61*, 209–261.

Long, A. C. and L. P. Brown (2011). *Composite reinforcements for optimum performance: Modelling the geometry of textile reinforcements for composites: TexGen*. Woodhead Publishing.

Luger, G. F. (2004). *Artificial Intelligence: Structures and Strategies for Complex Problem Solving*. Addison-Wesley.

Lukkassen, D., L.-E. Persson, and P. Wall (1995). Some engineering and mathematical aspects on the homogenization method. *Composite Engineering 5*, 519–531.

Maier, E. (2015). Vectoroptimization in EOS - Verification and Application. Master's thesis, Technical University of Munich, Institute of Lightweight Structures.

Mamdani, E. H. and S. Assilian (1975). An experiment in linguistic synthesis with a fuzzy logic controller. *Interantional Journal of Men-Machine Studies 7*, 1:13.

Marler, R. and J. Arora (2004). Survey of multi-objecitve optimization methods for engineering. *Structural and multidisciplinary optimization 26*(369-395).

Mazumdar, S. K. (2002). *Composite Manufacturing - Materials, Product and Process Engineering*. CRC Press LLC.

Miles, J. C. and C. J. Moore (2012). *Practical knowledge-based systems in conceptual design*. Springer Science & Business Media.

Müller, P. (2015). Entwicklung einer effektiven Methode zur Optimierung von kurzfaserversärkten Spritzgußbauteilen. Master's thesis, Technical University of Munich, Institute of Lightweight Structures.

Nadir, W., I. Y. Kim, and O. L. de Weck (2004). Structural shape optimization considering both performance and manufacturing cost. In *10th AIAA/ISSMO Multidisciplinary Analysis and Optimization Conference*, Volume 30.

Nagarajan, P. (2015). Incorporation of 3D Failure Criteria in Optimization of CFRP Chopper Disks. Master's thesis, Technical University of Munich, Institute of Lightweight Structures.

Nguyen, H. T. and M. Sugeno (2012). *Fuzzy systems: modeling and control*. Springer Science & Business Media.

Oertel, E. H. (2003). *Numerische Strömungsmechanik*. Braunschweig Wiesbaden.

Pareto, V. (1906). *Manuel d'économie politique*. F. Rouge.

Park, C. H., W. I. Lee, W. S. Han, and A. Vautrin (2004). Simultaneous optimization of composite structures considering mechanical performance and manufacturing cost. *Composite Structures 65*, 117–127.

Pereyra, V., M. Saunders, and J. Castillo (2013). Equispaced pareto front construction for constrained biobjective optimization. *Mathematical and Computer Modelling 57(9)*, 2122–2131.

Perez, R. E., P. W. Jansen, and J. R. R. A. Martins (2012). pyOpt: A Python-Based Object-Oriented Framework for Nonlinear Constrained Optimization. *Structures and Multidisciplinary Optimization 45*, 101–118.

Puck, A. (1996). *Festigkeitsanalyse von Faser-Matrix-Laminaten - Modelle für die Praxis*. Hanser.

Rao, S. S. (2009). *Engineering Optimization - Theory and Practice*. John Wiley & Sons Inc.

Rödl, S. (2014). Geometriebasierte Strukturoptimierung einer C-Faser geflochtenen A-Säule mit integriertem Meso-Materialmodell. Master's thesis, Technical University of Munich, Institute of Lightweight Structures.

Rosenman, M. A., J. S. Gero, P. J. Hutchinson, and R. Oxman (1986). Expert systems applications in computer-aided design. *Computer-Aided Design 18*(10), 546 – 551.

Russell, S. and P. Norvig (2009). *Artificial Intelligence: A Modern Approach* (3rd ed.). Prentice Hall.

Schaffer, J. D. (1985). Multiple objective optimization with vector evaluated genetic algorithms. *The First International Conference on Genetic Algorithms and their Applications*, 93–100.

Schatz, M. (2012). Multiscale Homogenization of Viscoelastic Unidirectional Composites. Diploma thesis, Space Structes Laboratory (CalTech).

Schatz, M. and H. Baier (2014). Structural optimization of braided structures including soft aspects such as manufacturing effort. In *Mechanics of Composites*.

Schatz, M., E. Wehrle, and H. Baier (2014). Structural design optimization of lightweight structures considering material selection and sizing. In *International Conference on Engineering Optimization*.

Schitttkowski, K. (2010). A robust implementation of a sequential quadratic programming algorithm with successive error restoration. *Optimization letters 5*, 283–296.

Schroll, M. (2013). Untersuchung analytischer Gradienten transienter nichtlinearer Strukturantworten nach Entwurfsvariablen anhand eines ebenen Fachwerks. Bachelor thesis, Technical University of Munich, Institute of Lightweight Structures.

Schürmann, H. (2005). *Konstruieren mit Faser-Kunststoff-Verbunden*. Springer.

Schwarz, C. (2013). Analysis and extension of composite optimization under manufacturing and strength constraints with OptiStruct. Master's thesis, Technical University of Munich, Institute of Lightweight Structures.

Shortliffe, E. H. and B. G. Buchanan (1975). A model of inexact reasoning in medicine. *Mathematical Biosciences 23*, 351–379.

Singh, G., B. Singh, and S. Singh (2012). Application of Artificial Intelligence Computational Techniques in Engineering Perspective: A Survey. *Artificial Intelligence and Soft Computing*, 56.

Siroky, G. (2014). Materialmodellierung von CFK-Flechtstrukturen und ihr Einfluss auf die Strukturantwort. Bachelor thesis, Technical University of Munich, Institute of Lightweight Structures.

Sobieszczanksi-Sobieski, J., A. Morris, and M. J. van Tooren (2015). *Multidisciplinary Design Optimization supported by Knowledge Based Engineering*. Wiley.

Stadler, J. (2015). Entwicklung und Implementierung eines Algorithmus zur Optimierung kurzfaserversärkter Druckgussbauteile. Term thesis, Technical University of Munich, Institute of Lightweight Structures.

Stadler, W. (1984). Multicriteria optimization in mechanics (A survey). *Applied mechanics revies 37*, 277–286.

Stadler, W. (1988). *Multicriteria Optimization in Engineering and in the Sciences*. Springer Science & Business Media.

Stegmann, J. and E. Lund (2004). Discrete Material Optimization of General Composite Shell Structures using a Discrete Constitutive Parameterization. *International Congress of Theoretical and Applied Mechanics*.

Sun, C. and R. Vaidya (1996). Prediction of composite properties from a representative volume element. *Composite Science and Technology 56*, 171–179.

Svanberg, K. (2005). The method of moving asymptotes - a new method for structural optimization. *Numberical methods in engineering 24*, 359–373.

Swanson, S. R. and L. V. Smith (1996). Comparison of the biaxial strength properties of braided and laminated carbon fiber composites. *Composites: Part B 27*, 71–77.

Swoboda, S. (2014). Parameterische Untersuchung des Einflusses von Prozessgrößen beim Spritzgießen auf das mechanische Bauteilverhalten. Master's thesis, Technical University of Munich, Institute of Lightweight Structures.

Thomas, R. (2014). MAI-Design: Flechttest in Kooperation mit dem IFB Stuttgart. Data sheets.

Tu, J., G. H. Yeoh, and C. Liu (2008). *Computation Fluid Dynamics: A Practical Approach*. Elsevier Ltd.

Vanderplaats, G. N. (1973). *CONMIN: A Fortran program for constrained function minimization*. Technical Memorandum TM X-62282.

Vanderplaats, G. N. (2007). *Multidiscipline Design Optimization*. Vanderplaats Research & Development Inc.

Wang, B. P. and D. P. Costin (1991). Optimum Design of a Composite Structure with Three Types of Manufacturing Constraints. *AIAA Journal 30*(6).

Wegmann, M. (2015). Parameteruntersuchung eines Faserverbundwerkstoffmodells unter Berücksichtigung progressiven Versagens nach Puck. Term thesis, Technical University of Munich, Institute of Lightweight Structures.

Wehrle, E. J. (2015). *Design optimization of lightweight space frame structures considering crashworthiness and uncertainty*. Doctoral Thesis, Technical University of Munich.

Weinzierl, M. (2014). A study of the structural dynamics of chopper disks. Master's thesis, Technical University of Munich, Institute of Lightweight Structures.

Witten, E., T. Kraus, and M. Kühnel (2014). Composites-Marktbericht 2014. *CC and AVK*.

Wrenn, G. (1989). An indirect method for numerical optimization using the Kreisselmeier-Steinhauser function. *Contrator Report NASA CR-4220*.

Xu, Q. (2014). *Extended Surrogate Modeling Techniques for Large Scale Structural Design Optimization*. Doctoral Thesis, Technical Univeristy of Munich - Institute of Lightweight Design.

Yildiz, A. R. (2013). A new hybrid differential evolution algorithm for the selection of optimal machining parameters in milling operations. *Applied Soft Computing 13*, 1561–1566.

Yu, Q. and J. Fish (2002). Multiscale asymptotic homogenization for multiphysics problems with multiple spatial and temporal scales: a coupled thermo-viscoelastic example problem. *International Journal of Solids and Structures 39*, 6429–6452.

Yu, V. L., L. M. Fagan, S. M. Wraith, W. J. Clancey, A. C. Scott, J. Hannigan, R. L. Blum, B. G. Buchanan, and S. N. Cohen (1979). Antimicrobial Selection by a Computer - A Blinded Evaluation by Infectious Diseases Experts. *The Journal of American Mecial Association 242*, 1279–1282.

Zadeh, L. A. (1965). Fuzzy sets. *Information Control 8*, 338–353.

Zadeh, L. A. (1994). Fuzzy Logic, Neural Networks, and Soft Computing. *Communications of the ACM 37*, 77–84.

Zhou, Y. and K. Saitou (2015). Multi-Objective Topology Optimization of Composite Structures Considering Resin Filling Time. In *Procedings of the 11th World Congress of Structural and Multidisciplinary Optimisation (WCSMO-11)*.